

**Cover illustration**

The Dome station at the Amundsen-Scott South Pole base illuminated by the aurora australis  
(photograph by Robert Schwarz, design by Sofie Vermeulen)



Vrije Universiteit Brussel



Faculteit Wetenschappen  
Departement Natuurkunde

---

# Search with the AMANDA detector for neutralino dark matter in the Sun

---

**Daan Hubert**

Promotor: Prof. Dr. Catherine De Clercq

Proefschrift ingediend met het oog op het behalen van  
de academische graad Doctor in de Wetenschappen

Mei 2009

## **Doctoral examination commission**

Chair: Prof. Dr. Robert Roosen (VUB)

Supervisor: Prof. Dr. Catherine De Clercq (VUB)

Prof. Dr. Per Olof Hulth (Stockholm University)

Prof. Dr. Carlos de los Heros (Uppsala University)

Prof. Dr. Ben Craps (VUB)

Prof. Dr. Irina Veretennicoff (VUB)

# Acknowledgements

This is probably the most important page in my doctoral dissertation. Not only because it is the very first page that the reader is looking for, but also because I, as the author, want to express my gratitude to several people.

I acknowledge the Interuniversity Institute for High Energies (IIHE), IWT-Vlaanderen, FWO-Vlaanderen and OZR-VUB, without whom this work would never have been possible in the first place. I want to thank my supervisor Catherine De Clercq for introducing me to dark matters and for giving me all these wonderful, unforgettable opportunities (especially the South Pole!!!) in the last couple of years.

The AMANDA/IceCube group at the IIHE has changed a lot during my membership. I thank my hard working fellow PhD students Alfio, Mathieu and Sabrina for the discussion, distraction and help. Believe me, your reward is coming a little closer each day. Even though their PhDs are already written and deserved, I still want to support Daniel, Philip, Peter, Othmane, Patrick, Bruny and Kael in their ongoing work. It has always been a pleasure to watch and learn from you. Furthermore, I should apologise to the Belgian AMANDA/IceCube groups in Mons and Gent, for they had to bear my completely incomplete ideas during our internal meetings. These were the best occasions to do so! I felt happy to be part of a large international collaboration, since it allowed me to meet people and their viewpoints from all over the world. Especially the Swedish collaborators, vital for the WIMP working group, were great fun to hang around with. I owe a special thanks to Thomas and Gustav, for their input in the likelihood-ratio code, and to Henrik, for being such an enthusiastic colleague astronaut.

I was lucky enough to be taken under the skilled wings of the IIHE secretaries Rosine and Marleen. Paperwork was never my worry, whenever I made a mess of it, sorry! The people in the computing support team probably have the most ungrateful job in the world, but they should know that they were essential in the success of this work. I also thank all the other IIHE members for showing our surrealistic country that cooperation over the language border is possible and needed. The time with Steven and Benoît at the BND summer schools was unforgettable, especially the moment our IIHE van ran out of gas. Finally, I can not forget my office mates Jorgen, who served as my analysis sounding board even when I couldn't make a clue out of what he said, and Olbren, who reminded me that I should keep smiling during work. All the best!

Dichter bij huis, bedank ik alle vrienden en voorbijgangers voor de vele ongelofelijk fijne momenten samen. Ik noem geen namen, want dat doet enkel onrecht aan degenen die me op dit troebele uur ontsnappen. Ik voel jullie steun en draag jullie allen in mijn hart, zelfs al ben ik al te vaak afwezig. Jan en Eileen, jullie verdienen een gouden regel, al was het maar omdat jullie de hobbelige rit zo zacht mogelijk probeerden te houden. Daar zal ik

jullie altijd dankbaar voor zijn. Ook mijn familie (mama, papa, Ben, Maud, ...) was er steeds met een warm nest wanneer nodig, vanaf de zijlijn moet het soms moeilijk toekijken geweest zijn. Sofie, mijn liefste, ontdaan van alle franje voelt enkel het simpelste zo juist aan: dank je om er te zijn, zelfs wanneer ik heel veraf was... De volgende woorden schenk ik jou...

**Om niet te verdwalen**

(Stef Bos)

heb ik de chaos  
toegelaten  
De weg  
weggedacht  
De sporen  
uitgewist  
De liefde  
geen gezicht gegeven  
De waarheid  
de deur gewezen  
En de spiegel  
ontoerekeningsvatbaar  
verklaard

En nog  
zoekt de klank  
een woord  
om thuis te komen

Om niet te verdwalen  
spreek ik een taal die ik niet ken  
En praat ik over alles  
waarvan ik niets weet

Bedreven  
in de onkunde  
ben ik  
om niet  
te verdwalen

# Contents

<b>Acknowledgements</b>	<b>v</b>
<b>Contents</b>	<b>vii</b>
<b>Introduction</b>	<b>1</b>
<b>1 The case for dark matter</b>	<b>3</b>
1.1 Evidence for dark matter	3
1.1.1 (R)evolutions in cosmology	3
1.1.2 The dark matter in $\Lambda$ CDM	6
1.1.3 The dark halo around the Milky Way	8
1.1.4 Challenges for dark matter	9
1.2 The lightest neutralino as dark matter	9
1.2.1 Necessary properties of dark matter	10
1.2.2 The lightest neutralino	11
1.2.3 Alternative candidates	13
1.3 Detection of dark matter	14
1.3.1 Collider searches	14
1.3.2 Direct searches	15
1.3.3 Indirect searches	17
<b>2 Neutrinos as neutralino probe</b>	<b>23</b>
2.1 Neutrinos from neutralinos in the Sun	23
2.1.1 Solar capture and annihilation	23
2.1.2 Neutrino oscillations	25
2.1.3 Neutrino interactions	26
2.2 Neutrino detection	28
2.2.1 Charged particles in ice	28
2.2.2 The Čerenkov effect	30
2.2.3 Neutrino signatures	31
2.2.4 Backgrounds	32
2.3 Experimental aspects	33
2.3.1 Conversion rate, annihilation rate and muon flux	33
2.3.2 Model independence	34

<b>3</b>	<b>The AMANDA-II neutrino telescope</b>	<b>37</b>
3.1	Characteristics of South Pole ice . . . . .	37
3.1.1	A short history of ice . . . . .	37
3.1.2	Optical properties of deep South Pole ice . . . . .	39
3.2	The AMANDA-II detector . . . . .	42
3.2.1	Geometry . . . . .	42
3.2.2	Operation . . . . .	43
3.2.3	Calibration . . . . .	48
3.2.4	Neighbouring detectors . . . . .	49
<b>4</b>	<b>Data samples</b>	<b>51</b>
4.1	Experimental data . . . . .	51
4.1.1	Data taking period . . . . .	51
4.1.2	Detector stability . . . . .	52
4.1.3	Detector live-time . . . . .	54
4.1.4	Sample definition . . . . .	56
4.2	Simulated data . . . . .	58
4.2.1	The AMANDA simulation chain . . . . .	58
4.2.2	Physics generators . . . . .	58
4.2.3	Muon propagation . . . . .	63
4.2.4	Photon propagation . . . . .	63
4.2.5	Detector simulation . . . . .	64
4.2.6	Simulation weighting schemes . . . . .	64
4.2.7	Checking the simulation . . . . .	67
<b>5</b>	<b>From raw data to event observables</b>	<b>71</b>
5.1	Preprocessing . . . . .	71
5.1.1	Calibration . . . . .	71
5.1.2	Hit cleaning . . . . .	72
5.1.3	Event cleaning . . . . .	73
5.1.4	File cleaning . . . . .	74
5.2	Event reconstruction . . . . .	74
5.2.1	Maximum likelihood reconstruction . . . . .	75
5.2.2	First guess methods . . . . .	79
5.3	Event observables . . . . .	80
5.3.1	Topology . . . . .	80
5.3.2	Reconstruction . . . . .	80
5.3.3	Hit-reconstruction . . . . .	81
5.4	Data processing software . . . . .	81
<b>6</b>	<b>Event selection</b>	<b>83</b>
6.1	Effective volume . . . . .	83
6.2	Trigger level . . . . .	84
6.3	Filter level 1 . . . . .	86
6.4	Filter level 2 . . . . .	90
6.5	Filter level 3 . . . . .	93

---

6.5.1	Introduction	95
6.5.2	Precuts	98
6.5.3	Optimization procedure	98
6.5.4	Results	105
6.6	Final sample	113
<b>7</b>	<b>Measurement of number of signal events</b>	<b>119</b>
7.1	The space angle to the Sun	119
7.2	Confidence interval for $\mu$	122
7.2.1	Space angle pdf	122
7.2.2	Signal content likelihood	123
7.2.3	Construction of the confidence interval	124
7.2.4	Properties of the confidence intervals	128
7.3	Results	130
7.3.1	Single stream $\mu$ : definition of the L3 filter	130
7.3.2	Combining all streams: final results	131
7.3.3	Effect of pdf binning	133
<b>8</b>	<b>Measurement of the neutralino-induced muon flux</b>	<b>135</b>
8.1	Uncertainties on $\mu$ , $V_{\text{eff}}$ and $t_{\text{live}}$	135
8.1.1	Statistical uncertainties	135
8.1.2	Systematic uncertainties	136
8.1.3	Total uncertainty	144
8.2	Calculation of physical quantities	146
8.2.1	Conversion rate	146
8.2.2	Annihilation rate	146
8.2.3	Muon flux	147
8.2.4	Neutralino-proton cross section	147
8.2.5	Incorporation of uncertainties	148
8.3	Final results	149
8.4	Comparison with other experimental results	153
8.4.1	Muon flux	153
8.4.2	Cross sections	155
<b>9</b>	<b>Conclusions and outlook</b>	<b>157</b>
	<b>Bibliography</b>	<b>161</b>
	<b>Glossary</b>	<b>173</b>
	<b>Samenvatting</b>	<b>175</b>



# Introduction

Whether invisible matter exists in the universe or not is since its first conjecture by Fred Zwicky in 1933 and especially since the measurements of the rotational velocity of galaxies in the 1970s one of the central questions in cosmology. In the last few decades astronomers have observed the gravitational influence of this so-called dark matter at all cosmic distance scales, thereby gradually accepting the dark matter as an inevitable element in the description of the composition of the universe. Today, most cosmologists are convinced that the majority of the matter in the universe is dark. Except for strong indications that it concerns non-baryonic particles, the cosmic observations remain inconclusive about the further physical nature of the dark matter. Unfortunately, the Standard Model of elementary particle physics does not provide a solution either, e.g. in the form of a known particle with the required properties. Therefore, the mystery around the nature of the dark matter may as well have far-reaching implications for our understanding of the subatomic world.

Particle physicists anticipated the possible discovery of new physics at the TeV energy scale in the upcoming collision experiments by exploring extensions to the Standard Model. Many of their proposals contain new, hypothetical elementary particles, some of which are interesting dark matter candidates. One of these candidates is the lightest neutralino, a stable, weakly interacting particle with GeV–TeV mass<sup>1</sup> that lives in supersymmetric models. If neutralinos constitute the dark matter in the universe, and more specifically in our galaxy, some of them will be captured by the Sun and sink to its core over cosmological timescales. There the neutralinos annihilate pairwise, ultimately leading to a steady flux of neutrinos with GeV–TeV energy. The objective of our work is to detect these neutrinos from the Sun, since their discovery would shed a fascinating light on the identity of the dark matter.

In this dissertation we present the results of our search for GeV–TeV neutrinos from the Sun, in a data set collected in 2001–2003 by the Antarctic Muon And Neutrino Detector Array (AMANDA) at the Amundsen-Scott South Pole base. The inspected AMANDA data set covers 384 effective days of operation and consists of 3.5 billion events, mostly downward-going muons created in the collisions of cosmic rays with nuclei in the atmosphere. We describe an analysis that removes the bulk of these background muons, before developing a novel method to estimate the number of events from the Sun in the remaining data sample. The outcome of the complete analysis is then interpreted in terms of the neutralino annihilation rate in the Sun, the neutralino-induced muon flux at the detector and the neutralino-proton elastic scattering cross section, for neutralinos in the mass range 50 GeV–5000 GeV and both extreme annihilation channels.

This thesis is structured as follows. Chapter 1 introduces the subject of dark matter in

---

<sup>1</sup>We will often employ so-called natural units, in which  $c = \hbar = 1$ .

the context of the current Standard Model of cosmology, motivates why neutralinos are a good dark matter candidate and summarizes various experimental techniques to determine the particle identity of the dark matter. In the second chapter, we present all the physics processes related to the indirect detection of dark matter in the Sun using neutrinos as messengers. The description of the AMANDA detector and the optical properties of the surrounding South Pole glacier, can be found in Chapter 3. In the fourth chapter we verify the stability of the detector during data taking and cross-check the different parts of the simulation. The experimental and simulated data samples used in this work are introduced as well. The processing steps to clean the events from spurious information, reconstruct their direction and calculate various event observables are explained in Chapter 5.

After all preparatory work, we attack the first objective of the data analysis in Chapter 6: the optimization of the event selection criteria required to remove the bulk of the downward-going background muons from the data sample. In Chapter 7 we set up a novel, likelihood-ratio method to estimate the number of events from the Sun and report the confidence interval on the number of signal events. After a study of the uncertainties, we finalize the analysis work by translating the results to various relevant physical quantities, e.g. the muon flux at the detector. This happens in Chapter 8. The final chapter summarizes our conclusions and the lessons to take away from our work.

# Chapter 1

## The case for dark matter

We start this dissertation with the evidence supporting the current standard model of cosmology, the  $\Lambda$ CDM model, and that for dark matter in particular. This invisible matter component apparently permeates the universe on all distance scales, but consists of unknown non-baryonic particles. In Section 1.2 we summarize the generic properties of a good dark matter candidate, and introduce the lightest neutralino as a particle that fulfils the necessary conditions. The final part of this chapter focuses on several possible detection methods, which can guide us to the particle identity of the dark matter.

### 1.1 Evidence for dark matter

The purpose of the following section is to give a sketch of the historical progress in the field of cosmology. To keep the discussion light and readable some terms in the equations are explained a short while after their introduction. Furthermore, we assume that the reader is familiar with general relativity, if that is not the case we refer to [1] (and references therein) for a review.

#### 1.1.1 (R)evolutions in cosmology

Our egocentric view on the universe suffered quite some strokes over time: we demoted from a geocentric picture over heliocentric to galactocentric, and, finally, acentric.

Almost 2000 years ago, Ptolemaeus imagined the Earth as the centre of the universe. Many epicycles later, in the 16th century, Copernicus favoured the Sun as the rightful centre of the universe [2]. In the following centuries the galaxy was mapped with the help of the telescope. Besides countless stars, mysterious nebulae were found as well. This culminated in 1920 in the great debate between Shapley (“the nebulae reside in the galaxy, the only one in the whole universe; but the Sun is far from its centre”) and Curtis (“the Sun is close to the centre of the galaxy, which is but one of many galaxies – the nebulae – in the universe”). Their discussion settled a couple of years later after Hubble had measured the distance to the nebulae: the Sun is far from the centre of the galaxy, and our galaxy is one of many in the universe.

But this was not the end, the idea of a static universe had to be abandoned too. Hubble announced in 1929 that most galaxies recede from us with a speed proportional

to their distance [3]. This was interpreted by Lemaître as due to the expansion of the universe. Applying Einstein's equations of general relativity (the left hand side represents the dynamics, the right hand side the matter-energy source terms;  $R_{\mu\nu}$  is the Ricci tensor,  $R$  the Ricci scalar,  $g_{\mu\nu}$  the metric tensor,  $G$  the gravitational constant,  $c$  the speed of light,  $T_{\mu\nu}$  the stress-energy tensor and  $\Lambda$  is defined later)

$$R_{\mu\nu} - \frac{1}{2}g_{\mu\nu}R = \frac{8\pi G}{c^4}T_{\mu\nu} - \Lambda g_{\mu\nu}$$

to the universe as a homogeneous, isotropic fluid with matter density  $\rho_m$  and pressure  $p$  (the metric is broken up in a time-like part and a spatial part expressed in spherical coordinates;  $k$  describes the spatial curvature and  $a(t)$  the time-dependent spatial scale factor)

$$ds^2 \equiv g_{\mu\nu}dx^\mu dx^\nu = -c^2 dt^2 + a(t)^2 \left( \frac{dr^2}{1 - kr^2} + r^2 d\Omega^2 \right)$$

he had found, like Friedmann several years earlier, that an expanding solution, in the form of an evolving spatial scale factor  $a(t)$ , is possible ( $H$  is also known as the Hubble parameter)

$$H^2 \equiv \left( \frac{\dot{a}}{a} \right)^2 = \frac{8\pi G}{3}\rho_m - \frac{kc^2}{a^2} + \frac{\Lambda c^2}{3}, \quad (1.1)$$

where the change in expansion rate is governed by

$$\frac{\ddot{a}}{a} = -\frac{4\pi G}{3} \left( \rho_m + \frac{3p}{c^2} \right) + \frac{\Lambda c^2}{3}. \quad (1.2)$$

Extrapolating to earlier times, this led Lemaître in 1931 to the idea of a primeval atom, now known as the *Big Bang*: the early universe must have been hotter and denser than today, and its contents must have emerged from one single point. Just after World War II, Gamow and collaborators showed how the nuclei of the light elements could have been created in the first few minutes after the Big Bang, a process dubbed Big Bang nucleosynthesis (BBN). Another of their predictions was that once, after sufficient cooling in the young universe, all electrons were captured by the nuclei to form neutral atoms, the radiation decoupled from the matter and the universe became transparent. This isotropic blackbody radiation would still permeate the universe today, but at a very low temperature, as a cosmic microwave background (CMB). It was not until 1965, with the detection of the CMB radiation by Penzias and Wilson at the predicted  $\sim 3$  K temperature [4, 5], that the Big Bang model was established as the standard model of cosmology.

In the 1980s, a short period of inflation was added to the Big Bang model to explain the extremely isotropic nature of the CMB temperature. Such an inflationary period had as consequence that the spatial geometry of the universe is flat, or  $k = 0$ . Then, following Eq. 1.1,

$$1 = \frac{8\pi G}{3H^2}\rho_m + \frac{\Lambda c^2}{3H^2}. \quad (1.3)$$

Previous expression is often rewritten in terms of dimensionless quantities (not to be confused with the angular term in the expression of the metric  $ds^2$ ), defined in Table 1.1,

$$\Omega = 1 - \Omega_k = \Omega_m + \Omega_\Lambda, \quad (1.4)$$

Parameter	Definition	Value	Description
$\Omega_k$	$1 - (\Omega_r + \Omega_m + \Omega_\Lambda)$	$[-0.0175, 0.0085]$	Spatial curvature
$\Omega_r$	$\rho_r/\rho_c$	$0.0010 \pm 0.0005$	Density photons, neutrinos
$\Omega_m$	$\rho_m/\rho_c (= \Omega_b + \Omega_{dm})$	$0.279 \pm 0.015$	Matter density
$\Omega_b$	$\rho_b/\rho_c$	$0.0462 \pm 0.0015$	Baryon density
$\Omega_{dm}$	$\rho_{dm}/\rho_c$	$0.233 \pm 0.013$	Dark matter density
$\Omega_\Lambda$	$\Lambda c^2/3H^2$	$0.721 \pm 0.015$	Dark energy density
$\rho_c$	$3H^2/8\pi G$	$1.88 \times 10^{-26} h^2 \text{ kg m}^{-3}$	Critical density
$h$	$H/100 \text{ km s}^{-1} \text{ Mpc}^{-1}$	$0.701 \pm 0.013$	Scaled Hubble parameter
$t_0$	–	$13.73 \pm 0.12 \text{ Gyr}$	Current age of universe

**Table 1.1** – Definition of several cosmological parameters and their inferred values from a fit to CMB, supernova and BAO data [8]. Errors denote 68% confidence, except for the  $1 - \Omega$  interval which contains 95% CL.

where  $\Omega_k \neq 0$  (or equivalently,  $\Omega \neq 1$ ) in a non-Euclidean geometry. Since people assumed that the cosmological constant  $\Lambda$  did not exist ( $\Omega_\Lambda = 0$ ), they started inventorising the total matter density  $\rho_m$  of the universe. The latter should equal the critical density  $\rho_c$  (defined in Table 1.1), or alternatively,  $\Omega_m = \rho_m/\rho_c = 1$ , to obtain a flat universe. Unfortunately, the observations were puzzling for quite some time.

The measurements of the primordial abundances of various light elements at early epochs were in perfect agreement with the prediction of Big Bang nucleosynthesis if the baryon density was  $0.017h^{-2} < \Omega_b < 0.024h^{-2}$ . Since  $h \simeq 0.7$  (defined in Table 1.1), the baryons (i.e. atoms) were surely not sufficient to reach the critical density. That was a serious blow, but not necessarily the death of the model of the flat inflationary universe.

In the meantime, astronomers had studied the mass-to-light ratios of large structures in the universe: from galaxies to clusters of galaxies. They concluded that much more matter exists than luminous matter, leading to  $\Omega_m \simeq 0.3$  at the large scale of clusters. This had two surprising consequences. First, the total matter density remained (much) smaller than the critical density ( $\Omega_m < 1$ ). In principle, that could have been rectified with a smaller value of  $h$ , but this was in slight contradiction with the observations. The second constatation, that baryons are a minor component of the matter density in the universe ( $\Omega_b < \Omega_m$ ), completely overturned our baryocentric view on the universe. The ubiquitous, but invisible, non-baryonic matter was coined *dark matter*. Hence,  $\Omega_m = \Omega_b + \Omega_{dm}$ .

Towards the end of the 1990s the observed luminosity-redshift relation of distant Type Ia supernovae showed us that the universe was in accelerated rather than decelerated expansion [6, 7]. Another surprise, which could be understood (second term in Eq. 1.2) as due to a nonzero, positive cosmological constant  $\Lambda$ , or vacuum energy, that exerts a repulsive force on matter. In analogy to the unknown dark matter, it was called *dark energy*. Furthermore, the same supernova observations indicated that the vacuum energy density,  $\Omega_\Lambda$  (see Table 1.1), was dominating over the matter density. And that it had a sufficiently high density to satisfy Eq. 1.3 and recover the predicted flat geometry,  $\Omega_m + \Omega_\Lambda \simeq 1$ .

This final piece, not more than ten years old, completes our present understanding of the cosmos: a spatially flat universe currently in accelerated expansion containing a small amount of baryons, a larger amount of dark matter (DM) and dominated by dark energy

( $\Lambda$ , which may or may not be a truly cosmological *constant*). In the last decade, various observations further established this model as the standard model of cosmology, also coined the  $\Lambda$ CDM<sup>1</sup> *model*.

The standard model of cosmology is a dramatic departure from our initial egocentric vision, showing that our place in the universe and even the material we are made of plays a minor role. Some important questions remain however, for instance “what is the dark matter?” and “what is the dark energy?”. In this work we will try to answer (part of) the first question.

### 1.1.2 The dark matter in $\Lambda$ CDM

We already mentioned the cosmic microwave background as one of the pillars of the Big Bang model. In 1992, the COBE satellite observed  $\mathcal{O}(10^{-5})$  anisotropies in the CMB temperature [9], interpreted as the imprints of the matter distribution at the time of matter-radiation decoupling. Nowadays, these anisotropies allow a powerful test of the  $\Lambda$ CDM model, which describes a flat spatial geometry with a small matter and a large cosmological constant component. The angular power spectrum obtained by decomposing the CMB temperature map  $\frac{\Delta T(\theta, \phi)}{T}$  in spherical harmonics contains a wealth of cosmological information, as shown in Fig. 1.1. For instance, the multipole moment  $\ell$  of the first peak determines the total density  $\Omega$ , or equivalently, the spatial curvature (through Eq. 1.4). The ratio of the heights of odd to even peaks determines the baryon density  $\Omega_b$ . And the third peak can be used to infer the total matter density  $\Omega_m$  [10].

The CMB power spectrum was recently measured with great precision by COBE’s successor, the WMAP satellite, at angular scales  $\alpha$  between  $90^\circ$  and  $0.2^\circ$ . Since  $\ell \approx 100^\circ/\alpha$ , these scales correspond to low multipole moments,  $\ell < 800$ . Figure 1.1 shows that the  $\Lambda$ CDM model is in very good agreement with the WMAP data. In addition, we can conclude that when this fit is extrapolated to even smaller angular scales ( $\ell > 800$ ), the data from various other CMB experiments are described as well [11].

Other, independent cosmological observations confirm the  $\Lambda$ CDM model as well, hence its alternative name *Concordance Model*. A combined  $\Lambda$ CDM fit to various data sets improves the constraints on the cosmological parameters. In Table 1.1 we present the baryon, dark matter and dark energy densities derived from a combined fit to the CMB data from WMAP, the distance measurements of Type Ia supernovae and the measured baryon acoustic oscillations (BAO) in the distribution of galaxies [8]. This results in a flat universe with 28% matter and 72% dark energy. Another conclusion is that dark matter is five times more abundant than normal, baryonic matter.

In the following we focus on additional evidence for dark matter.

The original hypothesis of the existence of invisible, or dark, matter dates back to the 1930s when Zwicky inferred the total mass of the Coma cluster by measuring the velocity dispersion of its constituent galaxies. He found that the total mass was 500 times larger than the luminous mass, and concluded the presence of a large amount of invisible matter in the cluster [12].

<sup>1</sup>We explain the origin of the “C” in Section 1.2.1.

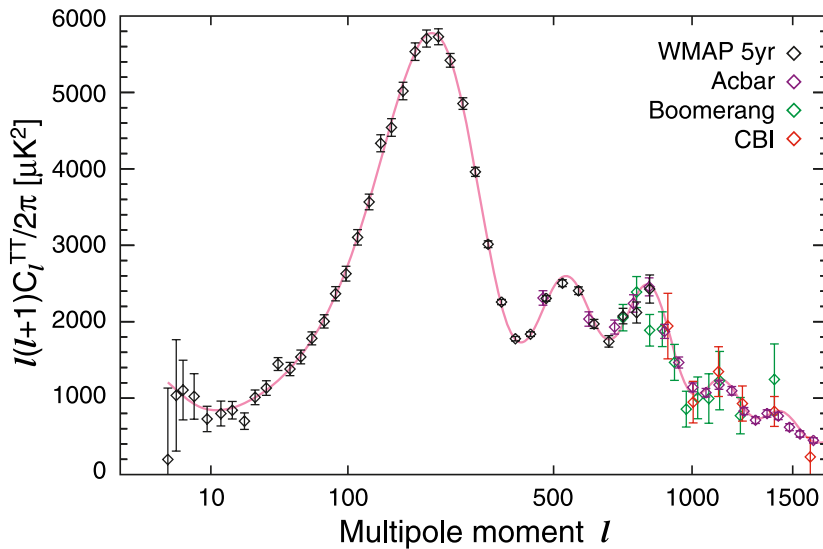


**Figure 1.1** – The angular power spectrum of the cosmic microwave background temperature map as measured by four experiments (markers) [11]. Low multipole moments  $\ell$  correspond to large angular scales  $\alpha$ :  $\ell \approx 100^\circ/\alpha$ . The solid line shows the fit of WMAP data to the  $\Lambda$ CDM model.

This idea was not taken seriously until the 1970s, when the rotational speed of stars around galaxies was measured [13]. According to Newton’s laws of gravity, the rotation velocity  $v_c(r)$  of a star depends on its radial position  $r$  from the centre of the galaxy:  $v_c(r) = \sqrt{GM(r)/r}$ . The enclosed mass distribution  $M(r)$ , the total visible mass within radius  $r$ , of spiral galaxies is almost constant outside their bulge, so at large distances we expect  $v_c(r) \propto 1/\sqrt{r}$  from the luminous matter. However, the data show a flat behaviour that continues to large radii, see Fig. 1.2 (left). This indicated the presence of a non-luminous component, which surrounds the galaxy as a spherical halo.

A similar conclusion was drawn when exploiting the gravitational lensing effect<sup>2</sup>, to infer the total mass of the lensing object, either galaxies or clusters of galaxies. The Bullet cluster in Fig. 1.2 (right) is a popular example of direct evidence for dark matter [15]. This cluster is actually an ongoing merger of two clusters, that we observe just after they passed each other. While the galaxies are collisionless and cross each other without problems, the intracluster plasma lags behind due to ram pressure (forming a bullet-shaped shock front). The galaxies of both clusters and the X-ray emitting plasma are clearly segregated. The epicenters of the gravitational potential, reconstructed from gravitational lensing effects on background galaxies, are not located at the centre of the plasma clouds, but around the galaxies. This is not expected, since a cluster’s mass is completely dominated by the plasma, not by its member galaxies. The explanation is that, instead of the plasma, dark matter dominates the mass of the clusters and, in addition, that it is collisionless.

Surveys have mapped the distribution of galaxies out to redshifts of  $z < 0.5$ , probing the large scale structure of the universe. Again, dark matter is needed too to account for the observations.

All observations point to the existence of invisible, dark matter with a cosmological

<sup>2</sup>The bending of light of a galaxy due to the curvature of space-time by a foreground galaxy, which is on the same line of sight.

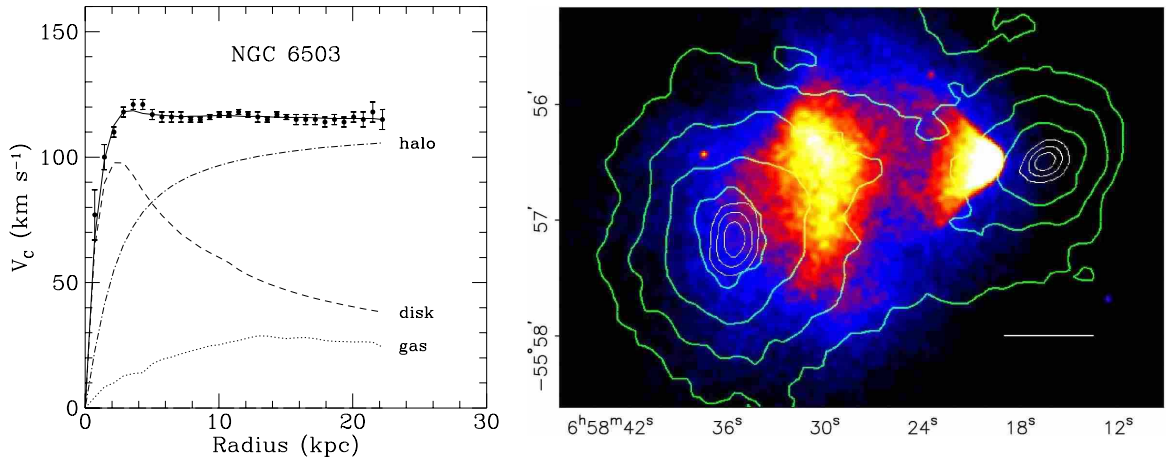


**Figure 1.2** – Left: typical rotation curve for a spiral galaxy; markers indicate observed velocities versus galactocentric distance, lines the predicted contribution from gas, disk and dark matter halo [14]. Right: ongoing merger in the Bullet cluster [15]; the hot plasma is visible in the X-ray image, gravitational lensing reveals the gravitational potential of the cluster (contours).

density that is consistent with  $\Omega_{dm} = 0.233$ . Furthermore, the dark matter is present at all distance scales, from galaxies to clusters of galaxies to the large scale structure. Invisible baryons can not explain all of the dark matter, to remain consistent with Big Bang nucleosynthesis. Yet, we have no idea what the dark matter (CDM) is.

### 1.1.3 The dark halo around the Milky Way

In Section 1.3 we describe direct and indirect methods to detect dark matter through non-gravitational processes. The prospects for detection and the interpretation in terms of the underlying particle physics models, depend on the properties of the galactic dark matter halo. These properties are difficult to measure and hence subject to sizable uncertainties.

The velocity distribution and the local density of the dark matter in the solar neighbourhood is inferred from the Milky Way rotation curve, which is difficult to measure from our location. Additionally, the distribution of the normal matter component should be subtracted from the total rotation curve, which introduces additional modelling uncertainties.

By convention, the standard halo model is isotropic and prescribes a Maxwellian velocity distribution with 3D-dispersion of  $\bar{v} = 270$  km/s and a local density of  $0.3$  GeV/cm<sup>3</sup>. However, the latter value carries an uncertainty of a factor of two [16]. The dark matter density profile at the galactic centre,  $\rho(r \rightarrow 0)$ , is even more uncertain. Neither observations nor theory are conclusive whether it is spiky ( $\sim r^{-2.5}$ ), cuspy ( $\sim r^{-1}$ ) or core-like ( $\sim r^{-0.2}$ ). This implies uncertainties spanning several orders of magnitudes at the galactic centre [17].

Furthermore, it is not likely that the halo is perfectly smooth. Subhalos of dark matter could exist in a variety of sizes, down to a scale of  $\sim 100$  pc [16]. It might even be that the existence of the Solar System itself is evidence for a local dark subhalo [18].

### 1.1.4 Challenges for dark matter

While the  $\Lambda$ CDM model is very successful in describing the large scale universe, it enters into difficulties at the galactic scale. Several aspects show that it predicts too much small scale structure.

One example is that of the dark matter halo density profile near the centre of galaxies. We have seen in previous section that the opinions diverge about the situation in our own galaxy in particular. This turns out for many other galaxies as well. Large N-body simulations in a  $\Lambda$ CDM universe predict a dark matter cusp at the centre of galaxies,  $\rho(r \rightarrow 0) \sim r^{-1 \dots -1.5}$  [19, 20]. This is in contrast to observations of supposedly dark matter dominated galaxies, e.g. low surface brightness galaxies, which favour a constant-density core  $\rho(r \rightarrow 0) \sim r^{-0.2}$  [21, 22]. Further discrepancies include the lack of observed dwarf galaxies [23–25] or the too low angular momentum to form baryonic disks [26].

While these issues need not be a show stopper for (cold) dark matter [27], other explanations have been proposed to explain the galactic scale. One of them is MOND [28–30], which modifies Newtonian dynamics at very small accelerations  $\vec{a}$  rather than introducing invisible matter

$$\vec{F} = m\mu\left(\frac{|\vec{a}|}{a_0}\right)\vec{a},$$

where  $a_0 = \mathcal{O}(10^{-8} \text{ cm/s}^2)$  and  $\mu(x)$  is a function that approaches  $\mu(x \gg 1) \simeq 1$  (Newtonian limit) and  $\mu(x \ll 1) \simeq x$  (MONDian limit). This idea works particularly well on galactic scales, with a better description of the observed rotation curves than that obtained with dark matter.

However, larger scales pose a challenge to MOND. The Bullet cluster in Fig. 1.2 is one of the arguments against MOND, since it is difficult to explain why the gravitational well is not centred on the baryonic mass in the plasma. Also, it is not straightforward to fit the purely baryonic MOND framework to the CMB data. Both issues could be resolved by a sizable dark component of relativistic particles in the universe, e.g. neutrinos with 2 eV mass [31]. Recent proposals call for a synergy between MOND and (cold) dark matter, to exploit the advantages of both models at the scales they work best [32].

## 1.2 The lightest neutralino as dark matter

About 23% of the density of the universe is occupied by dark matter (DM). Unfortunately, the  $\Lambda$ CDM model does not point towards a particular particle. In fact, as far as cosmology is concerned, there may even be multiple dark matter components<sup>3</sup>. Before introducing the lightest neutralino, appearing in supersymmetric extensions to the Standard Model of particle physics, as our favourite dark matter candidate, we summarize some of the necessary conditions that promote a particle to the status of a good dark matter candidate [33]. For the moment,  $\chi$  denotes a generic DM candidate, whose role will be taken later by the neutralino.

---

<sup>3</sup>It is interesting to remark that the Standard Model of particle physics describes less than 5% of the density of the universe with 17 particles.

### 1.2.1 Necessary properties of dark matter

Any good DM candidate should have a mass. In addition, the DM can not be baryonic, to comply with CMB and BBN measurements.

Since dark matter is produced along with the “normal” matter in the primordial Big Bang soup, it must be stable, or at least, have a lifetime  $\tau$  exceeding that of the universe,  $\tau > t_0 = 13.7 \text{ Gyr}$  (see Table 1.1). The traditional thermal production scenario goes as follows. As long as the universe is hot enough, DM particles  $\chi$  are constantly created and annihilated through interactions of the type  $\chi\bar{\chi} \leftrightarrow l\bar{l}$ , where  $l$  is a lighter particle than  $\chi$ . Once the temperature drops below the  $m_\chi$  threshold, the  $\chi$  number density decreases exponentially due to annihilations  $\chi\bar{\chi} \rightarrow l\bar{l}$ . However, when the annihilation rate becomes smaller than the expansion rate of the universe, the DM particles stop meeting each other. The annihilations terminate, the DM density *freezes out*, and the stable DM particles survive until today. The current density of a generic thermal relic, with a thermally averaged annihilation cross section times relative velocity  $\langle\sigma_{\text{ann}}v\rangle$ , is roughly [34]

$$\Omega_\chi h^2 \simeq \frac{3 \times 10^{-27} \text{ cm}^3 \text{ s}^{-1}}{\langle\sigma_{\text{ann}}v\rangle}.$$

According to this result, a weakly interacting thermal relic naturally produces the measured DM density,  $\Omega_{dm} h^2 = 0.114$ . Lower annihilation cross sections overproduce DM, while higher cross sections deplete the density too much. More realistic calculations include the effects of resonances and co-annihilations with other particle species of similar mass, but the conclusion remains that weakly interacting massive particles (WIMPs) are an attractive class of DM candidates.

Only one non-baryonic, stable, weakly interacting particle exists in the Standard Model of particle physics: the neutrino<sup>4</sup>. Unfortunately, this possibility is barred by structure formation arguments. Neutrinos are so-called *hot* matter (HDM), since they are light,  $m_\nu \lesssim 2 \text{ eV}$  [35], and hence relativistic. The primordial density perturbations are strongly washed out by even a small amount of relativistic species, which clumps only at the length scale of superclusters. In a hot dark matter dominated universe structures can therefore only form top-down; galaxies result from the fragmentation of clusters and superclusters. This is in disagreement with a number of observations: clusters turn out to be younger than their constituent galaxies, simulations of large scale structure in a HDM universe predict too inhomogeneous distributions of galaxies, no significant effect of HDM on the CMB angular power spectrum is seen [36]. With the exclusion of the hot neutrino, the Standard Model runs out of good DM candidates, which indicates the need of new physics beyond the model.

To avoid the small scale suppression and allow the more plausible bottom-up growth of structure, the dark matter particles must be heavier. Around the keV scale, the particles are semi-relativistic (or *warm* DM) and start to clump at the galaxy scale. Much heavier, non-relativistic particles, also *cold* dark matter (CDM), clump on even smaller scales. Although there are signs of a bit too much small scale structure, see Section 1.1.4, a cold dark matter universe seems to fit the CMB data best. The simulations suggest a mix of cold DM with a smaller contribution from warm DM.

<sup>4</sup>The neutrino has no mass in the Standard Model, but the observation of neutrino oscillations proves that this should be remedied.

A good DM candidate can not have an electric or colour charge either. This possibility is ruled out by unsuccessful searches for heavy isotopes [33] (see [37] for a critical note); positively charged DM particles could capture e.g. an electron to form heavy hydrogen. In addition, the candidate should have a very small effect on stellar evolution. There are well tested stellar evolution models that leave little room for new energy loss channels (due to production of  $\chi$  inside the star, which later escape) or energy production channels (due to annihilations of captured  $\chi$  in the stellar core) [38]. Too strong self-interactions, in the form of  $\chi\chi$  scattering, are not favoured either. Otherwise the centre of the gravitational well would not be located on top of the collisionless luminous galaxies in the Bullet cluster [39]. The DM is therefore expected to be virtually collisionless.

### 1.2.2 The lightest neutralino

Despite the tremendous successes of the now 35 year old Standard Model (SM) of particle physics in describing elementary particles and their interactions [40, 41], it fails to provide a solution to the (cosmological) dark matter problem. That should not necessarily be a surprise as it was conceived to explain (particle physics) phenomena up to the electroweak scale of 100 GeV. In fact, besides the dark matter issue, there are indications within particle physics that the current Standard Model is only the low energy description of a more fundamental theory. One of the most robust hints is that of the instability of the Higgs boson mass against quantum corrections, and by extension those of the other SM particles too. This is often called the *hierarchy problem*. A second indication originates in the unsuccessful unification of the electromagnetic, weak and strong gauge couplings at  $m_{\text{GUT}} \simeq 10^{16}$  GeV, which is expected in grand unification theories. New physics at the TeV scale possibly resolves all of these issues. Many extensions have been proposed to the Standard Model. In the following we focus on supersymmetry, but we briefly introduce the Standard Model first.

The Standard Model is a relativistic quantum field theory that contains fermionic and bosonic fields, corresponding to particles with half-integer and integer spin. Fermions, either leptons<sup>5</sup> or quarks, are the constituents of matter, and belong to one of three generations

$$\text{leptons : } \begin{pmatrix} \nu_e \\ e \end{pmatrix} \begin{pmatrix} \nu_\mu \\ \mu \end{pmatrix} \begin{pmatrix} \nu_\tau \\ \tau \end{pmatrix}; \quad \text{quarks : } \begin{pmatrix} u \\ d \end{pmatrix} \begin{pmatrix} c \\ s \end{pmatrix} \begin{pmatrix} t \\ b \end{pmatrix}.$$

Bosons on the other hand mediate the interactions between matter particles. Gravity, the fourth fundamental force in nature, is not included in the model because its effects are completely negligible in current particle physics experiments

$$\text{bosons : } \begin{cases} \text{photon } \gamma & \text{(electromagnetism)} \\ \text{vector bosons } W^\pm, Z & \text{(weak)} \\ \text{gluons } g & \text{(strong)} \end{cases}$$

The SM particles obtain a mass through interactions with the Higgs boson  $H$ , the only SM particle that remains undetected so far.

---

<sup>5</sup>The term *lepton* is often used as a synonym for *charged lepton*, making the distinction with *neutrinos* (neutral leptons) explicit.

Standard Model particles and fields			Supersymmetric partners				
$S$	Symbol	Name	Interaction eigenstates			Mass eigenstates	
			$S$	Symbol	Name	Symbol	Name
$1/2$	$q = u, d, c, s, t, b$	quark	0	$\tilde{q}_L, \tilde{q}_R$	squark	$\tilde{q}_1, \tilde{q}_2$	squark
$1/2$	$\ell = e, \mu, \tau$	lepton	0	$\tilde{\ell}_L, \tilde{\ell}_R$	slepton	$\tilde{\ell}_1, \tilde{\ell}_2$	slepton
$1/2$	$\nu = \nu_e, \nu_\mu, \nu_\tau$	neutrino	0	$\tilde{\nu}$	sneutrino	$\tilde{\nu}$	sneutrino
1	$g$	gluon	$1/2$	$\tilde{g}$	gluino	$\tilde{g}$	gluino
1	$W^\pm$	$W$ -boson	$1/2$	$\tilde{W}^\pm$	wino	$\tilde{\chi}_{1,2}^\pm$	chargino
0	$H^-$	Higgs boson	$1/2$	$\tilde{H}_1^-$	higgsino		
0	$H^+$	Higgs boson	$1/2$	$\tilde{H}_2^+$	higgsino	$\tilde{\chi}_{1,2,3,4}^0$	neutralino
1	$B$	$B$ -field	$1/2$	$\tilde{B}$	bino		
1	$W^3$	$W^3$ -field	$1/2$	$\tilde{W}^3$	wino	$\tilde{\chi}_{1,2,3,4}^0$	neutralino
0	$H_1^0$	Higgs boson	$1/2$	$\tilde{H}_1^0$	higgsino		
0	$H_2^0$	Higgs boson	$1/2$	$\tilde{H}_2^0$	higgsino		
0	$H_3^0$	Higgs boson					

**Table 1.2** – Standard Model particles and their superpartners in the MSSM. Adapted from Ref. [44].

Building upon the successes of gauge symmetry in the SM, a further symmetry was proposed in the 1970s: the *supersymmetry* between fermions and bosons, unifying the picture of matter and interactions [42, 43]. Supersymmetry (SUSY) predicts new particle states since none of the SM bosons can be turned into one of the SM fermions (or vice versa) under a supersymmetry operation. Except for the spin, each SUSY particle has identical quantum numbers as its SM sibling, which means that the SUSY particles are degenerate in mass and should have been detected already. That is not the case, so supersymmetry is not a symmetry of nature at the low energy scale of current experiments. The hierarchy problem, the dark matter problem and the gauge unification problem are possibly all solved by supersymmetry if the symmetry breaking scale is not much larger than the electroweak scale. The mass of the SUSY partners is therefore expected to be not more than  $\mathcal{O}(1 \text{ TeV})$ , which is within reach of the upcoming collider experiments.

The minimal supersymmetric extension of the Standard Model, or MSSM, is the supersymmetric model with minimal field content. To supply mass to both up-type and down-type particles, the MSSM Higgs sector needs two doublets, leading to five Higgs particles. Each SM particle has exactly one SUSY partner, see Table 1.2. Bosonic superpartners are given the prefix “s-”, fermionic superpartners are given the suffix “-ino”. The breaking of the supersymmetry adds more than 100 free parameters to the set of 19 SM parameters, which is of course a nightmare for the phenomenologists that need SUSY particle masses, couplings, ... to study signatures in a detector. Fortunately, theoretically motivated assumptions lead to simpler models, with a strongly reduced set of parameters. Several flavours exist, depending on the assumptions made.

To avoid that protons decay, a necessary MSSM ingredient is the conservation of  $R$ -parity. It is a multiplicative quantum number and defined as  $R \equiv (-1)^{3(B-L)+2S}$ , for a particle with baryon number  $B$ , lepton number  $L$  and spin  $S$ . So, SM particles have

$R = +1$ , while SUSY particles have  $R = -1$ . An immediate consequence of  $R$ -parity conservation is that the lightest SUSY particle (or LSP) can not decay, it must be stable. In the context of our search for a dark matter candidate, this rings a very loud bell.

The LSP is stable, but does it satisfy the other necessary conditions for a good dark matter candidate? In many MSSM scenarios the lightest neutralino turns out to be the lightest SUSY particle. The bino, wino and neutral higgsino interaction eigenstates (see Table 1.2) have the same quantum numbers and therefore mix to form four mass eigenstates, the neutralinos

$$\tilde{\chi}_i^0 = N_{i1}\tilde{B} + N_{i2}\tilde{W}^3 + N_{i3}\tilde{H}_1^0 + N_{i4}\tilde{H}_2^0. \quad (1.5)$$

Neutralinos are electrically and colour neutral. Additionally, they are Majorana particles, so they are their own anti-particles. Neutralinos interact strictly through the weak force, and with a mass at the electroweak scale they are highly non-relativistic too. These seemingly ideal properties drew the attention of a lot of people to the lightest neutralino,  $\tilde{\chi}_1^0$  (from now on referred to as  $\chi$ ), as the premium dark matter candidate.

The mass of the lightest neutralino and its couplings are completely determined by the coefficients  $N_{i1}$ , which, in turn, depend on the SUSY parameters. Different regions in the MSSM parameter phase space produce different signatures and event rates. This introduces model dependencies when searching for neutralinos.

### 1.2.3 Alternative candidates

A long list of dark matter candidates was proposed over the years. We briefly discuss two well-studied alternatives, the axion and the lightest Kaluza-Klein particle. For a review of other dark matter candidates, see [17].

Although at times not very much in focus of dark matter phenomenologists and experimentalists, the axion remains one of the earliest suggestions of a viable particle candidate for dark matter, and in fact one of the most attractive. This is not least due to the fact that its existence was motivated by solving the strong CP problem in particle physics. A disadvantage in the cosmological context is, however, that the axion needed to solve the CP problem only solves the dark matter problem for a small range of masses thus some fine-tuning mechanism seems to be needed. For a recent review of the field, see [45].

Kaluza-Klein particles arise in extra dimensional extensions of the Standard Model of particle physics [46]. In universal extra dimension models (UED) all Standard Model fields propagate in the higher dimensional bulk [47]. The extra dimensions would be compactified to a (very small) radius  $R$ , leading to the quantification of momentum for particles propagating in the bulk. Then, in UED models, all SM particles are accompanied by a tower of KK states. The mass of the  $n$ -th mode in a model with one extra dimension is given by  $m_{(n)} = \sqrt{(n/R)^2 + m_{(0)}^2}$ , where  $m_{(0)}$  is the mass at the electroweak scale. Conservation of momentum in the compactified dimensions implies the conservation of KK parity. This makes the lightest Kaluza-Klein particle (LKP) stable and a viable dark matter candidate. In most models the LKP is the first KK excitation of the  $B$  field,  $B^{(1)}$ , a weakly interacting massive particle. Unfortunately, although the unknown parameter space is quite small, much of the UED phenomenology is similar to that of SUSY. Two aspects could be used to differentiate between both scenarios [48]. The first is the existence of an infinite tower

of KK excitations. The second is related to spin-dependent phenomenology, since the LKP is a boson and the LSP a fermion.

## 1.3 Detection of dark matter

The following discussion focuses on the neutralino as dark matter, but the signatures are similar for other DM candidates, like  $B^{(1)}$ , the lightest KK particle. This also means that the detection of dark matter particles in any of the channels discussed below will not be sufficient to conclusively identify the nature of the dark matter. The direct or indirect detection of the dark matter particles making up our galaxy's halo is highly unlikely to provide enough information to reveal the underlying particle physics (supersymmetry, etc.) behind these particles. In contrast, collider experiments may identify a long-lived, weakly interacting particle, but will not be able to test its cosmological stability or abundance. Only by combining the information provided by many different experimental approaches is the mystery of dark matter's particle nature can be solved.

### 1.3.1 Collider searches

If the centre of mass energy  $\sqrt{s}$  of particle accelerators is high enough, supersymmetric particles may be produced in collision experiments. Under the assumption of  $R$ -parity conservation, SUSY particles are produced in pairs and their decay chain ends at the LSP, very likely the lightest neutralino, a weakly interacting and neutral particle that escapes detection. So, the general signature of supersymmetry is missing energy<sup>6</sup>,  $\cancel{E} \geq 2m_\chi$ . The Standard Model backgrounds for missing energy events mainly come from neutrino production in  $W$  and  $Z$  decays. Promising signatures with a controllable SM background include jets + no isolated leptons +  $\cancel{E}$ , three leptons +  $\cancel{E}$  (see Fig. 1.3), two same-charge leptons +  $\cancel{E}$ , ...

Searches in  $e^+e^-$  collisions at  $\sqrt{s} \leq 209$  GeV at LEP,  $e^\pm p$  collisions at  $\sqrt{s} = 320$  GeV at HERA and  $p\bar{p}$  collisions at  $\sqrt{s} = 1.96$  TeV at the Tevatron have not shown any evidence for SUSY particles so far. The non-detection in LEP implies that the superparticles (other than the gluino and the LSP) have a mass above roughly 100 GeV. Searches for sleptons, charginos and Higgs bosons were combined to set a lower bound of  $m_\chi \geq 47$  GeV on the lightest neutralino, under the assumption of gaugino and sfermion mass unification, see Fig. 1.3 (right) [1].

The almost operational LHC, a  $pp$  collider with envisaged  $\sqrt{s} = 14$  TeV, should have a realistic chance to detect supersymmetry, especially when squarks and gluinos are lighter than  $\sim 2$  TeV [49]. Some studies indicate that in most SUSY models it is likely that the neutralino mass will be measured with 10% precision [50]. Unfortunately, collider experiments can not distinguish between a relatively long-lived and a stable particle, so its relic density must be calculated to be established as the dark matter. This will require measurements of the other superparticle masses and couplings. A possible, future linear  $e^+e^-$  collider (ILC) offers a much cleaner environment and, with  $\sqrt{s} = 0.5 - 1$  TeV, would play an essential role towards a precision measurement of the cosmological neutralino

<sup>6</sup>At hadron colliders this can only be established in the transverse plane, since the non-interacting partons remain undetected in the beam pipe.

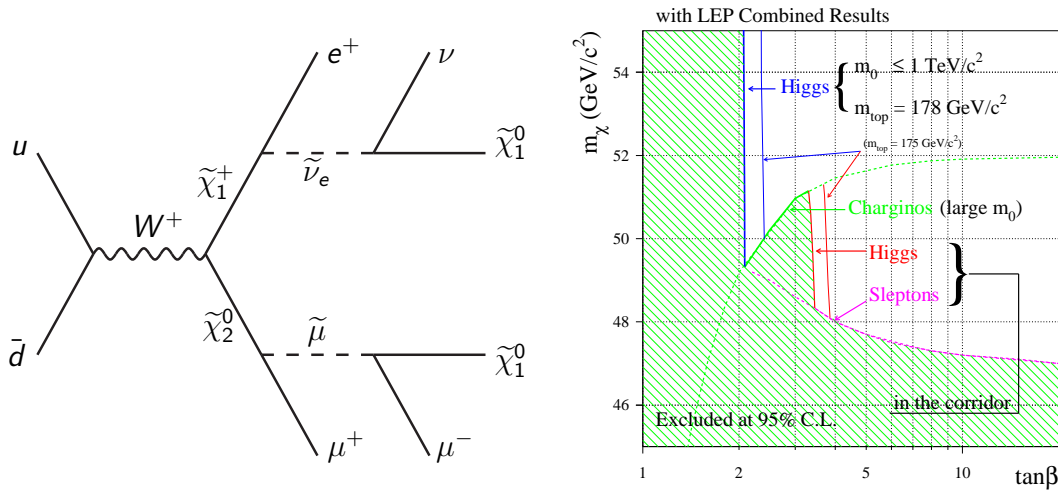


**Figure 1.3** – Left: a complete Feynman diagram for a clean (no high- $p_T$  hadronic jets) triplepton event at a hadron collider, from production of an on-shell neutralino and a chargino, with subsequent leptonic decays, leading in this case to  $\mu^+\mu^-e^+ + \cancel{E}_T$ . Right: lower mass limit for the lightest neutralino as a function of  $\tan\beta$ , inferred in the conventional scenario from searches at LEP for charginos, sleptons, and neutral Higgs bosons [1].

density. When found to be smaller than  $\Omega_{dm} = 0.233$ , the conclusion must be that the dark matter has multiple components.

In addition, the ILC should be able to discriminate supersymmetry from other Standard Model extensions, like that of universal extra dimensions. This goal will be extremely challenging to reach at the LHC experiments, unless these are able to detect second level KK modes [48]. In the meantime, direct and indirect dark matter search experiments can confirm or complement the collider data.

### 1.3.2 Direct searches

Dark matter is present at all distance scales in the cosmos, in particular in our own Milky Way. Although a WIMP is only weakly interacting it does scatter off normal matter. Direct search experiments try to observe the recoil of a nucleus after being hit by a particle from the Milky Way dark matter halo. The experimental efforts focus on elastic scattering, which dominates over inelastic interactions [51].

The elastic scattering rate per unit recoil energy  $dR/dE$  of a DM particle with mass  $m_\chi$  in 1 kg of detector material made up of nuclei with atomic number  $A$  is [52]

$$\frac{dR}{dE} = \frac{\rho_\chi \sigma_{\chi A} |F(E)|^2}{2m_\chi \mu^2} \int_{v_{\text{cut}}(E)}^{v_{\text{esc}}} \frac{f(\mathbf{v}, t)}{v} d^3v$$

where  $\sigma_{\chi A}$  is the total elastic scattering cross section on a nucleus  $A$ ,  $\mu$  is the reduced mass of the  $\chi$ -nucleus system,  $F(E)$  is a nuclear form factor that suppresses the cross section at high  $E$  due to the shape of the nucleus and  $v = |\mathbf{v}|$  is the relative velocity of the DM particle with respect to the detector. We remark that this expression involves astrophysical assumptions about the local density of the dark matter  $\rho_\chi$  and its velocity distribution

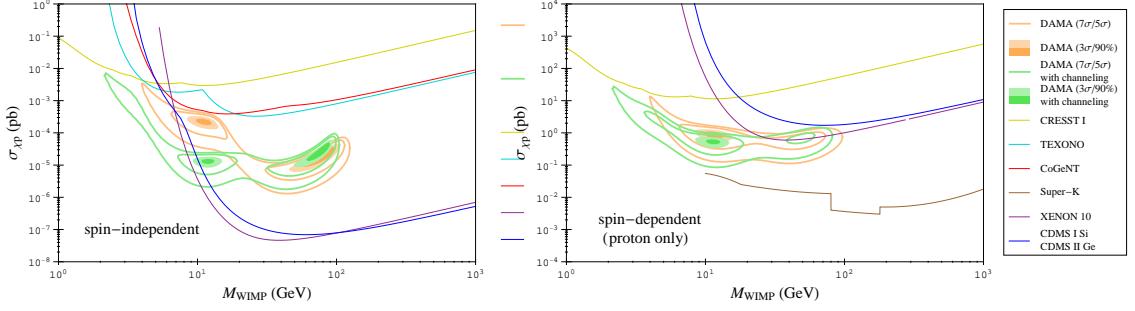


**Figure 1.4** – As a function of WIMP mass, the spin-independent (left) and spin-dependent (right) elastic scattering cross section on protons [54]. The shaded areas and thick lines indicate the DAMA favoured region (with and without ion channelling effect) at various CL, thin lines present the 90% CL upper limits from other direct searches. We note that Super-Kamiokande is an indirect detection experiment (cfr. Section 1.3.3).

$f(\mathbf{v}, t)$  at the Earth. This was discussed in Section 1.1.3 and found to introduce a factor two in uncertainty. Obviously this affects the event rates and their interpretation in terms of cross section [53].

Elastic scattering occurs either through a spin-independent (SI) or a spin-dependent (SD) process,  $\sigma_{\chi A} = \sigma_{\chi A}^{SI} + \sigma_{\chi A}^{SD}$ , so it is customary to constrain the  $m_\chi - \sigma$  plane for both interactions separately. While the scalar (spin-independent) couplings to nucleons  $N$  in a nucleus  $A$  add coherently ( $\sigma_{\chi A}^{SI} \propto A^4 \sigma_{\chi N}^{SI}$ , with  $N = p$  or  $n$ ), the axial (spin-dependent) couplings to nucleons with opposing spins interfere destructively. This implies that the spin-independent interaction is best constrained by heavy target materials, while the spin-dependent interaction needs unpaired protons or neutrons. Furthermore, the limits are set on cross sections at the nucleon level, such that the results from experiments with different target nuclei are easily comparable. The spin-dependent interaction on protons or neutrons is different ( $\sigma_{\chi p}^{SD} \neq \sigma_{\chi n}^{SD}$ ), the spin-independent coupling on the other hand is similar for both nucleons ( $\sigma_{\chi p}^{SI} \simeq \sigma_{\chi n}^{SI}$ ).

For a germanium target, a neutralino with  $m_\chi = 100$  GeV and a spin-independent cross section of  $\sigma_{\chi p}^{SI} = 10^{-7}$  pb the expectation is 0.05 events per day per kg with an average energy deposit of 26 keV. This clearly shows the need for large detector volumes, with a very low background and a low energy threshold. There are many direct search experiments, using different target materials and different strategies to measure the recoil energy. This recoil can be measured through phonons (heat), ionization or scintillation, but a combination of two techniques is more effective at rejecting the background from natural radioactivity ( $\gamma$ , electrons,  $\alpha$ , neutrons) and atmospheric muon induced neutrons.

We only mention a few direct search experiments. CDMS [55] exploits phonons+ionization in a cryogenic  $Ge-Si$  target, the XENON10 [56, 57] collaboration searches for scintillation+ionization signals in liquid Xe. These detectors have not seen any evidence for WIMP scattering and reported the most constraining bounds on the spin-independent cross section  $\sigma_{\chi p}^{SI} < \mathcal{O}(10^{-7}$  pb), see Fig. 1.4 (left), and on the spin-dependent cross section on neutrons  $\sigma_{\chi n}^{SD} < \mathcal{O}(0.1$  pb). The spin-dependent coupling with protons  $\sigma_{\chi p}^{SD} < \mathcal{O}(0.1$  pb), see Fig. 1.4 (right), is most constrained by the null searches at COUPP [58] and KIMS [59]. Actually, indirect searches for dark matter annihilations in the Sun offer better prospects to

constrain this coupling, since the Sun contains a lot of hydrogen.

All direct searches reported negative results, except for one. The DAMA experiment looked for and found [60] an annual modulation of the event rate due to the time-dependent relative velocity  $f(\mathbf{v}, t)$  of the neutralinos in the galactic halo in a detector rest frame that orbits the Sun. The DAMA modulation signal gives a lot of tension with other direct searches, which rule out the DAMA favoured  $m_\chi - \sigma$  phase space at very high confidence levels. This is shown in Figure 1.4 for the spin-independent (left) and spin-dependent (right) cross section. The ion channelling effect was only recently taken into account, but nevertheless, there is only a small remaining region (around  $m_\chi \simeq 10$  GeV) that reconciles all experiments [54].

Besides the neutralino-nucleon cross section, direct searches could infer the mass of the neutralino through the recoil energy spectra [61]. However much larger volumes than the current 10 kg detectors are needed to cross the discovery threshold. Multi-ton detectors will scan over the plausible cross section phase space, going down to  $10^{-10}$  pb. But at these low cross sections, the background from elastic scattering of solar fusion neutrinos compromises the dark matter interpretation of a positive detection [62]. The measurement of the direction of the nuclear recoil could solve this ambiguity.

### 1.3.3 Indirect searches

Rather than observing the dark matter directly inside the detector volume, indirect searches look for the products of DM annihilations occurring outside the detector. The annihilation rate scales as  $\rho_\chi^2$  because the process requires two DM particles. So, one should search for an annihilation signal from regions where the DM density is enhanced by gravitational processes. Typical source candidates are the centre of our galaxy, the surrounding galactic halo, neighbouring dwarf galaxies and, closer home, the Sun and the Earth.

Given that the DM particles are highly non-relativistic, the available energy is their rest mass, thus restricting annihilation products to particles lighter than  $m_\chi$ . Possible annihilation channels for the neutralino include

$$\chi\chi \longrightarrow \begin{cases} q\bar{q}, \ell^+\ell^-, W^+W^-, Z^0Z^0, H_1^0H_3^0, H_2^0H_3^0, & \text{(tree level)} \\ Z^0H_1^0, Z^0H_2^0, W^\pm H^\mp, W^+H^- & \\ gg, Z\gamma, \gamma\gamma, \dots & \text{(one loop level)} \end{cases}$$

Some Feynman diagrams are shown in Fig. 1.5. The branching ratio of each channel depends on the couplings and hence the admixture of the neutralino, Eq. 1.5. The electroweak and Higgs bosons are unstable and only detectable via their decay products. Even if the produced particles are stable, they must be able to reach us and must be distinguishable from background sources of such particles. These constraints leave four messengers for indirect detection. Anti-protons and positrons are interesting because the background fluxes are small. Photons and neutrinos are useful because they are neutral and thus point back to their astrophysical sources. Direct annihilations to  $\gamma$  and  $\nu$  are suppressed however. Photons are only produced at the one loop level, since the neutralino has no charge and therefore no direct couplings to photons. Fermion pair production is suppressed by a factor  $m_f^2/m_\chi^2$ , since the neutralino is a fermion, thereby closing the  $\nu\bar{\nu}$  channel<sup>7</sup>.

<sup>7</sup>This  $\nu\bar{\nu}$  suppression does not occur for the UED dark matter candidate,  $B^{(1)}$ , which is a boson.

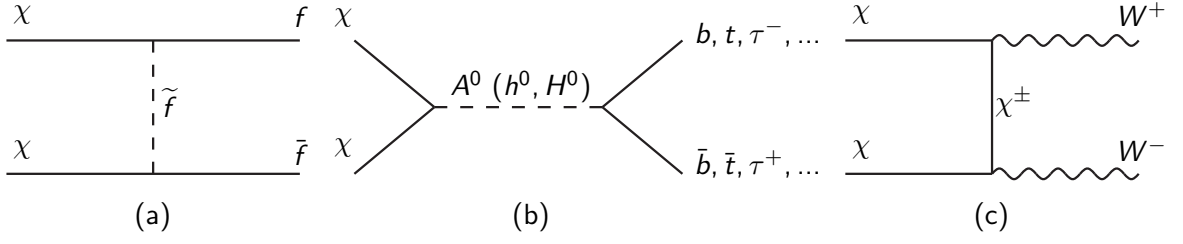


**Figure 1.5** – Contributions to the neutralino annihilation cross-section from (a) slepton and squark exchange, (b) near-resonant annihilation through a Higgs boson, and (c) chargino exchange. Taken from [43].

The energy spectrum of the dark matter messengers is rather hard, with a characteristic cutoff at  $m_\chi$ . This allows to discriminate the signal from the astrophysical backgrounds, which typically follow a falling power-law spectrum. So, one should look for a bump-with-cutoff in the energy distribution. When found, the DM induced energy spectrum can be used to extract information about the underlying particle physics of the dark matter. The cutoff reveals its mass, the shape can differentiate between the various DM candidates. In reality, experimental and theoretical limitations apply and no single channel detection will be sufficient to solve the dark matter problem.

## Photons

Gamma rays are particularly interesting messengers since they are not attenuated over cosmological distances and point back to their astrophysical source. The differential gamma ray flux from a direction  $\psi$  is [63]

$$\Phi_\gamma(E_\gamma, \psi) = \frac{1}{2} \frac{\langle \sigma v \rangle}{4\pi} \frac{dN_\gamma}{dE_\gamma} \int_{\text{l.o.s.}} dl(\psi) \frac{\rho_\chi^2(l)}{m_\chi^2},$$

where we integrate the square of the DM number density  $\rho_\chi(l)/m_\chi$  over the line of sight  $l(\psi)$ ,  $\langle \sigma v \rangle$  is the thermally averaged annihilation cross section and  $dN_\gamma/dE_\gamma$  is the gamma ray energy spectrum per annihilation. Note that the halo density profile can strongly boost the flux from very dense DM regions, like the centre of galaxies. However, it is not clear how the DM is distributed at the galactic centre, so the flux predictions are subject to sizable astrophysical uncertainties, see Section 1.1.3.

Besides the gamma ray line at  $E_\gamma = m_\chi$  from the  $\gamma\gamma$  and  $Z\gamma$  channels, a gamma ray continuum arises from the decays of the neutral pions produced in the hadronization of the quark-antiquark channel. The gamma line is a real *smoking gun* signature, because it is background free. Unfortunately this signal is very weak. There are more continuum gammas, but they compete with point-like and diffuse galactic and extragalactic backgrounds. If the signal is strong enough and the energy resolution of the detector good enough, it should be possible to discern a bump-with-cutoff on top of the power law background.

The search for DM annihilations at the galactic centre will be very challenging, since a bright gamma source was found there which is now thought to be of astrophysical origin [64]. Alternative targets are nearby dwarf galaxies, which seem to be dark matter dominated. Another option is to search for an annihilation signal from the DM halo that surrounds the Milky Way, and potentially contains a lot of massive dark subhalos.

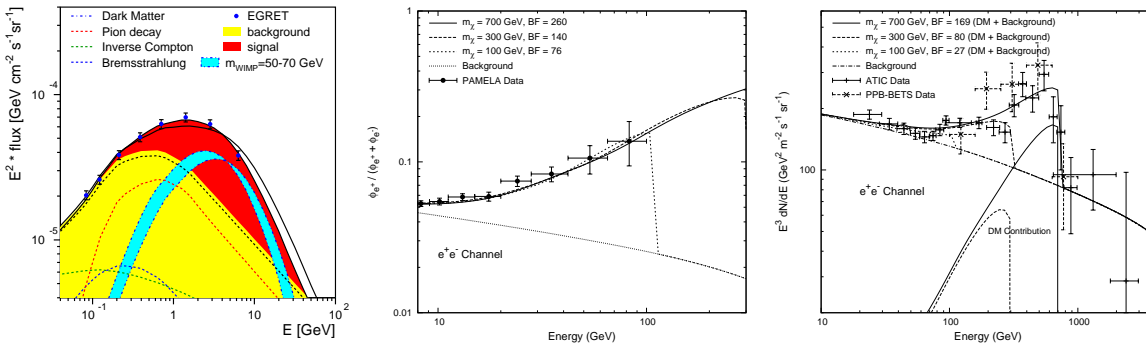


**Figure 1.6** – Left: indication of a neutralino induced excess of diffuse galactic gamma rays by EGRET [66], which was recently questioned by preliminary Fermi studies. Centre: fit of PAMELA’s positron fraction data to several neutralino scenarios. Right: fit of the  $e^-e^+$  flux measured by ATIC/PPB-BETS to several neutralino scenarios [69].

There are several ground-based Air Cherenkov Telescopes which can detect the faint Čerenkov light emitted by gamma ray induced air showers, e.g. MAGIC, VERITAS and H.E.S.S. Their energy threshold is around 100 GeV, so they are most sensitive to rather heavy neutralinos. The recently launched Fermi satellite has an energy reach between 20 MeV and 300 GeV, which is more favourable for lighter particles [65]. But this comes at the cost of a much smaller effective area.

Several indications of DM induced gammas have been claimed in the past, but none were confirmed. The EGRET instrument aboard the Compton Gamma Ray satellite found an excess of 1 – 10 GeV diffuse gamma rays, which could be interpreted as due to DM annihilations in the halo [66], see Fig. 1.6 (left). However, preliminary studies with Fermi show an agreement with the background expectation and suggest that the EGRET excess has an instrumental origin [67]. Various experiments also found a 511 keV line from the galactic centre, which could be attributed to  $e^+e^-$  annihilations at rest, where the positrons originate from DM annihilations. A recent reanalysis of INTEGRAL data indicated an astrophysical rather than a dark matter origin [68].

## Anti-matter

Neutralino annihilations in the halo produce charged anti-matter particles, which bend under the influence of the galactic magnetic field and lose energy along the way. Hence, a good galactic propagation model is needed to predict the energy spectra of positrons and anti-protons at the Earth, but these always show a cutoff at  $E = m_\chi$ . The background for these searches comes from secondary production of anti-matter in cosmic ray interactions on galactic nuclei. Again, the background energy spectrum approximately follows a falling power law and the neutralino induced signal would be seen as a small bump with the characteristic cutoff. Since anti-matter does not travel long distances, the anti-matter flux expectations depend on the rather nearby DM density profile. Hence, it suffers only mild astrophysical uncertainties, certainly not as much as the  $\gamma$  channel.

Anti-matter should be detected high in the atmosphere and preferably above. For quite some time balloon-borne and space based experiments have found an excess of

positrons above 10 GeV [70, 71]. This result was recently confirmed by the PAMELA satellite data [72], see Fig. 1.6 (centre). PAMELA also measured the anti-proton flux, but found no deviation from the expected background [73]. Other experiments, like ATIC [74], PPB-BETS [75] and H.E.S.S. [76], measured the electron+positron<sup>8</sup> spectrum above 100 GeV and reported an excess as well, see Fig. 1.6 (right).

These recent findings spurred a lot of phenomenological activity. The data seem to favour a rather heavy neutralino, but this dark matter interpretation faces some challenges too. The positron fraction and  $e^- + e^+$  energy spectra can be fit quite well, but only when the naturally expected flux level is scaled up by a large amount ( $\sim 100$ ). These boost factors would originate from local dark matter overdensities in our neighbourhood, but simulations expect them to be relatively small ( $\lesssim \mathcal{O}(10)$ ). Besides this drawback, it is remarkable that no excess was found in the anti-proton data. This indicates that the neutralino does not annihilate to quark pairs, which is an exotic scenario. Other astrophysicists point to relatively young pulsars in our neighbourhood as the source of the high energy positrons. These can accelerate cosmic-ray induced positrons to high energies and deliver them at the Earth atmosphere [77]. This ongoing debate could possibly be settled by Fermi.

## Neutrinos

Like photons, neutrinos are produced in the decays of the annihilation products, they do not suffer energy losses and point back to their source. The energy spectrum depends on the dominating annihilation channels, which is model dependent. Unfortunately, neutrinos are weakly interacting and therefore much harder to detect. From the bounds on the DM induced gamma ray flux from the galactic centre, one must conclude that it is very unlikely to detect a neutrino flux from the galactic centre in the next few years [78]. Other targets are the Sun and the Earth, which would have captured neutralinos from the galactic halo over cosmological times. These accumulated at the core, increasing the annihilation rate. Only neutrinos can escape these dense production regions however. Since this detection channel is the subject of this work we refer to the following chapter for the details about backgrounds and the neutrino detection principle.

This work exploits a data set taken with the AMANDA detector, in a search for neutralino annihilations in the centre of the Sun. Various experiments have already reported results from searches for neutrinos from the Sun or the Earth: MACRO [79], BAKSAN [80], BAIKAL [81], Super-Kamiokande [82, 83]. Several next-generation experiments are under construction, IceCube [84, 85] and ANTARES [86, 87], or in development phase, KM3NET [88, 89].

None of the completed searches have found any significant excess of neutrinos over the atmospheric background. Limits were set on the neutralino-induced muon flux from the Sun and the Earth as a function of neutralino mass, see Figure 1.7. The markers in the figure represent muon flux predictions for a simplified MSSM, often referred to as the phenomenological MSSM (pMSSM), which contains seven free parameters. A scan is made over this 7-dim phase space and several quantities computed at each point (relic density, muon flux, SI/SD cross sections, ...). The colour code indicates whether the model is either allowed or disfavoured by the spin-independent cross section bounds from XENON10

<sup>8</sup>At very high energies, it becomes increasingly difficult to disentangle electrons from positrons.

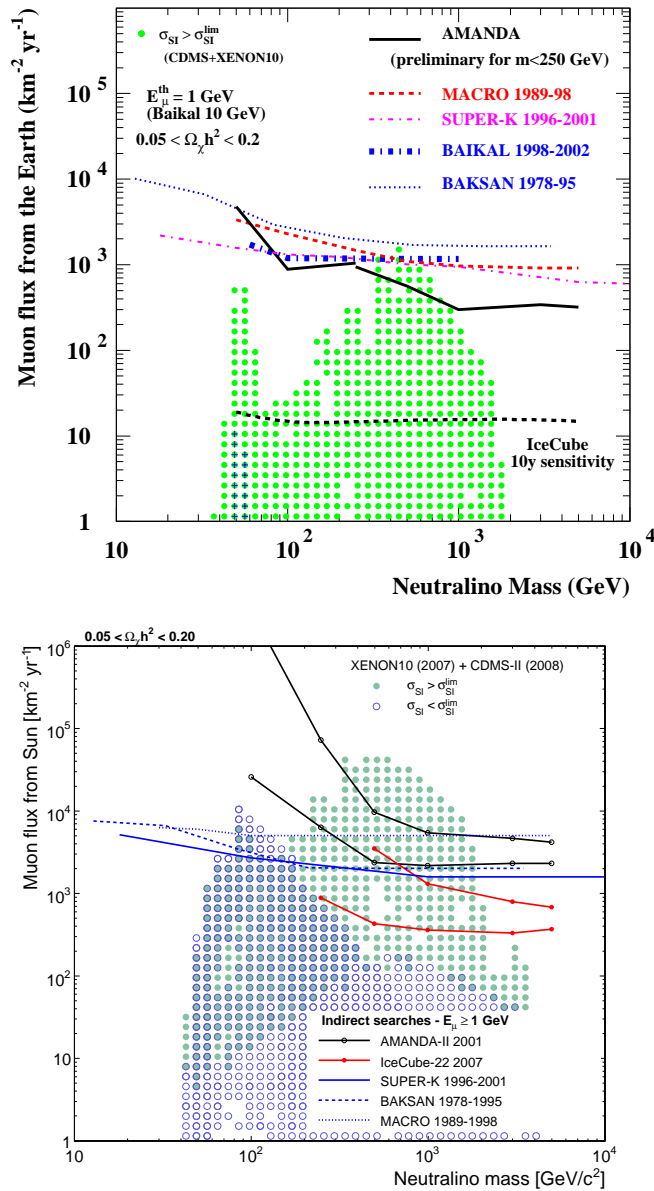


**Figure 1.7** – 90% CL upper limits on the neutralino-induced muon flux from the Earth (top) and Sun (bottom). Lines show the results from various indirect searches (references in text), markers denote the pMSSM parameter space and whether the flux prediction is allowed or disfavoured by direct searches.

and CDMS. Later, we will see that the constraints on the DM annihilation rate in the Sun can be translated to constraints on the neutralino-proton cross section, see e.g. the Super-Kamiokande result in Fig. 1.4 (right).

The outcome of our analysis on AMANDA data will be translated to a measurement of the neutralino-induced muon flux from the Sun, the neutralino annihilation rate in the Sun and the neutralino-proton scattering cross sections. This is presented in the final chapter of this dissertation.



# Chapter 2

## Neutrinos as neutralino probe

In this chapter we discuss all physical processes related to the detection of neutrinos from neutralino annihilations in the Sun. The first section describes the capture of neutralinos from the galactic halo and the subsequent production of neutrinos. In the following section we focus on the neutrino detection principles. At the end of this chapter several experimental aspects are highlighted.

### 2.1 Neutrinos from neutralinos in the Sun

#### 2.1.1 Solar capture and annihilation

During their galactic trip dark matter particles occasionally interact with other particles, losing part of their energy. When sufficient energy is lost and the surrounding gravitational well is deep enough, the particle becomes trapped. Once captured, the dark matter collects at the bottom of the gravitational potential due to subsequent scatters over cosmological timescales. In this section we focus on dark matter capture by the Sun.

The capture rate  $C_{\odot}$  of galactic dark matter particles  $\chi$  by the Sun can be approximated by [90, 91]

$$C_{\odot} \simeq 3.4 \times 10^{19} \text{ s}^{-1} \times \left( \frac{\rho_{\chi}}{0.3 \text{ GeV/cm}^3} \right) \left( \frac{270 \text{ km/s}}{\bar{v}_{\chi}} \right)^3 \times \left( \frac{\sigma_{\chi H}^{SD} + \sigma_{\chi H}^{SI} + 0.07 \sigma_{\chi He}^{SI}}{10^{-7} \text{ pb}} \right) \left( \frac{100 \text{ GeV}}{m_{\chi}} \right)^2, \quad (2.1)$$

where  $\rho_{\chi}$  denotes the local density,  $\bar{v}_{\chi}$  the velocity dispersion and  $m_{\chi}$  the mass of the dark matter. We motivated the lightest neutralino,  $\tilde{\chi}_1^0$ , as a good dark matter candidate in Section 1.2.2, and refer to it as  $\chi$  from now on. Capture by the Sun happens through elastic scatters off hydrogen and (to a lesser extent) helium nuclei, in both a spin-dependent and spin-independent fashion. Previous expression reflects the fact that slow, light particles are easier to capture, at a rate proportional to the neutralino number density and scattering cross section. While the first two bracketed factors represent astrophysical parameters, the latter two originate in particle physics. None of these are known accurately.

The standard halo model prescribes a density of  $\rho_{\chi} = 0.3 \text{ GeV/cm}^3$  with a dispersion of  $\bar{v}_{\chi} = 270 \text{ km/s}$ , see Section 1.1.3. Non-standard halo models, e.g. the recently suggested

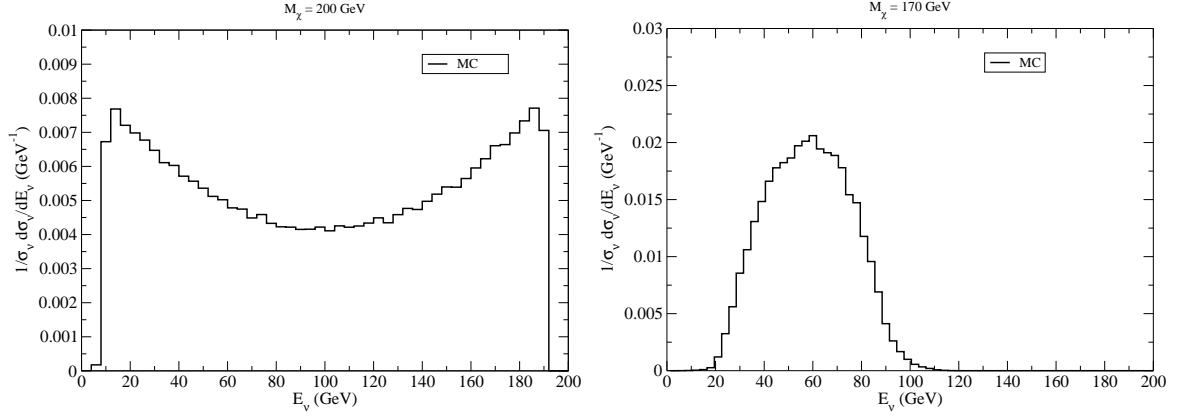


**Figure 2.1** – Normalized neutrino energy spectrum at the centre of the Sun from annihilations to  $W$ -bosons (left) and  $t$ -quarks (right), with a mean energy of respectively a half and a third of the neutralino mass [94].

existence of a dark disk [92], result in a different scale and velocity-behaviour of Eq. 2.1. From the particle physics side, the allowed mass range is  $47 \text{ GeV} < m_\chi < \mathcal{O}(10 \text{ TeV})$  [1, 93] for typical supersymmetric models. The neutralino-nucleon cross sections vary by several orders of magnitude over the supersymmetric parameter space but are constrained by direct searches. In previous chapter we have seen that the best current bounds are  $\sigma_{\chi P}^{SI} \lesssim \mathcal{O}(10^{-7} \text{ pb})$  [55, 56] and  $\sigma_{\chi P}^{SD} \lesssim \mathcal{O}(10^{-1} \text{ pb})$  [58, 59].

Neutralino annihilations and thermal evaporation<sup>1</sup> deplete the captured population. The evolution of the number of neutralinos  $N$  with time is given by

$$\frac{dN}{dt} = C_\odot - 2 \left( \frac{1}{2} C_A N^2 \right) - C_E N,$$

where  $\Gamma_A \equiv \frac{1}{2} C_A N^2$  is the annihilation rate and  $C_E$  the evaporation rate. Assuming a negligible evaporation rate (valid for masses above 10 GeV) and a constant capture rate we find

$$\Gamma_A(t) = \frac{1}{2} C_\odot \tanh^2 \left( t \sqrt{C_\odot C_A} \right).$$

Capture and annihilation equilibrate after a time  $t$  much larger than the timescale  $\tau \equiv (C_\odot C_A)^{-1/2}$ . For typical neutralino models, equilibrium in the Sun is already reached  $\tau \simeq 10^8 \text{ yr}$  after its birth. In equilibrium, the annihilation rate is directly proportional to the capture rate and, hence, the total elastic neutralino-nucleon cross section

$$\Gamma_A(t \gg \tau) = \frac{1}{2} C_\odot \propto \frac{\rho_\chi}{v_\chi^3} \times \frac{\sigma_{tot}}{m_\chi^2}. \quad (2.2)$$

This relation will be exploited at the end of this work.

The neutralino is a superposition of the bino, wino and CP-even higgsino eigenstates, Eq. 1.5. We have seen in Section 1.3.3 that such a particle has various channels open

<sup>1</sup>The velocity of captured neutralinos can suddenly pass the escape velocity of the Sun, due to interactions with nuclei which have a thermal velocity distribution. This process is called thermal evaporation.

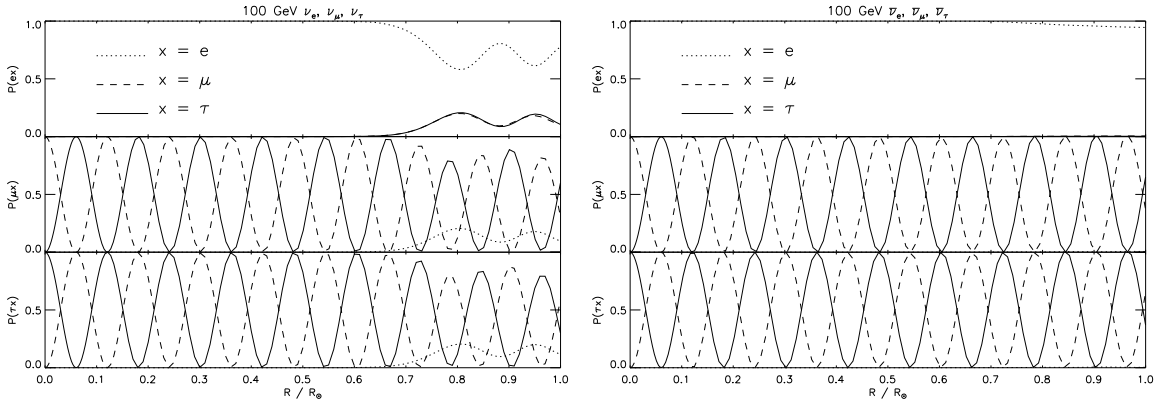


**Figure 2.2** – Probability to detect  $\nu_e$  (dotted),  $\nu_\mu$  (dashed) and  $\nu_\tau$  (solid) after propagation through a fraction  $R/R_\odot$  of the solar interior. Illustrated is a 100 GeV neutrino (left) and anti-neutrino (right), for three initial flavours (top, middle, bottom row) [96].

for annihilation – quarks, leptons, gauge bosons and Higgs bosons – each with a branching ratio determined by its admixture, which in turn depends on the supersymmetric parameters. Only Standard Model particles are produced, since (a) the annihilation happens essentially at rest and (b) the neutralino is the lightest supersymmetric particle. Neutrinos are the only messenger particles from neutralino annihilations that are able to escape a dense medium like the Sun and reach an earthbound detector. Unfortunately, annihilation to light fermions is suppressed by a factor  $m_f^2/m_\chi^2$ , excluding direct neutrino production. Instead, neutrinos are produced in the hadronization and decay of the annihilation particles, with a ratio  $\nu_e : \bar{\nu}_e : \nu_\mu : \bar{\nu}_\mu : \nu_\tau : \bar{\nu}_\tau = 1 : 1 : 1 : 1 : r : r$ .

For each channel, the influence of the unknown supersymmetric parameters on the neutrino energy spectrum solely comes from the neutralino mass. Indeed, annihilations only occur to Standard Model particles, whose decay processes are well understood. The single-channel spectrum  $(dN_\nu/dE_\nu)_X$  is simply obtained by boosting the known centre-of-mass spectrum by the mass of the neutralino. Gauge bosons decay semi-leptonically, leading to an average energy  $\langle E_\nu \rangle \simeq m_\chi/2$ . This is higher than that of quark channels which first hadronize,  $\langle E_\nu \rangle \simeq m_\chi/3$ , see Fig. 2.1. The total neutrino energy spectrum is the sum over all channels  $X$ , weighted by their branching ratio

$$\frac{dN_\nu}{dE_\nu} = \sum_X BR(\chi\chi \rightarrow X) \left( \frac{dN_\nu}{dE_\nu} \right)_X. \quad (2.3)$$

With  $47 \text{ GeV} < m_\chi < \mathcal{O}(10 \text{ TeV})$ , the neutrinos are expected in the GeV–TeV range.

The neutrinos are produced isotropically, in a region confined to the inner 1% of the solar radius [95]. This makes the Sun a point source of neutralino-induced signal for neutrino telescopes, which typically cannot resolve such a small angular region.

## 2.1.2 Neutrino oscillations

Since the flavour eigenstate  $\nu_{\alpha \in \{e, \mu, \tau\}}$  and mass eigenstate  $\nu_{i \in \{1, 2, 3\}}$  of a neutrino are different, the flavour of a massive neutrino *oscillates* during propagation. The survival/appearance probability of a particular flavour as a function of distance depends on the mass squared

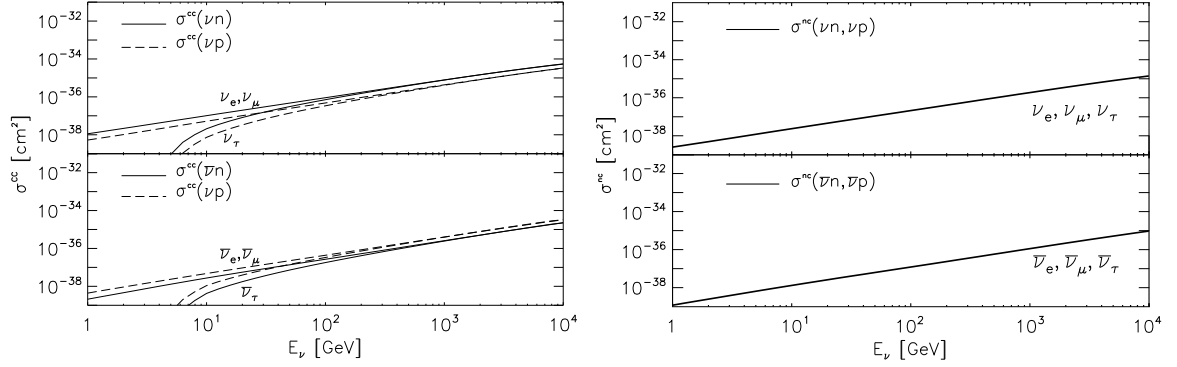


**Figure 2.3** – Cross section for charged-current (left) and neutral-current (right) interactions on protons and neutrons, for neutrinos (top) and anti-neutrinos (bottom). Figures adapted from [96].

differences ( $\Delta m_{21}^2$  and  $\Delta m_{31}^2$ ), the leptonic mixing angles ( $\theta_{12}$ ,  $\theta_{13}$  and  $\theta_{23}$ ) and the CP-violating phase ( $\delta$ ). Several oscillation experiments have measured these parameters, some remain inaccurately known. The standard scenario prescribes  $\Delta m_{21}^2 = 8.1 \times 10^{-5} \text{ eV}^2$ ,  $\Delta m_{31}^2 = 2.2 \times 10^{-3} \text{ eV}^2$ ,  $\theta_{12} = 33.2^\circ$ ,  $\theta_{13} = 0^\circ$ ,  $\theta_{23} = 45^\circ$  and  $\delta = 0^\circ$  [97].

The phenomenology of three-flavour oscillations is not trivial, we restrict ourselves to a brief discussion. The oscillation length scales linearly with energy, which means that higher energies oscillate less frequent. Also, the effect is different when in vacuum or in matter. In media with high electron densities, e.g. the solar interior, the matter eigenstate of  $\nu_e$  is altered which suppresses its oscillation. This is the so-called MSW effect [98, 99]. In that case only  $\nu_\mu \leftrightarrow \nu_\tau$  mixing occurs, which turns out to happen maximally. However, in the outer layers of the Sun, at a lower  $e^-$  density, a  $\nu_e$  oscillation resonance is encountered. Figure 2.2 illustrates the evolution of the oscillation probability with propagated distance from the centre of the Sun. Vacuum oscillations on the other hand mix all three flavours. But with  $\theta_{12}$  less than maximal,  $\nu_e$  does not mix completely with the other flavours.

The net result is that the neutrino flavour ratios at the detector,  $\nu_e : \bar{\nu}_e : \nu_\mu : \bar{\nu}_\mu : \nu_\tau : \bar{\nu}_\tau = r' : r' : 1 : 1 : 1 : 1$ , are different from those at the injection point in the centre of the Sun. The absolute neutrino flux remains unchanged however.

### 2.1.3 Neutrino interactions

Two types of weak interactions occur, depending on whether the neutrino exchanges a charged  $W$ -boson or a neutral  $Z$ -boson with a quark in nucleon  $N$ . The former process is referred to as a charged-current (CC) interaction, it transforms the neutrino  $\nu_\ell$  in its associated charged lepton  $\ell$

$$\nu_\ell (\bar{\nu}_\ell) + N \longrightarrow \ell^- (\ell^+) + X.$$

The latter process is a neutral-current (NC) interaction, which preserves the neutrino

$$\nu_\ell (\bar{\nu}_\ell) + N \longrightarrow \nu_\ell (\bar{\nu}_\ell) + X.$$

In both cases  $X$  represents a hadronic final state.

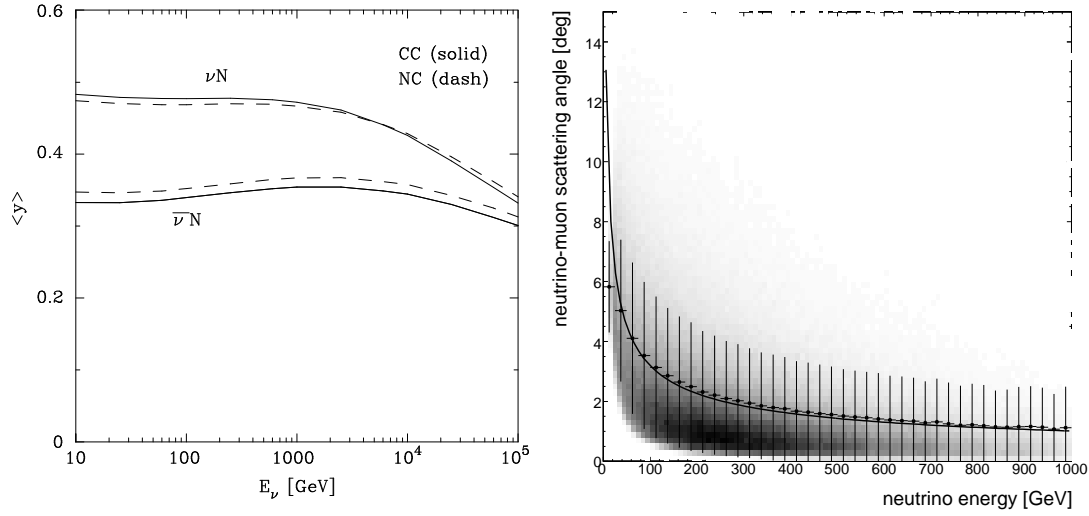


**Figure 2.4** – Left: evolution of the average inelasticity with energy for (anti)neutrinos in CC and NC interactions [102]. Right: distribution of deflection between neutrino and muon versus neutrino energy (shaded area), the average deflection and spread (profile histogram), and equation 2.4 (line).

The differential cross section for a charged-current interaction of a neutrino with an isoscalar nucleon<sup>2</sup> of mass  $M$  can be written as [100]

$$\frac{d^2\sigma_{\nu N \rightarrow \ell X}}{dx dy} = \frac{2G_F^2 M E_\nu}{\pi} \left( \frac{M_W^2}{Q^2 + M_W^2} \right)^2 [xq(x, Q^2) + x\bar{q}(x, Q^2)(1-y)^2],$$

where  $-Q^2$  is the invariant squared four-momentum transfer between the incident neutrino and the outgoing lepton,  $q(x, Q^2)$  and  $\bar{q}(x, Q^2)$  are the parton distributions of the nucleon,  $G_F$  is the Fermi constant,  $M_W$  is the  $W$ -boson mass,  $x$  (fraction of the nucleon momentum carried by the interacting quark) and  $y$  (fraction of the neutrino energy transferred to that quark) are the Bjorken scaling variables. A similar expression can be obtained for neutral-current interactions, or for non-isoscalar targets.

The CC and NC cross sections are well described by a linear function of energy, in the range  $1 \text{ GeV} < E_\nu < 10 \text{ TeV}$ . At higher energies, less relevant to this work, the increase in cross section becomes suppressed by the  $W$ -boson propagator. Fig. 2.3 shows the result of a calculation [96] with the CTEQ6 parton distribution functions [101] for a proton and neutron target. We observe that (a) the cross section is smaller for anti-neutrinos than for neutrinos and, along the same line, (b) the NC cross section is smaller than that of CC interactions. While the former process is completely flavour symmetric, for the latter that is only completely true at energies much larger than the tau-mass threshold.

The CC interaction hampers and permits neutrino detection at the same time. Charged-current interactions in the neighbourhood of a detector produce detectable charged leptons. However, the very same process reduces the flux of neutrinos on their way out of the Sun, this becomes particularly important for  $E_\nu > 100 \text{ GeV}$ . An exception is the tau-neutrino though. It is regenerated at a lower energy in the decay of the tau-lepton, and not absorbed

<sup>2</sup>An isoscalar target has an equal amount of protons and neutrons.

permanently like  $\nu_e$  or  $\nu_\mu$ . The NC interaction does not absorb the neutrinos, but reduces their energy (and hence their further interaction probability) instead. Almost all CC/NC interactions occur in the deepest part of the Sun, out to about  $0.1R_\odot$  [96]. The absorption in the Earth is negligible in the sub-TeV energy domain.

From the detection point of view, two further aspects are important. The first is the fraction  $E'/E_\nu$  of the incident neutrino energy transferred to the lepton. Alternatively, the inelasticity,  $y \equiv 1 - E'/E_\nu$ , quantifies the fraction of the energy lost to the hadronic final state. Fig. 2.4 (left) shows that the average inelasticity for  $\nu$  ( $\bar{\nu}$ ) is roughly constant and about 45% (35%) for energies below 10 TeV. At higher energies the average drops to around 20%. Secondly, the mean scattering angle between neutrino and the outgoing charged lepton  $\langle\theta_{\nu\ell}\rangle$  is energy dependent

$$\langle\theta_{\nu\ell}\rangle \simeq 3.2^\circ \sqrt{\frac{100 \text{ GeV}}{E_\nu}}. \quad (2.4)$$

This poses a physical limit to the precision with which the original neutrino direction can be known. The neutrino picture of the Sun becomes increasingly blurred at lower energies. In the sub-TeV energy domain, the deflection is larger than the angular resolution of neutrino detectors which is around  $1^\circ$ , see Fig. 2.4 (right).

## 2.2 Neutrino detection

The detection of neutrinos relies on their weak interaction with nuclei in and around a detector. The charged interaction products radiate Čerenkov photons which can be picked up by an array of photo-multipliers (PMTs). The combination of a small neutrino flux and a small interaction cross section implies that a large volume is required to obtain a meaningful rate of detected events. To keep the cost manageable the volume should be instrumented sparsely. The AMANDA detector, described in Chapter 3, employs such a large-volume (200 m wide, 500 m high) sparse-instrumentation (PMTs separated by  $\sim 30$  m horizontally,  $\sim 15$  m vertically) design in an attempt to detect astrophysical neutrinos in the Antarctic ice sheet.

### 2.2.1 Charged particles in ice

Before discussing neutrino detection, we need to understand how charged particles behave in matter, charged leptons in particular.

**Electrons** High energy electrons lose their energy essentially through bremsstrahlung. The emitted photon subsequently loses its energy by producing an  $e^+e^-$ -pair. This scenario repeats itself until the electron energy drops below roughly 92 MeV [103]. From then on ionisation starts to dominate the energy loss and the electromagnetic shower stops developing. A simulated example of a 100 GeV electron is shown in Fig. 2.5 (left). Many secondary particles are produced, leading to a shower around 10 m long.

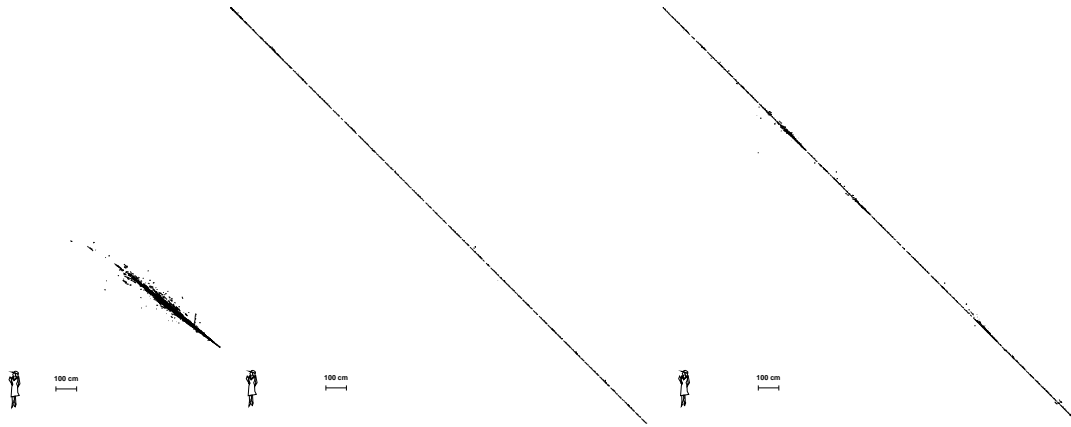


**Figure 2.5** – GEANT simulation of a 100 GeV electron (left), 100 GeV muon (centre) and 1 TeV muon (right) in water [103]. Only charged particles above the Čerenkov threshold are shown. The horizontal scales read 1 m, both muons start and stop outside the picture.

**Muons** The energy loss of muons is more versatile, see Fig. 2.6 (left). For muons below  $E_c = 600$  GeV ionisation dominates the energy loss, at a nearly constant rate of  $\sim 246$  MeV per traversed meter of ice. Above the critical energy  $E_c$ , radiative processes dominate –  $e^+e^-$ -pair production, bremsstrahlung and photonuclear interactions – each leading to showers with secondary particles. Figure 2.5 shows that sub-TeV muons are almost *naked*, with very few secondaries from stochastic losses. At higher energies muons become more dressed with showers. Generally, we can describe the muon energy loss by

$$-\frac{dE}{dx} = a(E) + b(E)E,$$

where  $a(E) = 0.268$  GeV/mwe and  $b(E) = 0.470 \times 10^{-3}$ /mwe are nearly energy independent constants<sup>3</sup> [104]. The parameters  $a$  and  $b$  quantify the relative strength of continuous and stochastic energy losses respectively. Integration of previous expression yields the following estimate of the average muon path length

$$R(E) = \frac{1}{b} \ln\left(1 + \frac{b}{a}E\right).$$

Figure 2.6 (right) shows that in the continuous regime the muon range is proportional to the energy, and that above the critical energy, there is a logarithmic increase. A 10/100/1000 GeV muon traverses on average roughly 40/375/2500 m of ice. Also shown is the maximum path length versus energy, defined as the length reached by at most 0.1% of the muons.

**Tau leptons** Tau-leptons are highly unstable particles and decay almost promptly to hadrons, electrons (19.6% of the decays) or muons (17.7%). The separation between the production and decay vertex is smaller than 1 m for  $E_\tau < 10$  TeV. The decay leads to a hadronic shower, an electromagnetic shower or a muon track.

<sup>3</sup>The quoted values of  $a$  and  $b$  are valid for an icy medium, but expressed in terms of *metres water equivalent*. The connection between water and ice happens through its density:  $1 \text{ mwe} = 1/\rho_{\text{ice}}$  m ice, where  $\rho_{\text{ice}} = 0.917$  g/cm<sup>3</sup>.

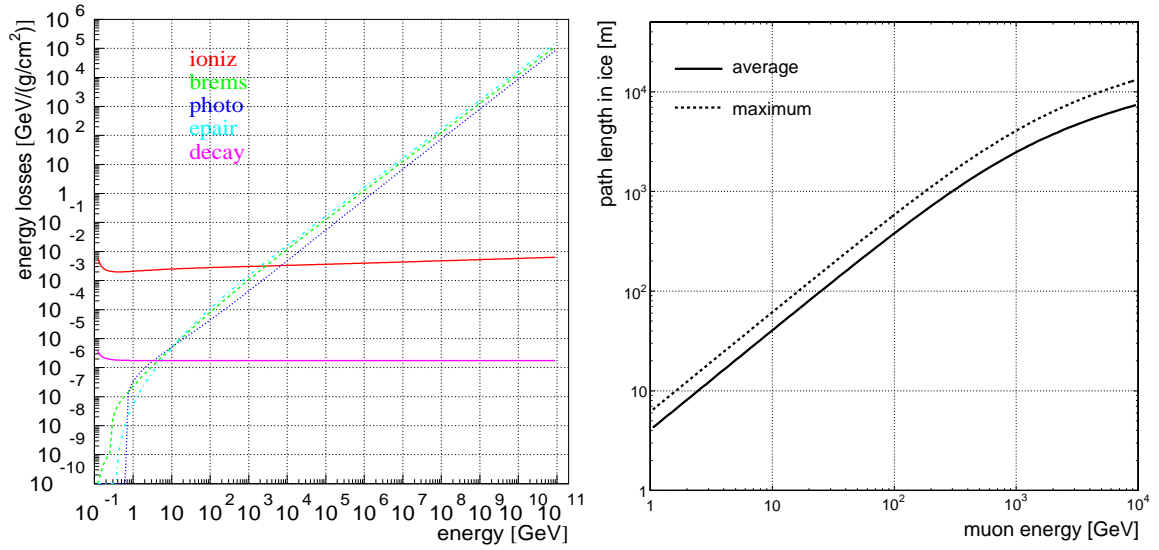


**Figure 2.6** – Left: energy dependence of the muon energy loss processes in ice [104]. From top to bottom at 100 GeV: ionization,  $e^+e^-$ -pair production, bremsstrahlung, photonuclear interactions and  $\mu$  decay. Right: average and maximum muon path length in ice.

**Hadrons** Hadrons have a similar fate as electrons. They experience further interactions to form additional hadrons of lower energy. The process repeats itself and a cascade of particles develops over a length of order 10 m.

## 2.2.2 The Čerenkov effect

When a charged particle propagates faster than the speed of light in its surrounding medium,  $v \geq c/n$  (where  $n$  is the refractive index of the medium), it radiates Čerenkov light. This condition can be translated to a threshold on the particle's energy,  $E > m/\sqrt{1 - n^{-2}}$ . The Čerenkov effect starts for electrons above 780 keV, muons above 162 MeV and taus above 2.7 GeV. The energy loss due to this effect is completely negligible with respect to the energy loss processes discussed in previous section.

The importance of Čerenkov light is not the energy loss, but the fact that all photons are emitted at an identical angle  $\theta_c$  relative to the particle track

$$\cos \theta_c = \frac{1}{\beta n},$$

where  $\beta \equiv v/c$  is the speed of the particle in units of  $c$ . For relativistic particles in an icy medium ( $n = 1.32$ ) the Čerenkov angle equals  $\theta_c = 41^\circ$ . A characteristic light cone, called the Čerenkov cone, accompanies the particle while it traverses the medium.

The Čerenkov light field of a muon is perfectly conical<sup>4</sup>. The measurement of the arrival times of photons in a three-dimensional grid allows to reconstruct this cone and find its axis, revealing the direction of the muon. An electromagnetic or hadronic shower produces a rather spherical shell of Čerenkov light, since the particle directions in the shower

<sup>4</sup>In reality, it can be distorted by varying optical properties of the detection medium.

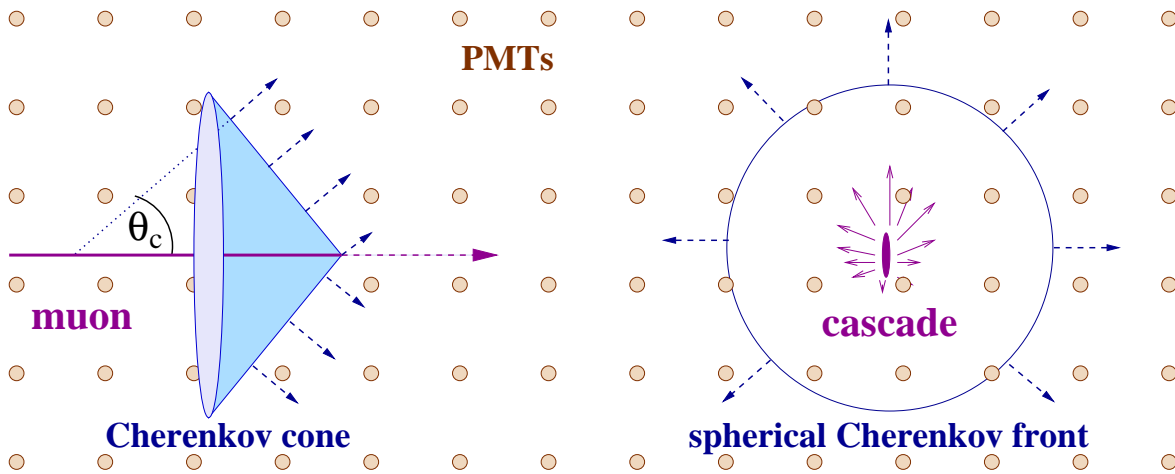


**Figure 2.7** – Čerenkov signature of muons and cascades in a PMT array.

are roughly isotropic. This spherical shell contains some directionality since the shower is elongated, but it is too short to allow an accurate angular reconstruction. Showers induced by radiative energy losses along the muon track slightly distort the Čerenkov cone from the *naked* muon. This complicates the reconstruction, especially at very high energies.

The Čerenkov light spectrum is peaked at short wavelengths, in the ultraviolet domain. A muon radiates about  $N_0 = 3.27 \times 10^4$  photons over the length of one meter in the wavelength range  $300 - 600 \text{ nm}$ <sup>5</sup>. The total light output of showers is conveniently parametrised as  $N_{\text{show}} = \kappa N_0 E/1 \text{ GeV}$ , where  $\kappa = 4.37 \text{ m}$  ( $3.50 \text{ m}$ ) for electromagnetic (hadronic) cascades [103].

### 2.2.3 Neutrino signatures

The neutrino signature left in the detector depends on the type of interaction and its flavour. Neutrinos and anti-neutrinos are impossible to distinguish.

The only detectable part after a neutral-current interaction is the hadronic final state, which develops a hadronic cascade of  $\sim 10 \text{ m}$ . The charged-current interactions on the other hand produce detectable charged leptons as well

- $\nu_e, \bar{\nu}_e$ : hadronic shower from CC interaction + electromagnetic shower from electron; a spherical Čerenkov light field is emitted, see Fig. 2.7 (right).
- $\nu_\mu, \bar{\nu}_\mu$ : hadronic shower from CC interaction + muon track with occasional showers along the track; a clear light cone is emitted, slightly distorted by spherical emission due to showers, see Fig. 2.7 (left).
- $\nu_\tau, \bar{\nu}_\tau$ : hadronic shower from CC interaction + second shower from  $\tau$  decay, occasionally followed by a muon track; since the separation between the CC and decay vertex is much smaller than the separation between the light sensitive devices (particularly below  $1 \text{ TeV}$ ) no difference can be made between  $\nu_\tau$  and  $\nu_e$  or  $\nu_\mu$ .

<sup>5</sup>This is the sensitive range for an AMANDA PMT, see Section 3.2.2.

In the next paragraph we will see that astrophysical neutrinos are hidden in a typical data set collected by a neutrino telescope. When searching for neutrino emission by a point-like source, e.g. the centre of the Sun, the most discriminating information comes from the reconstructed direction of the observed events. Cascade signatures from  $\nu_e$  and  $\nu_\tau$  are too short for a reliable angular reconstruction. Muons on the other hand have a long range which provides ample directional information for the reconstruction methods. Therefore, the search for neutralino annihilations is conducted through the  $\nu_\mu$  channel.

## 2.2.4 Backgrounds

Astrophysical sources accelerate and emit charged particles, some of which reach the Earth. Hydrogen and helium nuclei are the main components of these so-called *primary cosmic rays*. They collide with nuclei in the atmosphere of the Earth to provoke large showers of secondary particles. Muons and neutrinos are by far the most numerous secondaries that reach the surface of the Earth. They are produced in the decays of charged pions and kaons through the decay chain

$$\begin{aligned} p &\longrightarrow \pi^+ (+ K^+ \dots) \longrightarrow \mu^+ + \nu_\mu \\ n &\longrightarrow \pi^- (+ K^- \dots) \longrightarrow \mu^- + \bar{\nu}_\mu \end{aligned}$$

Originating in cosmic ray interactions with the atmosphere these particles are referred to as *atmospheric muons* and *atmospheric neutrinos*. They constitute a background (or maybe better, a foreground) to the search for astrophysical neutrinos.

The decay length of the  $\pi$  and  $K$  mesons increases with energy, until it meets the interaction length at the critical energy  $\epsilon$ . This turnover point occurs at higher energies for heavier mesons, since they have a shorter lifetime:  $\epsilon_\pi = 115$  GeV,  $\epsilon_K = 850$  GeV. As a result, below  $\sim 100$  GeV decay dominates over interaction and the atmospheric muon and neutrino energy spectra follow that of the primary cosmic rays,  $d\Phi/dE \sim E^{-2.7}$ . Above  $\sim 1$  TeV interactions steepen the spectrum by one power in energy,  $d\Phi/dE \sim E^{-3.7}$ . Around 1 PeV the spectrum flattens due to decays from charmed mesons, which are highly unstable and therefore have a much higher critical energy.

Below 10 GeV the angular spectrum is proportional to  $\cos^2 \theta$ , and flattens at higher energies to approach a  $\sec \theta$  distribution. Here, the zenith angle  $\theta$  spans the angle between the vertical and the direction of the particle's origin, see Fig. 5.2. The so-called *secant theta* effect is explained by the fact that at large zenith angles the pions and kaons have more low-density atmosphere to travel through and hence decay even at larger energies.

The intensity of atmospheric muons is strongly reduced once they reach the surface and start to penetrate the Earth. That is why neutrino detectors are installed deep underground, using the Earth as a muon shield. A vertical downward-going atmospheric muon needs at least 400 GeV to reach the AMANDA detector, 1730 m deep in the Antarctic glacier. The energy threshold increases with zenith angle, since more matter should be traversed to reach the detector. This suppresses the high zenith angles in the atmospheric muon flux at the detector, until they vanish around  $\theta \simeq 85^\circ$ . Hence upward-going and horizontal muons in the detector can only be created close to the detector and not in the atmosphere. This forms the heart of the neutrino detection principle.

Atmospheric neutrinos obey the same angular and energy directives as their muon siblings. However, neutrinos have an extremely small chance of being absorbed during their traversal of the Earth and are therefore able to produce horizontal and upward-going events in a detector. The same signature is left by neutrinos from astrophysical sources in the opposite hemisphere. This makes atmospheric neutrinos an irreducible physics background, especially in the GeV-TeV domain, where the flux is still strong.

A third background comes from interactions of primary cosmic rays with the atmosphere of the Sun, which, completely analogous to the case of the Earth, subsequently produce *solar atmosphere neutrinos*. The number of events expected is rather small however, less than 1 event per year in a detector like AMANDA [105]. This should be compared to the triggered rate of atmospheric muons of around 100 per second, and atmospheric neutrinos of about 30 per day. Nuclear fusion reactions in the centre of the Sun produce neutrinos with MeV energies, which is much lower than the energy threshold of a typical neutrino telescope, around  $\mathcal{O}(10 \text{ GeV})$ .

## 2.3 Experimental aspects

### 2.3.1 Conversion rate, annihilation rate and muon flux

Neutralino annihilations in the Sun produce an isotropic flux of neutrinos, at a steady rate  $\Gamma_A$ . The total number of neutrinos per unit volume and time that interact at a distance  $D$  from the Sun in a medium with nucleon number density  $n_N = N_A \rho_{\text{medium}}/M_{\text{medium}}$  is

$$\Gamma_{\nu \rightarrow \mu} = \frac{\Gamma_A}{4\pi D^2} \int_0^{m_\chi} dE_\nu \left( \frac{dN_\nu}{dE_\nu} \right)_{\text{det}} \sigma_{\nu N \rightarrow \mu \chi}(E_\nu | E_\mu \geq E_{\text{thr}}) n_N. \quad (2.5)$$

We refer to  $\Gamma_{\nu \rightarrow \mu}$  as the *neutrino-to-muon conversion rate* or the *volumetric flux*. The neutrino interaction probability per unit length,  $\sigma_{\nu N}(E_\nu | E_\mu \geq E_{\text{thr}}) n_N$ , explicitly takes an experimental threshold on the muon energy into account. The neutrino energy spectrum arriving at the detector  $(dN_\nu/dE_\nu)_{\text{det}}$  is the weighted sum over all single annihilation channel spectra, similar to Eq. 2.3. Due to oscillation and interaction processes on the way to the detection volume the arriving spectrum differs from the spectrum at the  $\nu$  production point,  $(dN_\nu/dE_\nu)_{\chi, \odot} \neq (dN_\nu/dE_\nu)_{\chi, \text{det}}$ .

To connect the volumetric flux to the observed event rate we need to know the *effective volume* of the detector. This can be seen as the volume of an ideal detector to which the real detector is equivalent. A detector is called ideal when it detects all the muons that start inside its volume, but none that are created outside. The efficiency with which an event is detected depends on its energy and, to a lesser extent, its zenith angle. Indeed, high energy muons have a long range and can be detected even when created far outside the actual detector volume, low energy muons on the other hand should be produced close by or even inside the detector to be observable. We therefore expect

$$\mu = \frac{\Gamma_A}{4\pi D^2} \left[ \int_0^{m_\chi} dE_\nu \left( \frac{dN_\nu}{dE_\nu} \right)_{\text{det}} \sigma_{\nu N \rightarrow \mu \chi}(E_\nu | E_\mu \geq E_{\text{thr}}) \rho_N V_{\text{eff}}(E_\nu) \right] t. \quad (2.6)$$

detected muons above the energy threshold during a time  $t$ . This can be rewritten in the simpler form

$$\mu = \Gamma_{\nu \rightarrow \mu} V_{\text{eff}} t. \quad (2.7)$$

where  $V_{\text{eff}}$  is the effective volume averaged over the interacting neutrino energy spectrum (see Section 6.1). We note that the neutralino-induced energy spectrum is absorbed in  $V_{\text{eff}}$ , which means that it should be evaluated individually for different neutralino models. The quantity  $V_{\text{eff}} t$  is often referred to as *exposure*.

After reducing the background, an experimenter measures  $\mu$ , estimates  $V_{\text{eff}}$  and infers the neutrino-to-muon conversion rate  $\Gamma_{\nu \rightarrow \mu}$  through Eq. 2.7. To accomplish these tasks we do not need to know the scale of the incoming flux (that is what we want to measure), only its energy spectrum (to optimize event selection criteria and evaluate the effective volume). The conversion rate is then translated to the annihilation rate  $\Gamma_A$  via Eq. 2.5. Historically, it became common practice to compare experiments and theoretical predictions through the muon flux and not the annihilation rate. The muon flux above some muon energy threshold is inferred from the annihilation rate

$$\Phi_{\mu}(E_{\mu} \geq E_{\text{thr}}) = \frac{\Gamma_A}{4\pi D^2} \int_{E_{\text{thr}}}^{m_{\chi}} dE_{\mu} \frac{dN_{\mu}}{dE_{\mu}}, \quad (2.8)$$

where  $dN_{\mu}/dE_{\mu}$  absorbs the effects of neutrino production (SUSY model dependent), propagation, the interaction kinematics and subsequent muon energy losses.

### 2.3.2 Model independence

In order to explain how one can overcome astrophysical and supersymmetric model dependencies of the analysis, we present a qualitative estimate of the number of observed events. The CC cross section is proportional to  $E_{\nu}$  in the energy range of interest (see Fig. 2.3). The effective volume is roughly proportional to the muon range, which is proportional to the muon energy at low energy, and, hence, also neutrino energy (see Fig. 2.4). This implies that the number of detected events is approximately proportional to the annihilation rate and the second moment of the neutrino energy distribution at the detector

$$\mu \propto \Gamma_A \int_0^{m_{\chi}} dE_{\nu} E_{\nu}^2 \sum_X BR(\chi\chi \rightarrow X) \left( \frac{dN_{\nu}}{dE_{\nu}} \right)_{\text{det}, X}.$$

Besides the unknown supersymmetric parameters the annihilation rate is determined by astrophysical uncertainties too. The energy distribution is only affected by supersymmetry, through the neutralino mass (determines the single-channel spectra at the detector,  $(dN_{\nu}/dE_{\nu})_{\text{det}, X}$ ) and its admixture (determines the branching ratios to the various annihilation channels,  $BR(\chi\chi \rightarrow X)$ ). Figure 2.8 shows the second moment of the energy distribution versus neutralino mass for various channels. Annihilation products ( $W$ ,  $\tau$ ,  $Z$ ,  $t$ ) that decay directly to neutrinos have harder neutrino energy spectra and therefore lead to more events. Annihilation to quark pairs produces softer energy spectra due to the hadronization process. Typically, the  $W^+W^-$  (or  $\tau$ -pairs when  $m_{\chi} < m_W$ ) and  $b\bar{b}$  channel produce most and fewest events, they are referred to as the *hard* and *soft* channel respectively.

The unknowns from astrophysics only enter through the total scale of the flux. These are not relevant as long as we do not optimize the event selection criteria based on the total number of signal events. The unknowns from supersymmetry are avoided by performing the analysis for various neutralino models, which straddle the extremes of the detector

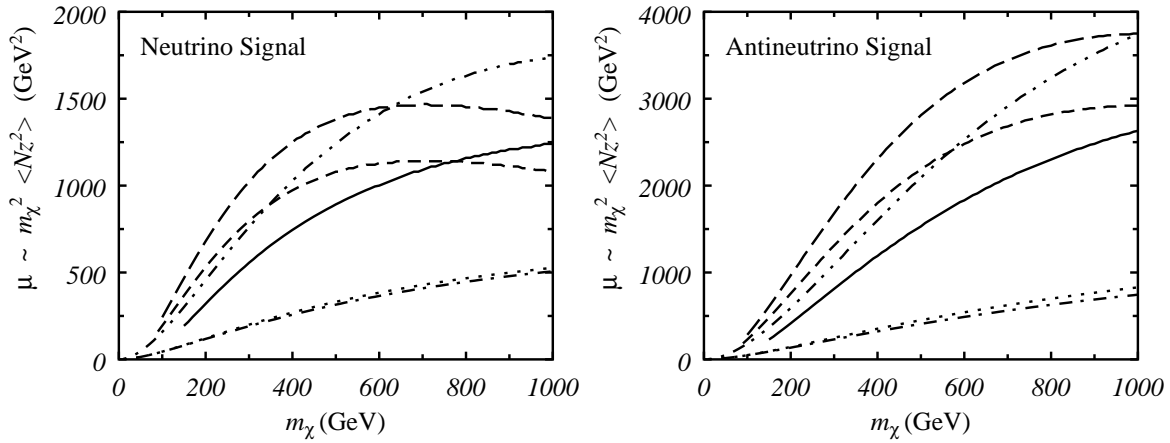


**Figure 2.8** – Left: second moment of the neutrino energy distribution at the centre of the Sun versus neutralino mass for various annihilation channels; from top to bottom at  $m_\chi = 500$  GeV:  $W^+W^-$  (dash),  $\tau\bar{\tau}$  (dot-dot-dash),  $ZZ$  (dash),  $t\bar{t}$  (solid),  $b\bar{b}$  (dot) and  $c\bar{c}$  (dot-dash) pairs. Right: same line style convention for anti-neutrinos. Figure taken from [106].

capabilities. In this work we will calculate  $V_{\text{eff}}$ , measure  $\mu$  and convert it to  $\Gamma_{\nu \rightarrow \mu}$  through Eq. 2.7 for several neutralino masses in the range 50–5000 GeV and, for each mass, the hard and soft annihilation channel. Other, less extreme, neutralino admixtures lead to intermediate energy spectra and therefore to experimental outcomes in between those of the hard and soft channel. The mass range covers a large part of the supersymmetric phase space.



# Chapter 3

## The AMANDA-II neutrino telescope

The combination of a small expected flux and a weak interaction cross-section makes the detection of extra-terrestrial neutrinos a real challenge. This endeavour becomes only feasible with an enormous, and hence naturally occurring, detection medium with good optical properties. Otherwise, the Čerenkov information from neutrino-induced charged leptons becomes blurred and even gets lost through scattering and absorption processes. Since optical sensors are spread rather sparsely over a large volume, the time registration should be accurate enough to allow a faithful reconstruction of the Čerenkov cone, from which the direction of the lepton (and the parent neutrino source) can be inferred. The Antarctic Muon and Neutrino Detector Array, also known as AMANDA, is such a Čerenkov detector. Embedded deep in the 2.8 km thick ice sheet at the geographical South Pole, AMANDA takes advantage of the excellent optical properties of the Antarctic glacier.

This chapter deals with all aspects of the AMANDA detector. The optical characteristics of the ice are described in the next section, followed by overviews of the detector geometry, the hardware components and their calibration.

### 3.1 Characteristics of South Pole ice

#### 3.1.1 A short history of ice

The glacier at the South Pole is approximately 2820 m thick and is the result of accumulation and consequent compaction of snow on the Antarctic continent over geological time scales. The pressure from overlying layers turns snow into a denser form, firn ice. Deeper still, the firn layers undergo further compression and become extremely transparent glacial ice.

However, snow is not the only substance that is accumulated and gets buried. E.g. air bubbles become trapped too, and are gradually compressed with depth until they experience a phase transition to air hydrate crystals [107]. Both phases coexist over several hundred meters of depth. Measurements with an AMANDA precursor revealed that 1300 m below the surface most air bubbles have finally disappeared [108]. Over the years there is a continuous deposition of dust on the surface of the glacier, at a rate depending on the atmospheric (and hence climatic) conditions. Very thin ash layers from occasional volcanic eruptions contaminate the ice too. As we will see, it turns out that these impurities (air bubbles, dust, ash), with their manifest depth dependent concentration, are vital to understand the

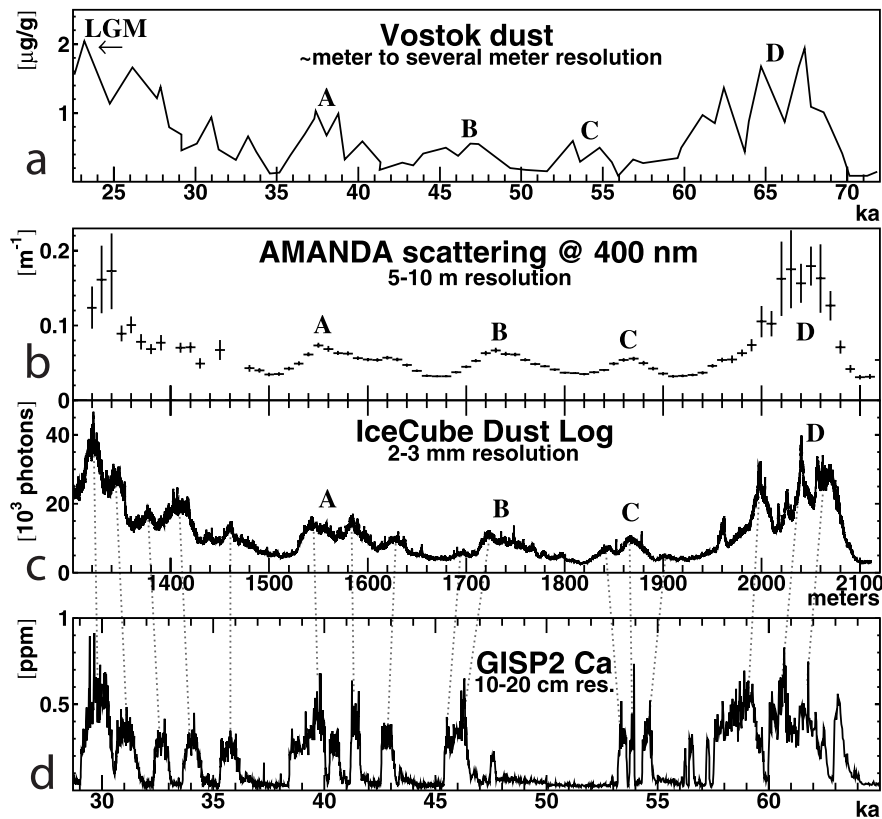


**Figure 3.1** – The vertical dust profile as found in ice cores from Vostok, Greenland and the first IceCube hole at the South Pole [109].

optical properties of the ice at the South Pole.

Ice core records from various polar sites show several distinctive peaks in the dust profile along the vertical, which were matched to those found by an optical logging device lowered in the first IceCube borehole at the South Pole [109], see Fig. 3.1 (1st, 3rd and 4th row). Below 1500 m, four broad layers of dust are easily visible, sedimented between  $\sim 39000$  and  $\sim 66000$  years ago. A more than 300 m thick and very dense layer of dust at  $\sim 1300$  m stems from the Last Glacial Maximum (LGM), about  $\sim 23000$  years ago. After that period, corresponding to shallower depths, a milder climate sets in with lower dust levels in the atmosphere.

As a side-note, we mention that the bedrock below the South Pole has a small downward slope towards the northwest, causing the surface of the ice sheet to flow at a steady rate of 10 meters per year. Models of this glacial flow indicate that the top 2000 m of the glacier move as a rigid volume, while the deeper ice advances gradually slower with depth, until it comes to rest at the bedrock [110]. Only the deepest modules on strings 11, 12 and 13 are not part of the rigid regime and, compared to the rest of the array, they lag behind, but not more than one meter per year. These modules are excluded from the analysis anyway, see Section 5.1. As a result we can safely assume that the detector geometry remains unchanged over the years.

### 3.1.2 Optical properties of deep South Pole ice

On their way through the glacier photons often get scattered (by air bubbles and dust), delaying their measured arrival time, and are occasionally absorbed (by ice, dust and volcanic ash), reducing the photon count. Therefore, we cannot perform any realistic simulation or advanced track reconstruction without knowing how light propagates from its point of production towards its point of detection.

The fate of photons is determined by their wavelengths and the depth dependent composition of the glacier. Optical scattering and absorption in South Pole ice were mapped with in situ measurements at various wavelengths and depths, with pulsed and steady light sources deployed along the AMANDA strings [111]. The optical properties are modelled over the full depth range of the detector (1100 m – 2300 m), and for the wavelength range the optical modules are sensitive to (300 nm – 600 nm), see Sections 3.2.1 and 3.2.2.

#### Optical background

The South Pole glacier is a perfectly dark medium, without the presence of bioluminescent organisms or radioactive isotopes, which are typical sources of background light in deep sea experiments [112, 113]. The only optical background for detectors in ice is radiated by radioactive isotopes (K, Th, U) in the glass spheres of the optical modules.

#### Scattering

Photons scatter when they cross a region with a refractive index different from that of ice ( $n_{\text{ice}} = 1.31$ ). In the Antarctic glacier this occurs predominantly on submillimeter-sized air bubbles and micron-sized dust grains, but not on air hydrate crystals which have a refractive index very similar to that of ice. The average path length, or geometrical scattering length, between two scatter centers

$$\lambda_s = \frac{1}{n_{\text{center}} \langle \pi r_{\text{center}}^2 \rangle} \quad (3.1)$$

is inversely proportional to their number density  $n_{\text{center}}$  and their geometrical cross section  $\pi r_{\text{center}}^2$  [114].

In the range of interest, the optical scattering angle  $\theta$  is independent of wavelength, but there is a dependence on the type of scatter center. Calculations based on Mie scattering theory show that air bubbles and dust grains tend to scatter photons in the forward direction, respectively with  $\langle \cos \theta \rangle = 0.75$  [114] and  $\langle \cos \theta \rangle = 0.94$  [111]. Because of the strong anisotropy of this process, the geometrical scatter length  $\lambda_s$ , Eq. 3.1, does not represent the length scale over which the photon direction becomes randomized. One can argue that it is more appropriate to introduce the effective scattering length

$$\lambda_e = \frac{\lambda_s}{1 - \langle \cos \theta \rangle} \quad (3.2)$$

in the context of anisotropic scattering, or, its reciprocal, the effective scattering coefficient  $b_e \equiv 1/\lambda_e$  [111].

The combined effect of a smaller size and more forward scattering, makes that scattering on dust grains can be neglected in the presence of air bubbles; as confirmed by in situ

measurements, see Fig. 3.2 (top left panel). Above 1300 m bubbles dominate scattering, even in the dense layer of dust from the Last Glacial Maximum. In lower lying layers the bubbles have completely converted to air hydrate crystals (with a similar refractive index as ice) and light scatters essentially on a strongly varying concentration of dust particles (a fingerprint of climate history). We identify the four peaks with high scattering as those from the dust profile in Fig. 3.1. Scattering in volcanic ash should be similar to scattering by dust, but the layers are too thin (of the order of a centimeter) to affect the timing of photons considerably.

From Mie scattering theory we expect a simple power law relation between effective scattering coefficient and wavelength

$$b_e \propto \lambda^{-\alpha}. \quad (3.3)$$

Fig. 3.2 (top right panel) shows that this relation is confirmed by measurements. Longer wavelengths suffer less scattering on dust; while, though not shown in this figure, scattering on air bubbles can be considered wavelength independent.

### Absorption

The absorption length  $\lambda_a$  of a medium is defined as the length scale with  $1/e$  survival probability. As opposed to scattering, absorption manifests a strong wavelength dependence. The absorption coefficient  $a = 1/\lambda_a$ , reciprocal of the absorption length, is well parameterized by an empirical model with three components [115]

$$a(\lambda) = A_U e^{-B_U \lambda} + C_{\text{dust}} \lambda^{-\kappa} + A_{\text{IR}} e^{\lambda_0/\lambda}, \quad (3.4)$$

as shown in Fig. 3.2 (bottom right panel).

Pure ice itself is responsible for absorption at short and long wavelengths, the first and last component. Infrared photons ( $\lambda > 500$  nm) are absorbed by molecular stretching, bending and vibration of  $\text{H}_2\text{O}$  in ice; the ultraviolet tail ( $\lambda < 200$  nm) corresponds to an 8 eV electronic band-gap energy of ice, but falls outside the sensitivity region of the optical sensors.

In the intermediate region, ice is the most transparent solid known and dust governs absorption, the second component in Eq. 3.4. The amount of absorption should trace the dust concentration, which is nicely confirmed by in situ measurements in this wavelength range, Fig. 3.2 (bottom left panel). All dust layers are clearly visible in the ultraviolet and blue, and at 532 nm even the one at 1300 m from the Last Glacial Maximum (obscured by bubbles in the scattering measurements).

### Hole ice

Due to the rapid refreezing and the slow phase transition process, air bubbles remain trapped in the 60 cm wide hole around an instrumented string. The effective scattering length of this hole ice is estimated to be only 0.5 m, much smaller than that for the bulk of the ice. Fortunately the additional arrival time of photons is negligible, because of the small hole diameter. Instead, one should think of the hole ice as if it changes the angular acceptance of the modules: bubbles scatter photons from the dark side of the module back on the photocathode.

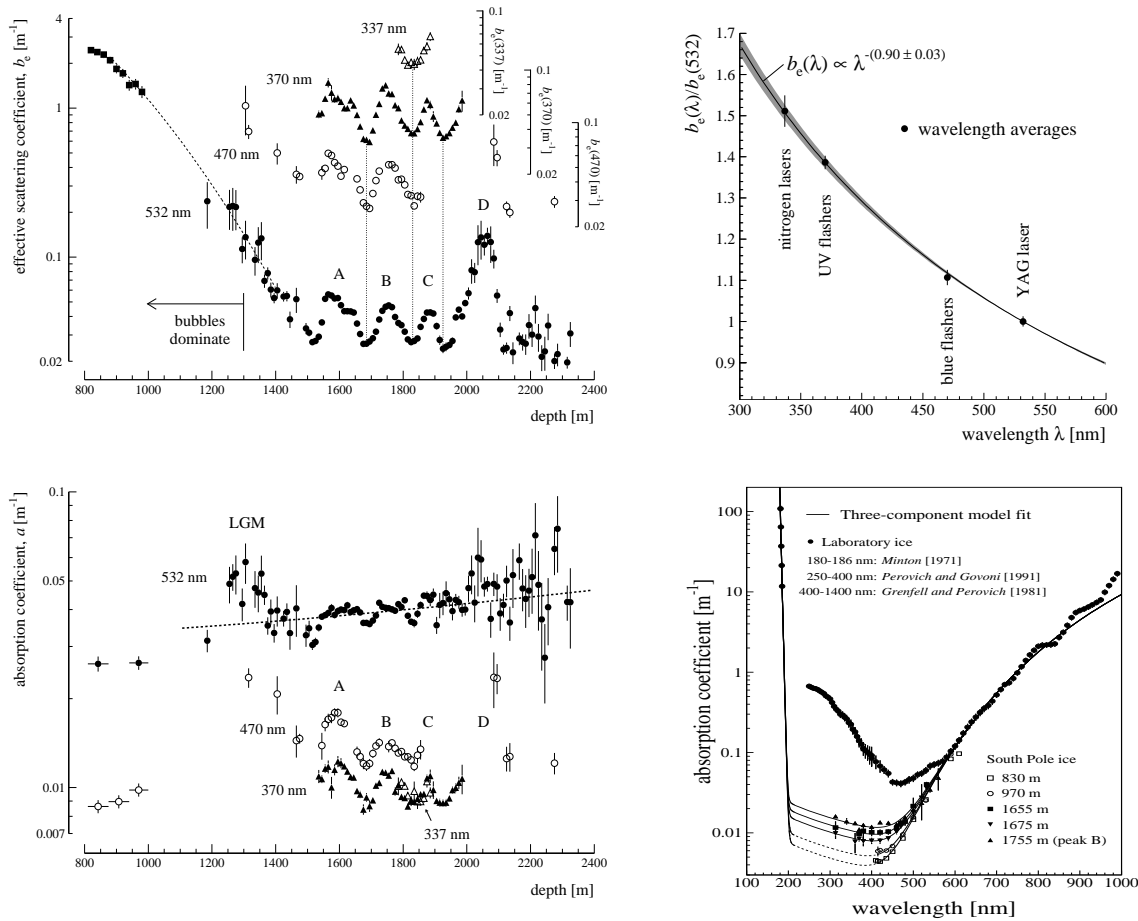


**Figure 3.2** – Depth (left column) and wavelength dependence (right column) of the effective scattering coefficient (top row) and the absorption coefficient (bottom row). Higher coefficients indicate more scattering or absorption. For clarity, the scattering measurements at 470, 370 and 337 nm are scaled according to the axes to the right. Retrieved from [111].

## Discussion

As we will see, convoluting the wavelength dependencies of the glass transmittance, the PMT quantum efficiency and the Čerenkov spectrum the sensitivity of the optical modules peaks near 400 nm, fortunately exactly where the ice is most transparent. For this wavelength and the depth range where most AMANDA modules reside (1500 – 2000 m) the effective scattering length varies between 13 m and 31 m, the absorption length is much longer and lies between 85 m and 137 m.

Experiments in the Mediterranean sea water, e.g. NESTOR [116] and ANTARES [117], typically report longer scattering lengths ( $\sim 120$  m) but smaller absorption lengths ( $\sim 30$  m) than in ice. Scattering blurs the image of the Čerenkov cone, limiting the intrinsic resolution of the detector; absorption dims the Čerenkov cone, reducing the effective volume of the detector. Therefore deep sea neutrino telescopes have a better pointing accuracy, but at the cost of a smaller effective size of the detector.

## 3.2 The AMANDA-II detector

### 3.2.1 Geometry

As we have seen, below 1500 m the Antarctic glacier becomes transparent enough for the detection and reconstruction of high energy neutrinos. The austral summer campaign of 1995/96 marks the beginning of the construction of the Antarctic Muon And Neutrino Detector Array, also known as AMANDA. Near the Amundsen-Scott South Pole base, four 60 cm wide holes were drilled with hot water in the ice sheet down to a depth of around 2000 m, and a cable (referred to as *string*) with optical modules (OMs) lowered in each of them. In February 2000, after three more installation campaigns, the final detector configuration was reached with 677 OMs attached to 19 strings arranged over three concentric rings. The instrumented array is located at a depth between 1500 m and 2000 m. With a height of 500 m and a diameter of 200 m it envelops a cylindrical volume of roughly  $0.016 \text{ km}^3$ , see Fig. 3.3.

During the deployment, optical modules are attached to a cable, while it is lowered in the borehole. Once the water in the hole is refrozen, it becomes impossible to retrieve the OMs to the surface for repair, upgrade or calibration. Hence, a robust technical design of the optical module was chosen, one that ensured a successful deployment and refreezing process, and continuous stable operations over more than 10 years. Strings were deployed during several installation campaigns, gradually enlarging the detector from the innermost to the outer ring (see Fig. 3.4 (left)); the four inner strings during 1995/96, the six strings of the second ring in 1996/97, the first three strings (long) of the outermost ring in 1997/98 and the final six strings in 1999/2000. The detector configurations reached after each of these campaigns are referred to as AMANDA-B4, AMANDA-B10, AMANDA-B13 and, finally, AMANDA-II. Since we only look at data taken with AMANDA-II, we use its shorthand AMANDA notation in the following.

The amount of OMs and their vertical spacing differed for each of these campaigns, as can be seen in Fig. 3.4 (right). The distance between OMs varies between 10 – 20 m, depending on the string. Several modules are located outside the main instrumented volume and are as a consequence not used for this work's purposes.

The AMANDA frame of reference is a right-handed orthogonal system, with the  $Y$ -axis pointing towards Greenwich and the  $Z$ -axis vertically up, towards the sky. The origin of the coordinate system is located close to OM69<sup>1</sup> on string 4, at a depth of 1730 m below the surface. This OM is close to the centre of the array, see Fig. 3.4. The zenith angle  $\theta$  of a particle track is measured from the  $Z$ -axis to the track origin (backwards from the direction of travel). Vertically downward-going and upward-going tracks therefore have a zenith of respectively  $\theta = 0^\circ$  and  $\theta = 180^\circ$ . The azimuth angle  $\phi$  of the particle track is measured counterclockwise from the  $X$ -axis to the point of the track origin. This is illustrated in Fig. 5.2.

Due to its location at the rotation axis of the Earth, astrophysical sources remain at a constant zenith in the AMANDA system. Our signal source, the Sun, is nearby and has a

---

<sup>1</sup>Historically, the origin was defined as the central optical module on the central string 4 (OM70). Later on, a more refined geometry calibration showed that the OM locations should be slightly revised. It was decided however that the absolute position of the origin of the frame of reference would not follow OM70, thereby promoting its nearest upper neighbour to be closest (but not identical) to the origin.

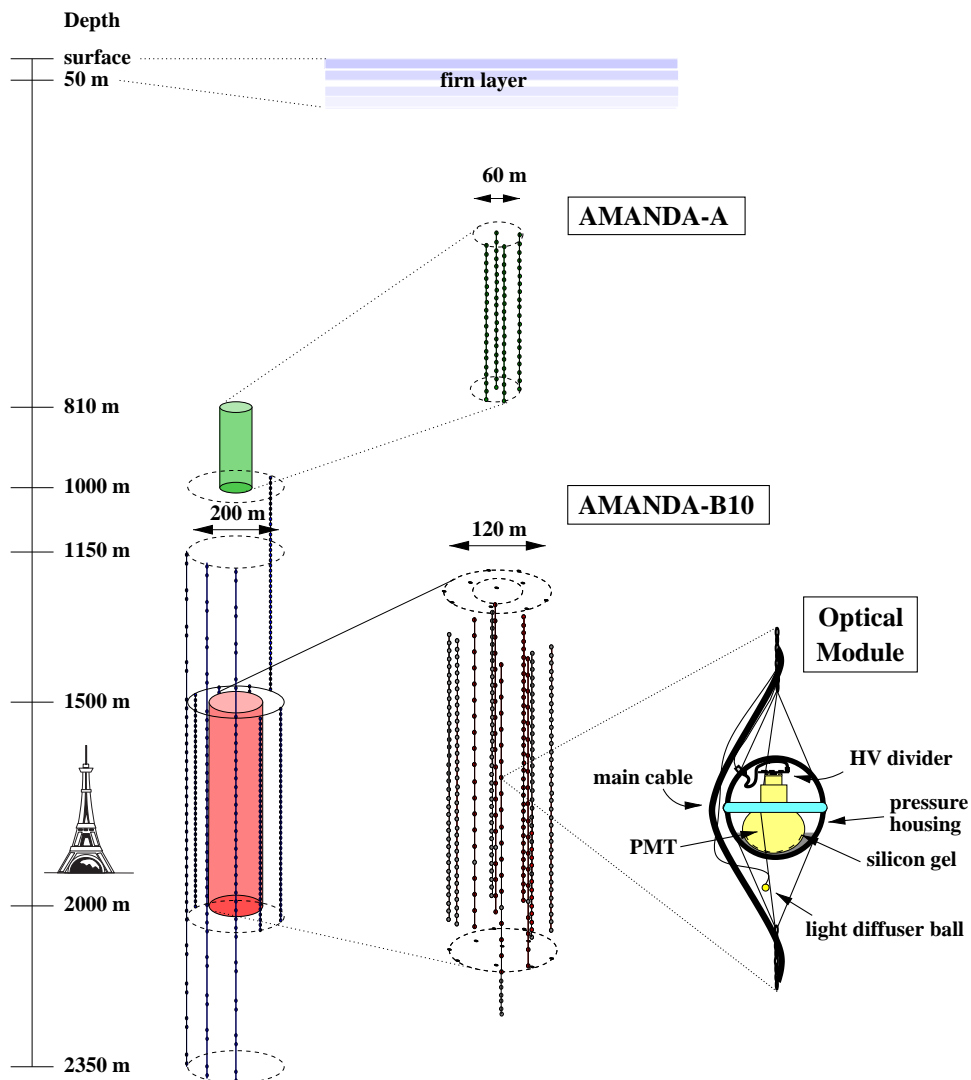


**Figure 3.3** – Schematic overview of the AMANDA detector (left), close-up on one optical module (right). Two historical stages in this neutrino detector project are also shown (middle): AMANDA-A and AMANDA-B10.

slow evolution in zenith, at most  $0.4^\circ$  per day (see Fig. 4.1). That is very convenient for our purpose.

### 3.2.2 Operation

When a photon impinges on an optical module, an amplified pulse is sent to the data acquisition system in the Martin A. Pomerantz<sup>2</sup> Observatory (MAPO) at the surface. There, hits are defined and collected from all OMs, which may ultimately lead to a triggered read-out of the whole detector. Fig. 3.5 outlines the data acquisition electronics.

<sup>2</sup>The first Antarctic astronomer (1916-2008).

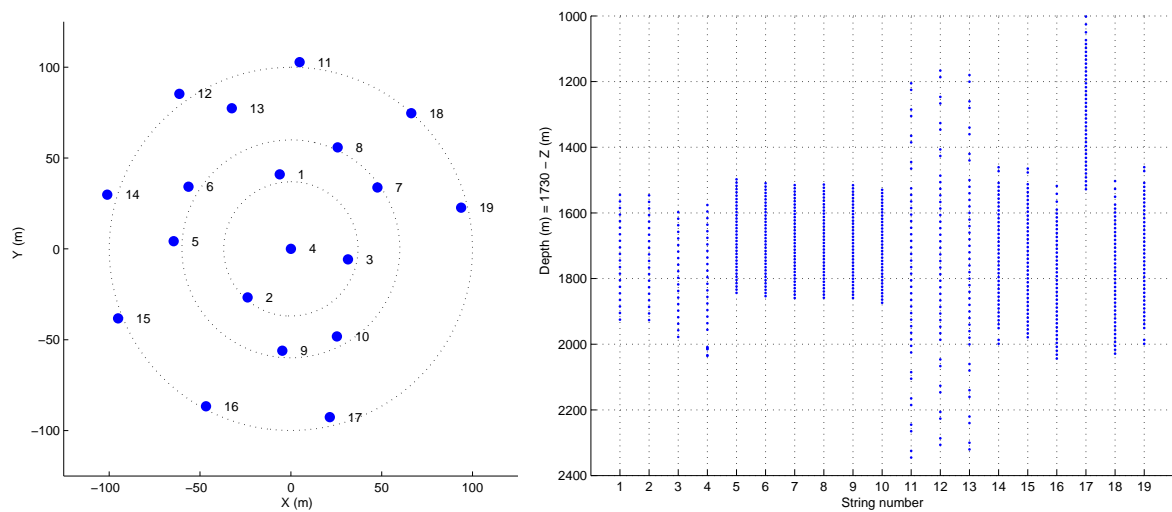


**Figure 3.4** – (Left) Geometry of the 19 AMANDA strings in the horizontal ( $X$ ,  $Y$ ) plane of the AMANDA coordinate system; (right) depth below the ice surface for the optical modules along each string.

### The optical module

The optical module is made up of an 8 inch Hamamatsu photo-multiplier tube (PMT), whose photo-cathode is optically connected to a glass pressure housing by silicon gel, see Fig. 3.3 (right). The PMTs of the first four strings are housed in spheres manufactured by the Billings company, all other modules are equipped with Benthos spheres. When the PMT is operated at a high gain of  $10^9$  the OM is sensitive to single photo-electrons in the wavelength range between 300 nm and 600 nm. The poor UV transmission of the glass sphere limits sensitivity in the important short wavelength region, with Benthos spheres offering better UV transmission than Billings spheres. The poor quantum efficiency of the photo-cathode is the limiting factor for long wavelengths. The peak sensitivity is reached around 400 nm, for which the deep South Pole ice happens to be most transparent.

High voltage is generated in the counting house at the surface and supplied to the PMT over the same electrical cable that carries the analog PMT signal to the surface electronics. The optical modules are connected to the surface either with a coaxial cable (strings 1-4) or a twisted-pair cable (strings 5-19). Both types of cable disperse the PMT signals considerably during their journey of more than 2 km. When transmitted over coaxial cable 10 ns PMT pulses of 1 V arrive at the surface with a width of more than 400 ns and an amplitude of several mV, a twisted-pair cable stretches the same pulse to 150 – 200 ns. Optical modules from the later deployed strings (11-19) are therefore also equipped with an optical fibre, which is essentially dispersion-free. Pulses are read out through the (more fragile) optical fibre rather than the electrical cable, if the former survived the deployment and the refreezing process.

Not all pulses detected at the surface originate from high energy charged leptons in the detector volume. Several classes of non-photon (background) pulses are produced by the detector hardware itself: noise pulses, afterpulses, and crosstalk pulses. Noise pulses are induced by radioactive elements in the OM material (Billings spheres are more radio-quiet

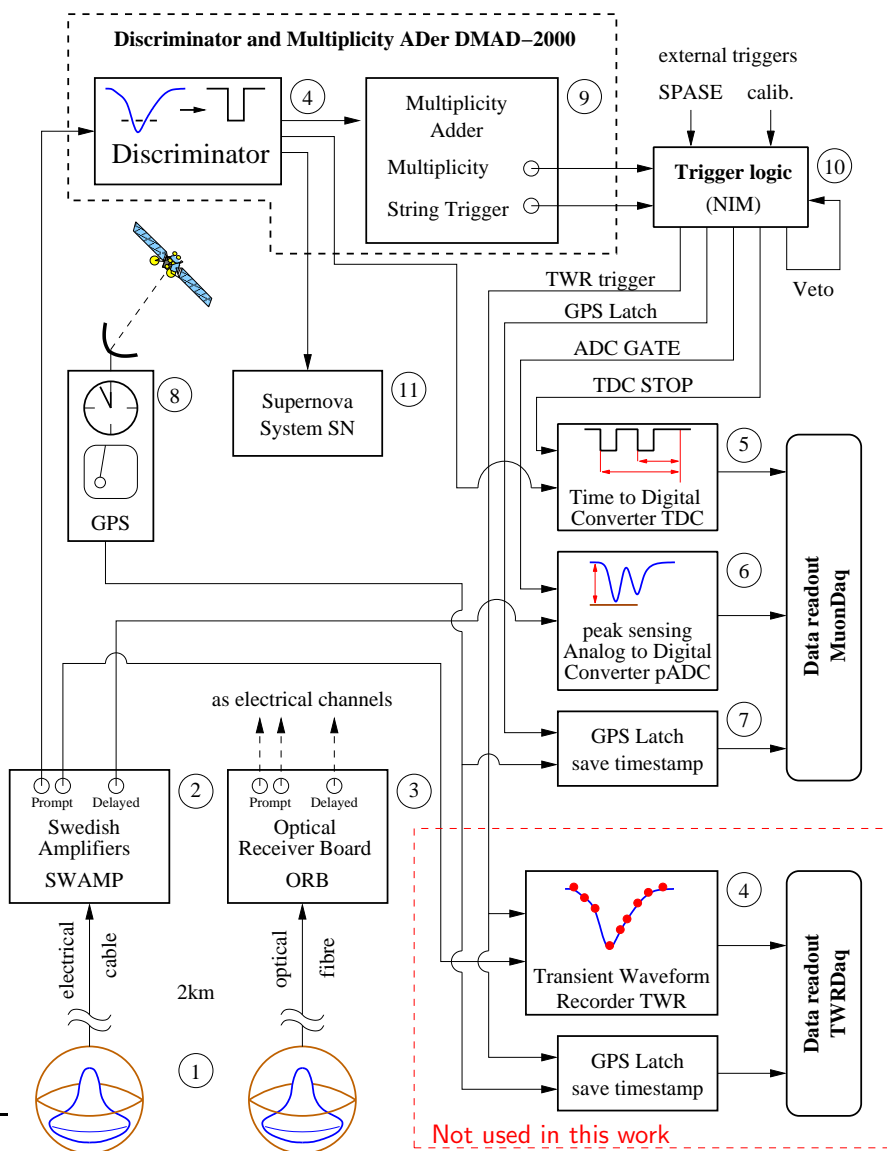
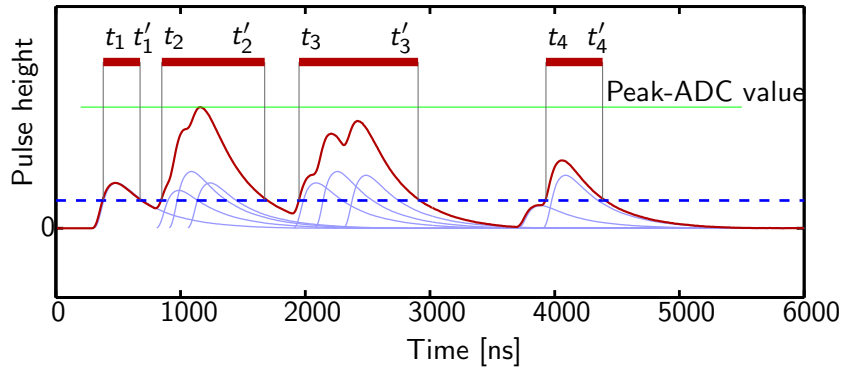


Figure 3.5 – Scheme of the AMANDA data acquisition. Figure taken from [118].

than Benthos spheres) and by thermal noise. Afterpulses are caused by ionization of residual gas in the PMT tubes. Pulses from one OM can be picked up by a neighbouring cable of another OM, a phenomenon known as crosstalk. Yet unidentified disturbances outside the detector occasionally produce a large amount of non-photon pulses too, so-called flare events. Most of these background pulses can be removed from the raw data. Their sources and remedies to prevent them from entering the final data stream are discussed in more detail in Chapter 5.

### The hit

Upon its arrival at the surface, a PMT pulse is first amplified by, depending on the cable type, a *SWedish AMPlifier* (SWAMP) or an *Optical Receiver Board* (ORB). Both components



**Figure 3.6** – Illustration of TDC and pADC information for one optical module. A pulse from the PMT (thin red curve) becomes a hit when it passes the discriminator threshold (blue dashed line). The TDC records the time of the leading edge  $t_i$  and trailing edge  $t'_i$  of up to eight hits (thick red lines). The recorded pADC value is common for all hits in a given OM: that of the maximum pADC of all pulses (horizontal green line) [119].

have two prompt outputs and one  $2 \mu\text{s}$ -delayed output.

One of the prompt outputs is sent to a discriminator integrated in the *Discriminator and Multiplicity ADder* (or DMAD), and continues to a *Time to Digital Converter* (TDC). The latter measures the time of the leading and trailing edge of the pulse, corresponding to the positive and negative crossing point with the discriminator threshold, see Fig. 3.6. The TDC stores at most 16 edges, or 8 complete pulses, in its  $32 \mu\text{s}$  buffer. This implies a possible loss of information for ultra bright events ( $\gtrsim 10^5 \text{ GeV}$ ). A *peak sensing Analog to Digital converter* (pADC) receives the delayed SWAMP/ORB output and registers the maximum pulse amplitude among the pulses arriving within a  $6 \mu\text{s}$  window around the trigger time. Hence, hits are defined by their leading edge (LE), trailing edge (TE) and amplitude (pADC, which is ambiguous information since common for all hits in the same OM). This is illustrated in Fig. 3.6.

Besides the MuonDaq system described above, there is a second more advanced system that records the full waveform information of the pulse (rather than just two edges crossing the discriminator threshold). It is referred to as the Transient Waveform Recorder system, or TWRDaq [118, 120]. However since data from the TWRDaq were not used in this work, it is not described in further detail.

### The trigger

AMANDA triggers are built in the second component of the DMAD, the multiplicity adder. It adds the discriminated pulses of all OMs in a sliding time window of  $2.5 \mu\text{s}$  and verifies whether a predefined threshold value is reached. When this happens a trigger signal is sent to read out the information from the GPS clock and the TDC and ADC buffers. During this time the detector is unable to record information, this so-called *dead-time* typically lasts about 2.2 ms.

Two trigger conditions are implemented:

- The first condition, responsible for the majority of the triggers, is the *multiplicity*

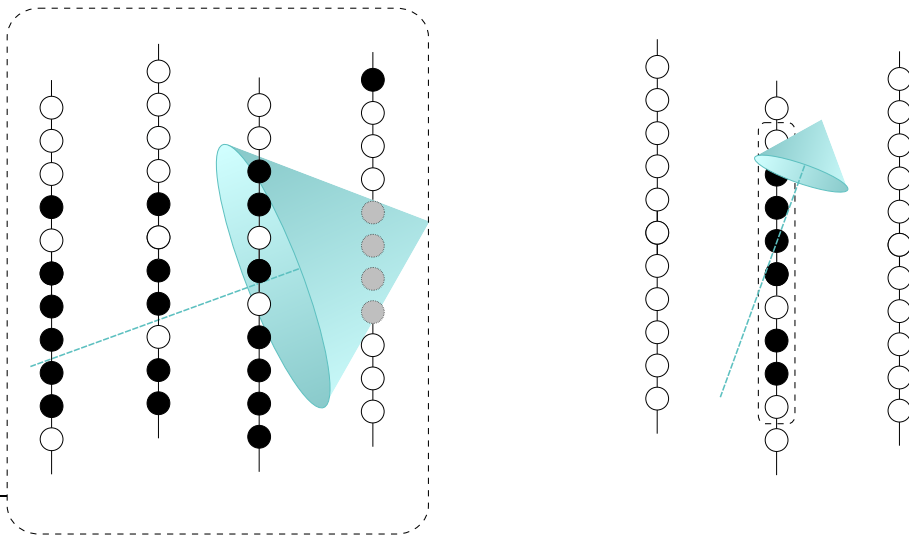


**Figure 3.7** – Illustration of the AMANDA triggers: the  $M = 24$  multiplicity trigger condition (left) and a  $M/N = 6/9$  string trigger set-up (right).

*trigger*. It requires  $M = 24$  hit optical modules within the trigger window of  $2.5 \mu\text{s}$ , see Fig. 3.7 (left). This setting is a compromise between trigger efficiency to high and low energy events. A too low threshold triggers many atmospheric muons which are of relatively low energy. During the resulting frequent detector read-outs higher energy, astrophysical neutrinos will not be detected. Increasing the multiplicity threshold reduces the undesirable dead-time, but, at the same time, the trigger efficiency for low energy neutrinos as well.

- The *string trigger*<sup>3</sup> condition tries to recuperate some of the signal events that fail to satisfy the multiplicity trigger. It does so by lowering the required number of OMs within the sliding window of  $2.5 \mu\text{s}$ . However, to reduce noise effects the hits have to be correlated in space: at least  $M$  out of  $N$  consecutive modules on a string should see a hit. Such a coincidence is illustrated in Fig. 3.7 (right). While for the inner four strings  $M/N = 6/9$  is chosen, the condition is set to  $7/11$  on the remaining strings (which have a smaller vertical spacing between OMs). This trigger became operational in 2001, and to keep the dead-time within reasonable bounds it was decided in 2002 to downscale the string trigger by a factor two<sup>4</sup>.
- Additional trigger signals are possible as well, e.g. from the calibration system or neighbouring air shower detectors (see next section). In practice these triggers are not of neutrino origin and therefore not useful in our search for low energy neutrinos from the Sun. They are discarded from our data set.

The spacing between OMs is much larger in the horizontal than in the vertical direction, reducing the trigger acceptance in the former direction. Below  $\sim 25 \text{ GeV}$  horizontal muons are extremely difficult to detect without the string trigger. Since the solar neutralino signal

<sup>3</sup>Some prefer the term *correlation trigger*.

<sup>4</sup>Only half of the events that exclusively satisfy the string trigger are written to hard disk.

is expected in this regime, we consider two disjoint classes of events in the high level analysis. The first contains the events triggered by the multiplicity trigger, the second class collects the events exclusively triggered by the string condition. Both event streams are referred to as the *standard* and *string* stream.

### 3.2.3 Calibration

Reconstruction algorithms exploit the hit information of a triggered event to provide observables that are useful for the data analysis, see Chapter 5. Before that can start, the measured arrival time of each pulse should be corrected for its time delay due to the transmission from the OM to the surface and due to the electronic components in the DAQ. Besides this, the measured amplitude has to be converted to number of photo-electrons and the position of the OMs should be accurately known.

#### Time calibration

After a photon hits the PMT cathode at time  $t_{\text{true}}$ , the pulse takes a time  $t_0$  to propagate to the discriminator at the surface. There, due to dispersion during the cable transit the fixed discriminator threshold is crossed earlier for large pulses than for small pulses. This time-slew is inversely proportional to  $\sqrt{pADC}$ , so a smaller delay for larger amplitudes. The purpose of the calibration campaign is to find the constants  $t_0$  and  $\alpha$  for each OM, such that the true arrival time can be inferred from the measured time  $t_{\text{meas}}$

$$t_{\text{true}} = t_{\text{meas}} - t_0 - \frac{\alpha}{\sqrt{pADC}}. \quad (3.5)$$

The calibration constants are revised whenever DAQ components are replaced or DAQ settings changed. That is done in the following way [121].

Short pulses from a YAG laser are sent from the surface through a light fibre to small diffuser balls below the OM (see Fig. 3.3). The photons almost immediately hit the photocathode of the PMT. This occurs at a well-known time, since the distance laser-diffuser ball is very accurately measured with an Optical Time Domain Reflectometer. Once enough statistics are collected, the  $t_0$  and  $\alpha$  values are extracted from a fit to Eq. 3.5. Such a procedure is repeated for all OMs in the array.

A different method, using downward going muons, confirmed the calibration constants in a completely independent way. After calibration the arrival time of a photon at any PMT is known with  $\sim 5$  ns precision. This is accurate enough to obtain a negligible systematic effect on the reconstruction results [122].

The effect of the calibration on the arrival time can be seen in Fig. 5.1.

#### Amplitude calibration

When several photons arrive almost simultaneously their pulses merge as a consequence of dispersion during the cable transport. The discriminator then defines a long hit, see Fig. 3.6, but with larger amplitude. The peak-ADC value (in *mV*) of a hit is hence a rough<sup>5</sup> measure of the amount of impinging photons.

<sup>5</sup>Remember that all hits within the same OM receive the same amplitude value, that of the largest pulse.

Atmospheric muons are on average not very bright, so they typically produce only single photo-electrons (spe) in the PMTs. The pADC distribution of such events is a Gaussian spe-peak superimposed on a rapidly falling exponential contribution from PMT noise. The mean amplitude for single photo-electrons  $pADC_{spe}$  is found from a fit to the position of the Gaussian peak in the pADC spectrum, and is different for each OM. Assuming a linear response we can convert the measured pADC value to the number of photons  $npe = pADC/pADC_{spe}$ .

The 35% resolution of the amplitude calibration is caused by the width of the spe pADC peak. However, the linearity of the amplitude response only holds for  $npe < 5$ .

### Geometry calibration

The relative position an OM in the array can be inferred from the time-of-flight between the OM and various light sources. Short laser pulses are injected in the diffuser ball of one OM, while the other OMs are read out. Most photons in the distant modules are scattered, but occasionally a photon arrives unscattered. These photons are exploited in the further analysis. Knowing the injection time of the laser pulse and the time calibration constants we deduce the unscattered propagation time in the ice. This is directly proportional to the distance emitter-receiver. Repeating such an exercise for various emitter-receiver combinations, the relative position of all OMs is measured with  $\sim 1$  m precision. Similar results are obtained with data from the drill-head while the hole was created. These data also allow an absolute position measurement of the global detector with  $\sim 2$  m accuracy.

### 3.2.4 Neighbouring detectors

Throughout its lifetime the AMANDA array has had several neighbouring detector systems, and joint data taking modes were operational for all of these.

- A smaller precursor detector, AMANDA-A, was deployed in 1993/94 at shallower depths where it unfortunately turned out that air bubbles spoil the directional information from the Čerenkov cone. Several years later AMANDA-A was taken out of service, once its results were superseded by the deeper AMANDA array.
- The purpose of the South Pole Air Shower Experiment, or SPASE, is to study primary cosmic rays. It is located at the ice surface and was operational while the data for this work were collected (in 2001, 2002 and 2003). The cosmic ray induced events observed by the SPASE detector constitute a background for this work and are therefore discarded from the joint event stream.
- In 2004/05 the construction phase of AMANDA's large-scale and technologically superior successor started, with an envisaged completion around 2011. This project was named IceCube, a natural choice for a detector covering  $1 \text{ km}^3$  of instrumented volume. Today, with 75% of the IceCube strings deployed, AMANDA is completely surrounded by its successor and technically considered as an IceCube-subsystem. In the coming years the AMANDA array will be switched off, and replaced by several densely packed IceCube strings without which the low energy domain ( $E_\nu < 50 \text{ GeV}$ ) would be out of reach.



# Chapter 4

## Data samples

In this chapter we introduce the experimental and simulated data samples used throughout this work. After describing all programs in the simulation chain, we examine several signal simulation set-ups.

### 4.1 Experimental data

The experimental data sample used for this work was collected with the AMANDA detector between March 6th 2001 and October 19th 2003. Before proceeding with the analysis the good data taking periods should be identified. First, we select the time periods relevant for analysis, which are then checked for detector instabilities. In the last section we give the definition and some relevant statistics of the experimental data samples cleared for analysis.

#### 4.1.1 Data taking period

Major detector service work can only be done in the austral summer, between early November and mid February. During this period the regular data taking is often interrupted by hard- and software replacements and/or upgrades, tests and calibration runs. Once the South Pole station is closed the detector configuration remains stable, and data is continuously collected. Each day a new run is automatically started and the triggered events are written to a fresh file every ten minutes or so. At the beginning of the next summer season, the whole (taped) raw data set is sent to the northern hemisphere for further processing. This naturally divides the data sample in consecutive years, runs and files.

Over the years the detector characteristics alter, but only slightly and in a way that doesn't prevent the combination of the events from 2001, 2002 and 2003 in one analysis sample, see Section 4.1.4.

Solar neutralino-induced events are usually only searched for in the experimental data registered when the Sun is below the horizon (i.e.  $\theta_{\odot} > 90^{\circ}$ <sup>1</sup>), since the Earth acts as a muon filter and a signal source below the horizon is then easier to discriminate from the downward-going atmospheric muon background. An additional data sample, collected when the Sun is at most 10 degrees above the horizon, is used as a background sample for the optimization of the event selection. There is no physical reason to discard the remaining

---

<sup>1</sup>The zenith angle is defined in Section 3.2.1.

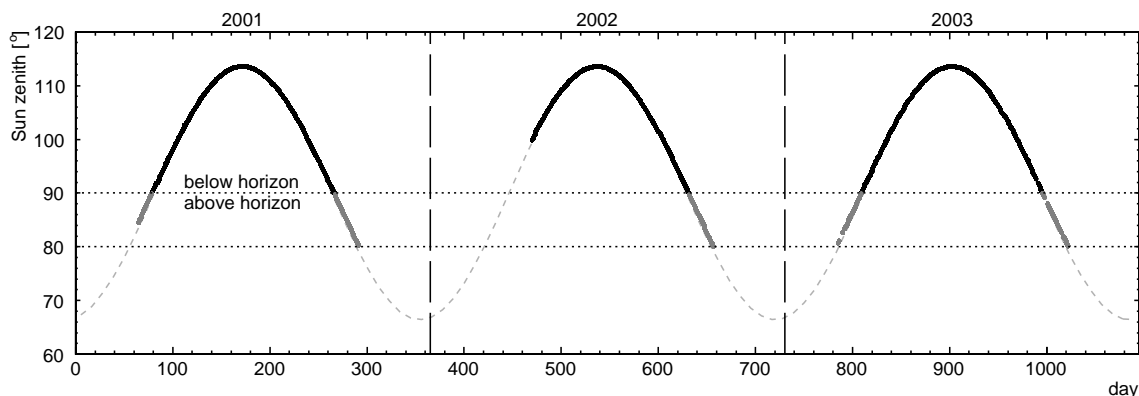


**Figure 4.1** – Evolution of the zenith position of the Sun from Jan 1st 2001 until December 31st 2003 (dashed line). Markers indicate the start of each run in the considered data set.

part (with  $\theta_{\odot} < 80^{\circ}$ ) of the AMANDA data set. The statistics in the optimization sample are sufficient for a robust analysis.

At the Earth's rotation axis the height of the Sun is only determined by the Earth's orbital position around the Sun. Therefore the evolution of the solar zenith during the day is extremely small, and inhabitants of the South Pole experience six consecutive months of night and six months of day. As seen in Fig. 4.1, this fact simplifies the selection of our data samples. Only the runs considered for this work are shown, but the full AMANDA data taking period continues outside the marked region. Black (grey) markers show the sample when the Sun is below the horizon (between  $80^{\circ} < \theta_{\odot} < 90^{\circ}$ ). Table 4.1 gives more specifics about the selected run period. A further discussion on the stability of these experimental data samples follows in the next section.

### 4.1.2 Detector stability

While the detector operates smoothly most of the time, some periods show unstable detector conditions. Automatically compiled plots allow to monitor the performance of the global detector (trigger rates, dead-time, ...) as well as of the individual optical modules (dark noise rates, TDC/ADC information, ...). These reports are consulted to identify stable data taking periods.

#### Long-term variations

After the departure of the seasonal AMANDA workers in February, it takes the winter-over team and their northern collaborators a while to reach stable data taking conditions: any left over service work from the summer season is finished, issues with the new detector set-up are resolved. Once this initial period is over, the detector takes data almost uninterruptedly throughout the rest of the year, as can be seen in Fig. 4.1.

The string trigger, see Section 3.2.2, was introduced in 2001 and went through some changes over the years. In its first year of operation the string trigger was set to 6/9

$\theta_{\odot}$	Year	First run	Last run
$> 80^{\circ}$	2001	Mar 6th (3145)	Oct 18th (3397)
	2002	Apr 15th (5634)	Oct 19th (5914)
	2003	Feb 24th (6940)	Oct 19th (7341)
$> 90^{\circ}$	2001	Mar 19th (3159)	Sep 23rd (3369)
	2002	Apr 15th (5634)	Sep 23rd (5884)
	2003	Mar 20th (6985)	Sep 22nd (7309)

**Table 4.1** – Selection of data taking runs and corresponding dates with  $\theta_{\odot} > 80^{\circ}$  and  $\theta_{\odot} > 90^{\circ}$ .

coincidence on the inner four strings and 7/11 coincidence on the other strings (the latter have a smaller vertical OM spacing). Later that year, on June 29th 2001, these settings were relaxed to 6/9 on all strings, causing an additional 20 Hz in trigger rate, see Fig. 4.2 (top row). In the offline data analysis, this non-uniformity in the 2001 string trigger settings is dealt with by a retriggering procedure, see Section 5.1.3.

In the beginning of 2002 the string trigger settings changed on various occasions in order to keep the trigger rate and the detector dead-time (see Section 4.1.3) within acceptable bounds. For this reason, the events collected during the first part of 2002 are excluded from this work, see Fig. 4.1. From April 15th 2002 onwards, the string trigger was set to 6/9 on strings 1-4 and 7/11 on strings 5-19, but half of the string exclusive triggers were disregarded. This measure, also called *downscaling*, resulted in a supportable event rate and these settings were preserved throughout the rest of 2002 and 2003.

The first row in Fig. 4.2 shows the evolution of the global trigger rate (referred to as  $L0$ ) for 2001, 2002 and 2003; the second row shows the rate evolution of the events passing both the first level selection criteria (also  $L1$ ) and the retriggering requirements. At  $L1$  with retriggering ( $L1+retrigger$ ) three sets of events are distinguished: *all* triggers, the events having only a string trigger flag (*exclusive string*) and the events satisfying the multiplicity trigger and possibly another trigger as well (*inclusive multiplicity*). The event rates are corrected for the dead-time of the detector. More details about the event selections can be found in Sections 6.2 and 6.2.

Even though there is an obvious non-uniformity at the trigger level in 2001, the retriggering procedure is able to recreate uniform conditions at a later analysis level (second/fourth row). Also, as a result of the string trigger downscaling, trigger rates are lower in 2002 and 2003 than in 2001.

At trigger level the experimental data set is completely dominated by atmospheric muons, whose event rate depends on the interaction length of  $\pi^-$  and  $K$ -mesons in the Earth atmosphere (Section 2.2.4). This in turn depends on the density and hence temperature of the atmosphere above the South Pole. Therefore, it is completely natural to observe a seasonal variation (higher in the austral summer, lower during the winter) of the trigger rates in Fig. 4.2. The connection between atmospheric temperature and atmospheric muon rates opens the opportunity of doing physics of the Earth atmosphere with AMANDA [123, 124]. E.g. around September 25th 2002 (day 268) warm air suddenly penetrated the cold air Polar vortex, splitting the ozone hole. It can be seen that the

AMANDA trigger rate suddenly increased due to this remarkable event.

### Short-term variations

Fig. 4.2 also shows evidence of rate variations on smaller timescales than the previously described effects, induced by temporarily unstable hardware components. These instable periods are removed on a file-by-file<sup>2</sup> basis.

In this work we start with an existing list of stable files as compiled by various AMANDA collaborators following slightly different criteria [125–127]. The string trigger plays an important role in this work and has only been used in a few AMANDA analyses so far, so we pay extra attention to the stability of this trigger.

Especially for 2002 and 2003, it turns out that the existing standard list is not sufficient to remove all instabilities seen at the trigger level and even at higher filter levels. We identified additional unstable periods by requiring a smooth evolution of the event rate after trigger level and after the first selection level with retriggering.

Fig. 4.2 shows the situation (before and) after removing all identified unstable data taking periods. No sudden, unphysical jumps in the event rate remain (bottom half of the figure) and we conclude that the selected data sample is safe for analysis purposes. Another conclusion that can be drawn is that the string trigger performance is at least as stable as that of the multiplicity trigger. Any additional unstable periods with respect to the standard list are primarily induced by the main AMANDA trigger and not related to the string trigger.

### 4.1.3 Detector live-time

When the trigger logic accepts an event, the GPS clock and all ADC and TDC buffers are read out and stored to a hard disk. During this process, which takes around  $2.2 \mu\text{s}$ , the detector can not record any additional events, it is called *dead*. As a consequence, the total time of data taking as read from a wall-clock ( $t_{\text{obs}}$ ) overestimates the period that the detector is actually *alive* ( $t_{\text{live}}$ ) and able to detect events.

A higher trigger rate leads to a higher dead-time too. So it is important not to trigger just any event, otherwise, sought after signal events accidentally arriving closely after background events will remain undetected. Here the terms *signal* and *background* depend entirely on the high-energy neutrino source one hopes to detect. Some analyses benefit from a low energy threshold, which at the same time increases the dead-time and the background rate for other analyses.

Except for the initial  $\sim 2 \mu\text{s}$ , the time gap between consecutive events follows an exponential distribution, allowing us to determine the actual event rate  $R_{\text{true}}$ . This is then compared to the observed rate  $R_{\text{obs}}$  to find the dead-time  $\mathcal{D} = 1 - R_{\text{obs}}/R_{\text{true}}$  of the DAQ. This procedure is repeated for every experimental data file [128], which allows to correct the data taking time  $t_{\text{obs},i}$  of each file for dead-time to obtain its live-time

$$t_{\text{live},i} = t_{\text{obs},i} \times (1 - \mathcal{D}_i). \quad (4.1)$$

<sup>2</sup>Each file contains around ten minutes of data.

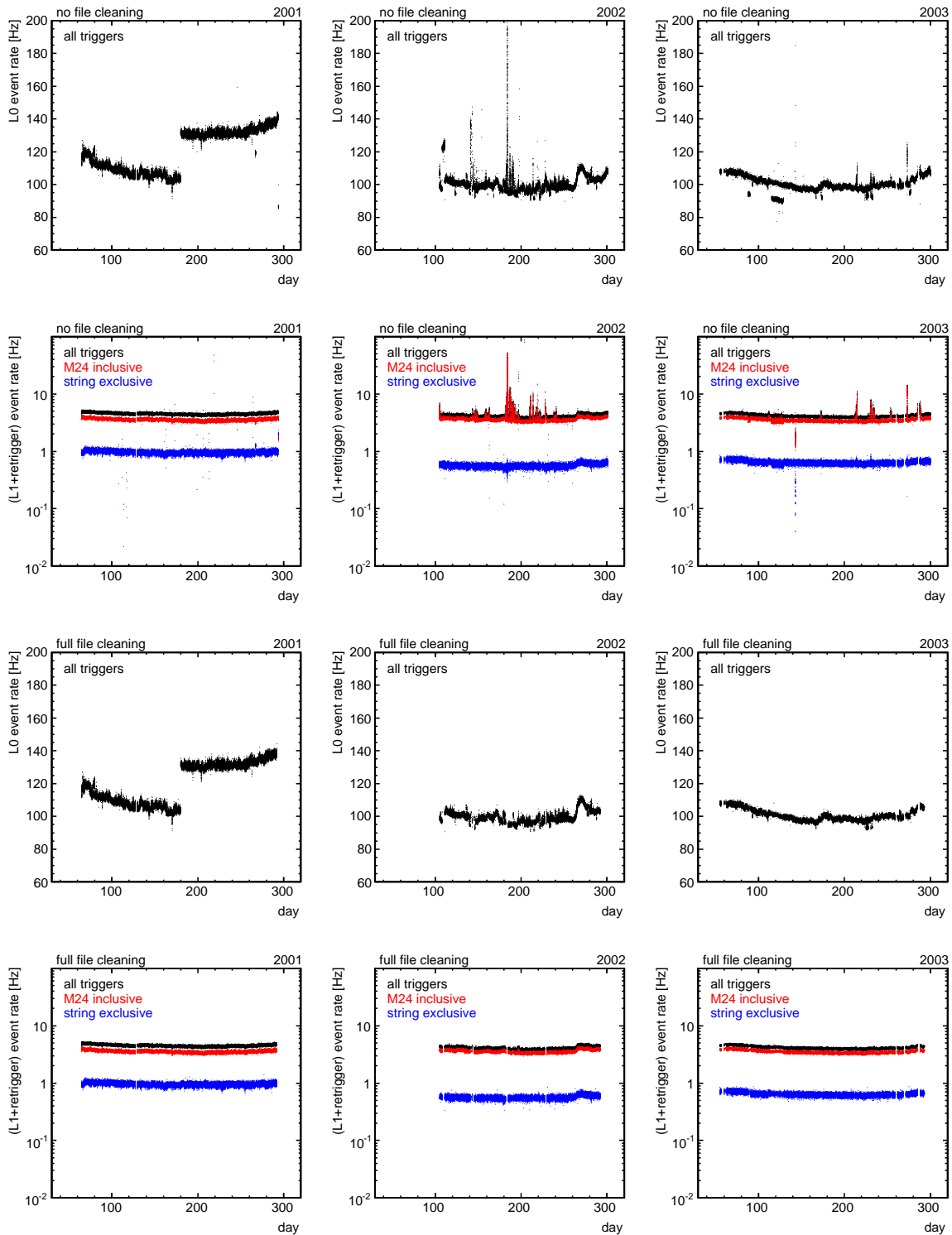


**Figure 4.2** – Evolution of the dead-time corrected event rate after trigger level (row 1 and 3) after filter level L1 with retriggering (row 2 and 4). The rates are shown before (top) and after (bottom) exclusion of all the unstable data periods.

	Year	$t_{\text{obs}}$ [days]	$\mathcal{D}$ [%]	$t_{\text{live}}$ [days]	$N_{\text{trig}} (\times 10^9)$	$R$ [Hz]
<i>train sample</i> ( $80^\circ < \theta_\odot < 90^\circ$ )	2001	39.0	22.8	30.1	0.337	129.6
	2002	25.6	12.5	22.4	0.204	105.4
	2003	33.0	15.8	27.8	0.252	104.9
	2001–2003	97.6	17.7	80.3	0.793	114.3
<i>test sample</i> ( $\theta_\odot > 90^\circ$ )	2001	181.0	21.3	142.5	1.456	118.3
	2002	124.5	13.4	107.8	0.921	98.9
	2003	156.8	15.0	133.3	1.146	99.5
	2001–2003	462.3	17.0	383.6	3.523	106.3

**Table 4.2** – Observation time, dead-time, live-time, number of triggered events and dead-time corrected trigger rate of the experimental data samples.

The statistical error from the exponential fit to the time gap distribution translates to an error of less than 0.1% on the live-time of a data file. Hence, the live-time of the total data sample is known with an accuracy of less than five minutes.

#### 4.1.4 Sample definition

We already mentioned that the total set of data files accepted for further analysis is divided in two samples, see Fig. 4.1. The first sample contains the events collected when the Sun’s zenith position is within the  $80^\circ - 90^\circ$  range. It is very hard to disentangle downward-going low energy neutrino events from atmospheric muons. Therefore this sample offers little hope for the detection of high-energy neutrinos from the Sun, and it is used for the optimization of background-rejecting selection criteria (*train* sample) instead. The rest of the event set, with the Sun below the horizon, is exploited at the end of the analysis, when the optimized event selection is applied and the final results calculated (*test* sample). Statistics for the train and test samples are summarized in Table 4.2.

The experimental data in the train and test sample were taken during different seasons, with different atmospheric conditions and resulting in different trigger rates. Fortunately it turns out that the characteristics of the additional atmospheric background events in the summer are not different from those collected in the winter. This was verified at various filter levels in the analysis (Section 6.5.3) and for various observables, see e.g. Fig. 4.3. Our conclusion is that the atmospheric background in the train and test samples behave identically and that it is safe to use the train sample in the optimization procedure.

The total live-time of the various samples are found in Table 4.2: 383.6 days for the 2001–2003 test sample and 80.3 days for the train sample. The downscaling of the string trigger in 2002–2003 reduces the dead-time from about 20% to less than 15%, and obviously the trigger rate too. The issues with string trigger settings in the beginning of 2002 result in considerably lower live-times for that year. The 2001 and 2003 test sample live-time is in agreement with previous analyses [129, 130].

As opposed to some other analyses [125, 131] which take advantage of the string trigger in the 2001–2003 data set, we do not distinguish 2001 from 2002–2003 during the optimization of the event selection criteria. The two trigger classes (multiplicity inclusive or string exclusive) have their own characteristic event topology properties, see Fig. 4.4. The

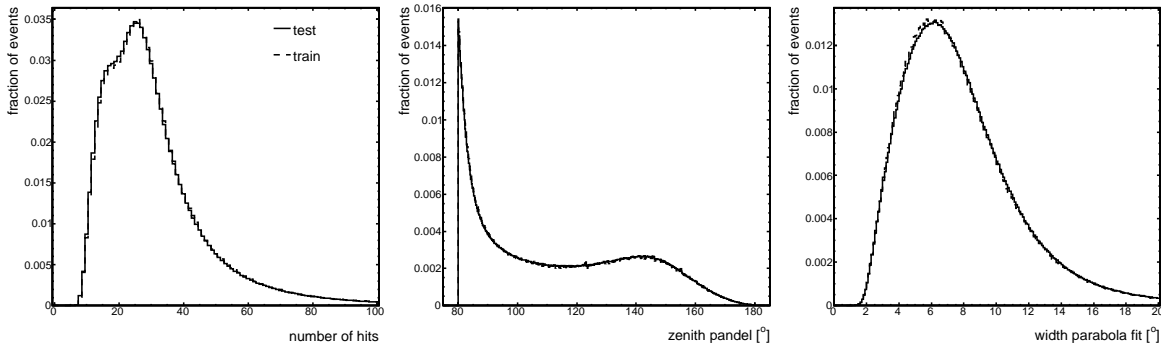


**Figure 4.3** – Normalized observable distributions for experimental data at filter level 2 (Section 6.4), for the test and train sample.

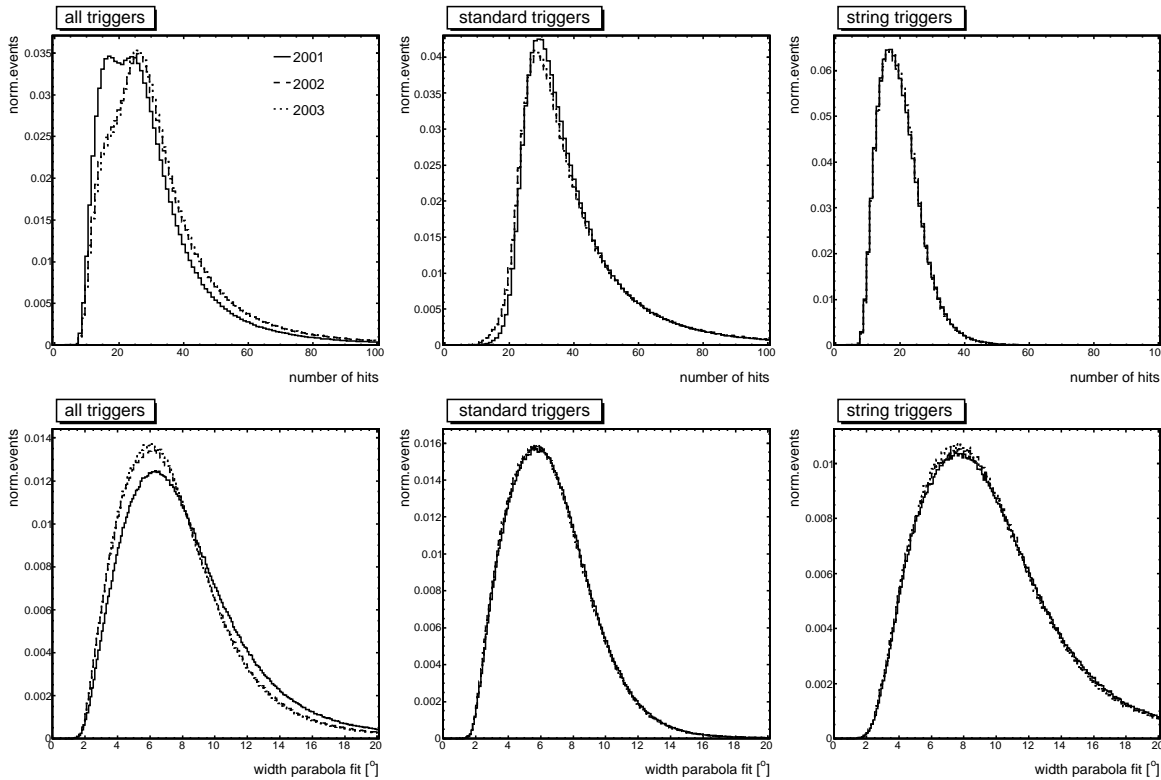


**Figure 4.4** – Normalized observable distributions for experimental data at filter level 2 (Section 6.4), before (2001) and after (2002–2003) downscaling the string trigger. The distributions for the individual std (middle) and str (right) event classes are similar over the years, this is less obvious for the global sample (left).

event topology distributions in 2001 and 2002–2003 are hence different due to the string downscaling, which is the reason for [125, 131] to optimize according to the year of data taking. Instead, it is more natural to separate the samples according to trigger class, in that way the distributions for each year are very similar.

## 4.2 Simulated data

Simulated (also *Monte Carlo* or *MC*) signal and background events are necessary when trying to understand and optimise the performance of the detector, the event selection and its prerequisite tools. Of course, this only makes sense if the simulated data accurately describe the experimental data. This task is done by chaining together several independent programs, each focusing on a different aspect of neutrino detection. This chapter outlines the AMANDA simulation chain, its associated weight schemes and a consistency check of the neutralino simulations.

### 4.2.1 The AMANDA simulation chain

In order to reproduce experimental data, the physics and detector hardware processes described in detail in Chapters 2 and 3 have to be taken into account. Apart from the physics generators we use the same program versions and settings for all simulated physics processes.

The event flow in the AMANDA simulation chain contains four distinctive steps: *generation*, *lepton* and *photon propagation* and *detector simulation*. The generation phase generates a lepton track in the vicinity of the detector which is induced by one of the relevant sources: atmospheric muons, atmospheric neutrinos or neutralino-induced neutrinos. The energy losses suffered by the lepton during its propagation through the volume around the detector are then simulated by the MMC program. PTD traces the Čerenkov photons radiated by leptons and their secondaries through the South Pole ice and stores this information in lookup tables. Finally, the AMASIM code models the response of the detector hardware components.

### 4.2.2 Physics generators

#### Atmospheric muons

The simulation of the collision of high energy cosmic rays with nuclei in the Earth atmosphere is a serious challenge in many different ways. First of all, the elemental composition of the primary flux is not well known at the highest energies. Secondly, the interaction and subsequent fragmentation happen in energy and rapidity ranges not covered by present-day accelerator experiments. And finally, the development of the shower is an intricate process involving many particles, all of which undergo interactions and/or decays.

Nonetheless CORSIKA [132], originally developed for the KASCADE experiment [133], reproduces particle numbers, their lateral and energy distributions and many other features observed in a variety of air shower experiments reasonably well. Version 6.0201 of this program was adapted and optimized to AMANDA-specific needs [134, 135] for the generation of atmospheric muons at the Earth surface. The simulation of the neutrino-component of the shower is left to another code, described in the following section, which avoids the time consuming simulation of the full shower.

Hadrons sampled from the Wiebel-Sooth [136] parametrisation of the cosmic ray composition are collided in the October template atmosphere at the South Pole. Their energies range between 800 GeV and  $10^{11}$  GeV, following a  $d\Phi/dE \propto E^{-2.7}$  spectrum, and their

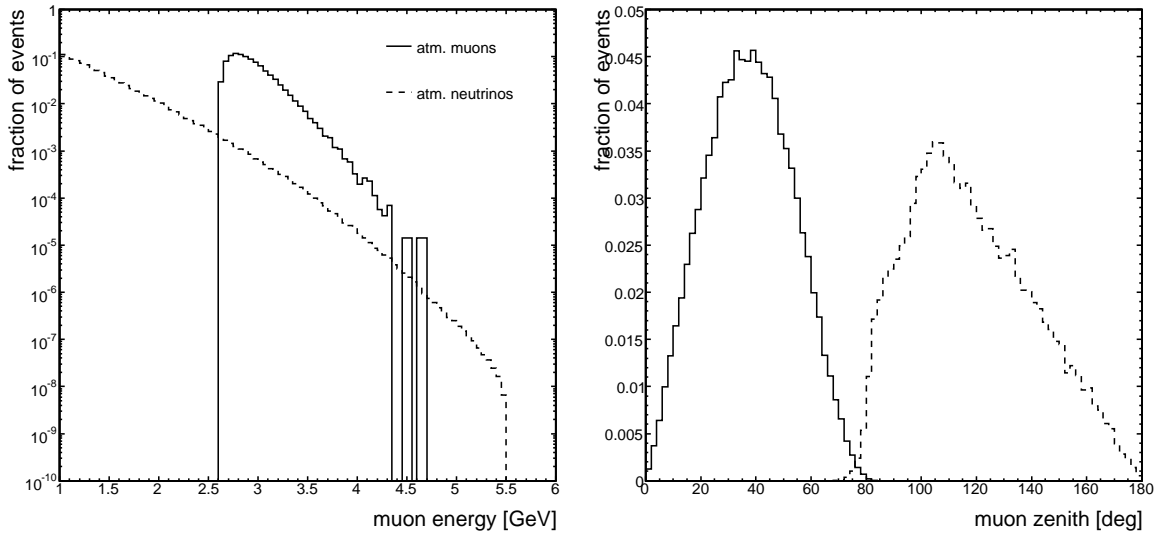


**Figure 4.5** – Energy (left) and zenith (right) distribution of atmospheric muons and atmospheric neutrino induced muons at the generator level.

directions are distributed isotropically over the Southern hemisphere<sup>3</sup>. The high energy hadronic interaction is then modelled by QGSJET [137–139], shown to be the fastest code with among the best performances of the available interaction models. Each muon that reaches the detector neighbourhood is written to disk ten times with randomized right ascensions.

In total we generated  $1.8 \times 10^{11}$  air showers, leading to  $1.3 \times 10^9$  (unweighted) atmospheric muons. This corresponds to 4.6 days of detector live-time (see Section 4.1.3) per year of data taking. The energy and zenith distributions of the atmospheric muons generated by CORSIKA are shown in Fig. 4.5 (top).

### Atmospheric neutrinos

The ANIS program [140] is a general tool for generating neutrinos of all flavours in the  $10 \text{ GeV} - 10^{12} \text{ GeV}$  range. The code distributes neutrinos isotropically on the Earth surface, with energies sampled from a power law spectrum. These neutrinos are then propagated through the Earth and finally forced to interact (CC or NC) around the detector. For muon neutrinos, the charged-current scattering angle is taken into account. This is especially important for sub-TeV energies, for which scattering becomes of the same order as the detector resolution.

Flux weights assigned to individual events allow to use the same Monte Carlo sample for neutrino flux models other than the generated isotropic power law spectrum. In the same way an interaction weight corrects for the energy, declination and flavour dependent neutrino interaction probabilities. More details follow in Section 4.2.6.

For each year  $5 \times 10^7$  muon neutrinos are generated according to a  $d\Phi/dE \propto E^{-1}$  spectrum, which are then weighted to the Lipari parametrisation of the atmospheric neutrino

<sup>3</sup>Atmospheric muons from the Northern hemisphere never reach the detector.

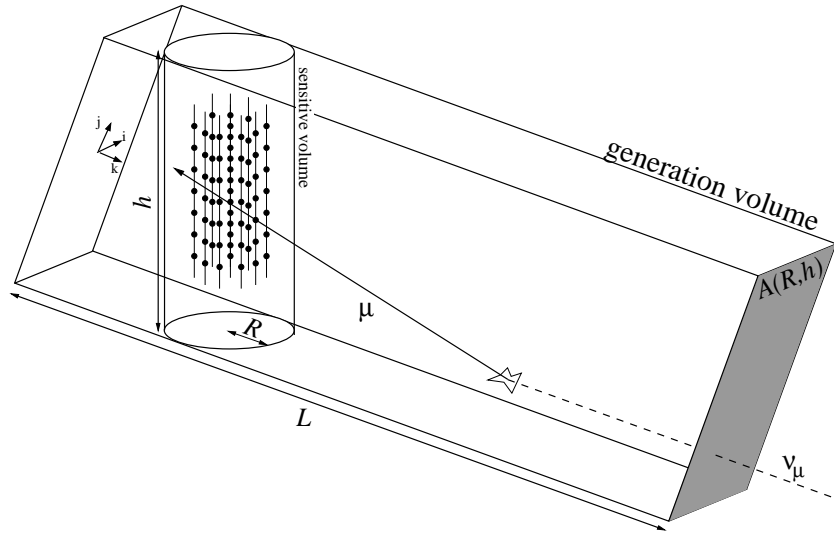


**Figure 4.6** – The GENN++ generation volume, determined by its length  $L$  and the sensitive cylinder  $(R, h)$  around the detector array. Adapted from [142].

spectrum [141] and the experimental sample live-time (Section 4.1.3). Energies range between 10 GeV and 325 TeV, zenith angles between  $80^\circ$  and  $180^\circ$ . Neutrino oscillations of  $\nu_\mu$  to  $\nu_\tau$  are not taken into account. These alter the declination spectrum, but mainly for neutrinos at or below the energy threshold of the trigger. Therefore, oscillations only minimally affect the atmospheric muon neutrino sample.

Considerable processing time can be saved by optimizing the size of the cylindrical volume in which the final interaction vertices are spread out. The volume is aligned with and extends to the incident direction of the neutrino. Its dimensions should be as small as possible, without altering the shape of the triggered spectra. It turns out that a cylinder with a radius of 375 m and a length of 15 km before the detector centre and 375 m behind is the optimal choice for atmospheric spectra triggered by AMANDA.

The generated energy and zenith distributions of the atmospheric neutrino induced muons are shown in Figure 4.5 (centre).

### Neutralino annihilations

Neutralino annihilations produce neutrino fluxes of all flavours, but muon neutrinos offer the best hopes for background rejection and signal detection. For reasons described in Section 2.3.2, a separate dark matter search is performed for several neutralino models. So, a sample of simulated muon neutrino events is prepared for each neutralino model, defined by the choice of neutralino mass  $m_\chi$  and annihilation channel  $C_\chi$ .

We simulate seven neutralino masses, covering the range motivated by experimental and theoretical results (Section 2.1.1): 50, 100, 250, 500, 1000, 3000 and 5000 GeV. For each mass, two annihilation channels are simulated, corresponding to the extremes of the expected neutrino energy spectra. Annihilations in  $b\bar{b}$ -pairs produce a soft neutrino energy spectrum. Hard neutrino spectra are expected for annihilation in  $W^+W^-$ -pairs, but that is only kinematically possible for  $m_\chi > m_W$ . Hence, for  $m_\chi = 50$  GeV the role of the hard spectrum is taken by the  $\tau^+\tau^-$  channel.

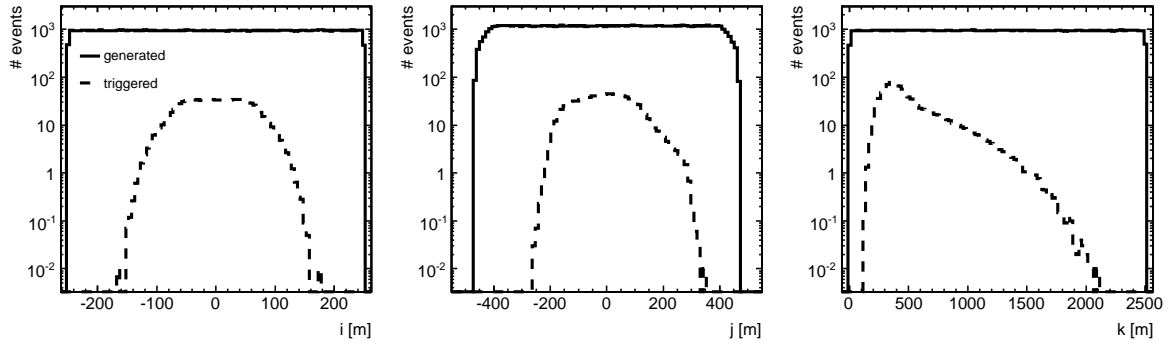


**Figure 4.7** – Optimisation of the `GENN++` generation volume for the (500 GeV, hard) neutralino model. Shown are generated (solid) and triggered (dashed) distributions of the vertex position  $(i, j, k)$  in the generation volume.

In practice, the generation of dark matter induced events is conducted by a chain of three separate programs. `WIMPSIMP` and `WF2F2000` respectively generate neutrino energies and directions, `GENN++` performs the propagation of the neutrino through the Earth and the charged-current interaction in the vicinity of the detector. Again no neutrino oscillations are included in the simulation. The effect of this simplification is incorporated as a source of systematic uncertainties on the final results.

Neutrino energies, expected for a given neutralino model, are sampled by `WIMPSIMP` 1.2 [143] from tables generated with the `DARKSUSY` 3.07 package [63]. The latter code simulates the annihilation process of neutralinos in the centre of the Sun, interactions of the annihilation products with the surrounding medium, their decays and finally the propagation of the neutrinos towards the Earth surface.

Since the neutrino-nucleon cross section increases with energy and all generated neutrinos are forced to interact, we prefer to sample energies from the interacting rather than from the annihilation spectrum. In this way the distributions for the important, high energy part of the spectrum will be less prone to statistical fluctuations. A consequence is that all generated events have to be weighted, in order to recover the physical spectrum, see Section 4.2.6.

Neutrino directions are generated by `WF2F2000` 1.22 [144], following the declination of the Sun throughout the year. It is very hard to disentangle downward-going sub-TeV neutrino events from atmospheric muons, reducing the possibility to detect a neutrino signal from the Sun during daytime. We therefore only generate neutrinos when the Sun is below the horizon (or  $\theta_{\odot} > 90^{\circ}$ ).

The last part in the chain, `GENN++` 1.1 [142], takes care of the propagation of the neutrinos from the Earth surface to the AMANDA detector, where a charged-current interaction is forced. `GENN++` calls the `PYTHIA` 6.321 routines [145] to create the muon and its accompanying hadronic shower. Both `PYTHIA` and `GENN++` apply cut-offs on the energies of respectively the neutrino ( $E_{\nu} > 15$  GeV) and the muon ( $E_{\mu} > 10$  GeV). We

Neutralino model	$R(\text{adius})$ [m]	$h(\text{eight})$ [m]	$L(\text{ength})$ [m]	$\langle V_{\text{gen}} \rangle$ [ $\times 10^9 \text{ m}^3$ ]	$N_{\text{gen}}$ ( $\times 10^7$ )
5000 hard	250	800	8000	3.59	2.19
3000 hard	250	800	8000	3.59	1.99
1000 hard	250	800	4000	1.79	1.05
500 hard	250	800	2500	1.12	0.95
250 hard	250	800	1700	0.76	1.11
100 hard	200	700	900	0.28	2.05
50 hard	160	700	700	0.17	5.47
5000 soft	250	800	4000	1.79	3.29
3000 soft	250	800	4000	1.79	3.77
1000 soft	250	800	3000	1.34	3.42
500 soft	250	800	1700	0.76	3.12
250 soft	200	800	1200	0.42	3.50
100 soft	160	700	800	0.19	5.37
50 soft	160	700	700	0.17	11.3

**Table 4.3** – The optimized dimensions ( $R, h, L$ ) of the GENN++ volume, its average size  $\langle V_{\text{gen}} \rangle$  and the unweighted number of generated events, for each neutralino model.

keep this threshold in mind when calculating the muon flux.

The interaction vertices are spread uniformly in a volume around the detector array, further referred to as the generation volume  $V_{\text{gen}}$ . Its box geometry is defined by the (event-independent) length  $L$  along the incoming neutrino direction and the (event-dependent) projected area  $A(R, h)$  of the sensitive volume on the perpendicular plane. The sensitive volume can be thought of as a cylindrical region, described by a radius  $R$  and a height  $h$ , around the detector where photons emitted by passing muons are able to be picked up by the optical modules. Figure 4.6 illustrates this geometry.

Again, considerable CPUtime can be saved by optimizing the generation volume parameters ( $R, h, L$ ) for each of the fourteen neutralino models. This is accomplished by looking at the vertex positions  $(i, j, k)$  of triggered events, and selecting the smallest volume where muons trigger the detector. An example for the 500 GeV neutralino annihilating in  $W^+ W^-$  is shown in Fig. 4.7.

The results of this conservative procedure are summarized for all neutralino models in Table 4.3. Obviously, the GENN++ volumes scale with muon energy and are larger than the instrumented volume. The average size of the generation volume  $\langle V_{\text{gen}} \rangle$  can be compared to the effective volume (see Section 6.1) at trigger level, Table 6.2, to get an idea of the trigger efficiency.

In an effort to reduce the influence of statistical fluctuations on the outcome of the analysis, we generate events until roughly  $10^5$  unweighted triggers are gathered. The generated number of events per year is found in the last column of Table 4.3.

Finally, we refer to Section 4.2.6 for the appropriate neutralino weight scheme and to Section 4.2.7 for a sanity check of the neutrino propagation and interaction part of the dark matter and atmospheric neutrino simulation chains. Figures with the energy and

zenith distributions can be found in the latter section.

### 4.2.3 Muon propagation

The MMC 1.2 program [104] propagates the generated muons in three dimensions through up to four different media around the detector (air, firn, ice and rock). All continuous and stochastic processes contributing to the energy loss of muons, described in Section 2.2.1, are modelled in the simulation. A lot of effort was put in keeping the computational rounding errors to an absolute minimum, since these may become important for very high energy muons that undergo up to hundreds of interactions. The remaining errors are caused by uncertainties in the cross section formulae, claimed to be valid within 1% for  $E_\mu \lesssim 10$  TeV, and their parametrisations [104].

Most light able to reach detector modules is emitted in a cylinder with radius 400 m and height 800 m, the active volume. This is the region where the highest simulation precision for energy loss secondaries is required, because these radiate the photons that are actually observed by the experiment. Therefore, inside the active cylinder the bare muon track and all individual tracks of secondaries are stored to file, awaiting further evaluation of the Čerenkov light yield by the detector simulation. The energy losses suffered before reaching, and also after leaving, the active volume are treated in a more approximate way. But they are still sufficiently precise for an estimation of the total muon path length and of the muon energy at the entry point in the active volume.

### 4.2.4 Photon propagation

The next step in the simulation, one of major importance, is that of the Čerenkov light yield at the detector modules produced by the muon and its associated energy loss secondaries. For each optical module we need to know the number of detected photons and their individual arrival times. This involves the tracking of photons in a large volume of ice with strongly varying scattering and absorption properties (Section 3.1). Typically more than 30000 detectable photons are emitted by a muon per traversed meter, see Section 2.2.2. Obviously this is a highly CPU-intensive task, necessitating simplifications of the simulation model.

The basic idea is that instead of tracking all photons individually through some optical ice model for each event, this is done once for a large number of photons and track-OM configurations. The resulting probability density distributions for photon flux and arrival times are then stored in lookup tables, referred to as *photon tables*. For technical reasons not only the optical properties of the bulk of the ice are included, but also those of the ice in the bore hole, the glass sphere and the optical gel around the photo-cathode and its quantum efficiency. To study the effect of another bulk ice model, hole ice model, ... a new set of photon tables should be constructed.

An additional complication is that of the memory requirements of these tables. A high resolution treatment of the track-OM configurations and especially of the depth- and wavelength-dependent glacial optics easily results in tables of the order of 10 GB, more than commonly available in computer cluster nodes. This approach is pursued by the PHOTONICS photon tracking tool [146], and only became feasible while this analysis was in its final stage.

The memory requirements can be relaxed by reducing the depth-resolution and the dimensionality of the probability density distributions, as implemented by the PTD program [147]. The strongly depth-varying optical properties are approximated by discrete, 10 to 50 m thick layers of ice, in which the optical properties are assumed constant. Photons detected by a certain detector module will only scatter and get absorbed according to the properties of the ice layer in which the module resides. This is a good approximation for photons emitted nearby the OM, but not for those coming from far away. The reference ice model used as input to the PTD photon tracking simulation is the MAM model [148]. This model is constructed from in-situ calibration source measurements of absorption and scattering and then tuned to improve the agreement of time residuals of simulated and experimental photons.

The light yield for the simulated events used in the optimization of event selection criteria is generated by randomly sampling from the PTD flux and arrival time probability density distributions. At the moment, the usage of the more detailed PHOTONICS tables is only practicable for smaller, signal event samples. These samples are used at a later stage for the evaluation of the systematic errors induced by the simplified PTD implementation of the optics of the South Pole glacier.

#### 4.2.5 Detector simulation

After retrieval from the photon tables of the number of detected Čerenkov photons and their arrival times in every optical module, the detector response to the photo-electrons is simulated by the AMASIM GRAPEFRUIT-FIX3 program [149]. This encompasses the modelling of the pulses leaving the photo-multiplier tube, the cable transport, the surface amplifiers, the discriminators, the TDCs and ADCs and finally the trigger logic.

Apart from photon induced pulses, AMASIM generates noise and afterpulse hits as well. Most of the simulated electronic behaviour is characterized and calibrated individually for the optical modules, Section 3.2.3. This is done in an effort to reproduce the actual experimental situation as truthfully as possible.

Even though most detector features are implemented, some are not, for instance crosstalk processes and detector instabilities. This necessitates a hit and event cleaning procedure that aims to improve the agreement between experiment and simulation, see Section 5.1. Also, the string trigger can not be downscaled in the GRAPEFRUIT-FIX3 version of AMASIM. In order to describe the experimental trigger situation in 2002 and 2003 (Section 3.2.2), all simulated events for those years are scaled offline by 1/2 when they exclusively satisfy the string trigger condition.

#### 4.2.6 Simulation weighting schemes

The neutrino and neutralino generators adopt an importance sampling approach which oversamples low statistics regions in the parent distribution. This reduces the processing time needed to populate those low statistics regions, but also biases the generated angular and energy spectra. Assigning a statistical weight to each event, compensates for that. But first of all, we mention the downscaling of the simulated string triggers in 2002 and 2003.

## String trigger downscaling

During 2002 and 2003 the string trigger was downscaled by 1/2 in the experimental set-up, see Section 3.2.2, such that only half of the events that exclusively satisfy the string condition are triggered and written to tape. The GRAPEFRUIT-FIX3 version of AMASIM is not capable of reproducing this, instead we weight each simulated event exclusively triggered by the string condition with  $w_{\text{downscale}} = 0.5$ .

## Atmospheric neutrinos

The ANIS weight for atmospheric neutrino events has four components

$$\begin{aligned} w_{\text{atm.}\nu}(E_\nu, \theta_\nu) &= R_{\text{atm}}^{\nu\mu}(E_\nu) && \text{(at Earth surface)} \\ &= R_{\text{atm}}^{\nu\mu}(E_\nu) \times P_{\text{int}}(E_\nu, \theta_\nu) \times N \times t_{\text{live}}, && \text{(after trigger)} \end{aligned} \quad (4.2)$$

with  $R_{\text{atm}}^{\nu\mu}$  the normalized spectral shape for atmospheric muon neutrinos [141] at the surface of the Earth,  $P_{\text{int}}$  the interaction probability and  $N$  the normalization constant that gives the correct amount of events per year in the chosen volume. A final factor  $t_{\text{live}}$  scales the simulation to the experimental live-time (Section 4.1.3).

By replacing  $R_{\text{atm}}^{\nu\mu}$  other neutrino source spectra can be obtained from a sample of ANIS events generated from a  $E^{-\gamma}$  distribution. E.g. a spectral shape  $\Phi(E_\nu)$  is recovered with  $E^\gamma \Phi(E_\nu)$  as event weight. Similarly, with a direction-dependent factor in the weighting scheme one can recover non-isotropic sources as well.

## Neutralinos

Constant factors in any neutralino event weight scheme can be disregarded, since the analysis and its results only depend on signal efficiency information. This, in turn, is determined by spectral shapes, but not by the absolute number of arriving signal events.

Depending on the simulation step of interest, up to four components are needed in the event weight for neutralinos that are generated with the WIMPSIMP-WF2F2000-GENN++ chain

$$\begin{aligned} w_\chi(E_\nu, \theta_\nu) &= w_{\text{surf}}(E_\nu) && \text{(at Earth surface)} \\ &= w_{\text{surf}}(E_\nu) \times w_{\text{abs}}(E_\nu, \theta_\nu) && \text{(after propagation)} \\ &= w_{\text{surf}}(E_\nu) \times w_{\text{abs}}(E_\nu, \theta_\nu) \times w_\sigma(E_\nu) && \text{(after interaction)} \\ &= w_{\text{surf}}(E_\nu) \times w_{\text{abs}}(E_\nu, \theta_\nu) \times w_\sigma(E_\nu) \times w_{\text{vertex}}(E_\nu, \theta_\nu), && \text{(after trigger)} \end{aligned} \quad (4.3)$$

where  $w_{\text{surf}}$  recovers the unbiased neutralino-induced neutrino energy spectrum at the surface of the Earth,  $w_{\text{abs}}$  subsequently incorporates possible absorption of the neutrino during its propagation towards the detector,  $w_\sigma$  handles the energy dependent neutrino-nucleon cross section and  $w_{\text{vertex}}$  takes care of the (possibly energy and direction dependent) generation volume.

Simulated trigger efficiencies are enhanced by generating the interaction point in a volume whose size  $V_{\text{gen}}$  depends on properties of the event (e.g. energy and direction).

To maintain the correct interaction density (number of interactions per unit volume) the importance of each event should scale with its particular generation volume [150]. Therefore,  $w_{\text{vertex}} = V_{\text{gen}}$  compensates for the introduced bias, and can be understood as the incorporation of part of the detector trigger efficiency.

A remark is suitable here. Since part of the trigger efficiency is incorporated in  $w_{\text{vertex}}$  it should be omitted in the weight scheme for the calculation of the effective volume  $V_{\text{eff}}$  (Section 6.1). Otherwise the trigger efficiency is included twice.

### Neutralinos: alternative approach

An alternative approach to neutralino simulations is possible with ANIS. In this work it is only followed for samples meant to cross-check the standard simulation chain (see next Section), and not for the neutralino signal sample used in the final analysis.

ANIS is a general tool to generate isotropic neutrinos that follow an  $E^{-\gamma}$  spectrum. The weighting technique allows to exploit these events for neutralino purposes as well. In order to do so, we need two weight functions  $w_E$  and  $w_\theta$  to correct the biased energy and zenith spectrum

$$w_\chi^{\text{ANIS}}(E_\nu, \theta_\nu) = w_E(E_\nu) \times w_\theta(\theta_\nu) \times P_{\text{int}}(E_\nu, \theta_\nu), \quad (4.4)$$

and, again, any constant factors are ignored.

For each neutralino model  $\chi$ , the neutrino energy spectrum  $\Phi_\chi(E_\nu)$  at the surface of the Earth can easily be fitted to the spectrum of WIMPSIMP events. The energy weight function then looks like

$$w_E(E_\nu) = E_\nu^\gamma \times \Phi_\chi(E_\nu). \quad (4.5)$$

The angular correction is derived in the following way. The expected event rate  $(dN/dt)_{\text{exp}}$  from dark matter annihilations in the Sun is constant and distributed along the zenith path of the Sun  $\theta_\odot(t)$ , see Fig. 4.1. This evolution is described by

$$\theta_\odot(t) = 90^\circ - 23.45^\circ \cos(2\pi t), \quad (4.6)$$

where  $t \in [0, 1]$  parametrises the time of the year. The weighting function  $w_\theta$  correcting for isotropically generated zenith angles is identified as following

$$\begin{aligned} \left(\frac{dN}{dt}\right)_{\text{exp}} &= C && \text{(constant rate)} \\ &\propto \left(\frac{dN}{d \cos \theta_\nu}\right)_{\text{gen}} && \text{(isotropic generation)} \\ &= \left(\frac{dN}{dt}\right)_{\text{gen}} \times \left(\frac{dt}{d \cos \theta_\nu}\right)_{\text{gen}} \\ &= \left(\frac{dN}{dt}\right)_{\text{gen}} \times w_\theta(\theta_\nu). \end{aligned}$$

Using Eq. 4.6 we obtain

$$w_\theta(\theta_\nu) = \frac{1}{\sin \theta_\nu} \frac{1}{\sqrt{1 - \left(\frac{90 - \theta_\nu}{23.45}\right)^2}}, \quad (4.7)$$

disregarding the irrelevant constant factors.

### 4.2.7 Checking the simulation

By definition an undetected signal can only be modelled from simulated events. A serious flaw in the (signal) simulation chain can compromise our final result, and thus, should be prevented at any cost. To verify the total signal simulation chain a distinction is made between (a) the generation of signal and (b) the rest of the simulation (muon and photon propagation and detector simulation).

The latter part of the signal simulation process is identical for atmospheric background events. If the corresponding simulation programs and settings are accurate the simulated background events should reproduce the characteristics of the experimental data. We can therefore gain confidence in the (signal) simulation by observing good agreement between experiment and background simulation. That is done at various stages in the event selection process, as we will see in Chapter 6.

The signal generation part can only be cross-checked against the results from other existing codes (hopefully sufficiently verified too). Since the task of the generator is to provide the energy and the direction of the neutrino and the muon and hadronic shower, we compare the results of our WIMPSIMP-WF2F2000-GENN++ set-up to those of the following alternative program chains: (WIMPSIMP-WF2F2000)-GENNIUP, (WIMPSIMP)-ANIS and WIMPSIM-WIMPEVENTF2K. A description of the non-bracketed programs and a discussion of the related cross-check is given below. But first we present the results.

For the different chains, we show the energy and zenith angle distributions of neutralino-induced neutrinos at the surface of the Earth (first row), the interacting neutrinos and the associated muons (2nd and 3rd row) and finally the muons that trigger the detector (last row). Fig. 4.8 shows solar neutralinos of mass 500 GeV and annihilating to  $W^+W^-$ , similar results are found for the other neutralino models.

**Genniup** GENN++ (solid line) is a C++ translation (adding some improvements in the definition of the generation volume) of the FORTRAN-based GENNIUP [151], which was used in a previous AMANDA solar neutralino analysis [129, 152]. The cross-check reveals issues related to the generation volume or PYTHIA version dependencies. After correcting for a bug in GENNIUP (dashed line), no significant discrepancies are noticed. Minor differences remain at muon energies close to the detector threshold, caused by the older PYTHIA version and a slightly too small generation volume in GENNIUP. A thorough investigation can be found in [150].

**Anis** The comparison with an ANIS sample (dotted line) properly weighted according to Eq. 4.4 allows for an independent check of the neutrino propagation through the Earth and the charged-current interaction routines. If these are treated differently, it would be revealed at the interaction level. Again, no disagreement with GENN++ is found and we also conclude that ANIS can be used to generate any high-energy spectrum of neutrinos originating from the Sun.

**WimpSim** The latest DARKSUSY-based neutralino generator WIMPSIM [97, 153] (coupled to WIMPEVENTF2K [154]) is not only a more detailed successor of WIMPSIMP

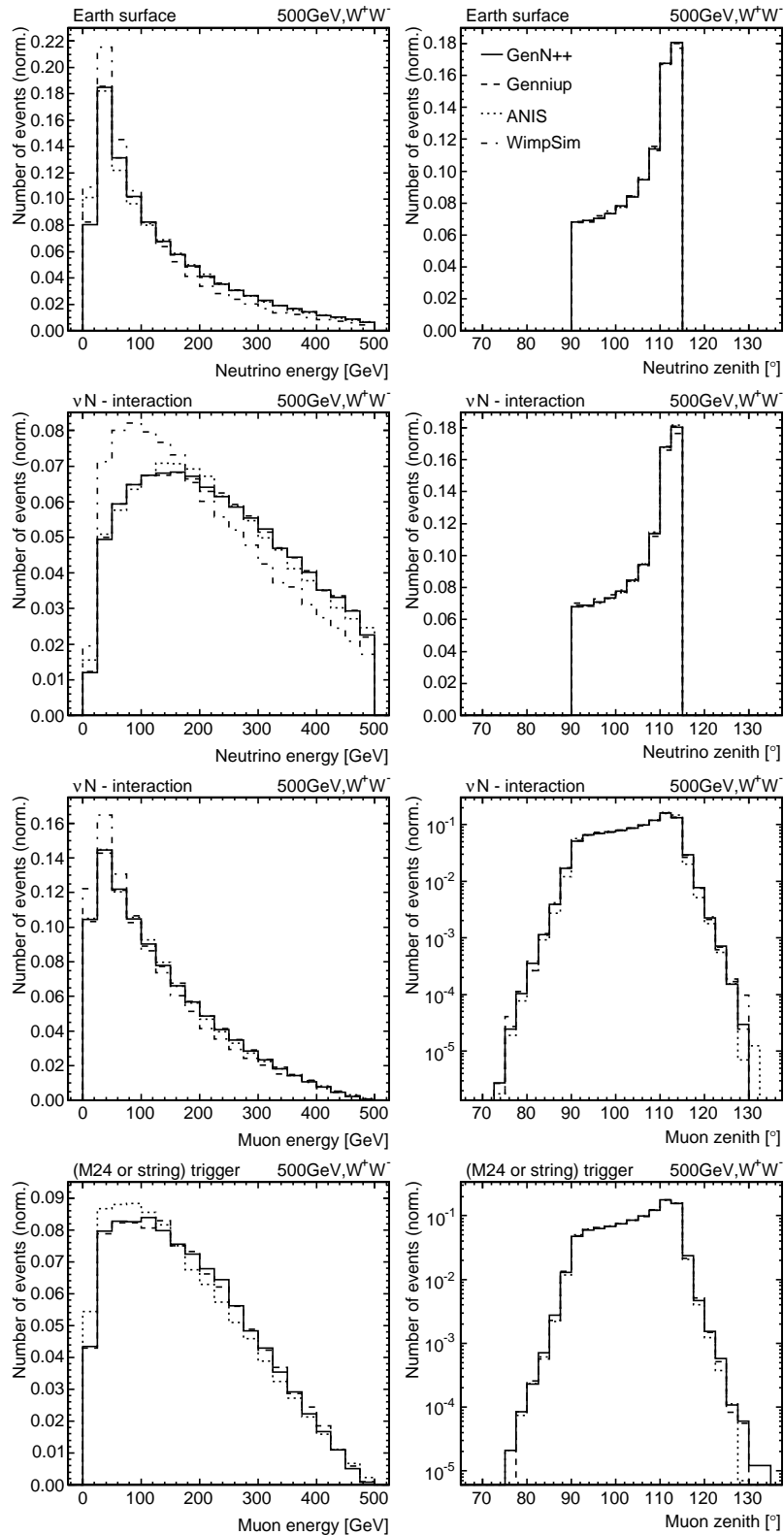


**Figure 4.8** – Normalized energy (left column) and zenith (right) distributions of the neutrinos arriving at the surface of the Earth (top row), the interacting neutrinos (second row), the muons produced in the  $\nu N$ -interactions and the muons triggering the AMANDA detector (bottom row). The lines represent the various programs generating 500 GeV solar neutralino annihilations to  $W^+W^-$ .

(all  $\nu$  flavours, three flavour oscillation model, both CC and NC interactions, ...), but also completes the whole chain with neutrino propagation through the Earth and its own neutrino interaction routines, thereby avoiding the hard-coded phase space cuts by `PYTHIA`. `WIMPSIM` samples (dash-dotted line) allow an almost completely independent cross-check of the whole neutralino generator chain. Except for the neutrino energy, all other distributions are very similar to those obtained with our set-up. The difference in interacting  $E_\nu$ -spectrum does not influence our later analysis, since that is solely based on what the detector actually sees: muons. Besides this check, the `WIMPSIM` program is used as well to evaluate the systematic effect of oscillations on the final result. We will come back to this later.

Having verified various parts of the signal generation, we conclude that our set-up is consistent with other available codes. That paves part of the way for the further analysis.



# Chapter 5

## From raw data to event observables

Now that the data samples are described, we are ready to explain how these events are prepared for further analysis. The goal is to calculate observables that characterise an event in various useful ways. This is necessary to shed a light on the nature of the event: neutralino signal or atmospheric background?. In a first, preprocessing step the data are calibrated and cleaned from electronic artefacts, Section 5.1. Afterwards the event direction is reconstructed with powerful methods, Section 5.2. The idea behind and merits of several event observables are presented in Section 5.3. The final section of this chapter briefly describes the software used to perform these tasks.

### 5.1 Preprocessing

As we have seen in Section 3.2.2, some recorded information is caused by electronic processes rather than particles crossing the detector. This information is removed at various levels: single hits, full events and complete data files.

We do not want that spurious hits, produced by anything but particles in the detector, distract the reconstruction algorithm from the relevant, Čerenkov light-induced information. These electronic hits are inevitable (Section 3.2.2), but fortunately identifiable. A hit cleaning procedure strips the non-particle information away from the events<sup>1</sup>. Some electronic phenomena are very hard to simulate. To bring simulation and experiment back in accord a further cleaning is necessary: at the level of complete events, and at the level of complete data files.

But first of all, the hit information is only meaningful after calibration.

#### 5.1.1 Calibration

The raw information of each hit (OM position, peak amplitude, leading and trailing edge time) is corrected with the geometry, amplitude and time calibration constants described in Section 3.2.3. Figure 5.1 (left) shows how the calibration affects the leading edge (LE) time distribution. The calibrated distribution is shifted to smaller times, due to the subtraction

---

<sup>1</sup>Although we mention that hits are cleaned, they are never completely removed from the data set. The bad hits are simply flagged as bad and consequently neglected in further processing steps.

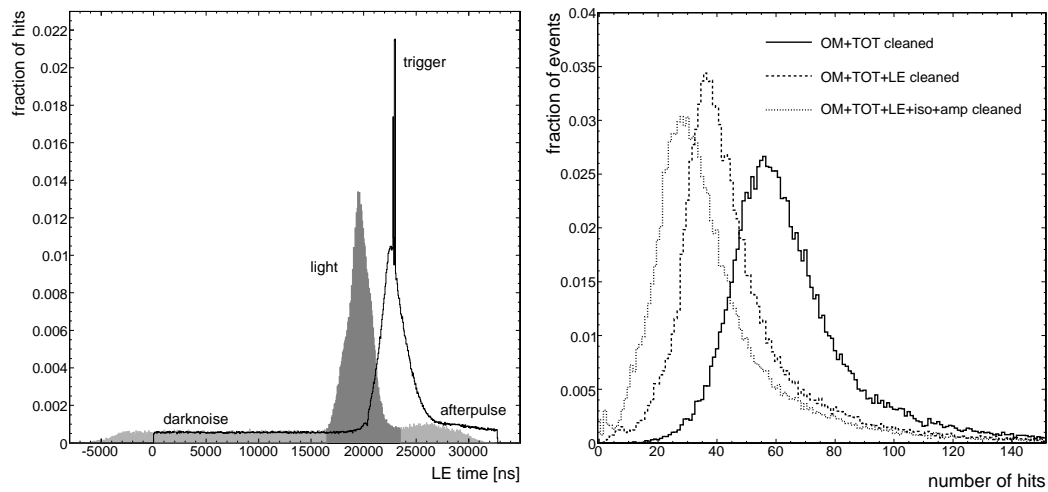


**Figure 5.1** – Left: normalized distribution of the leading edge time of raw (line) and calibrated (light shade) hits. The dark shaded area illustrates the (calibrated) LE cut window. Right: normalized distribution of the number of hits after three sequential hit cleaning steps. Both plots are for experimental data collected during 2003.

of the time delays. Different classes of hits (see next section) at the PMT level become apparent.

### 5.1.2 Hit cleaning

Figure 5.1 (right) illustrates the effect of the hit cleaning steps described below, fewer and fewer hits remain per event while tightening the hit selection criteria.

#### Bad OMs

Not all optical modules are reliable. That can happen for various reasons: some OMs are considered dead (too low darknoise rate), some are noisy (too high darknoise rate), some show transient behaviour (too variable darknoise rate), some are not well calibrated and some are located outside the main detector volume (top and bottom modules on strings 11 – 13 and the entire string 17, see Fig. 3.4). All the hits in these *bad* OMs are discarded.

Due to sudden changes or an occasional discovery of malconnected modules, some bad OMs can at some point become good, or vice versa. So, a fresh list with bad OMs is compiled each year. The number of OMs approved for further analysis was 513, 534 and 540 in 2001, 2002 and 2003 respectively. That is 75 – 80% of the total deployed array.

#### Noise and afterpulses

Noise pulses are predominantly due to decays of radioactive K, Th and U isotopes in the glass sphere of the OM and the PMT material, and to a lesser extent due to thermal noise, since reduced at the low temperatures in South Pole ice. The average darknoise rate for modules on strings 1-4 is 400 Hz, and 1200 Hz for those on strings 5-19. The much larger contamination of radioactive  $^{40}\text{K}$  in the Benthos glass explains the difference [155].

These hits occur almost randomly in time as can be seen in Figure 5.1 (left). Besides the noise plateau, the LE time distribution shows the pronounced *light* peak around the trigger time. It mainly consists of the Čerenkov photons from relativistic particles that trigger the detector. The trigger is set to happen at the same (uncalibrated) time for each event, around  $22.8 \mu\text{s}$  after the opening of the TDC buffer.

Most of the noise is removed by simply requesting calibrated leading edges in the range  $16500 - 23500 \text{ ns}$ , a  $7 \mu\text{s}$  time window around the trigger time (see dark shade in the figure). This condition also removes an additional class of electronic hits from ionization of residual gas in the PMT tubes. These so-called afterpulses typically occur a couple of microseconds after the primary photo-electron pulse, visible as the smaller bump after the light peak.

The LE window cut is not sufficient to remove the noise recorded during the light peak. Some of these hits are identified and discarded when they are isolated in a  $200 \text{ m}$  wide sphere during a  $500 \text{ ns}$  time window.

The remaining occasional noise, in OMs close in space and time to the Čerenkov wavefront, can not be excluded.

## Crosstalk

Crosstalk hits are a consequence of transmitting PMT pulses over several kilometres of densely packed cabling. Especially pulses in twisted-pair cables (strings 5-19) induce signals in the neighbouring cables of optical modules on the same detector string. In addition, interference in the surface electronics boards is possible too. These electronic artefacts are not simulated.

A very short *time-over-threshold* (TOT), the time between the leading and trailing edge, is indicative of such electronic interference processes. For modules that are read out through an optical fibre a minimum of  $5 \text{ ns}$  is demanded. For electrical channels dispersion plays an important role and a minimum TOT of  $75\text{-}200 \text{ ns}$  is required, depending on the OM. Hits with a too long TOT, above  $2 \mu\text{s}$ , on the other hand are more likely to be caused by a missing edge than by a particle event, and hence rejected too.

A simple TOT cut window is not enough to kill all crosstalk pulses, two additional precautions are taken. From the time calibration runs a talker-receiver map was constructed that identifies which OM pairs interfere strongly. With this map additional crosstalk from talker to receiver OMs is rejected. In a final step, crosstalk pulses in the twisted-pair cables are identified based on their position in pADC versus TOT space. Compared to light-induced hits, crosstalk pulses have a smaller TOT value for a given pADC value.

## Amplitude

And finally, the calibrated amplitude should be in the range  $0.1 - 1000$  photo-electrons.

### 5.1.3 Event cleaning

#### Retrigger

With the events stripped from spurious hits we verify whether they continue to satisfy either one of the multiplicity or string trigger requirements. Such a procedure reduces the

observed discrepancies between simulation and experiment [156]. By nature, transient OM behaviour can not be simulated and this leads to a lower effective trigger threshold for experimental events. The same effect is caused by crosstalk, since also not simulated.

For these reasons we strip the event from the hits in bad OMs and outside the TOT cut window. The remaining (uncalibrated) hit set is then passed through the (software) trigger logic, consisting of the multiplicity and string trigger. This step removes about 30% of the experimental events, while at most 10% of the simulated events.

### Non-particle events

Yet unidentified disturbances outside the detector occasionally produce a large amount of non-photon pulses which in the end trigger the detector. These so-called non-particle or flare events are potentially dangerous for searches for ultra high energy neutrinos, which deposit a lot of hits in the detector. Flare events are identified by several indicators [157] based on their electronic fingerprint. Less than 0.5% of the experimental events and no simulated events are thrown away, see Section 6.5.3.

#### 5.1.4 File cleaning

While the detector operates smoothly most of the time, some periods show unstable detector conditions. Again, these unstable conditions can not be simulated by nature. The experimental data during these periods are therefore removed on a file-by-file basis. Details and results were already presented in Section 4.1.2.

## 5.2 Event reconstruction

The calibration and hit cleaning procedures disclose the underlying photon information of the event. Since charged leptons leave a well-known Čerenkov fingerprint, see Section 2.2.3, the measurement of the amplitude and arrival time of photons over a three-dimensional array allows us to reconstruct the lepton track direction and its energy, with an accuracy depending on the event topology.

The energy loss per length unit is small for muons, so they typically have a long track. In this case there is ample directional information, allowing a good angular resolution. Electrons and tau events on the other hand deposit all their energy in electromagnetic and hadronic cascades. These develop over a relatively small volume, hampering an accurate reconstruction of the direction. Instead the real benefit of the cascade events is that their energy can be fairly well reconstructed. Such a feat is impossible for muons, which leave only part of their energy in the detector.

Angular resolution is essential when searching for neutrino point sources, like the Sun. That is why we will focus on the reconstruction methods for muons [158]. Some information about cascade reconstruction can be found in [159].

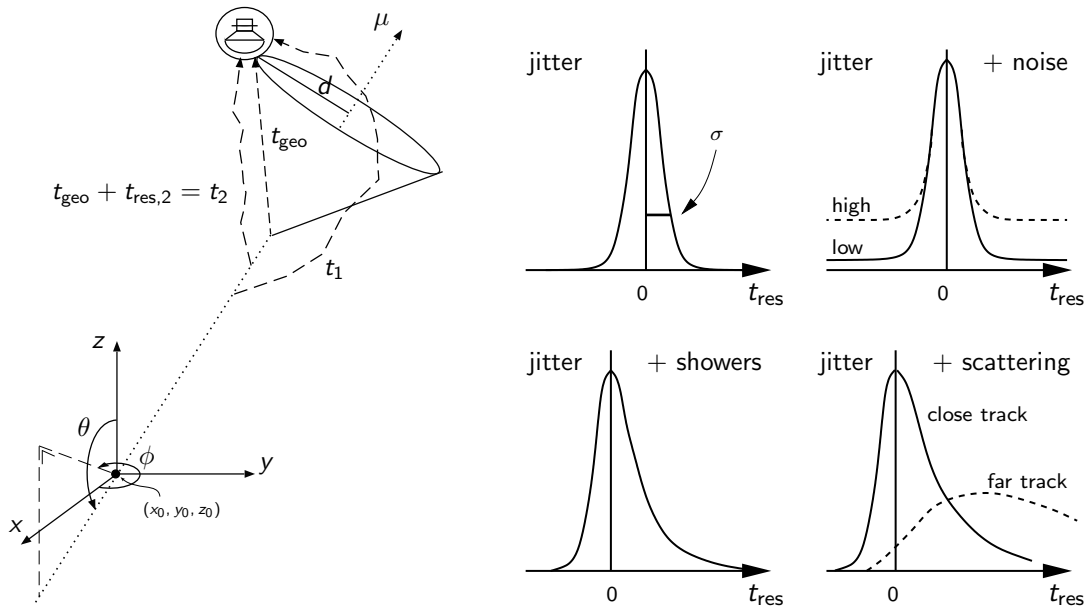


**Figure 5.2** – Left: scheme of geometric time and measured arrival time of two scattered photons in an OM at a distance  $d$  from the muon track [119]. Right: effect on time residual distribution of various processes [158].

## 5.2.1 Maximum likelihood reconstruction

### Arrival time of photons

The track of an infinitely long muon propagating with constant speed  $\beta = 1$  is described by five parameters: a direction  $\Omega = (\theta, \phi)$  and a vertex on the track  $\vec{r}_0 = (x_0, y_0, z_0)$ , see Figure 5.2 (left). Under previous assumptions the time  $t_0$  when the vertex is passed is irrelevant, since the vertex can be arbitrarily chosen on the track. And since we do not use the energy of the reconstructed track in the following, the energy at the vertex  $E_0$  is ignored too.

We have seen that photons are emitted at the fixed Čerenkov angle  $\theta_c = 41^\circ$  relative to the muon track. An optical module therefore detects photons from a unique point on the muon track. The time between photon emission and detection is then only determined by the radial distance  $d$  of the OM to the track, and is called the *geometric time*  $t_{\text{geo}}$ . Scattering processes change this ideal picture. First of all, some light from the  $\theta_c$  emission point arrives later than expected; and, secondly, photons from other points, with relative angle  $\theta \neq \theta_c$ , can be detected as well. In both cases the measured time  $t_{\text{meas}}$  differs from the geometrical time. Fig. 5.2 illustrates the geometrical time and the detection of two scattered photons.

We define the *residual time*  $t_{\text{res}}$  as

$$t_{\text{res}} \equiv t_{\text{meas}} - t_{\text{geo}}.$$

In the absence of scattering all photons are detected at  $t_{\text{res}} = 0$ . For OMs close to the muon track the effect of scattering will be small, with most photons having a small residual time (solid line, Fig. 5.3 left). Hits with a small residual time, typically in the

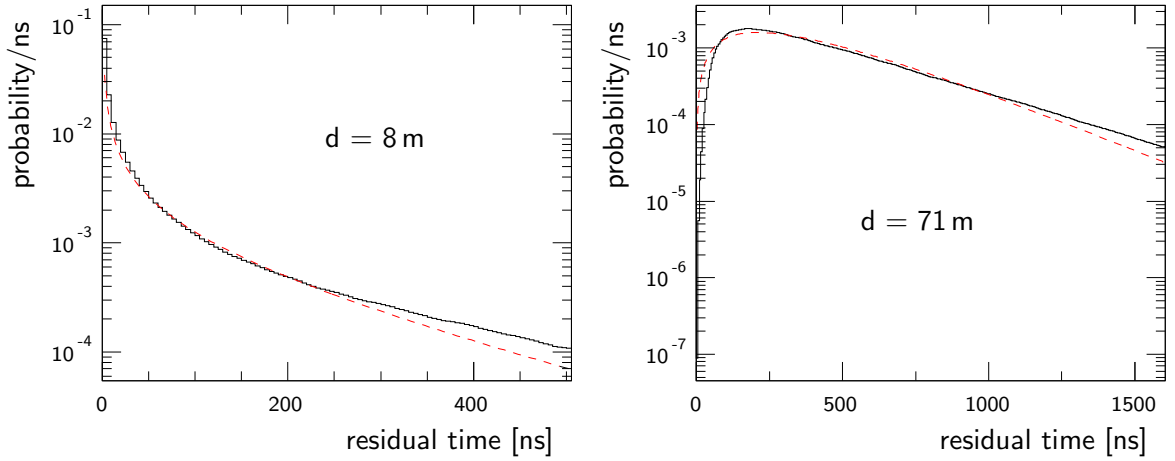


**Figure 5.3** – Probability density function of the time residual at two distances  $d$  from the muon track. The Pandel function (dashed curve) is compared to detailed simulations (solid histogram) [158].

range  $[-25$  ns,  $+75$  ns], are called *direct hits*. Photons observed by distant modules are more scattered, with much larger  $t_{\text{res}}$  as a consequence (Fig. 5.3 right). For large distances absorption plays a role too, suppressing heavily scattered photons. We remind the reader that South Pole ice has a scattering and absorption length of respectively around 30 m and 100 m.

The distance-dependence of the residual time turns out to be well modelled by the Pandel function  $p(t_{\text{res}}|d)$ , although originally suggested in the context of isotropic, monochromatic and point-like light sources [160]

$$p(t_{\text{res}}|d) \equiv \frac{1}{N(d)} \cdot \frac{\tau^{-(d/\lambda)} \cdot t_{\text{res}}^{(d/\lambda) - 1}}{\Gamma(d/\lambda)} \cdot e^{-\left[ t_{\text{res}} \left( \frac{1}{\tau} + \frac{c_{\text{ice}}}{\lambda_a} \right) + \frac{d}{\lambda_a} \right]}, \quad (5.1)$$

$$N(d) = e^{-d/\lambda_a} \cdot \left( 1 + \frac{\tau \cdot c_{\text{ice}}}{\lambda_a} \right)^{-d/\lambda},$$

where  $c_{\text{ice}} = c_{\text{vac}}/n$  is the speed of light in ice,  $\Gamma(d/\lambda)$  the Gamma function and  $N(d)$  a normalization factor. This formulation contains  $\lambda = 33.3$  m,  $\lambda_a = 96$  m and  $\tau = 557$  ns, which were determined from a fit to detailed Monte Carlo simulations of photon propagation, see Fig. 5.3 (dashed line).

The incorporation of scattering and absorption through the Pandel function is not the whole story. PMT jitter limits the knowledge about the true arrival time of photons. Instead of a delta function, unscattered photons follow a Gaussian distribution around  $t_{\text{res}} = 0$  with a spread of about  $\sigma = 15$  ns. PMT noise adds hits with a uniform distribution, at a rate of 1 kHz. Finally, secondary radiative energy losses along the muon track produce late photons. The effect of these processes on the residual times is illustrated in Fig. 5.2 (right) and all should be incorporated to obtain a realistic probability density function of the photon arrival time. Scattering remains the dominant effect though.

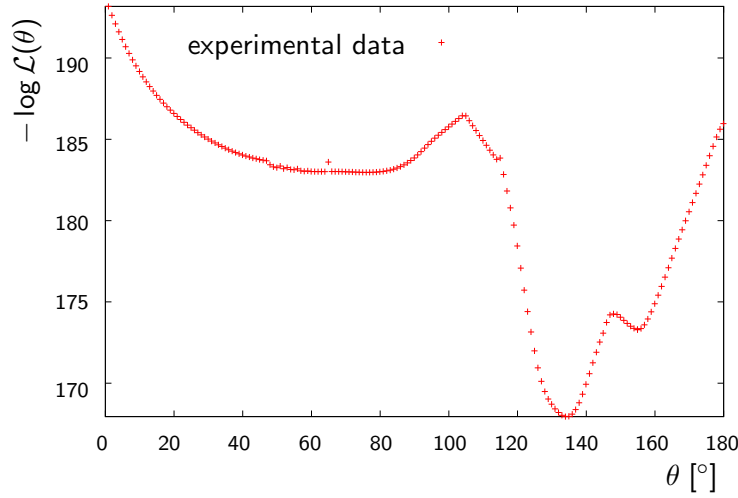


**Figure 5.4** – The likelihood landscape for one experimental event, with one track parameter left free and the others fixed [158].

## Reconstruction

The track parameters  $\vec{a}$  can be estimated by maximizing their likelihood with respect to a set of measurements  $\{\vec{x}_i\}$

$$\mathcal{L}(\vec{a}) = \prod_i p(\vec{x}_i | \vec{a}), \quad (5.2)$$

where  $p(\vec{x}_i | \vec{a})$  is the probability density function (*pdf*) for a single measurement  $\vec{x}_i$  due to a track described by  $\vec{a}$ .

We already mentioned that we are interested in the five geometrical track parameters  $\vec{a} = (\Omega, \vec{r}_0)$ . Since the arrival time (or equivalently residual time) is most sensitive to the track parameters, we neglect the other hit information (time over threshold and peak amplitude), hence  $\vec{x} = t_{\text{res}}$ . Furthermore, in the event of multiple photons in one optical module we only consider the first photon. Later photons are more likely to be scattered, providing less pronounced information (broader Pandel pdf). In this case the likelihood function becomes

$$\begin{aligned} \mathcal{L}(\Omega, \vec{r}_0) &= \prod_{i=1}^{N_{\text{hits}}} p(t_{\text{res},i} | \Omega, \vec{r}_0), \\ p(t_{\text{res},i} | \Omega, \vec{r}_0) &= \text{Pandel} \otimes \text{PMT}, \end{aligned} \quad (5.3)$$

where the product runs over all  $N_{\text{hits}}$  first photons and  $p(t_{\text{res},i} | \Omega, \vec{r}_0)$  is a convolution [161] of the Pandel pdf, Eq. 5.1, with a PMT pdf (incorporating Gaussian jitter and uniform noise). This is the basic likelihood description for muon reconstruction, and therefore referred to as the *vanilla* likelihood.

At least five hits are needed to find five free parameters. In practice, the computationally more advantageous –  $\log \mathcal{L}$  is minimized, which is equivalent to maximizing  $\mathcal{L}$ . Finding the global minimum of a function with five parameters is not always an easy task. When little photon information is gathered (e.g. for horizontal, low energy events) the likelihood function may have several competing minima. Moreover, from the technical point of view, it

is impossible to scan over the entire 5D parameter space due to time constraints. Figure 5.4 shows an example of how the likelihood function varies with one track parameter, while the other parameters remain fixed. The minimization algorithm may well end up and get stuck in a local minimum, e.g. caused by a subset of ambiguous hits that favour another track direction. It is crucial to start the minimization process from a good point in the 5D space, meaning that it should not be too far away from the true minimum. In addition, the local minima can be avoided by repeating the minimization procedure several times, each time starting from a different track hypothesis (keeping the vertex fixed, but with randomized direction). Once all iterations are finished, the parameters associated with the smallest found log-likelihood are taken as the solution. Figure 5.5 shows the reconstructed zenith distribution, when running the likelihood reconstruction with one iteration over experimental data at the trigger level.

Several so-called first guess methods will be discussed in the next section. The likelihood minimization of an average event takes about 20 ms per iteration. With 3.5 billion triggered experimental events, it is simply impossible to reconstruct all events with the likelihood method. First guess methods, on the other hand, are typically fast algorithms. Therefore a data reduction is done on the basis of the direction suggested by the first guesses, before performing a likelihood reconstruction.

The angular resolution, defined as the median space angle between true and reconstructed direction, depends on the event set. Since the event selection is aimed at finding the well reconstructed events, the resolution is better at the final level than at the trigger level. Table 7.1 presents the resolution of the likelihood reconstruction at the final cut level, it is of the order of  $3^\circ$  for high energy signal neutrinos and degrades with decreasing energy.

### Adding more information

The general likelihood of Eq. 5.2 is in no way limited to the formulation of Eq. 5.3.

For instance, it can be extended with a Bayesian prior that parameterises the zenith dependence of the atmospheric muon flux

$$p(t_{\text{res},i}|\Omega, \vec{r}_0) = \text{Prior} \otimes \text{Pandel} \otimes \text{PMT}.$$

Such a muon flux prior gives progressively lower probability towards the horizon and becomes zero for upward-going events. As a result all solutions are downward-going,  $\theta < 90^\circ$ . We are looking for upward-going tracks, so the track parameters of these Bayesian solutions are not that useful in their own right. It is the likelihood value of the Bayesian solution that is of interest. This value can be compared to that of the vanilla likelihood solution, which allows both hemispheres. When the likelihood of an upward-going vanilla and downward-going Bayesian solution is very close, the upward-going hypothesis becomes not very convincing. This can (and will) be used in the later event selection to reject misreconstructed muons.

Other extensions of the basic model are possible as well, although not used in this work. One can decide to use all hits in the OMs, and not only the first hits. The measured amplitudes could be incorporated to estimate the energy of the track. The information from OMs that do not see photons is useful as well. These methods are discussed in [158].

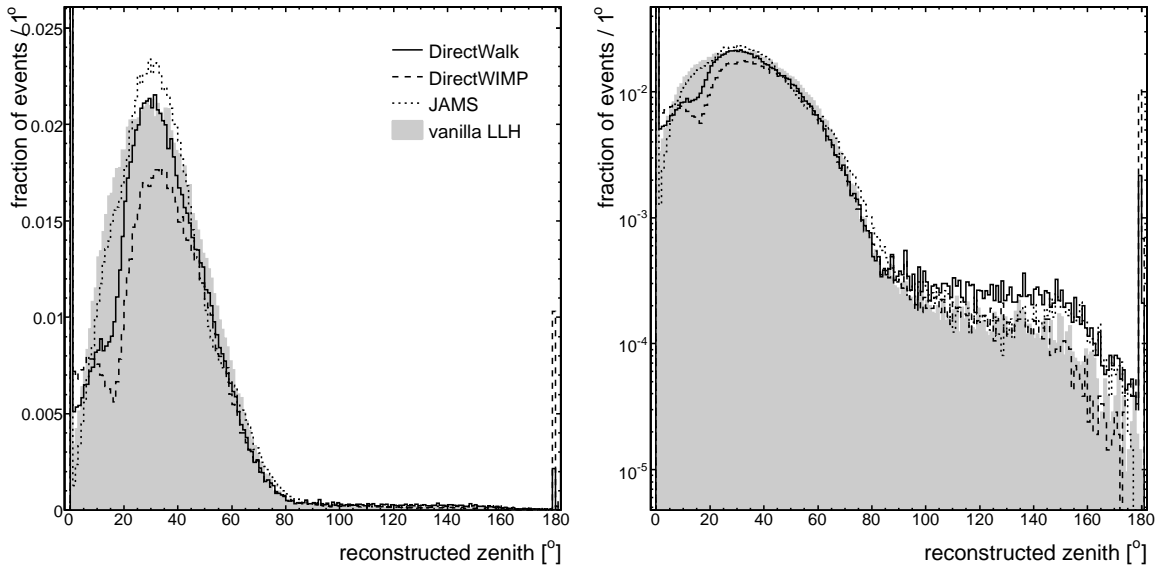


**Figure 5.5** – Distribution of the zenith angle found by four reconstructions for experimental data at the trigger level (left: linear scale, right: log scale). Failed reconstructions are set to  $\theta = 0^\circ$  or  $180^\circ$ , we normalized to the total number of events.

## 5.2.2 First guess methods

An initial track is needed to start the minimization of the likelihood reconstruction. This seed is delivered by a first guess (FG) method that does not require an initial hypothesis. First guess algorithms are based on fast, pattern recognition techniques, such that all triggered events can be reconstructed in a reasonable amount of time. We will focus on the three FG methods used in this work: DirectWalk, DirectWIMP and JAMS. The zenith distribution of trigger level experimental data, as reconstructed by three first guesses, is shown in 5.5.

The DirectWalk algorithm [162] starts off by finding pairs of sufficiently distant hits, which are strongly causally connected through a particle with speed  $c$ . The line segment between the OMs of a hit-pair is then promoted to a track candidate, when it satisfies several quality criteria that indicate compatibility with a muon track (large number of associated hits, large spread of hits along the track, ...). In the final step, a cluster search finds the  $15^\circ$  wide cone with most track candidates. The average direction of the candidates in the cone is taken as the first guess solution.

When no line segments fulfil the quality criteria, the DirectWalk method does not return a solution. This mainly affects low energy events which have fewer hits. A modification of DirectWalk was proposed by [163] in the context of low energy vertically upward-going tracks, DirectWIMP. The internal quality criteria were relaxed, especially for vertical elements, leading to almost a factor two improvement in reconstruction success for low energy, vertical tracks. This comes at a small cost of resolution however, but in many cases that can be compensated by a later likelihood reconstruction.

The best first guess algorithm is JAMS<sup>2</sup> [164], which has a different approach. For each

<sup>2</sup>JAMS means *Just Another Muon Search*.

of fifty directions on an isotropic grid, a search for clusters of hits along that direction is performed. When the cluster is densely populated, its direction and vertex are reconstructed with a simple likelihood method (not the one from previous section). Then several indicators of track quality (number of early/late hits, spread of hits along track, distance of hits to track) are fed to a neural network trained to separate low quality from high quality events. The cluster of maximal quality  $Q$  is chosen as the final solution.

## 5.3 Event observables

In Chapter 6 we develop several filters against the atmospheric background. This section describes the various event observables used in the selection process. We divide them in several classes: topology, reconstruction and hit-reconstruction. Examples of these observables are shown in a later chapter, Fig. 6.7-6.10.

### 5.3.1 Topology

Topological observables are solely based on the hit information.

Simple examples are the number of hits, the number of hit OMs or the number of hit strings. These are a measure of the amount of light deposited in the detector, and hence a proxy of energy.

The distribution of hits is relevant as well. The radial (distance to vertical axis) and vertical position of the centre of gravity of the hits indicate whether the event happens well inside the detector, or rather outside. In the latter case, it may suffer a poor reconstruction. Additional information comes from the spread of the hits along the vertical or in time.

### 5.3.2 Reconstruction

Reconstruction observables are provided by the reconstruction algorithms.

The most natural example is the zenith angle  $\theta$ . The reconstructed azimuth or vertex do not play a discriminative role.

We already suggested to compare the likelihood of the vanilla and Bayesian solutions. In practice, we take the difference of the reduced log-likelihoods<sup>3</sup>,  $\Delta rLLH = rLLH_{\text{Bayes}} - rLLH_{\text{van}}$ . Large values indicate a big difference between the downward-going and all-sky hypotheses, revealing an unlikely downward-going hypothesis.

Another likelihood related observable is the width of the log-likelihood function around the minimum. In principle, the log-likelihood function is parabolic around the minimum and its width tells us something about the event resolution [165]. Fig 5.4 is a nice illustration of this: a parabola fit around the local minimum at  $\theta = 60^\circ$  is much broader than a parabola around the global minimum  $\theta = 135^\circ$ . This is very powerful information, we can select well reconstructed events by demanding a small paraboloid width  $\sigma_{\text{PARA}}$ . We should be careful though with low energy signal events, since these are unavoidably harder to reconstruct.

The JAMS first guess method selects the cluster of highest quality. This value  $Q_{\text{JAMS}}$  is higher for better reconstructed tracks, and can be used in the event selection. The

<sup>3</sup>The *reduced log-likelihood* is the log-likelihood divided by the number of degrees of freedom in the fit (number of hits - five parameters).

DirectWIMP algorithm also provides an internal parameter,  $\sigma_{\psi}^{WIMP}$ , which is a measure of the angular resolution of the solution, small values are obtained for more accurate solutions.

### 5.3.3 Hit-reconstruction

And then there is a hybrid class, where the relation of the hits to the track is considered.

A good reconstruction should have its hits smoothly distributed along the track. This culminated in the smoothness parameter  $\mathcal{S}$  and its spread  $\sigma_{\mathcal{S}}$ . Technical details can be found in [166]. When the hits gravitate towards the beginning or the end of the reconstructed track, the smoothness will be well different from zero. The latter value is expected for a perfectly smoothly distributed set of hits. When the projected length of direct hits (hits with small time residual) on the track is large, we can assume that the reconstruction does a good job at describing the hit pattern over large distances. That is a strong indication of a good solution.

The radial position of hits around the reconstructed track is powerful as well. A good solution for low energy events will lead to small average distances, and the average increases with energy. When the solution is bad, the hits will not be centred around the track and the average radial distance becomes very large. A variant uses only direct hits in the calculation. We can also look at the fraction of OMs that are hit within 100 m from the track, or the number of active OMs within 100 m. The latter observable can be used to avoid corner clippers, by requiring a large amount of OMs close to the track.

On the basis of the probability to detect a photon at a certain distance from the track, we can calculate the expected number of hits in the detector. In the same philosophy the expected hit distribution can be compared to the observed one. The ratio of the expected and observed average radial distances or the separation of the expected and observed hit clouds are observables that can discriminate atmospheric background from upward-going neutrino events.

## 5.4 Data processing software

All data, experimental and simulation, are processed with AMANDA's data processing software, called SIEGLINDE<sup>4</sup>. This object-oriented program handles all of the above described tasks in a modular way: input/output, calibration, hit cleaning, reconstruction, observable calculation, event stream definition, ... The output file is either in the plain text F2K format or the analysis-ready ROOT format.

Two independent implementation models coexist in the SIEGLINDE program. The first, coined *classic*, was coded, thoroughly checked and declared ready for analysis at the time of the first level processing, see Section 6.3. Several months later, when the second filter level was designed (Section 6.4), the final implementation model, called *SLART*, became available for large scale processing. The code of both implementation models is completely separated, but based on the same hit calibration, cleaning, event selection and reconstruction principles. The *SLART* reconstructions are slightly more elaborated and perform better

---

<sup>4</sup>SIEGLINDE is the successor of AMANDA's former processing software SIEGMUND. Both characters appear in a Richard Wagner opera very much appreciated by the founding fathers of the code.

than their *classic* siblings. To make the distinction between the reconstructions added with the classic and SLART flavour, we add the prefix “c” to the name of the classic result.

The classic version is used for the processing of the low level event filters, the SLART version for the higher level filters.

# Chapter 6

## Event selection

In the domain of high energy physics, the discovery of new physics is often complicated by large backgrounds and a small expected signal count. It occurs very rarely that a predicted signal will manifest itself with a clear, *smoking gun* signature. Most searches have to face a substantial amount of background events that strongly resemble signal events, by nature or due to detector or reconstruction imperfections. Therefore, it is an impossible task to classify events as background without loss of signal.

In this chapter we explain how the atmospheric background is reduced to a level where a search for neutrinos from the Sun becomes feasible, while simultaneously minimizing the loss of signal. That is accomplished in several steps, or filter levels. The first two filters, described in Sections 6.3 and 6.4, simply discard downward-going events. The third and final filter level is more complex and involves various event quality observables, see Section 6.5. It is very important to note that we keep ourselves blind to the position of the Sun throughout the whole optimization of the event selection, in an effort to reduce experimenters bias. At the end of this chapter we discuss the characteristics of the selected final event sample.

But first, we introduce a concept needed in the further analysis, that of effective volume.

### 6.1 Effective volume

The *effective volume* couples the volumetric flux  $\Gamma_{\nu \rightarrow \mu}$  with the observed muon event rate, see Eq. 2.7. It should be interpreted as the volume of an ideal detector to which the real detector is equivalent. In this context a detector is called ideal when each muon produced in neutrino-nucleon interactions within its volume is triggered by the detector, reconstructed and selected at the final filter level. Obviously there is an energy dependence of the effective volume, increasing with muon energy due to its longer range.

In the following chapter we calculate the effective volume at various filter levels. This is done for neutralino models that produce a flux  $dN_{\mu}/dE_{\mu}$ , rather than a monochromatic flux of muons. More technically, our calculation goes as follows

$$V_{\text{eff}}^{\text{trig}} = \frac{\sum_{i=1}^N w_i \delta_{ij}^{\text{trig}} V_{\text{gen},i}}{\sum_{i=1}^N w_i}, \quad (6.1)$$

The sum runs over all  $N$  generated muons  $i$ , produced in a volume  $V_{\text{gen},i}$ , with an associated

event weight  $w_i$  (see remarks in Section 4.2.6) and  $\delta_{ij}^{\text{trig}}$  is 1 (0) if it passes (or not) filter level  $L_j$  and was triggered by *trig* (either all, std or str).

## 6.2 Trigger level

In Section 3.2.2 we mentioned that events are recorded when they satisfy at least one of two trigger requirements<sup>1</sup>. Most recorded events satisfy the multiplicity trigger, demanding 24 hit OMs in the whole detector during a  $2.5 \mu\text{s}$  time window. Low energy (below roughly 25 GeV) events will have difficulty to fulfil this condition though. Therefore the string trigger lowers the threshold by requiring fewer hit OMs, but instead they should be correlated in space (vertically, along a string, hence the name) to reduce random noise triggers. As we will see, the search for low mass neutralinos benefits significantly from the string trigger, even though neutrinos from the Sun leave horizontal rather than vertical muons in the detector.

Each triggered event is considered a member of either the *standard* (std) or the *string* (str) class of triggers. The former class contains the events for which the multiplicity requirement is met, while the latter collects the events *exclusively* triggered by the string condition. Most AMANDA analyses discard string-exclusive triggered events, since they do not contribute significantly to the sensitivity of searches for astrophysical neutrinos above 1 TeV. Therefore, the term *standard* reflects the fact that it is the default data stream for AMANDA data analysis, and the *string* class allows to focus explicitly on the additional event stream introduced by the string trigger.

Table 6.1 summarizes the (weighted) number of events at trigger level for experiment (first line) and simulation (remaining lines). The left side of the table shows the annual contribution to the total set of triggered events, the right-hand side disentangles both trigger classes (the term *all* refers to the union set of triggers). Since the absolute number of neutralino events is irrelevant in this analysis we arbitrarily set the total amount of signal events at trigger level to one. We refer the reader to Chapter 4 for further explanation of the various samples.

The relative size of the annual trigger sets reflects the live-time and the string trigger downscaling in 2002. The experimental data sample at trigger level contains about 3.5 billion events. Almost all these events are downward-going atmospheric muons, apart from about 11000 upward-going atmospheric neutrinos and, possibly, not more than a couple of tens to hundreds neutralino-induced neutrinos.

The background Monte Carlo simulation predicts 28% less triggers compared to experimental data, which can be attributed to rather large theoretical uncertainties on the primary cosmic ray flux and to experimental uncertainties on the absolute sensitivity of the optical modules. Such a mismatch is not uncommon in AMANDA analyses and is not necessarily a cause for concern, since the final result of this work does not depend on Monte Carlo information about the background. What is more important is to verify the experiment/simulation agreement of the *shape* of observable distributions. That is the only way to gain confidence in the simulation of the signal events.

Figure 6.1 (top) is a graphical representation of Table 6.2: the effective volume at

<sup>1</sup>Other trigger conditions exist as well, but the resulting data streams are not considered for this work.

	all triggers			2001–2003		
	2001	2002	2003	all	standard	string
exp. data ( $\times 10^9$ )	1.456	0.921	1.146	3.523	—	—
atm. $\mu$ ( $\times 10^9$ )	1.003	0.707	0.850	2.560	1.999	0.561
atm. $\nu$ ( $\times 10^3$ )	4.732	3.219	3.518	11.47	8.037	3.436
5000 hard (arb.)	0.379	0.286	0.335	1.000	0.804	0.196
3000 hard „	0.378	0.288	0.334	1.000	0.813	0.187
1000 hard „	0.377	0.288	0.335	1.000	0.807	0.193
500 hard „	0.383	0.286	0.331	1.000	0.783	0.217
250 hard „	0.388	0.285	0.327	1.000	0.726	0.274
100 hard „	0.440	0.263	0.297	1.000	0.408	0.592
50 hard „	0.513	0.219	0.268	1.000	0.050	0.950
5000 soft „	0.391	0.282	0.327	1.000	0.706	0.294
3000 soft „	0.391	0.282	0.327	1.000	0.708	0.292
1000 soft „	0.395	0.282	0.323	1.000	0.683	0.317
500 soft „	0.407	0.277	0.316	1.000	0.609	0.391
250 soft „	0.434	0.265	0.301	1.000	0.455	0.545
100 soft „	0.500	0.228	0.272	1.000	0.116	0.884
50 soft „	0.526	0.209	0.265	1.000	0.007	0.993

**Table 6.1** – Weighted number of events at trigger level for the experimental data (first line) and the simulated atmospheric background (line 2-3). The various neutralino models (remaining lines) are normalized to one. The central columns show the annual contribution from all triggers, the columns on the right show the individual trigger contributions for 2001–2003. This table represents the statistics in the *test* samples.

trigger level for each neutralino model and the various trigger classes, see Eq. 6.1. For the highest energy models, the effective size is (slightly) larger than the instrumented volume (horizontal line) due to the long range of high energy muons and the large absorption length of light in Antarctic ice. The limited size and the sparseness of the detector in the horizontal plane, pose a real challenge to detect low energy events in this angular range. The effective volume is more than two orders of magnitude smaller than the actual detector for the lowest energy model. If we would switch off the string trigger the quest for 50 GeV neutralinos already becomes hopeless at the trigger level.

Previous results were for the whole data set. We now consider each of the three years of data taking separately, Fig. 6.1 (bottom). The downscaling of the string trigger obviously halves the effective volume after 2001, but otherwise the different years are equivalent. We observe a larger annual variation for the standard stream, since a global trigger is more sensitive to the OM selection than a localized trigger. In 2001 there were slightly fewer stable modules than for the other years (see Section 5.1), leading to a less efficient trigger.

According to the simulation, the string trigger class represents about 22% and 30% of the triggers for the atmospheric muons and neutrinos respectively. Unfortunately, we did not have the experimental values at our disposal. The same order of magnitude can be found for the most massive neutralinos. For models with a mass below  $\lesssim 100$  GeV the string trigger dominates the total trigger rate. Without this trigger the signal efficiency

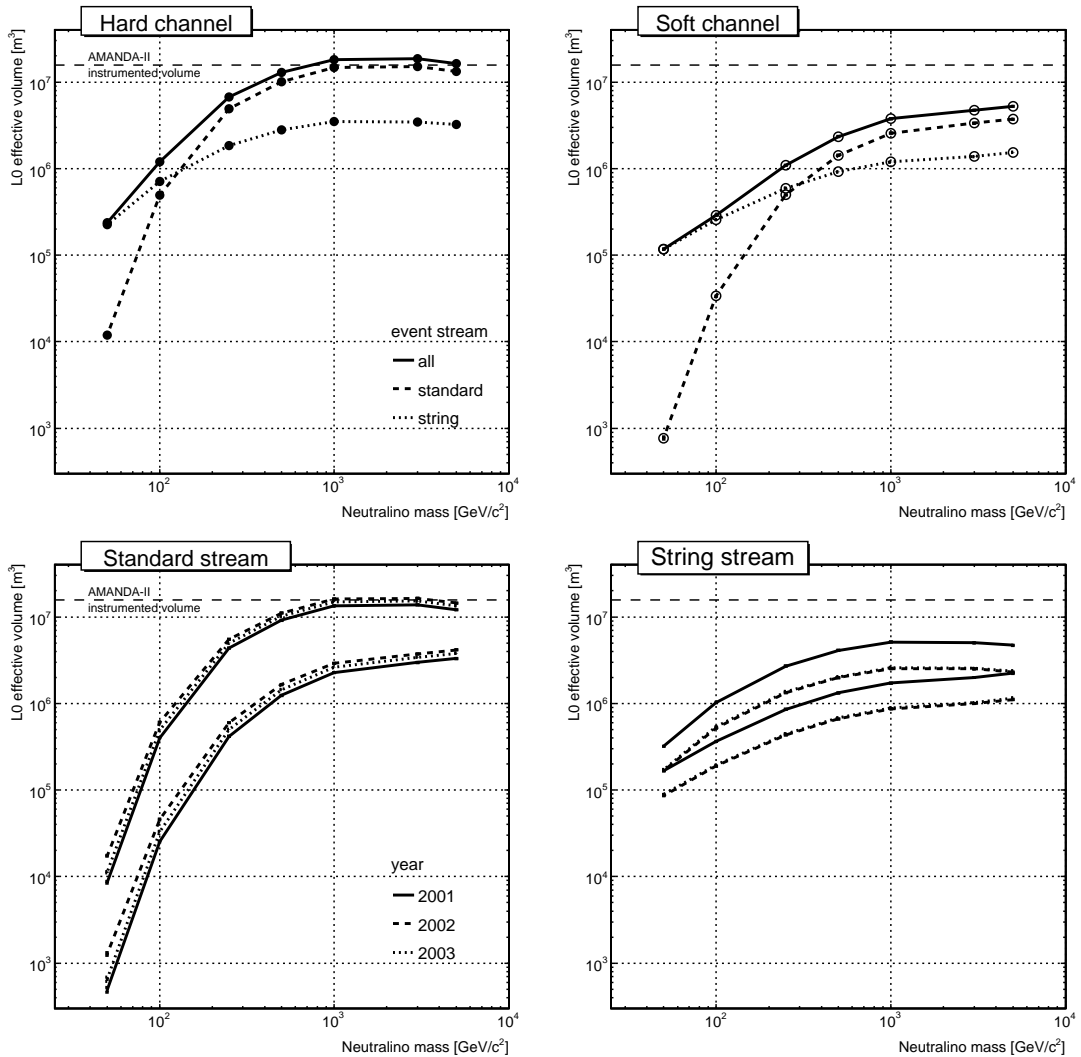


**Figure 6.1** – Top row: effective volume at trigger level for the whole data set and for the various trigger classes; the left (right) panel shows the results for the hard (soft) annihilation channel. Bottom row: as before, but the data taking years are disentangled; left (right) is the standard (string) trigger set, lines at the top (bottom) are for the hard (soft) channel. (Invisible) vertical bars represent statistical errors.

for the 50 GeV soft model would suffer a loss of a factor 140. Since the string trigger was downscaled from 2002 onwards, the triggered sample for these low energy signal models consists mainly of events acquired during 2001 (also because it represents a slightly larger live-time).

### 6.3 Filter level 1

As we explained in the previous chapter, the raw triggered data are not immediately suitable for consumption. All hit information (time and amplitude) of each recorded event is first calibrated, then tagged as an electronic artefact or not. Once a good hit set is defined, it

		[m <sup>3</sup> ]	5000	3000	1000	500	250	100	50
$V_{LO}^{all}$	hard		$1.64 \times 10^7$	$1.85 \times 10^7$	$1.82 \times 10^7$	$1.28 \times 10^7$	$6.76 \times 10^6$	$1.21 \times 10^6$	$2.38 \times 10^5$
	soft		$5.26 \times 10^6$	$4.72 \times 10^6$	$3.76 \times 10^6$	$2.34 \times 10^6$	$1.09 \times 10^6$	$2.90 \times 10^5$	$1.18 \times 10^5$
$V_{LO}^{std}$	hard		$1.32 \times 10^7$	$1.50 \times 10^7$	$1.47 \times 10^7$	$1.00 \times 10^7$	$4.90 \times 10^6$	$4.92 \times 10^5$	$1.20 \times 10^4$
	soft		$3.72 \times 10^6$	$3.34 \times 10^6$	$2.57 \times 10^6$	$1.43 \times 10^6$	$4.97 \times 10^5$	$3.38 \times 10^4$	$7.71 \times 10^2$
$V_{LO}^{str}$	hard		$3.22 \times 10^6$	$3.47 \times 10^6$	$3.52 \times 10^6$	$2.79 \times 10^6$	$1.86 \times 10^6$	$7.14 \times 10^5$	$2.26 \times 10^5$
	soft		$1.54 \times 10^6$	$1.38 \times 10^6$	$1.19 \times 10^6$	$9.17 \times 10^5$	$5.95 \times 10^5$	$2.57 \times 10^5$	$1.17 \times 10^5$

**Table 6.2** – Neutralino effective volume at trigger level, for the different trigger classes.

is fed to a first guess reconstruction. The first guess solution (or shorthand *FG*) could then be seeded to a more refined, but also more CPUtime intensive likelihood reconstruction. Unfortunately, it is impossible to do that for all triggered events and a reduction of the data sample is needed. That is the principal goal of the first level filter, also denoted *L1*. The first reduction of the atmospheric muon background is done by removing the events reconstructed as clearly downward-going by the *FG* algorithms.

Processing 3.5 billion triggered events is a very time consuming task, which asks for a centralized effort. Therefore, the first filter level is completed in two steps, carried out by the AMANDA groups at DESY-Zeuthen and at the University of Uppsala respectively. The “Zeuthen processing” provides a sample that is general enough to be useful for most analyses within the collaboration. The “Uppsala processing” extracts the event streams useful for low energy analyses and adds more event information. In the next few paragraphs, we discuss the parts that are relevant for this work.

**Zeuthen processing** A schematic overview of the relevant parts of the Zeuthen processing can be found in Table 6.3, for a full description we refer to [167]. The raw event information is read from a plain text file in the AMANDA f2k-format, calibrated, three hit selections defined based on a preliminary list of good OMs, and provided to three first guess reconstructions. Various L1 event selections are defined (of interest to the various searches for astrophysical neutrinos) and the inclusive sum<sup>2</sup> written to f2k-formatted file. To facilitate a later, more refined, calibration all hit information is stored uncalibrated.

The processing was performed with the *classic* implementation of the SIEGLINDE program, since the SLART implementation was still under development. Version 1.5.2\_P2-\_\_RC2 was used for experimental data and a later version CVS\_24\_05\_2006 for simulated samples. We verified and concluded that the difference in SIEGLINDE version does not introduce a bias between experiment and simulation. Technical details about the implementation model, the hit selection and reconstruction methods can be found in Chapter 5.

**Uppsala processing** The second step of the L1 filter is done by the Uppsala group and outlined in Table 6.4, complete details can be found in [168]. The Zeuthen L1 event streams are read in from f2k, and their hits recalibrated with improved calibration files. The flare indicators are calculated, along with the retrigger flags. An additional hit selection is defined, based on the final list of reliable OMs and introducing crosstalk cleaning. This

<sup>2</sup>With inclusive sum, we mean that an event satisfying any of the various L1 event selections is retained.

---



---

<b>Zeuthen L1 processing</b> with classic SIEGLINDE 1.5.2_P2_RC2	
1.	read uncalibrated f2k
2.	calibrate pADC, TDC, geometry
3.	hit selections
	<i>HitSel0</i> : (prelim.) bad OM, TOT cleaning
	<i>HitSel1</i> : (prelim.) bad OM, TOT, LE cleaning
	<i>HitSel2</i> : (prelim.) bad OM, TOT, LE, amplitude, isolation cleaning
4.	first guess reconstructions
	<i>cDW</i> : DirectWalk (using <i>HitSel1</i> )
	<i>cWIMP</i> : DirectWIMP (using <i>HitSel2</i> )
	<i>cJAMS</i> : JAMS (using <i>HitSel0</i> )
5.	define various L1 streams
6.	write uncalibrated f2k

---



---

**Table 6.3** – Schematic overview of Zeuthen's L1 processing [167].

final hit set is given to a 32-fold iterative patched Pandel-likelihood reconstruction, which only takes the first hit of every hit OM into account and uses the JAMS solution as seed track. Finally, the events that pass the hereafter defined L1 selection criteria are written to f2k file (this time with calibrated hit information).

---



---

<b>Uppsala L1 processing</b> with classic SIEGLINDE CVS_11_11_2005	
1.	read uncalibrated f2k from Zeuthen L1
2.	recalibrate pADC, TDC, geometry
3.	calculations
	flare indicators (from uncalibrated hits)
	retrigger information (using <i>HitSel0</i> )
4.	hit selection
	<i>Final HitSel</i> : (final) bad OM, TOT, LE, amplitude, isolation, extended (map + pADC-TOT) xtalk cleaning
5.	event selection
	( $\theta_{cDW} > 70^\circ$ AND M24) OR ( $\theta_{cWIMP} > 70^\circ$ )
6.	LLH reconstructions
	<i>c32JAMS</i> : 32x patched 1pe Pandel (seeded by <i>cJAMS</i> , using <i>Final Hitsel</i> and only first LE in OM)
7.	write calibrated f2k

---



---

**Table 6.4** – Schematic overview of Uppsala's L1 processing [168].

Again, the classic implementation of the SIEGLINDE algorithms is used, with experimental data processed with version CVS\_11\_11\_2005 and simulation with a slightly newer version CVS\_24\_05\_2006.

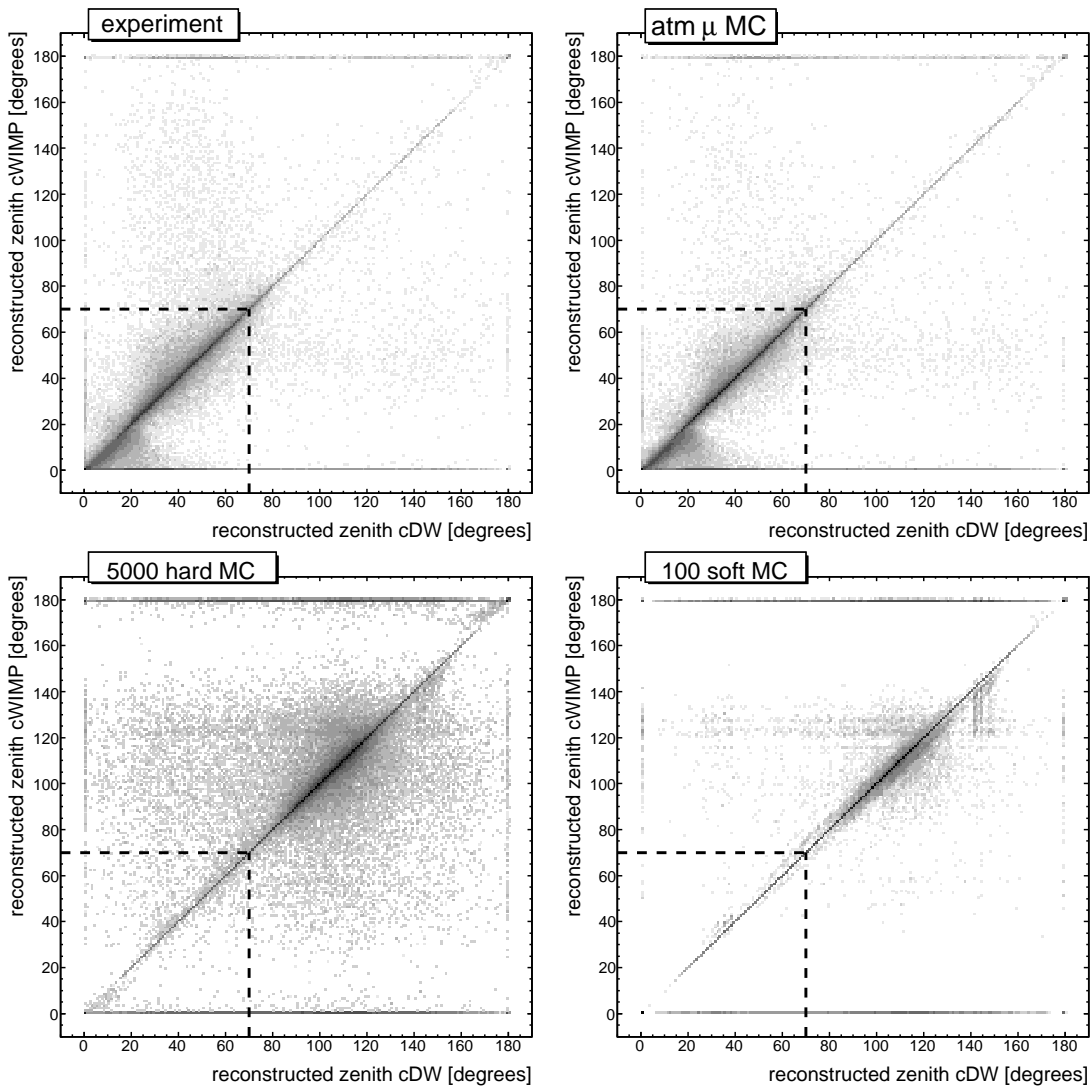


**Figure 6.2** – Correlation of the reconstructed zenith angle from *DirectWalk* and *DirectWIMP* at trigger level. The four panels (experiment, atm.  $\mu$  MC and two simulated neutralino models) are normalized to one, the colour scale is logarithmic. The dashed lines illustrate the L1 selection.

**L1 event selection** The most natural way to reduce the atmospheric muon background is to remove clearly downward-going events. Since most AMANDA analyses do not benefit from the string trigger, the standard L1 filter unfortunately explicitly removes them together with downward-going *DirectWalk* solutions:  $(\theta_{cDW} > 70^\circ \text{ AND } M24)$ . Here,  $\theta_{cDW}$  is the zenith angle as reconstructed by the classic *DirectWalk* reconstruction, and *M24* refers to the 24-fold multiplicity trigger. Therefore a parallel event stream, rejecting clearly downward-going *DirectWIMP* tracks but without a harmful trigger condition is put in place:  $(\theta_{cWIMP} > 70^\circ)$ . In this way some string-exclusive events are recovered. Figure 6.2 illustrates the L1 event selection for experimental data, simulated atmospheric muons and two neutralino models.

The impact of the L1 event selection can be seen in Table 6.5 (left side). This table contains the exclusive efficiency  $\epsilon_{L1}^{\text{trig}}$  of the L1 selection with respect to the trigger level, for

each trigger class separately. In the case of experimental data and simulated background this quantity is defined as the ratio of the *trig* class specific number of events after and before the L1 cut

$$\epsilon_{\text{Li}}^{\text{trig}} \equiv \frac{n_{\text{Li}}^{\text{trig}}}{n_{\text{Li}-1}^{\text{trig}}}. \quad (6.2)$$

For simulated signal we consider the ratio of the effective volumes

$$\epsilon_{\text{Li}}^{\text{trig}} \equiv \frac{V_{\text{eff,Li}}^{\text{trig}}}{V_{\text{eff,Li}-1}^{\text{trig}}}, \quad (6.3)$$

since this is more relevant for the final calculation.

More than 95% of the experimental events are rejected, compared to 96% of the simulated atmospheric muons. Figure 6.2 shows that the atmospheric muon simulation reproduces the experimental distribution very well. The upward-going atmospheric and neutralino-induced neutrinos on the other hand are well retained: only the very lowest energy models lose more than 20% of the signal, most others keep 90% selection efficiency.

For the standard trigger class the first guess methods are able to find accurate solutions, since there is ample hit information to resolve ambiguities in the track direction. As it should, upward-going events are > 95% of the times reconstructed as upward-going, while 97% of the downward-going events are reconstructed as downward-going. The bulk of the remaining 3% atmospheric muons comes from more horizontal directions, which could have been removed by a tighter selection window.

The small string events on the other hand pose a challenge not only to the FG methods but to any reconstruction algorithm. And if a solution is found after all, it can well point rather far away from its source, due to the larger intrinsic neutrino-muon scattering angle at small energies and due to the sparseness of the hit information. Therefore the efficiency for upward-going neutrinos is lower, and higher for downward-going muons compared to the larger standard events.

## 6.4 Filter level 2

**Introduction** The principal goal of the second level filter (or shorthand *L2*) is to reconstruct the remaining L1 events with a maximum-likelihood method, and again reject clearly downward-going solutions. We already explained in the previous chapter that the Pandel likelihood (or shorthand *LLH*) reconstruction is more powerful than a first guess algorithm, since the photon time delay due to scattering in the ice is taken into account explicitly. Repeated trials to locate the global maximum of the likelihood function are more likely to be successful, but that comes at the cost of extra CPUtime. Another goal of the L2 filter is to calculate advanced event observables, which will be used for the following level three filter.

From now on we continue with the SLART flavour of AMANDA's processing software SIEGLINDE, for two main reasons. It conveniently provides output directly in the analysis-ready ROOT format. Secondly, the parts of the code that handle LLH fits were improved considerably with respect to SIEGLINDE's classic flavour. More technical information about SIEGLINDE can be found in Section 5.4.

	L1 passing wrt L0			L2 passing wrt L1		
	all	standard	string	all	standard	string
exp. data	0.049	—	—	0.057	—	—
atm. $\mu$	0.038	0.033	0.058	0.055	0.040	0.084
atm. $\nu$	0.883	0.945	0.737	0.822	0.850	0.738
5000 hard	0.923	0.966	0.746	0.853	0.875	0.733
3000 hard	0.925	0.966	0.746	0.852	0.872	0.741
1000 hard	0.925	0.967	0.748	0.854	0.876	0.735
500 hard	0.918	0.967	0.744	0.845	0.867	0.740
250 hard	0.905	0.969	0.735	0.833	0.859	0.743
100 hard	0.811	0.975	0.698	0.778	0.808	0.748
50 hard	0.592	0.957	0.573	0.694	0.688	0.695
5000 soft	0.900	0.970	0.733	0.836	0.863	0.751
3000 soft	0.899	0.970	0.726	0.833	0.859	0.749
1000 soft	0.891	0.970	0.723	0.834	0.863	0.749
500 soft	0.871	0.972	0.713	0.812	0.845	0.741
250 soft	0.817	0.974	0.685	0.783	0.822	0.737
100 soft	0.644	0.968	0.601	0.710	0.764	0.698
50 soft	0.481	0.919	0.478	0.646	0.582	0.647

**Table 6.5** – Exclusive selection efficiencies for experiment and simulation; (left side) for the level 1 filter with respect to trigger level, for the various trigger classes; (right side) for the level 2 filter with respect to level 1.

The level two filter was designed in the frame of this analysis, but remains general enough to be useful for most analyses looking for upward-going or horizontal muon-neutrinos. The scheme is outlined in Table 6.6.

**L2 event selection and processing** We read the calibrated L1 events and verify whether they also satisfy the (multiplicity or string) trigger condition after removal of the spurious hits<sup>3</sup>. This so-called *retriggering* procedure provides a better agreement between experiment and simulation, see Section 5.1.3. E.g. transient OM behaviour and crosstalk phenomena are not simulated, which implies more electronic, and hence rejected hits in experiment than in simulation. The result is that fewer experimental events (roughly 70%) survive the retrigger condition than simulated events (more than 90%).

We then repeat the DirectWalk, DirectWIMP and JAMS first guess reconstructions, this time with the SLART methods. Time constraints force us to perform another data reduction before the iterative LLH reconstruction. Roughly two thirds of the experimental sample and 68% of the atmospheric muon MC is rejected by asking *JAMS* solutions above 70° in zenith. This is a relatively mild cut window for genuine neutrino events, with a selection efficiency between 80% for low mass and 90% for high mass neutralinos and atmospheric neutrinos.

Many string triggered atmospheric muons that survive the L1 selection criteria have

<sup>3</sup>A mild hit selection was chosen based on good OMs and reasonable TOT values.

---



---

<b>L2 processing</b> with SLART SIEGLINDE CVS_24_05_2006	
1.	read calibrated f2k from Uppsala L1
2.	first guess reconstructions (identical hit selections as for Zeuthen L1 processing)
	<i>DW</i> : DirectWalk
	<i>WIMP</i> : DirectWIMP
	<i>JAMS</i> : JAMS
3.	LLH reconstruction (using <i>Final Hitsel</i> and only first LE in OM)
	<i>32JAMS</i> : 32x convoluted 1pe Pandel (seeded by <i>JAMS</i> and <i>c32JAMS</i> )
	<i>32PARA</i> : parabola fit around best <i>32JAMS</i> solution
	<i>32BAYES</i> : 32x downgoing Bayesian Pandel
4.	event selection
	retrigger
	$\theta_{JAMS} > 70^\circ$
	$\theta_{32JAMS} > 80^\circ$
5.	calculate observables (with <i>32JAMS</i> as reference track)
6.	write SLART tree

---



---

**Table 6.6** – Schematic overview of the L2 processing.

a hit set dominated by several neighbouring hits on the same string. Such a vertical hit geometry naturally suggests a track with its Čerenkov wave front (close to) parallel to the string, or  $\theta \sim \theta_c$  and  $\theta \sim 180 - \theta_c$ . This is illustrated by Fig. 6.3 (right panel), with two clear bumps close to  $40^\circ$  and  $140^\circ$ . The consequence is that for atmospheric muons, the string stream passes the *JAMS* selection more easily than the standard stream.

The events that pass the previous selection criteria are then subject to three likelihood reconstructions, technical details can be found in the previous chapter. The first, *32JAMS*, scans 32 times over a LLH function that combines the arrival time likelihoods of the first hit in each hit OM, given the six track parameters. The hit times are assumed distributed according to the convoluted Pandel probability density function. The second reconstruction, *32PARA*, fits a parabola to the LLH valley around the best *32JAMS* solution, the  $1\sigma$  area of which is a measure for the event resolution. And, finally, the *32BAYES* reconstruction maximizes the same LLH function as *32JAMS*, but incorporates an additional, zenith-dependent penalty function to enforce a downward-going solution. The likelihood value of the best downward-going solution can then be compared to that of *32JAMS* to discriminate upward- from downward-going events.

With the best estimate of the muon track at hand, the *32JAMS* solution, we select the events that have a zenith angle above  $80^\circ$ , see Fig 6.4. This criterion removes 80% of the experimental and simulated muons, but only 5-10% of the atmospheric neutrinos and dark matter signal. The signal passing rate for this selection is higher than for the previous cuts. This is partly because the latter already removed the events that are difficult to reconstruct, and partly because the LLH reconstruction exploits more information than the first guess methods and therefore leads to a better resolution.

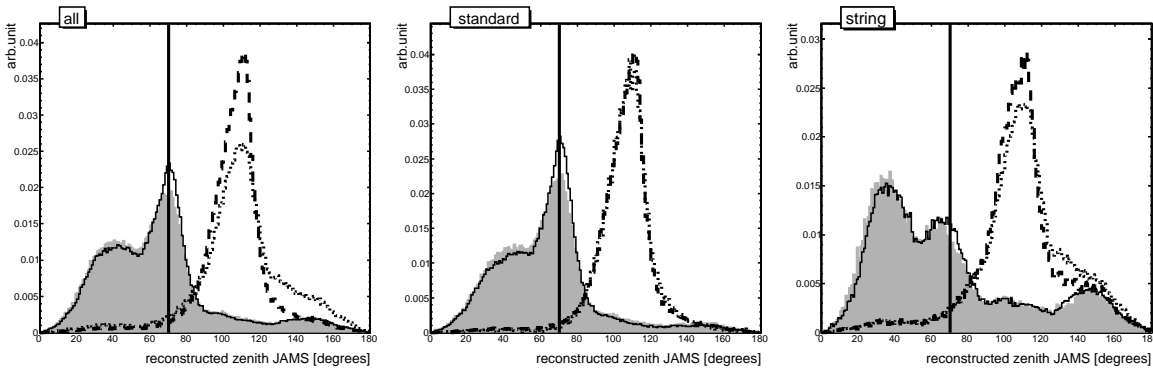


**Figure 6.3** – Normalized distributions of the zenith angle as reconstructed by *JAMS* after the L1 selection and retriggering. Each panel represents a trigger class. Experimental data is shown as a filled area, simulated data as lines: atm.  $\mu$  MC (solid), 5000 GeV hard MC (dashed) and 100 GeV soft MC (dotted). The vertical line indicates the position of the L2 cut.

**Discussion** One can see in Table 6.5 that after all L2 selection criteria roughly 6% of the L1 experimental data sample remains. The atmospheric muon MC indicates a very similar value and a passing rate for string events twice higher than for standard events. The high mass neutralino models lose about 15-20% of their signal due to the L2 cuts, slightly more than for the L1 filter. For the string stream the L2 selection is less severe than L1, but that is only moderately due to the better resolution of the LLH reconstruction. Once reconstructed, the bulk of the signal events do not have a lot of difficulty to survive an angular cut above 70 degrees. The main reason for the lower L1 signal efficiency is the inefficiency of the first guess methods to find a solution for small events. Many string triggered events are simply too difficult to reconstruct at all. That becomes more and more pronounced at lower energies, such that for the string dominated models the L2 selection efficiency is substantially larger than for L1.

Figure 6.11 and 6.12 on p.111-112 show the L1 and L2 exclusive efficiencies (right panel) and the efficiency relative to the trigger level (left panel) for the 5000 GeV hard and the 100 GeV soft signal models respectively. Also shown are experimental data and atmospheric muon MC. The atmospheric neutrino MC is scaled to the live-time of the data sample, to reflect its contribution to the experimental sample. Each row represents one of the trigger classes, and the results are scaled such that the total trigger set equals one at trigger level. A good agreement between muon MC and experiment can be observed. The total reduction of the experimental data set after the L1 and L2 filters amounts to  $3 \times 10^{-3}$ , while less than 30% of the background neutrinos are rejected. The high energy signal models retain 79% of their events, the lowest energy models are challenging with signal efficiencies around 30-40%.

## 6.5 Filter level 3

The level 1 and level 2 filters remove the events that are clearly reconstructed as downward-going, thereby rejecting 99.8% of the triggered data sample. The ten million experimental

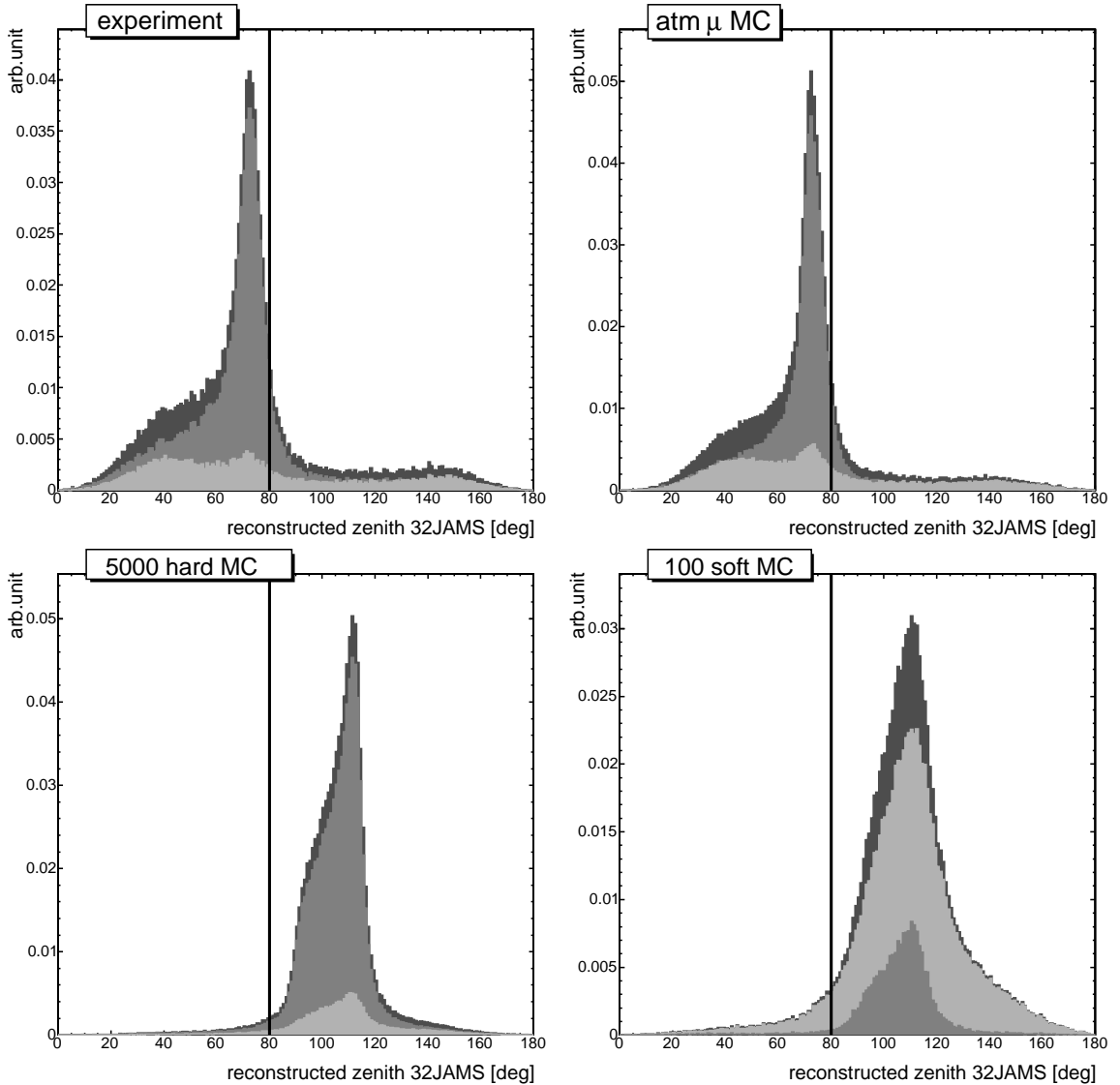


**Figure 6.4** – Distribution of the zenith angle as reconstructed by *32JAMS* after the L1 selection, retriggering and the cut on  $\theta_{JAMS}$ ; for experiment, atm.  $\mu$  MC and two simulated neutralino models. Each panel shows the distributions from *all* triggers (dark, normalized to one) and the relative contribution from the *standard* (medium grey) and *string* (light grey) streams. The vertical line indicates the L2 cut.

events at L2 remain dominated by atmospheric muons. If we would consider an angular cone around the Sun at this moment in the analysis, the neutralino signal would still drown in the atmospheric background. Since the L2 data sample consists mainly of events falsely reconstructed as upward-going, the sensitivity to the dark matter signal can be improved by selecting well reconstructed events. The following section describes how additional, more advanced event information is exploited to reach the background rejection (roughly  $10^{-7}$ ) desired for a search for neutrinos from the Sun. This level 3 filter (also *L3*) is specifically tailored for solar dark matter searches and concludes the event selection part of this work.

### 6.5.1 Introduction

As we noted earlier, searches for rare signals become very challenging when the background resembles the signal characteristics. With ten million background events reconstructed as upward-going we start to enter this phase. Considering additional useful event information during the classification process reduces the risk of losing signal events. One could think of a long list of event observables, many of which may help separate the signal from the background. Given the complexity of the problem, there is unfortunately no single approach that leads to *the optimal* set of observables. And along the same line, there is no method that provides *the optimal* set of selection criteria on the chosen observables.

The reconstructed direction is not the only information that we have at hand to classify an event as background-like or signal-like. Various event observables can be computed from the hit set and the reconstructed track. E.g. the location of the hits in the detector, or their distribution in time and space relative to the reconstructed track, or information from the LLH reconstruction methods. But how can we take advantage of that information?

For this analysis we adopt a straightforward method that iteratively adds selection criteria to the level 3 filter, until the optimal<sup>4</sup> sensitivity is reached. This is reasonable as long as the observables are not too correlated, see Fig. 6.5. The method starts off by comparing the signal and background distribution of many observables at filter level 2, from which their discriminative power is evaluated. If the most powerful observable survives various verification checks, we optimize the selection window. This selection criterion is then applied to all data samples, and the whole process is repeated.

Our iterative optimization procedure can in principle be continued until no background events remain. However, that is not a good idea. It is sensible and required to remove most if not all atmospheric muons, since they only constitute a background because the detector and the reconstruction methods are imperfect. The atmospheric neutrino events on the other hand are a truly physical background, which cannot be completely removed without rejecting the neutralino signal as well, even with a perfect instrument. The iterative procedure is stopped once the sensitivity of the dark matter search does not improve significantly. This decision can only be made when the following step in the analysis is performed, see Section 7.3.1. The details of the optimization procedure are explained in a following section.

Where does the signal and background distribution come from? The signal distribution is derived from simulated neutralino events. Unfortunately, the live-time of the simulated atmospheric muon sample is 30 times smaller than that of the experimental sample. If we use the atmospheric muon MC to model the background distribution the selection criteria will become vulnerable to large statistical fluctuations early on in the iteration process. Therefore, in cases where a feeble signal is expected, it is quite common in particle physics to use the experimental data itself to extract the background distribution. The simulated atmospheric muon and neutrino samples therefore only serve to verify whether the simulation describes the experimental data, which provides additional confidence in the signal simulation.

A further statistical bias of the analysis is prevented by basing the optimization of the L3 cuts on background and signal samples that are statistically completely independent

---

<sup>4</sup>Optimal, in the sense that the method does not provide a better classification with the given method. This does not mean that we claim that the actual optimum is found.

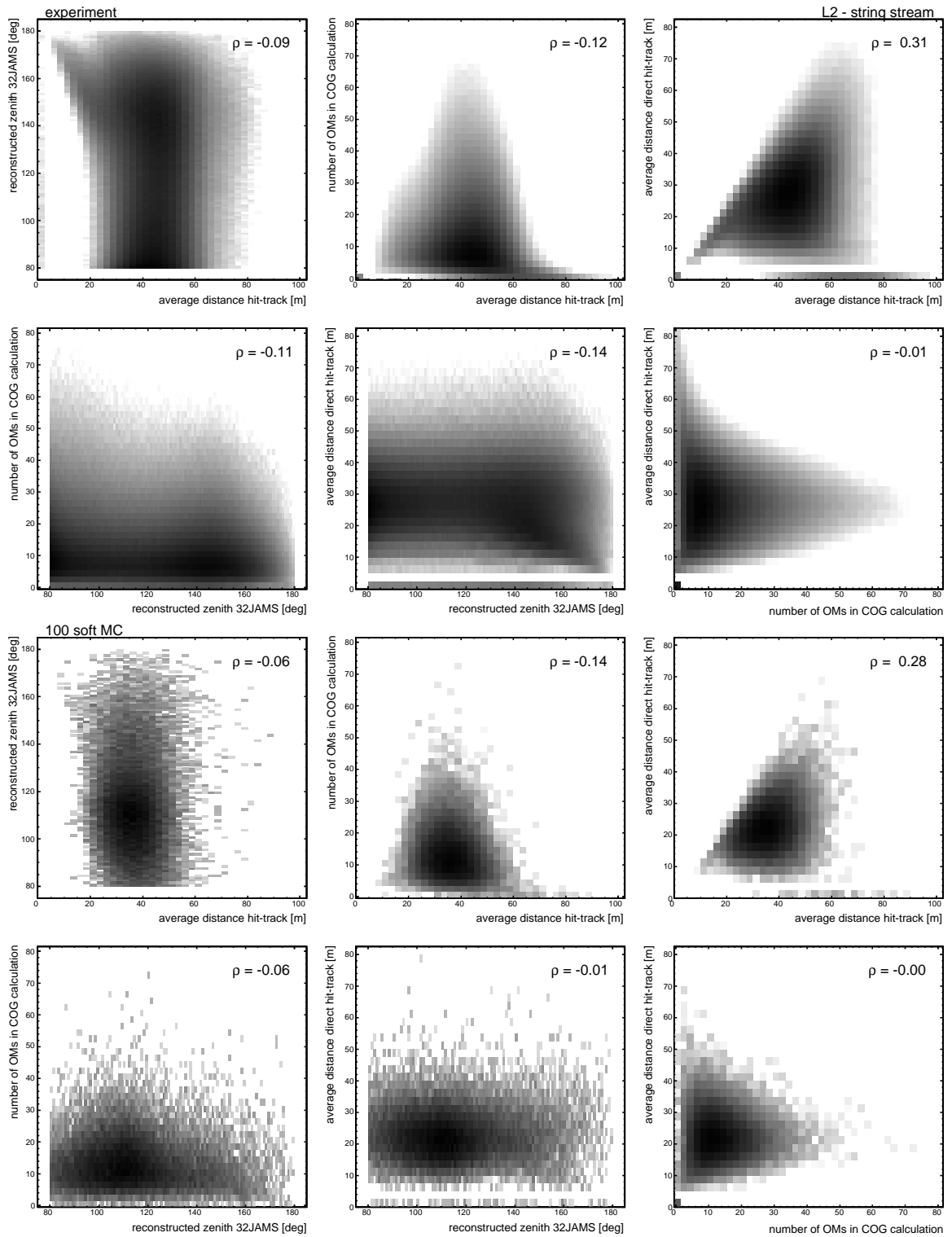


**Figure 6.5** – Correlations between the observables with the lowest signal efficiency of the LE string filter (defined in Table 6.8) for experimental data (top half) and the 100 GeV soft model (bottom half).

from the samples used to calculate the final results. The former and latter samples are respectively referred to as *train* and *test* samples.

The total simulated neutralino sample is split in two disjoint sets of events: 40% goes to the test sample, the remaining 60% to the train sample. For the experimental data sample a natural choice is made. When the Sun is above the horizon the events are directed to the train sample (80.3 days of live-time), otherwise they end up in the test sample (383.6 days). We will see that one of the first L3 cuts will be on the reconstructed zenith angle, rejecting solutions from above the horizon. That means that the experimental train sample will be extremely signal poor after this cut (since the Sun is in the other hemisphere) and hence very convenient for background studies. In Section 4.1.4 we showed that the difference in atmospheric conditions between both samples does not alter the event characteristics at L2, only the absolute rate. Therefore, the backgrounds present in the experimental train and test sample are identical.

We conclude the bias discussion by repeating that during the optimization we never know or take advantage of the actual position of the Sun. As such, we perform a so-called *blind* analysis. In this way we minimize the risk of biasing ourselves, even unconsciously, by tuning the selection criteria to statistical downward fluctuations in the background directly around the source, potentially leading to a false claim to discovery [169].

Actually, there is no good reason at all to focus only on the data sample in the angular region around the Sun. First of all, the background in such a cone is identical to the background found in a cone at a different azimuthal angle, but with the same angular size and at the same zenith angle. That is due to the almost isotropic nature of the primary cosmic ray flux at high energies and the cylindrical geometry of the AMANDA detector, which makes the event patterns essentially only zenith (and energy) dependent. With this in mind we could resort to extracting the background information from a cone centred around a fake position of the Sun, sufficiently different in azimuth. But the relatively small amount of statistics could then bias the event selection. For these reasons it is not necessary to know where the Sun is located, and this analysis remains blind to it until all selection criteria (and the shape analysis, described in the following chapter) have been set up. Only after the AMANDA collaboration approved the complete analysis, we were allowed to look at the actual position of the Sun and calculate our final results.

The detector response for horizontal muons will be very similar when their energy is roughly between  $\sim 50$  GeV and  $\sim 1$  TeV. When created right before the detector a horizontal muon above 50 GeV is able to traverse the whole detector, see Fig. 2.6 (right). Below  $\sim 1$  TeV the muon energy loss is dominated by ionisation processes which have a very weak energy dependence. Of course the quoted energy domain is not a very serious quantitative estimate, since it ignores that photons from outside the instrumented volume can be detected too and that few triggered events are produced right at the edge of the detector. Nonetheless, it can be seen as a qualitative argument for the conclusion that it does not make much sense to perform a dedicated optimization of the selection criteria for all fourteen signal models.

Two neutralino models are chosen as signal template. The high energy template (also *HE*) is given by a 5000 GeV neutralino annihilating to *W*-boson pairs (hard channel); the low energy template (also *LE*) by a 100 GeV particle annihilating to bottom quark pairs

(soft channel). We have optimized several other signal models as well, but concluded that with our optimization procedure the additional effort did not improve the sensitivity significantly. To simplify the analysis we decided to stick to these two signal templates for which a separate L3 filter is built.

When compared to the standard stream the string trigger stream contains much more low energy events, with quite different topologies and observable outcomes. This is independent of the origin of the event, signal or background. It suggests a second, natural break-up of the L3 filter. Therefore, the L3 event selection is optimized separately for the standard and the string event stream as well.

With such an approach we take full advantage of the specific signal and background characteristics of each trigger class. This is particularly useful in the case where the relative size of both trigger classes is different for signal and background. At L2 the relative size of both classes is comparable for the experimental data, while for the high (low) energy signal template the sample is dominated by the standard (string) stream. We will see that e.g.  $\rho_{COG}$ , the centre of gravity of hits in the horizontal plane, is a very powerful observable to separate signal from background in the string stream, but much less so for the standard stream. If we would not divide the total sample according to the trigger, the intrinsic power of the  $\rho_{COG}$  observable is lost. That will ultimately lead to a less sensitive dark matter search.

A second advantage is that we can simply merge the data samples of 2001, 2002 and 2003 and avoid non-uniformities induced by the string trigger downscaling (Section 4.1). E.g. the global multiplicity distributions for 2001 and 2002–2003 are rather different, while the three years are very similar for each trigger stream individually, see Fig. 4.4.

We summarize this introduction by repeating that the L3 filter will actually be composed of four L3 filters. A separate optimization of the event selection is done for both signal templates, and, given a signal template, for both trigger streams as well. Both HE filters will be applied to the following nine, high energy neutralino models: 5000 – 250 GeV hard and 5000 – 500 GeV soft channel. The LE filters will be applied to the remaining five models: 100 – 50 GeV hard and 250 – 50 GeV soft channel.

### 6.5.2 Precuts

Before optimizing the L3 filter we discard a small amount of background events of atmospheric and electronic origin. The first class is composed of non-multiplicity and non-string triggered events that slipped through a very small hole in the low level filters. The second background class contains non-particle events of unknown origin, which can be rejected by looking at odd features in their electronic fingerprint. The various types of odd behaviour are quantified by nine flare indicators, whose non-exponential tails identify the non-particle events [157]. Table 6.7 presents the year-dependent flare criteria that remove less than 0.5% of the experimental data and a completely negligible amount of simulated events.

### 6.5.3 Optimization procedure

Before entering into details of the iterative cut optimization procedure, we explain how the sensitivity of an analysis can be evaluated.

Flare indicator		2001	2002	2003
long_noise_1	<	3	5	5
long_missing_2	<	3.5	3	7
only_adc_3	<	18	20	3
nch_dead_4	<	4	9	4
short_H_5	<	4	4	6.5
short_M_6	<	3	5	3.5
missing_ch_7	<	6	3	3
induc_B10_8	<	5	4	5
induc_1119_9	<	3	3	9

**Table 6.7** – Year-dependent criteria that reject non-particle events, the indicators are described in [157].

### Definition of discriminative power

It is easy to understand that the goal of this work should be to develop the analysis with the best possible sensitivity to the dark matter signal. But what exactly does *sensitivity* mean? Several definitions are possible, depending on the judgement of the experimenter in the capability of his experiment. If the experimenter assumes that the instrument is capable of detecting the signal, he will prefer to perform an analysis with the highest probability to claim a discovery. If the experimenter on the other hand is convinced that the signal is too weak to be discovered, he will be more interested in setting the strongest possible constraints on the signal parameters. In the former example the sensitivity of an analysis refers to the potential to discover the signal, while in the latter case it is the potential to rule out signal parameter space. In practice the difference between these concepts fortunately only becomes relevant when the number of background events leaves the Gaussian regime. For large backgrounds, the sensitivity is equivalent to the statistical concept of significance.

In statistical theory the significance of an observation is usually defined by  $n_S/\sigma_B$ , with  $n_S$  the number of observed signal events and  $\sigma_B$  the uncertainty on the background count. For large number of events and neglecting systematic errors, we can approximate the distribution of  $n_B$  (the number of background events) by a Gaussian with an uncertainty or spread of  $\sigma_B \simeq \sqrt{n_B}$ . For this simple case, the significance  $n_S/\sqrt{n_B}$  of the observation can be translated in the probability to observe at least  $n_S + n_B$  events assuming a background-only scenario of  $n_B$  events.

Significance is not merely the result of an analysis, but a goal in itself as well. An experimenter will try to increase the significance of his measurement by reducing backgrounds, improving the resolution, reducing measurement errors, etc. Consider the simple example of deciding which one of two proposed cut windows  $x_{\min}^1 \leq x < x_{\max}^1$  or  $x_{\min}^2 \leq x < x_{\max}^2$  on an observable  $X$  is the better selection. Counting the amount of events in the first (second) window results in  $n_S^1$  ( $n_S^2$ ) for signal and  $n_B^1$  ( $n_B^2$ ) for background. Then the previous theory tells us that the window with the highest significance, either  $n_S^1/\sqrt{n_B^1}$  or  $n_S^2/\sqrt{n_B^2}$ , will produce the more sensitive measurement of the signal.

In practice, when searching for the best cut window on  $X$  we do not need to know the absolute level of the signal and background count. The window-dependent significance

$n_S(x_{\min}, x_{\max})/\sqrt{n_B(x_{\min}, x_{\max})}$  can be rewritten as  $\left(n_S^0/\sqrt{n_B^0}\right) \times \left(\epsilon_S(x_{\min}, x_{\max})/\sqrt{\epsilon_B(x_{\min}, x_{\max})}\right)$ , with  $n_{S \text{ or } B}^0$  the number of events before the selection and  $\epsilon_{S \text{ or } B}(x_{\min}, x_{\max})$  the fraction of events present in the cut window (also referred to as *cut efficiency*). Since  $n_S^0/\sqrt{n_B^0}$  is common to all possible cut windows, the only relevant information needed to find the optimal window is the signal and background efficiency. This is a very convenient fact for our purpose, because we do not know the absolute strength of the dark matter signal flux, unless we choose a point in the supersymmetric parameter space. However, we do not want and, as it turns out, do not need to do that.

So, the significance figure of merit simplifies to (from here on we drop the  $(x_{\min}, x_{\max})$  notation for the efficiencies)

$$\kappa_{S/\sqrt{B}}(x_{\min}, x_{\max}) \equiv \frac{\epsilon_S}{\sqrt{\epsilon_B}}, \quad (6.4)$$

and the optimal window  $[\hat{x}_{\min}, \hat{x}_{\max}]$  is defined to maximize previous function

$$\hat{\kappa}_{S/\sqrt{B}}(\hat{x}_{\min}, \hat{x}_{\max}) = \max_{x_{\min}, x_{\max}} \left\{ \kappa_{S/\sqrt{B}}(x_{\min}, x_{\max}) \right\}.$$

Figure 6.6 (right panels) illustrates a scan over various cut windows for the  $S/\sqrt{B}$  figure of merit (from now on *f.o.m.*), for four observables. The optimal window is marked by a cross.

After the first cut was optimized and applied to the signal and background samples, we could decide to use another observable. Of course, that only makes sense as long as the additional selection improves the sensitivity. How do we decide what observable to pick from a list of candidates? Again, we can follow the advice of the above *f.o.m.* and define the power  $\zeta$  of an observable  $X$  as the significance of its optimal cut window  $\zeta_X \equiv \hat{\kappa}_{S/\sqrt{B}}(\hat{x}_{\min}, \hat{x}_{\max})$ . The optimal observable  $\hat{X}$  is simply defined as the one having the highest power. Once this second selection is optimized and applied, the whole procedure can be repeated.

A typical outcome of iteratively optimizing for  $S/\sqrt{B}$  is that the background is reduced quite rapidly with a couple of hard cuts. This is the logical consequence of the  $1/\sqrt{\epsilon_B}$  factor in the significance which has an asymptotic behaviour for low backgrounds, sometimes even leading to fluctuation driven cuts. For instance, the significance *f.o.m.* will prefer an event selection resulting in  $10^{-5}$  background and 0.1 signal events over a situation with 1 background and 10 signal counts. In the former case the analysis is finished, while in the latter we could decide to add another cut which leads to an overall better sensitivity. The message here is that by using softer cuts on more observables a higher final significance can be achieved than an analysis with a few hard cuts with individually the best significance. Again, more information helps to disentangle signal from background.

Hence we do not want to cut too hard, but also not too soft. Since there is so much background, the latter approach would complicate the analysis. The following figure of merit

$$\kappa_{S(1-B)}(x_{\min}, x_{\max}) \equiv \epsilon_S \times (1 - \epsilon_B) \quad (6.5)$$

seems a good intuitive compromise between both scenarios, without dependence on the absolute signal level. It aims at a high signal efficiency and a low background efficiency. But

it avoids the asymptotic behaviour of the  $S/\sqrt{B}$  criterion when the number of background events becomes very small. Figure 6.6 (left panels) illustrates for four observables that this criterion (solid vertical line) indeed results in softer cuts than the significance f.o.m. (dashed vertical line).

After a large reduction of the background we leave the Gaussian regime, and the difference between discovery and limit setting becomes important. Based on statistical grounds the usual  $S/\sqrt{B}$  criterion should then be replaced by more suitable figures of merit.

It can easily be seen from Eq. 2.7 that, under the assumption of no signal, the upper limit on the signal flux that would be reported on average for repeated experiments is inversely proportional to the *Model Rejection Potential* [170]

$$\kappa_{MRP}(x_{\min}, x_{\max}) \equiv \frac{\epsilon_S}{\bar{\mu}_{90}(n_B)}. \quad (6.6)$$

Here,  $\bar{\mu}_{90}(n_B)$  is the average 90% CL upper limit (derived with the Feldman-Cousins unified approach [171]) for an ensemble of observations without signal events

$$\bar{\mu}_{90}(n_B) = \sum_{n_{\text{obs}}=0}^{\infty} p(n_{\text{obs}}|n_B) \mu_{90}(n_{\text{obs}}, n_B),$$

where  $p(n_{\text{obs}}|n_B) = \frac{(n_B)^{n_{\text{obs}}}}{n_{\text{obs}}!} \exp(-n_B)$  is the Poisson probability of occurrence of  $n_{\text{obs}}$  events in a background-only scenario with  $n_B$  expected events, and  $\mu_{90}(n_{\text{obs}}, n_B)$  is the 90% CL upper limit for such a realisation. By maximizing the MRP one aims for the most stringent upper limit on the signal flux.

To optimize for discovery, one can maximize the *Model Discovery Potential* as defined in [172]

$$\kappa_{MDP}(x_{\min}, x_{\max}) \equiv \frac{\epsilon_S}{\frac{a^2}{8} + \frac{9b^2}{13} + a\sqrt{n_B} + \frac{b}{2}\sqrt{b^2 + 4a\sqrt{n_B} + 4n_B}}. \quad (6.7)$$

The idea behind this f.o.m. is to minimize the strength of the signal flux needed for a  $5\sigma$  discovery ( $a = 5$ ) in e.g. 90% of the experiments ( $b = 1.28$ ). It is similar to another definition of the discovery potential [173], but has the advantage that it provides an analytical expression.

The denominator for the MRP and the MDP figure of merit have a square root like dependence for large number of background events. Therefore, in the Gaussian regime both are equivalent to the standard significance. For small backgrounds on the other hand they deviate from  $S/\sqrt{B}$ , but behave non-asymptotical and hence much better.

To conclude this discussion, we note that previous figures of merit only focus on the background reduction capabilities of the event selection. We have seen in Section 2.3.1 that the muon flux is calculated from what the detector actually measures, the number of signal-induced muons per unit volume and time,  $\Gamma_{\nu \rightarrow \mu} = \frac{\mu_s}{V_{\text{eff}} t_{\text{live}}}$ . The next chapter explains how we extract the number of signal-induced muons from the angular distances to the Sun of the events in the final sample. Two elements determine the outcome of such a calculation: the total number of background events and the angular resolution for signal events, defined in Section 7.1. The former is dealt with with previous figures of merit, the latter however is

only indirectly taken into account. In principle a *good* cut selects well reconstructed events, which will reduce misreconstructed background muons and increase the signal resolution. But that is not always the case, and the above defined figures of merit sometimes prefer a hard cut for background that at the same time degrades signal resolution. And since that leads to a worse sensitivity we should not blindly follow the above figures of merit and keep an eye on the signal resolution too.

### List of observables

An extended list with various observables is compiled for use in the iterative process. It can be broken up in following classes. This list is described in more detail in Section 5.3.

- Hit topology: number of hits, number of hit OMs, number of strings, centre of gravity of hits.
- Information from the reconstruction itself: reconstructed direction and reconstructed vertex position, (reduced) likelihood values, difference in reduced likelihood between downward-going and all-sky hypotheses, area of  $1\sigma$  error ellipse.
- Relation between the hits and the reconstruction: number of direct hits, number of strings with direct hits, projected length of direct hits on the track. Smoothness of hits along, average distance of hits to and fraction of (hit) channels in a cylinder around the track.

### Procedure

As mentioned before, the L3 filter is optimized separately for high and low energies, respectively with 5000 GeV hard and 100 GeV soft as the template signal model. Both filters are a double set of consecutive cuts. Double, since we differentiate between each trigger class. Cuts (for a given template signal model and trigger class) are iteratively optimized, preferring many soft cuts over a couple of hard cuts, which allows a better sensitivity by using more information.

#### Step 1: cut observable candidates

For every observable  $X_i$  in the list we perform a 2-dim scan over  $x_{\min,i}$  and  $x_{\max,i}$  to find the optimal window  $[\hat{x}_{\min,i}, \hat{x}_{\max,i}]$  with maximal  $\hat{\kappa}_i$ . Only the observables with highest optimal  $\hat{\kappa}_i$  are promoted to the list of cut observable candidates, for which the optimization procedure continues.

This is done for two figures of merit,  $\kappa_{S/\sqrt{B}}$  and  $\kappa_{S(1-B)}$ . These could in principle result in a different list of cut observable candidates, but it turns out that this list is not very sensitive to the choice of f.o.m..

We only use the train sample for this step.

#### Step 2: observable verification

The next step is to perform three checks for each observable candidate in order to minimize any risk of bias.

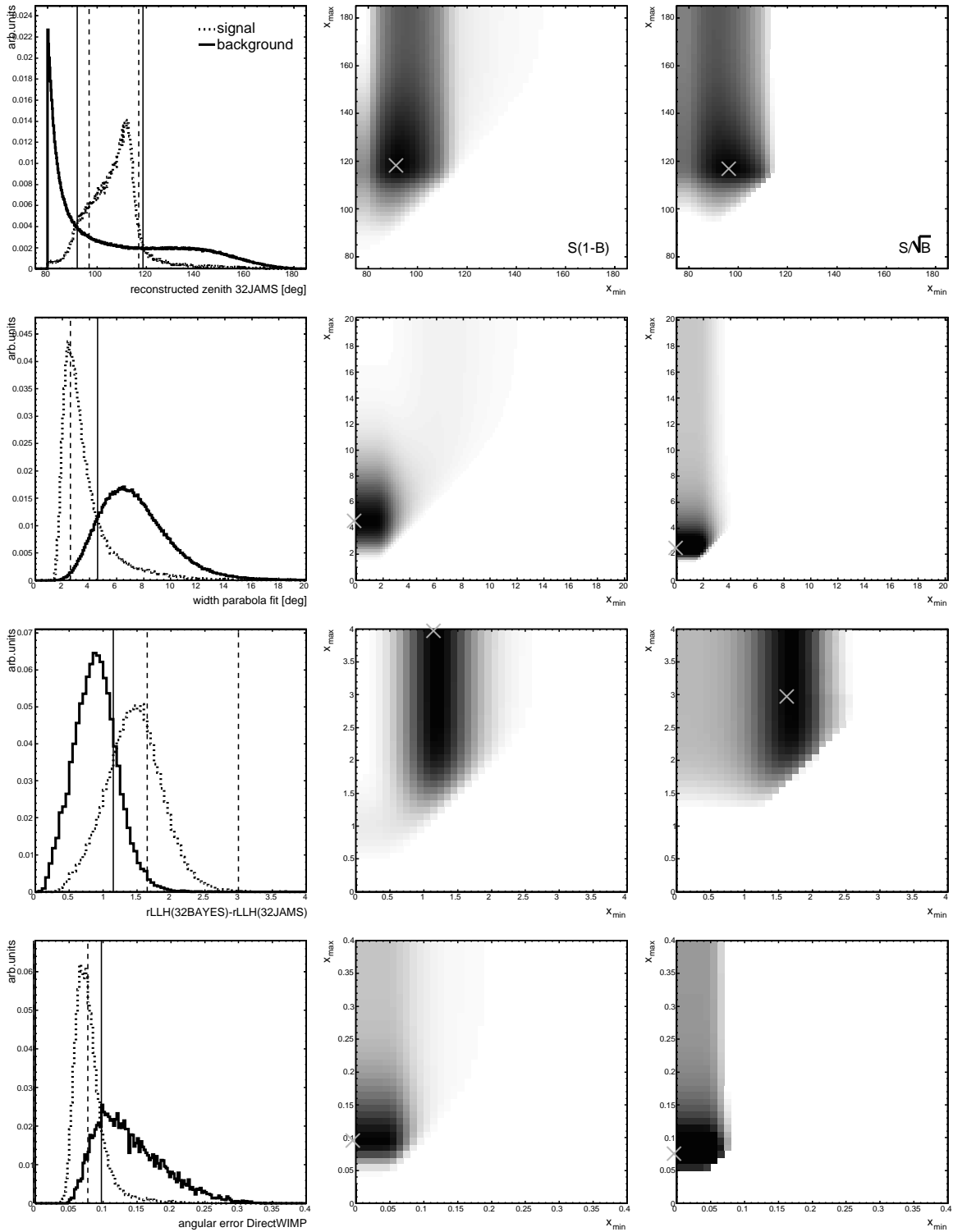


**Figure 6.6** – Illustration of the iterative cut optimization, for the first four cuts in the HE standard L3 filter. Each row shows one observable in the filter. Left panel: normalized signal (5000 GeV, hard channel) and background distribution. Figure of merit (colour, darker is higher) as a function of  $x_{\min}$  (X-axis) and  $x_{\max}$  (Y-axis) for  $S(1 - B)$  (middle) and  $S/\sqrt{B}$  (right). In the left panel the vertical lines indicate the optimal window found by  $S(1 - B)$  (solid) and  $S/\sqrt{B}$  (dashed), while these are marked by a cross in the other panels.

- We make sure the observable is well described by the simulation by comparing the 2001–2003 (test sample) distributions for simulated and experimental events.
- We verify that the distributions of the train and test sample are the same, especially for the background (experimental data taken during different seasons).
- We check that the distributions for each individual year are similar for the simulated and experimental events in the test sample.

### Step 3: optimize cut window

In the third step we select the observable candidate  $\hat{X}$  that satisfies all verification checks and that gives the highest  $\hat{\kappa}$ .

At the very beginning of the optimization process there is so much background that the *MRP* and *MDP* figures of merit are equivalent to  $S/\sqrt{B}$ , and therefore ignored. With the *many soft cuts* strategy in mind, we always pick the larger window of the one suggested by  $S/\sqrt{B}$  and  $S(1 - B)$ , see Fig. 6.6. Typically, the latter f.o.m. produces softer cuts, but the roles change slowly when more atmospheric muons are removed.

For the final two, three cuts a slightly different approach is taken. These final cuts are optimized to obtain roughly 90% signal efficiency, for two reasons. Firstly, it avoids fluctuation-driven cuts due to the by now very small background train sample. Secondly, it allows us to perform the shape analysis without large steps in its outcome.

Adding gradually more cuts, with background events becoming very signal-like, it becomes increasingly important to keep an eye on the signal resolution too. If the resolution is degraded, we pick another cut window or even observable.

We only use the train sample for this step.

### Stop (?): calculate muon flux sensitivity

We evaluate the muon flux sensitivity, but only when not more than 2000 events remain in the experimental test sample. Until that point is reached, the muon background is so prominent that we are confident that the sensitivity of the L3 filter can be further improved. So it does not make much sense to invest time in the CPU-intensive task of performing the shape analysis, presented in the next chapter.

With less than 2000 events remaining, we perform the shape analysis, which returns the median upper limit  $\bar{\mu}$  on the number of signal events, in the absence of signal (Section 7.3.1). Together with effective volume and experimental live-time this is then translated (Section 2.3.1) to the median upper limit on the muon flux, also referred to as *muon flux sensitivity*. The iterative procedure is stopped once we observe that the muon flux sensitivity of the L3 filter can not be further improved.

We conclude with a short remark. The shape analysis is only evaluated using the events from the inspected L3 filter, the standard and string streams remain separated, more details in Section 7.3.1. In Section 7.3.2 we will see that the final muon flux measurement for one particular signal model is the result of a shape analysis combining both trigger streams. It is not necessary to do this combination right now, since the most sensitive combined result will automatically occur when the trigger-specific L3 filters are tuned for maximum sensitivity.

	high energy (HE)		
	standard	string	
c1	$92 \leq \theta_{32JAMS} < 119$	$90 \leq \theta_{32JAMS} < 121$	c1
c2	$\sigma_{32PARA} < 4.6$	$0 < \rho_{COG} < 81$	c2
c3	$1.15 \leq \Delta rLLH < 4.0$	$\sigma_{32PARA} < 5.8$	c3
c4	$\sigma_{\psi}^{WIMP} < 0.0975$	$\sigma_{\psi}^{WIMP} < 0.1375$	c4
c5	$153 \leq N_{OM}^{100}$	$0.968125 \leq Q_{JAMS}$	c5
c6	$0 < \langle \rho_{meas} \rangle / \langle \rho_{exp} \rangle < 1.05$	$\sigma_{32PARA} < 3.8$	c6
c7	$\langle \rho \rangle < 46$	$ S_{phit}  < 0.35$	c7
c8	$13 \leq \sigma_{ZCOG}$	$0 < \langle \rho_{meas} \rangle / \langle \rho_{exp} \rangle < 1.05$	c8
		$121 \leq N_{OM}^{100}$	c9
	low energy (LE)		
	standard	string	
c1	$1.2 \leq \Delta rLLH < 4.0$	$0 < \rho_{COG} < 80$	c1
c2	$9.5 \leq N_{exp} < 16.5$	$\langle \rho \rangle < 40$	c2
c3	$92 \leq \theta_{32JAMS} < 118$	$95 \leq \theta_{32JAMS} < 127$	c3
c4	$ S_{phit}  < 0.365$	$-85 \leq Z_{COG} < 140$	c4
c5	$0.97 \leq Q_{JAMS}$	$0 < \Delta \rho_{COG}^* < 9.0$	c5
c6	$1.45 \leq \Delta rLLH$	$12 \leq N_{OM}^{COG}$	c6
c7	$N_{hit}^{100} / N_{OM}^{100} < 0.13$	$\langle \rho_{dir} \rangle < 23.5$	c7
c8	$\sigma_{\psi}^{WIMP} < 0.1275$	$\sigma_{32PARA} < 10.8$	c8
c9	$\sigma_{32PARA} < 5.0$	$\sigma_{dE/dx} < 0.55$	c9
c10	$L_{dir} < 190$	$\sigma_S < 0.29$	c10
		$65 \leq \sigma_{LECOG}$	c11
		$\sigma_{\rho}^{JAMS} < 5.0$	c12

**Table 6.8** – Overview of the cuts in the four L3 filters: high/low energy signal template (top/bottom), and standard/string trigger class (left/right).

Part of the iterative procedure is illustrated in Fig. 6.6, for the first four cuts in the *HE standard* filter. The first row shows how the first cut window is found. After step 1 and 2, the reconstructed zenith angle from *32JAMS* turned out to be the most powerful observable. The signal and background distributions are given in the left panel. We then evaluate the  $S(1 - B)$  (middle panel) and  $S/\sqrt{B}$  (right) figures of merit (grey scale) for each possible cut window  $[x_{min}, x_{max}]$ . The optimal cut window found by both criteria are indicated by a marker (middle, right) and vertical lines in the left panel. The  $S(1 - B)$  f.o.m. (solid lines) indeed finds a softer cut compared to  $S/\sqrt{B}$  (dashed lines). This first selection is then applied to all data and the optimization process repeated. The following rows show the results of the next three cuts in the filter.

### 6.5.4 Results

The first four cuts in the *HE standard* filter were already motivated by Fig. 6.6. In a similar fashion the remaining cuts for the *HE standard*, *HE string*, *LE standard* and *LE string* L3

Type	Observable	Description
Topology	$N_{OM}^{COG}$	Number of OMs in COG calculation
	$\rho_{COG}$	Radial position centre of gravity
	$Z_{COG}$	Depth centre of gravity
	$\sigma_{Z_{COG}}$	Spread in depth COG
	$\sigma_{LE_{COG}}$	Spread in LE time COG
Reconstruction	$\theta_{32JAMS}$	Zenith 32x LLH Pandel
	$\sigma_{32PARA}$	$1\sigma$ width parabola fit
	$\Delta r_{LLH}$	Difference in reduced $\log \mathcal{L}$ (32BAYES-32JAMS)
	$\sigma_{\psi}^{WIMP}$	Estimated angular error DirectWIMP
	$Q_{JAMS}$	Internal quality parameter JAMS
Hit-reconstruction (longitudinal)	$ \mathcal{S}_{hit} $	Absolute value $P_{hit}$ smoothness
	$\sigma_S$	Spread in vanilla smoothness
	$L_{dir}$	Projected length of direct hits
(transverse)	$N_{OM}^{100}$	Number of active OMs within 100 m from track
	$N_{hit}^{100} / N_{OM}^{100}$	Fraction of active OMs within 100 m from track that are hit
	$\sigma_{\rho}^{JAMS}$	Spread in distance from hit to JAMS
	$\langle \rho \rangle$	Average distance from hit to track
	$\langle \rho_{dir} \rangle$	Average distance of direct hits to track
(hit-nohit probability)	$\sigma_{dE/dx}$	Spread in $dE/dx$
	$N_{exp}$	Expected number of hits
	$\langle \rho_{meas} \rangle / \langle \rho_{exp} \rangle$	Ratio of measured and expected (based on $P_{hit}/P_{nohit}$ ) average distance hit-track
	$\Delta \rho_{COG}^*$	Distance between measured and expected (based on $P_{hit}/P_{nohit}$ ) COG, in plane perpendicular to track

**Table 6.9** – Description of the observables in the various L3 filters ( $32JAMS$  is the default reference track). More information can be found in Section 5.3.

filters are found. Table 6.8 presents the outcome of the iterative procedure for all filters. A short description of the cut observables can be found in Table 6.9.

Figures 6.7-6.10 illustrate the distribution of each cut observable in the four L3 filters, at the level right before the cut on the inspected observable is optimized. As a result of our verification procedure, the atmospheric muon MC (thin solid line) resembles the experimental data (shaded region). Atmospheric (dashed) and dark matter (dotted) induced neutrinos are in mutual agreement too, except for the difference in reconstructed direction.

The high energy filters (with 5000 GeV hard as template) are applied to the following nine models: 5000 – 250 GeV hard and 5000 – 500 GeV soft. Performing the shape analysis for various cut levels it turns out that the best sensitivity for all these models is obtained after respectively eight and nine cuts on the standard and string streams. The details can be found in Section 7.3.1. The final experimental event sample is identical for all these models (but the effective volumes differ). The low energy filters (with 100 GeV soft as template) are applied to the remaining five models: 100 – 50 GeV hard and 250 – 50 GeV

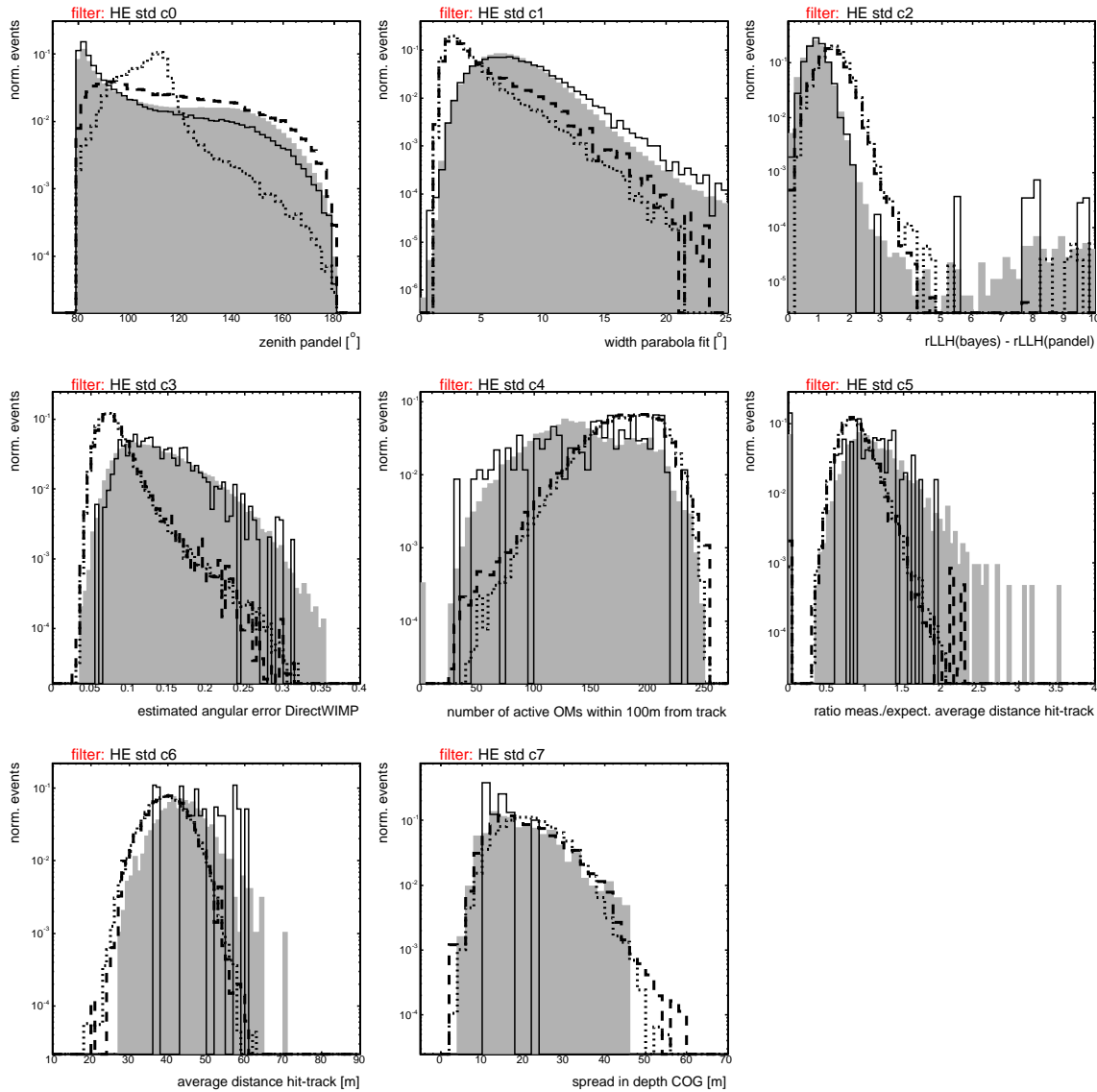


**Figure 6.7** – Normalized distributions for all observables  $X$  from the *high energy standard* filter, at the level prior to the cut on  $X$ . The filled area represents experimental data, simulated samples are indicated by lines: atm.  $\mu$  (solid), atm.  $\nu$  (dashed) and 5000 GeV hard neutralino (dotted).

soft. After ten and twelve cuts on the standard and string triggers the best sensitivity is reached, except for 100 GeV hard and 250 GeV soft for which the final  $L_{dir}$  cut is dropped from the standard stream filter. That means that there are two final experimental event samples for these models, but they differ by only one cut.

Table 6.10 summarizes the selection efficiency of L3 with respect to L2 for all fourteen neutralino models. For most signal models (bottom right quadrant) about 20% of the L2 events are retained, while the muon background (top half) is reduced by more than four orders of magnitude. The improvement in sensitivity with respect to L2 is between a factor 7 for the lowest energy model, and 28 for the highest energy model.

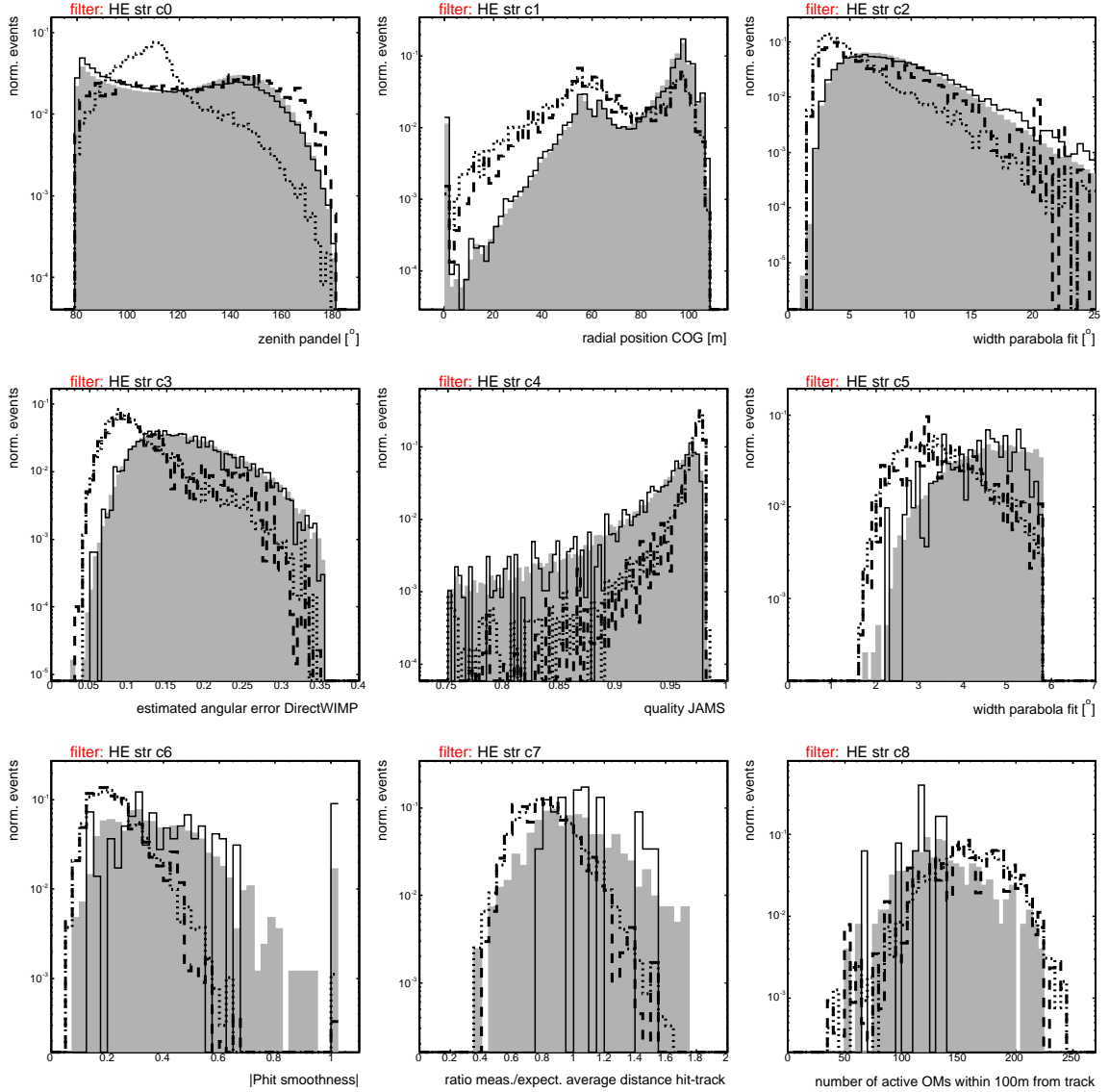


**Figure 6.8** – Normalized distributions for all observables  $X$  from the *high energy string* filter, at the level prior to the cut on  $X$ . The filled area represents experimental data, simulated samples are indicated by lines: atm.  $\mu$  (solid), atm.  $\nu$  (dashed) and 5000 GeV hard neutralino (dotted).

The evolution of the selection efficiency with cut level is shown in Fig. 6.11 (6.12) for the HE (LE) filter and the various trigger streams (rows). Cut levels 0, 1 and 2 represent trigger level, L1 and L2; the remaining cuts are those from the L3 filters<sup>5</sup>. The trigger lines are normalized to the full trigger set, such that the sum of the standard (2nd row) and string (3rd row) stream equals the total trigger set (1st row). The left panels shows the efficiency relative to the trigger level, with the atmospheric neutrino background normalized to the experimental live-time. In this way the lines of the experimental data and background simulation are proportional to the actual number of events. The signal is normalized to

<sup>5</sup>E.g. cut level 8 corresponds to the sixth L3 cut, as listed in Table 6.8.

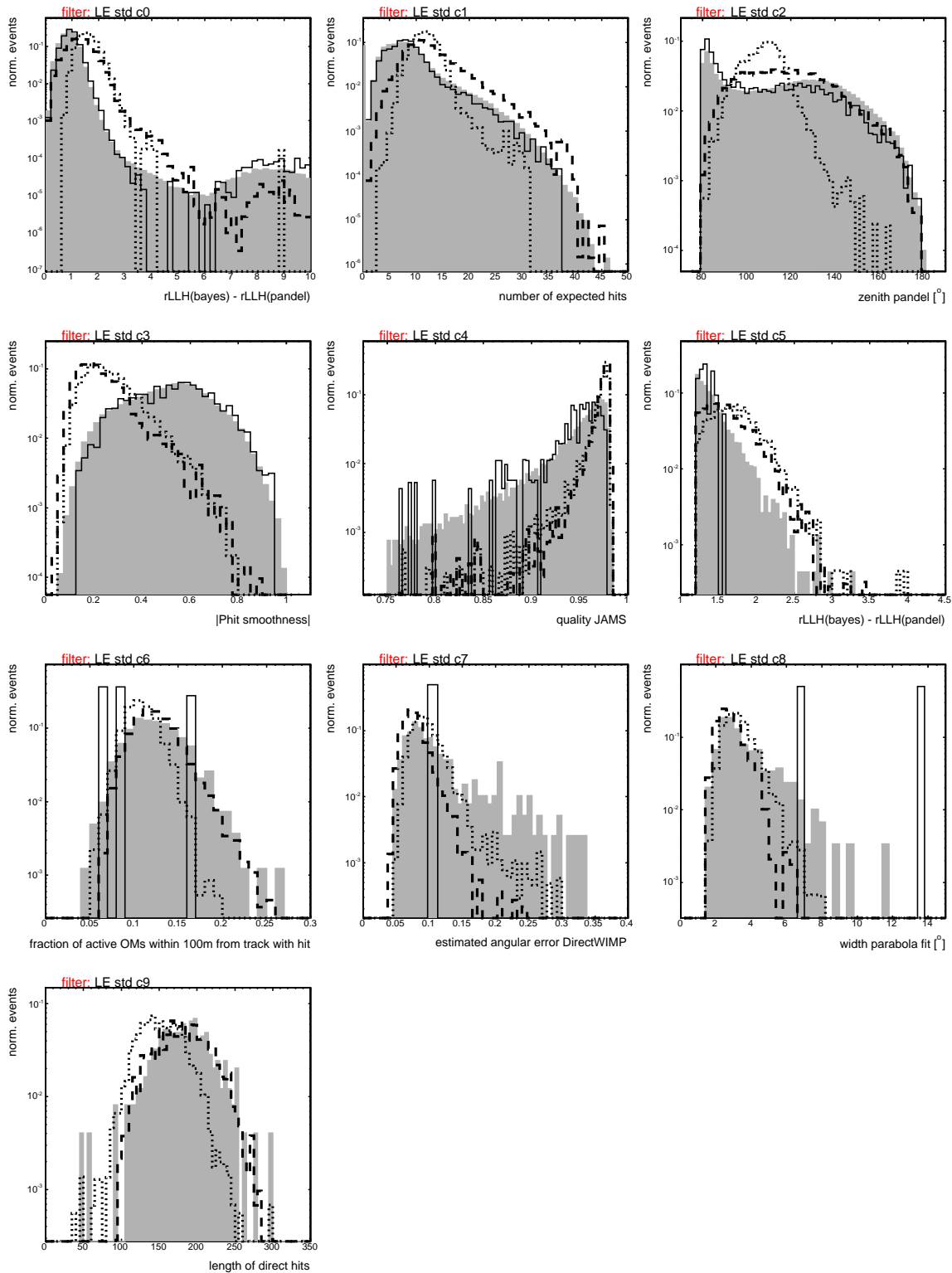


**Figure 6.9** – Normalized distributions for all observables  $X$  from the *low energy standard* filter, at the level prior to the cut on  $X$ . The filled area represents experimental data, simulated samples are indicated by lines: atm.  $\mu$  (solid), atm.  $\nu$  (dashed) and 100 GeV soft neutralino (dotted).

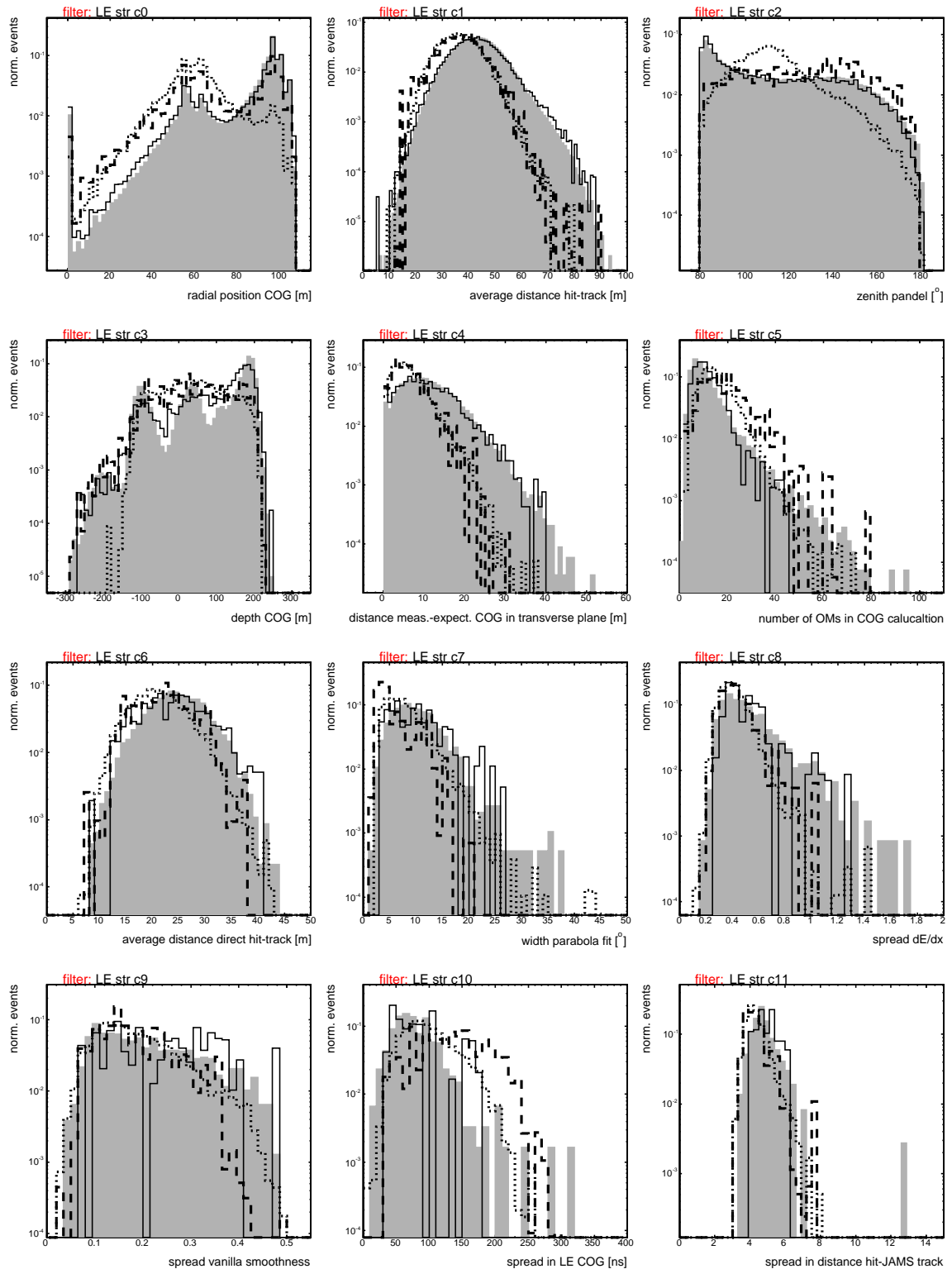


**Figure 6.10** – Normalized distributions for all observables  $X$  from the *low energy string* filter, at the level prior to the cut on  $X$ . The filled area represents experimental data, simulated samples are indicated by lines: atm.  $\mu$  (solid), atm.  $\nu$  (dashed) and 100 GeV soft neutralino (dotted).

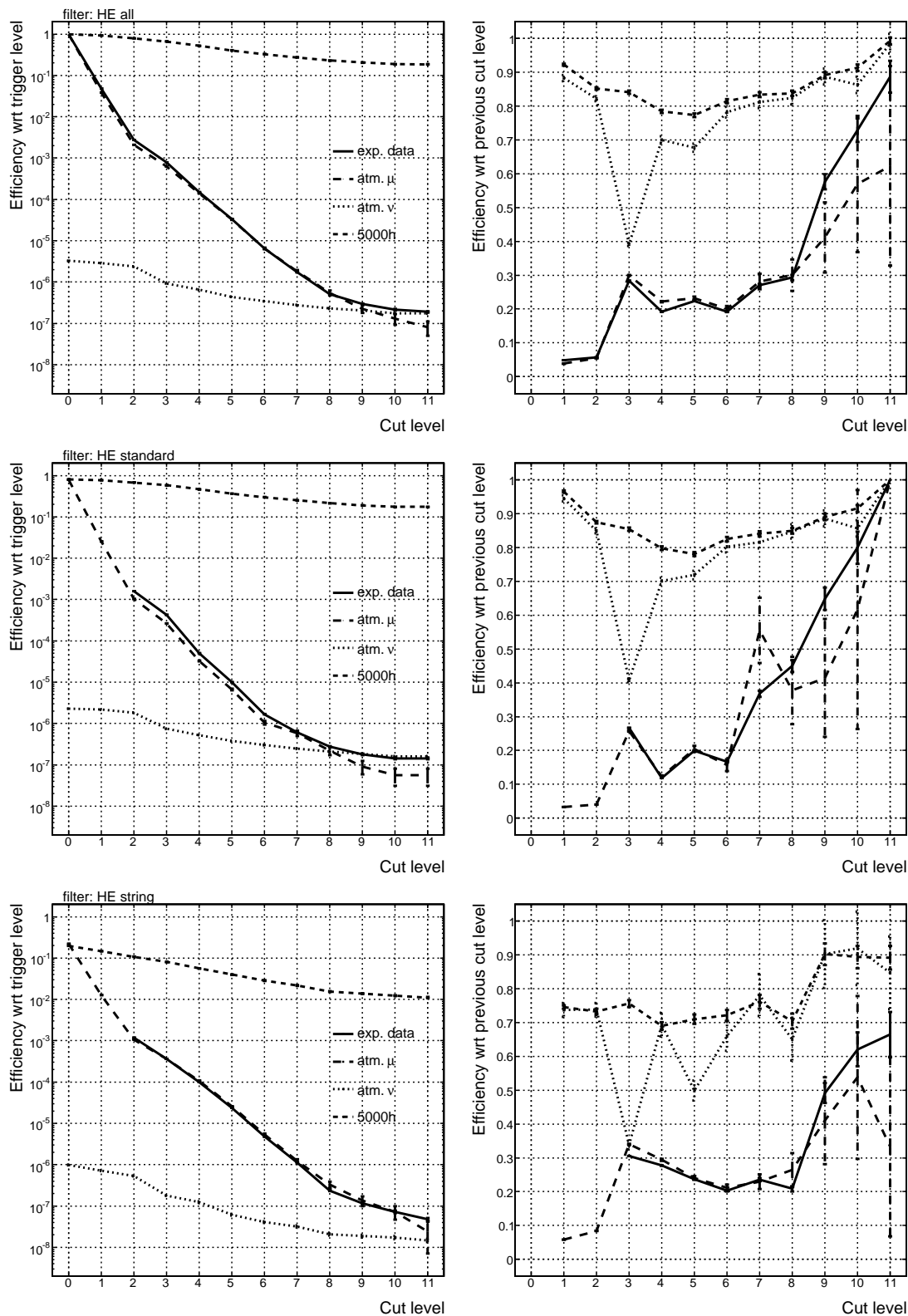


**Figure 6.11** – For the analysis of the 5000 GeV hard neutralino model: evolution of selection efficiencies with respect to trigger level (left column) and the previous cut level (right column), broken up for the various trigger classes (top: all; middle: std; bottom: str). The high level filter represents cut levels 3-11, statistical errors are shown.

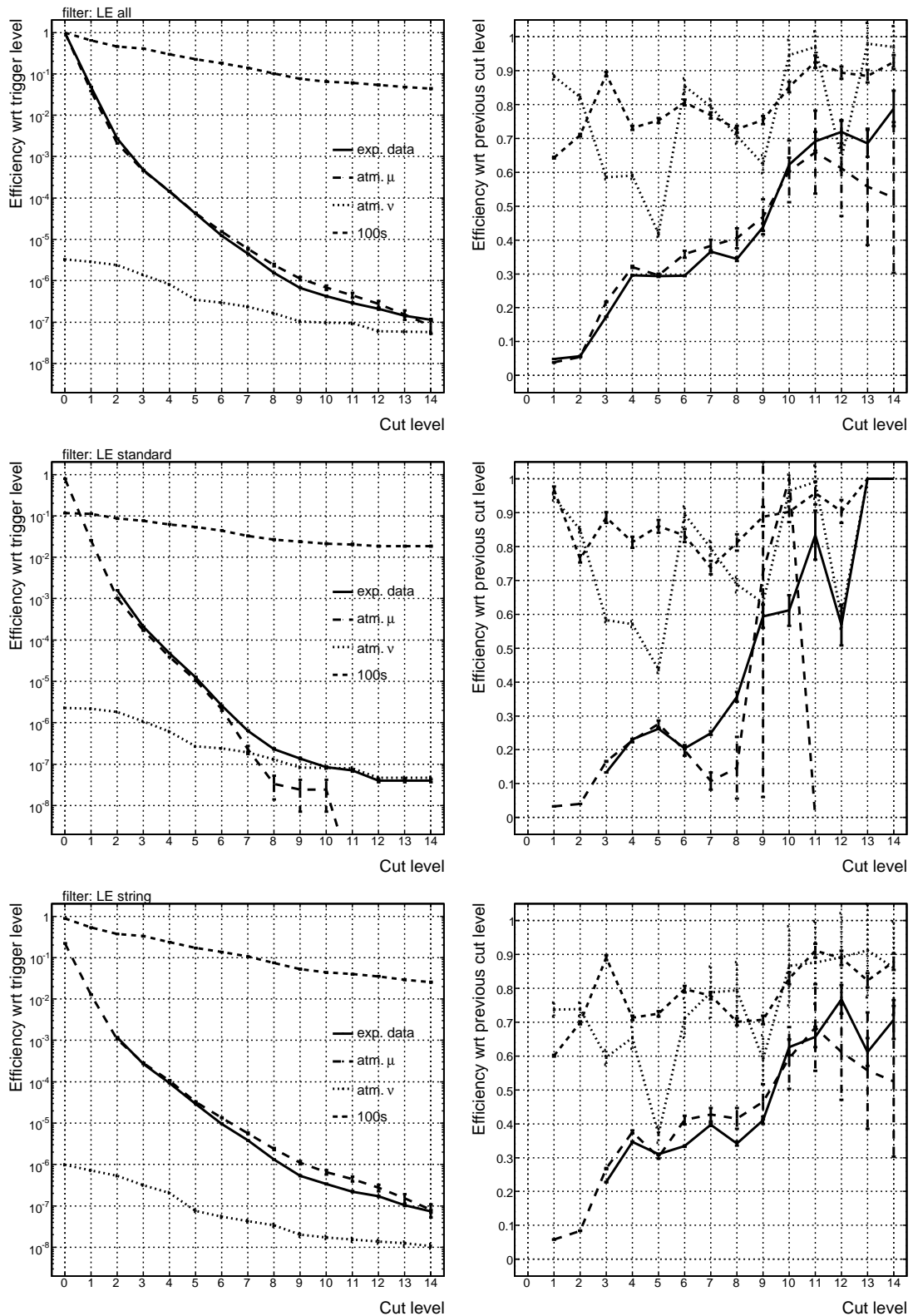


**Figure 6.12** – For the analysis of the 100 GeV soft neutralino model: evolution of selection efficiencies with respect to trigger level (left column) and the previous cut level (right column), broken up for the various trigger classes (top: all; middle: std; bottom: str). The high level filter represents cut levels 3-14, statistical errors are shown.

one at trigger level, and reflects the loss of effective volume. Only the efficiency of the signal templates is shown, but the evolution for the twelve other signal models follows the same trend. The right panel gives the efficiency of each individual cut with respect to the previous cut level, making the evaluation of how hard a cut is easier. Vertical bars represent statistical errors.

From these figures it is obvious that only a cut on the reconstructed zenith window is able to reject a lot of atmospheric neutrinos. For most other cuts the efficiency of both sources (dark matter and atmospheric background) of upward-going neutrinos are very similar, as expected. At the beginning, the downward-going muon background is rejected quite efficiently with the quality cuts, at each step removing more than 70% of the muons and less than 20% of the signal. Towards the end of the analysis the background becomes gradually more signal-like, and the background rejection power weakens. For the final few cuts we request a  $\sim 90\%$  signal efficiency, as can be seen.

The good agreement between experimental data and atmospheric muon MC for each cut observable in Fig. 6.10 is reflected as well in the good mutual agreement for the efficiency evolution. That is due to the verification procedure, and it increases the confidence in the simulation set-up. As told before, that is vital since the signal efficiency is used for our final measurement and this can only be extracted from simulation.

It does not come as a surprise that the separation between signal and background is much more difficult for string triggered events, even with the quality observables. Signal (background) selection efficiencies are lower (higher) than for the standard stream. It even turns out that the downward-going muon background should not be removed completely from the string stream to reach the optimal sensitivity, since the neutrino background level is so low and since the muon background is too signal-like (see Fig. 6.7-6.10). For the standard stream however it does prove useful to remove most muons, see Fig. 6.11 and 6.12. The optimal sensitivity for the standard stream is reached once the experimental data become dominated by atmospheric neutrinos, see Section 7.3.1.

## 6.6 Final sample

After imposing the L1, L2 and L3 event selections the final event sample emerges, within which the search for a signal continues. In the previous section we assigned L3 cuts to each of the fourteen signal models, and we have seen that three final event samples (*A*, *B* and *C*) are extracted. This section discusses the characteristics of the final samples for experiment and background and signal simulation.

Table 6.11 specifies the L3 filter that defines the final sample for each neutralino model. For both trigger streams the number of events observed and expected are shown in the second part of the table. A couple of hundred events remain at the final selection level for all three data taking years. We went from an observed event rate of roughly one hundred per second at trigger level to one or two per day after all cuts, corresponding to a data reduction of  $1-2 \times 10^{-7}$ . The observed number of events is in reasonable agreement with the background expectation from simulation. That indicates that the number of signal events is not extremely high, if present at all.

The generated atmospheric muon sample is too small and the background reduction too high to obtain a precise estimate of the downward-going muon content in the final sample.

L3 passing wrt L2	filter	exp. data ( $\times 10^{-5}$ )			atm. $\mu$ ( $\times 10^{-5}$ )		
		all	standard	string	all	standard	string
5000 hard	HE c8c9	6.915	9.049	4.063	3.833	5.456	2.271
3000 hard	HE c8c9	"	"	"	"	"	"
1000 hard	HE c8c9	"	"	"	"	"	"
500 hard	HE c8c9	"	"	"	"	"	"
250 hard	HE c8c9	"	"	"	"	"	"
100 hard	LE c9c12	5.197	4.426	6.227	3.833	0.000	7.525
50 hard	LE c10c12	4.106	2.519	"	"	"	"
5000 soft	HE c8c9	6.915	9.049	4.063	3.833	5.456	2.271
3000 soft	HE c8c9	"	"	"	"	"	"
1000 soft	HE c8c9	"	"	"	"	"	"
500 soft	HE c8c9	"	"	"	"	"	"
250 soft	LE c9c12	5.197	4.426	6.227	3.833	0.000	7.525
100 soft	LE c10c12	4.106	2.519	"	"	"	"
50 soft	LE c10c12	"	"	"	"	"	"
L3 passing wrt L2	filter	atm. $\nu$ ( $\times 10^{-2}$ )			neutralino $\chi$		
		all	standard	string	all	standard	string
5000 hard	HE c8c9	7.331	8.654	2.763	0.235	0.256	0.103
3000 hard	HE c8c9	"	"	"	0.234	0.254	0.103
1000 hard	HE c8c9	"	"	"	0.234	0.254	0.103
500 hard	HE c8c9	"	"	"	0.234	0.259	0.096
250 hard	HE c8c9	"	"	"	0.228	0.264	0.086
100 hard	LE c9c12	3.798	4.317	2.005	0.154	0.231	0.073
50 hard	LE c10c12	2.435	2.559	"	0.073	0.190	0.063
5000 soft	HE c8c9	7.331	8.654	2.763	0.223	0.262	0.083
3000 soft	HE c8c9	"	"	"	0.223	0.262	0.079
1000 soft	HE c8c9	"	"	"	0.219	0.262	0.076
500 soft	HE c8c9	"	"	"	0.212	0.271	0.068
250 soft	LE c9c12	3.798	4.317	2.005	0.145	0.204	0.067
100 soft	LE c10c12	2.435	2.559	"	0.097	0.215	0.069
50 soft	LE c10c12	"	"	"	0.045	0.043	0.045

**Table 6.10** – Exclusive L3 selection efficiencies with respect to L2, broken up the for different trigger classes. The second column indicates the set of L3 cuts applied for each neutralino model (first columns). (Top left) experimental data, (top right) simulated atmospheric muons, (bottom left) simulated atmospheric neutrinos, (bottom right) simulated neutralino signal. Mind the different scales!

	neutralino model	L3 filter	exp	atm. $\mu + \nu$	atm. $\mu$	atm $\nu$
A	$\geq 250$ hard, $\geq 500$ soft	HE std c8	502	$702.2 \pm 65.6$	$143.5 \pm 64.5$	$558.7 \pm 11.8$
		HE str c9	168	$113.7 \pm 44.2$	$62.0 \pm 43.9$	$51.7 \pm 4.8$
B	100 hard, 250 soft	LE std c9	246	$278.7 \pm 9.8$	–	$278.7 \pm 9.8$
		LE str c12	258	$243.0 \pm 70.6$	$205.5 \pm 70.5$	$37.5 \pm 4.4$
C	50 hard, $\leq 100$ soft	LE std c10	140	$165.2 \pm 7.9$	–	$165.2 \pm 7.9$
		LE str c12	258	$243.0 \pm 70.6$	$205.5 \pm 70.5$	$37.5 \pm 4.4$

**Table 6.11** – Number of events (with statistical error) in each of the three final samples for experimental data and simulated background, broken up for both trigger classes. The second column connects each signal model to its corresponding sample.

	[m <sup>3</sup> ]	5000	3000	1000	500	250	100	50
$V_{L3}^{\text{all}}$	hard	$3.04 \times 10^6$	$3.42 \times 10^6$	$3.37 \times 10^6$	$2.33 \times 10^6$	$1.16 \times 10^6$	$1.17 \times 10^5$	$7.15 \times 10^3$
	soft	$8.85 \times 10^5$	$7.88 \times 10^5$	$6.12 \times 10^5$	$3.50 \times 10^5$	$1.01 \times 10^5$	$1.28 \times 10^4$	$1.65 \times 10^3$
$V_{L3}^{\text{std}}$	hard	$2.86 \times 10^6$	$3.22 \times 10^6$	$3.17 \times 10^6$	$2.18 \times 10^6$	$1.08 \times 10^6$	$8.96 \times 10^4$	$1.50 \times 10^3$
	soft	$8.15 \times 10^5$	$7.29 \times 10^5$	$5.63 \times 10^5$	$3.18 \times 10^5$	$8.12 \times 10^4$	$5.38 \times 10^3$	$1.78 \times 10^1$
$V_{L3}^{\text{str}}$	hard	$1.82 \times 10^5$	$1.97 \times 10^5$	$2.00 \times 10^5$	$1.48 \times 10^5$	$8.68 \times 10^4$	$2.72 \times 10^4$	$5.65 \times 10^3$
	soft	$7.05 \times 10^4$	$5.90 \times 10^4$	$4.90 \times 10^4$	$3.27 \times 10^4$	$2.01 \times 10^4$	$7.44 \times 10^3$	$1.64 \times 10^3$

**Table 6.12** – Neutralino effective volume at filter level 3, for the different trigger classes.

Nevertheless, one can conclude from Fig. 6.11-6.12 and Table 6.11 that for all three samples the standard (string) stream is dominated by atmospheric neutrinos (muons). Except for the string stream in sample A, with a similar contribution from muons and neutrinos.

These findings are supported by Fig. 6.13 too. It shows how the distribution of experimental data and background simulation evolves with L3 cut level, for both signal templates (HE and LE) and trigger classes (standard and string). For each filter an observable was chosen for which the muon and neutrino background are well separated at L2 (left column). While the agreement between experiment and atmospheric neutrino simulation is apparent after the L3 cuts (right column) for the standard stream (row 1 and 3), that is not the case for the string stream (row 2 and 4). The central column illustrates the situation halfway the L3 cuts.

The reconstructed direction of the events in sample A and B are shown in Figure 6.14 for each year and trigger separately. Apart from some structure in azimuth (especially for the string event stream), due to the geometry of the detector, the distribution of the observed events seems isotropic. Again, since solar neutralinos peak<sup>6</sup> around  $\theta = 113^\circ$ , this indicates that the signal is very weak.

In the next chapter, a statistical method will be developed that measures the number of signal events within the experimental data set. To translate this measurement to a muon flux, we also need the effective volume after all event selections.

The effective volume for neutralinos after the L3 filter<sup>7</sup> is presented in Fig. 6.15 and Table 6.12. The statistical error on the effective volume is below 1% for most models, and

<sup>6</sup>Fig. 4.1 shows that most of the data are taken when the Sun is positioned at  $\theta_\odot \simeq 113^\circ$ .

<sup>7</sup>Of course, this can also be calculated with  $V_{L3}^{\text{trig}} = V_{L0}^{\text{trig}} \times \epsilon_{L1}^{\text{trig}} \times \epsilon_{L2}^{\text{trig}} \times \epsilon_{L3}^{\text{trig}}$  from the information in Tables 6.2, 6.5 and 6.10.

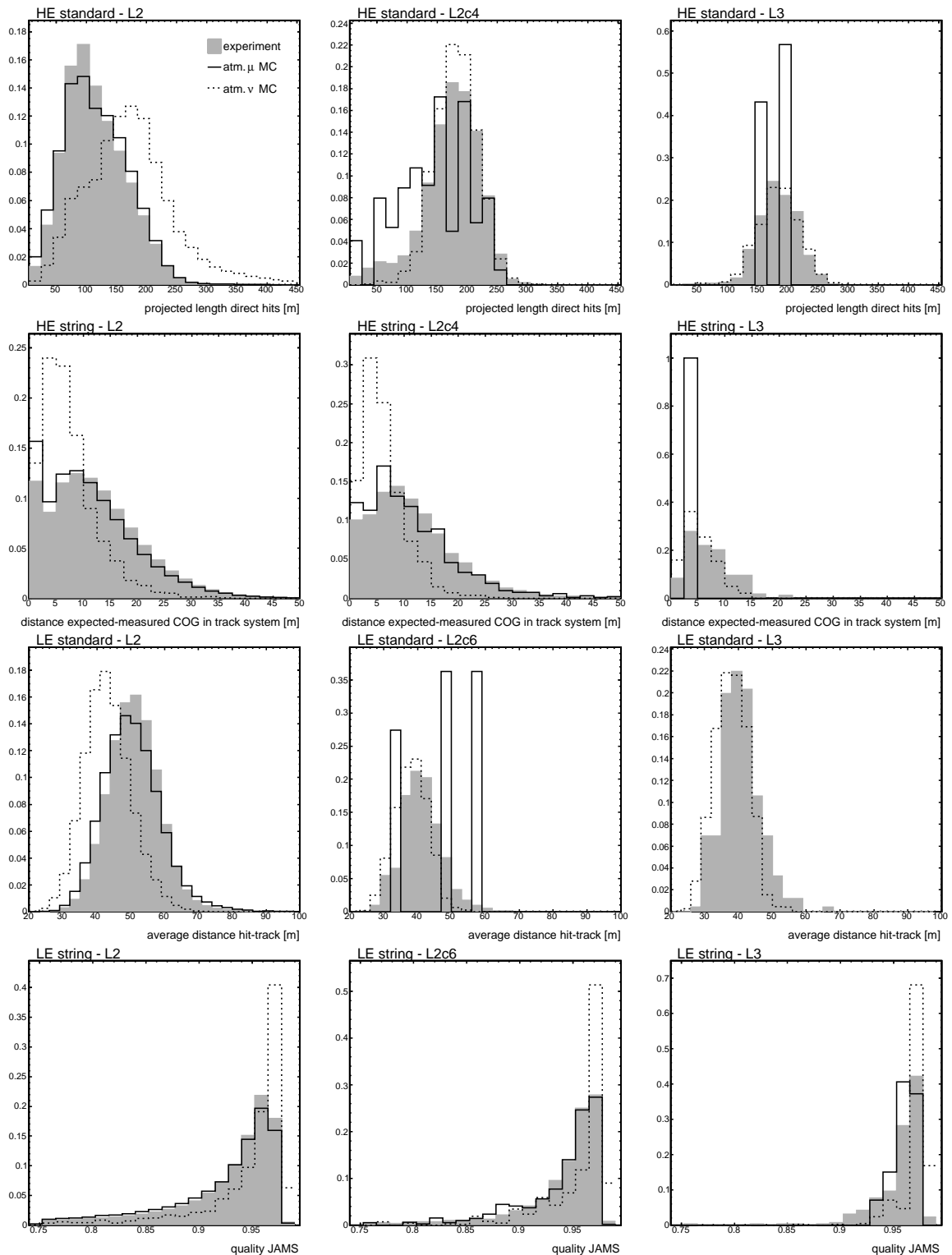


**Figure 6.13** – Evolution of normalized observable distributions with L3 cut level (columns) for all four L3 filters (rows). Shown are experimental data (filled area) and atmospheric muon (solid) and neutrino (dotted) MC.

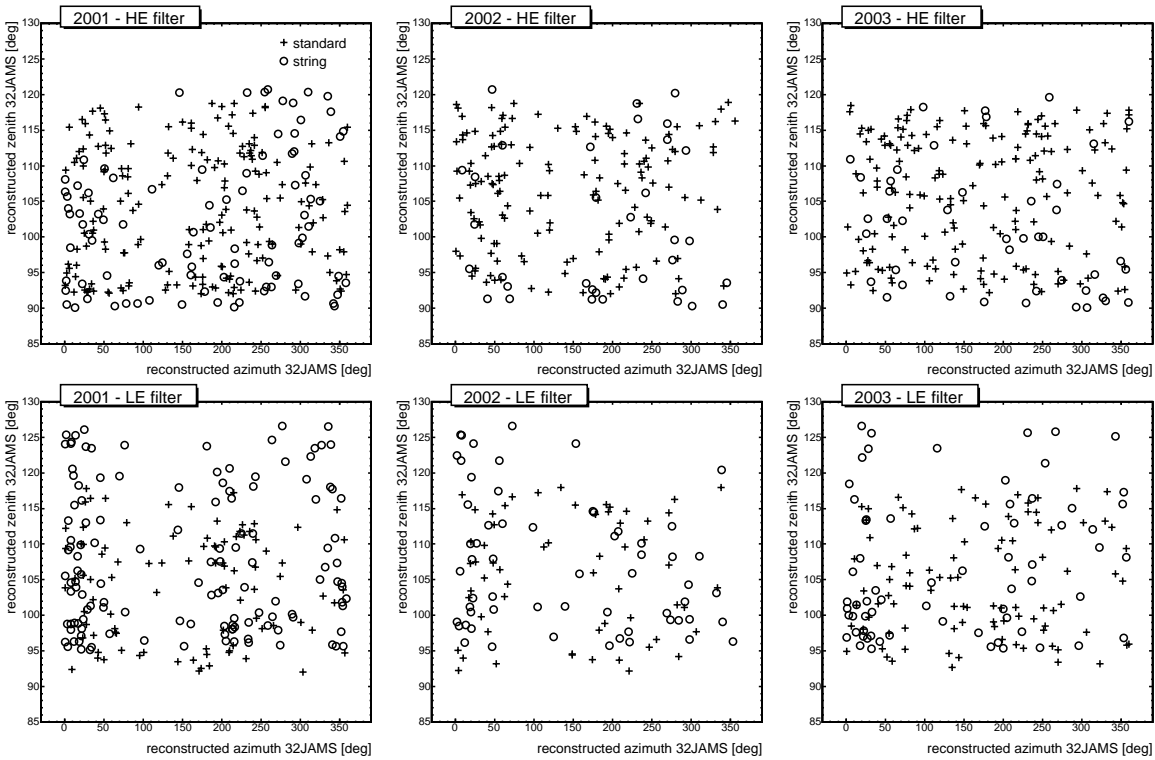


**Figure 6.14** – Reconstructed direction of the experimental events in the final samples A and B (see Table 6.11 for details). Each year and trigger class are differentiated.

below 3% for all models. The price paid for the large background rejection is the loss of a factor 5 to 70 in effective volume compared to trigger level (see Fig. 6.1). But this sacrifice improves the significance by a factor 40-400.

While 15-20% of the triggered signal events in the standard stream pass all selection criteria, that is only 2-6% for the string stream. For neutralinos with a mass of 50 GeV the string trigger remains vital even at the final selection level, for the 100 GeV soft model more than a factor of two is gained in signal efficiency with respect to the standard trigger only scenario. The efficiency of the other, higher energy models is completely dominated by the standard trigger.

The bottom part of Fig. 6.15 presents the effective volume for each year separately. With the verification step during the iterative procedure in mind it comes as no surprise that no discrepancy is observed between the years. The string trigger downscaling is obvious for 2002 and 2003 on the right hand side.

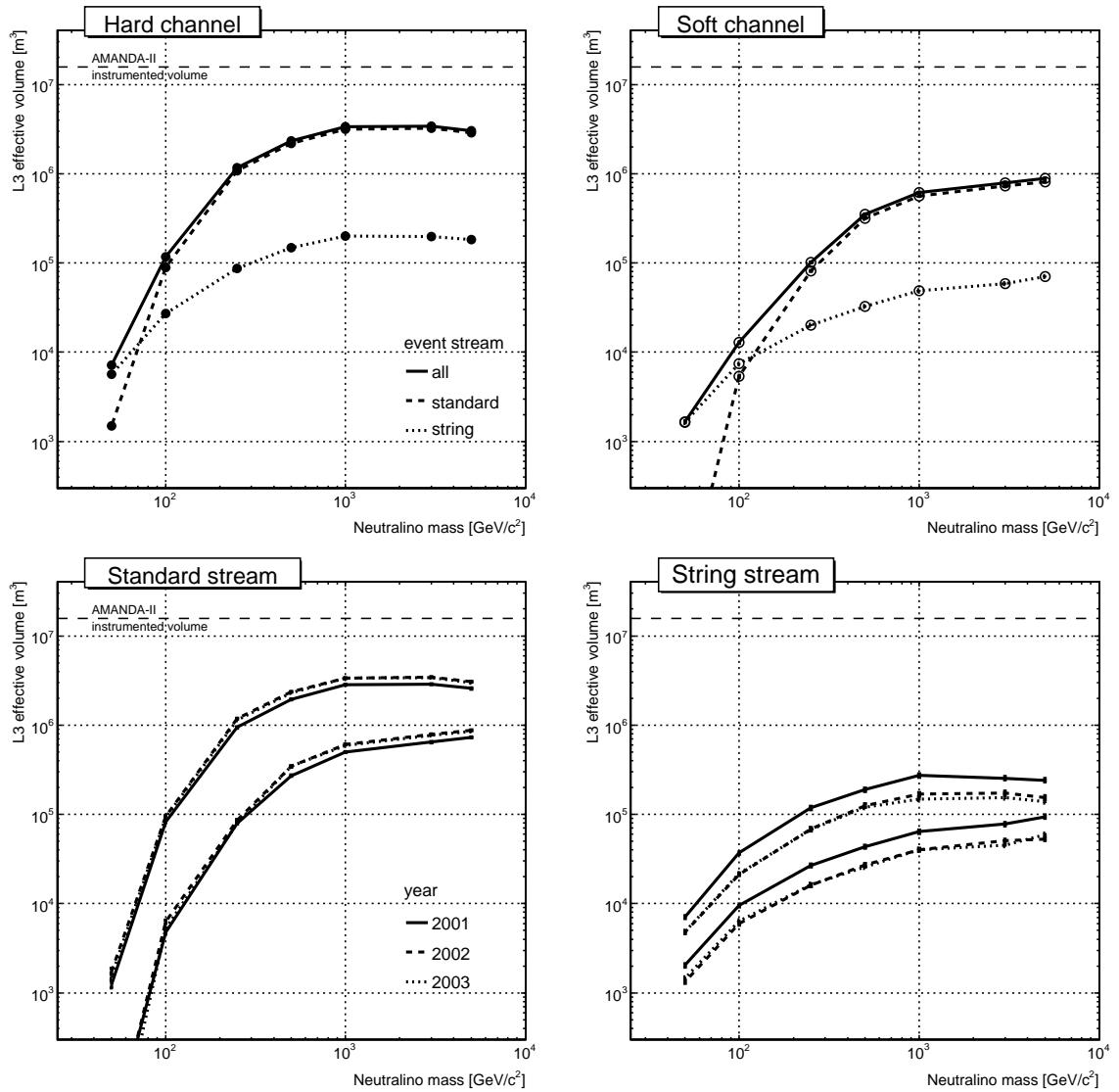


**Figure 6.15** – Top row: effective volume at filter level 3 for the whole data set and for the various trigger classes; the left (right) panel shows the results for the hard (soft) annihilation channel. Bottom row: as before, but the data taking years are disentangled; left (right) is the standard (string) trigger set, lines at the top (bottom) are for the hard (soft) channel. (Invisible) vertical bars represent statistical errors.

# Chapter 7

## Measurement of number of signal events

Our next objective is to measure the number of dark matter induced events in the final experimental data sample. Here, the term *measurement* involves the derivation of the number of signal events and its associated statistical error. This is accomplished by a likelihood-ratio test procedure that exploits the angular distance of the observed events to the Sun. Systematic errors are not incorporated due to the complexity of the method. They are addressed in the following chapter.

### 7.1 The space angle to the Sun

The number of signal events  $\mu$  in a certain data set can be estimated in various ways. The simplest method would be to inspect the total data set and count the number of observed events  $n_{\text{obs}}^{\text{tot}}$  and estimate the number of expected background events  $n_{\text{B}}^{\text{tot}}$ , see Table 6.11. The test statistic, total number of observed events, follows Poisson statistics for which the confidence interval at the desired confidence level can easily be looked up.

Contrary to searches for a diffuse flux of neutrinos over the whole sky, we are interested in a potential neutrino source with known location, the Sun. In this case, the *space angle*<sup>1</sup>  $\psi$  between the direction of the source  $(\theta_{\odot}, \phi_{\odot})$  and that of the reconstructed event  $(\theta, \phi)$ , defined as

$$\psi \equiv \arccos [\cos \theta \cos \theta_{\odot} + \sin \theta \sin \theta_{\odot} \cos(\phi - \phi_{\odot})],$$

can be exploited to improve the sensitivity of the measurement. It does not make much sense to count the events that are observed far away from the source, since these essentially have an atmospheric origin. Instead, one defines an angular cone around the Sun, with half opening angle  $\psi_{\text{cone}}$ , and considers only the events reconstructed inside this so-called *search cone*. We then repeat the same, simple exercise from previous paragraph, counting the number of observed  $n_{\text{obs}}^{\text{cone}}$  and background  $n_{\text{B}}^{\text{cone}}$  events inside the cone  $\psi < \psi_{\text{cone}}$ . Again, the test statistic is Poisson distributed and the confidence interval readily available.

The best sensitivity is in principle expected when one looks in an infinitely small search cone, containing (almost) no background and all signal events. Unfortunately the latter

---

<sup>1</sup>From now on, when we refer to *the* space angle of an event (without mentioning the Sun) we actually mean the angular separation between the reconstructed track and the Sun.

final sample	[°]	5000	3000	1000	500	250	100	50
hard	std	2.7	2.7	2.7	2.9	3.1	4.0	4.8
	str	3.2	3.2	3.2	3.2	3.7	7.0	9.8
soft	std	3.1	3.1	3.2	3.4	3.8	4.6	12.3
	str	3.6	3.6	3.7	3.8	6.7	8.9	11.9

**Table 7.1** – Median space angle between the Sun and the reconstructed track for neutralino signal at the final level, broken up for both trigger classes.

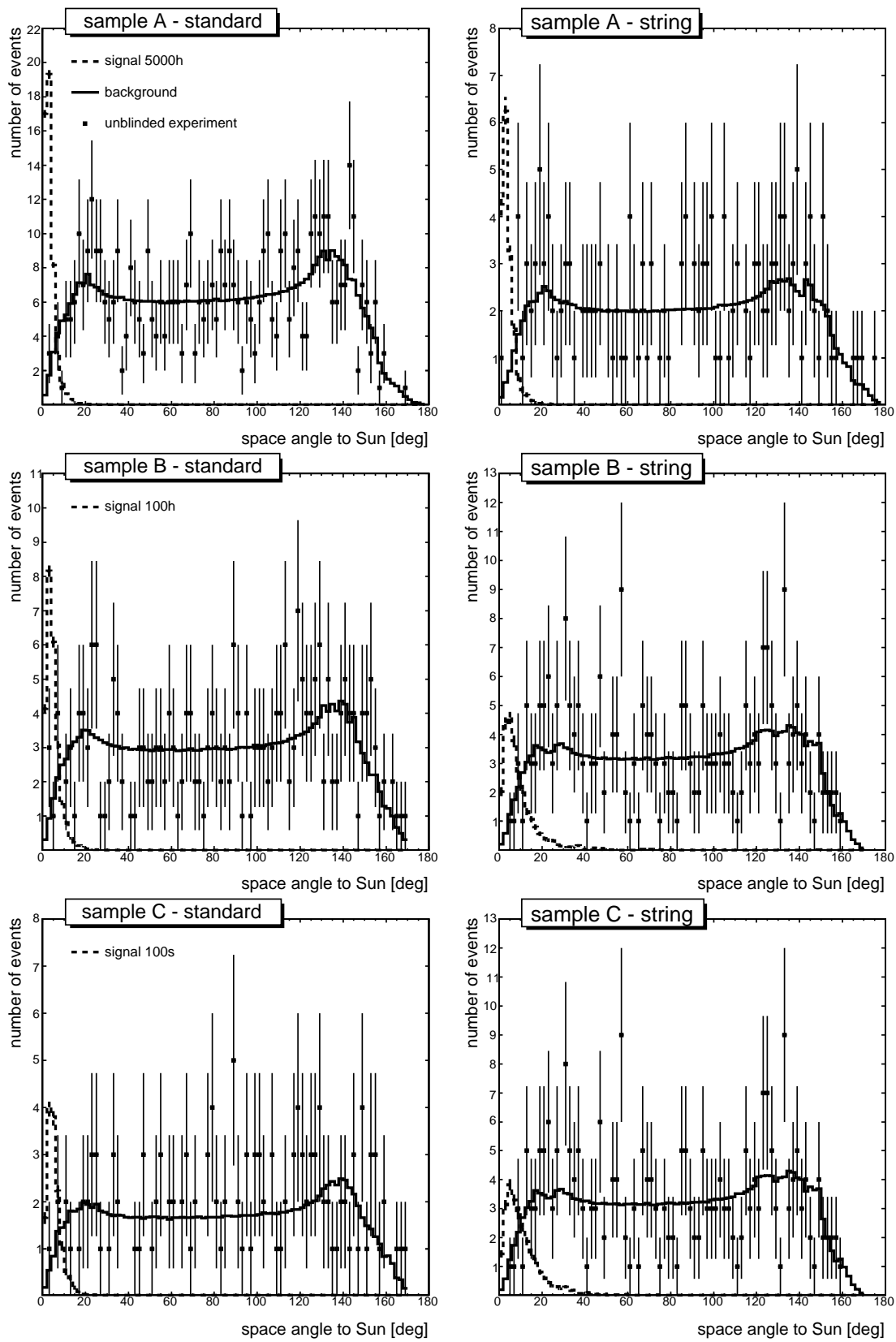
statement is not entirely true, not all reconstructed tracks of solar neutralino-induced events point back to the Sun. There are two main culprits. First of all, the reconstruction methods do not reproduce the true direction, not even for the events in the high quality final event sample. Reconstructed directions are smeared around their true values, an effect that tends to become more important for low energy events. But, even with a perfect reconstruction, there is an unavoidable physical bound to know the exact position of a neutrino source. That is because the detector does not observe the neutrino, but rather the muon from its charged-current interaction with a nucleus. Both leptons are well aligned but not perfectly, with an angular separation that increases with decreasing energy, see Fig. 2.4 and Eq. 2.4.

Figure 7.1 illustrates the space angle distribution for three neutralino models and both event streams. The (dashed) distributions peak close to the Sun and drop rapidly with increasing angle. Table 7.1 presents the 50% quantile of such distributions, defining the *angular resolution*, for all inspected neutralino models and both event streams. As expected, higher energy events (originating from a heavy neutralino or triggered by the standard trigger) are much more concentrated around the Sun, 50% of these are reconstructed within 3 – 4°. For the lowest energy models, a cone of 12° is needed to contain only half of the signal events.

These figures also show that the background distribution is similar for all L3 event selections. In the following section we will explain how the background distribution is extracted from off-source experimental data. Since atmospheric background events are, by definition, not correlated with the position of the Sun, the distribution is rather uniform between 20° – 140° and drops outside this region due to lack of phase space. The same behaviour is seen for the unblinded experimental data. The absence of a large bump close to 0° seems to indicate that no or little signal is present.

It is clear that a model-dependent cone size is needed to obtain the optimal result: a five degree cone is reasonable for high energy models, but certainly not for the lowest energies. Since the search cone essentially represents an additional event selection, we can use the tools presented in the previous chapter to find the optimal opening angle. It is therefore also referred to as a *cut-and-count* approach.

Even though the cut-and-count approach uses more information than the simplest method, there is still room for improvement. Once the opening angle is chosen, no differentiation is made between the events inside the cone, and the events outside are completely neglected. That means that all repeated experiments (assuming identical background) observing e.g. ten events within a ten degree wide search cone, will lead to the same confidence interval. However, an experiment observing eight out of ten events within two degrees from the Sun should give a stronger hint for the existence of a solar signal than



**Figure 7.1** – Space angle distribution for both event streams (columns) and the three final samples (rows). Shown are the unblinded experiment, the background (normalized to data) and three different signal models (normalized to 10% of the data).

an outcome showing a background-like behaviour. This illustrates that the cut-and-count technique neglects useful information.

Therefore, a more refined approach is taken, coined the *fit* approach. Treating the signal strength as a free parameter, we fit the sum of the known background and signal distributions to the complete space angle distribution of all data events, not just those in a certain cone. The confidence interval is then calculated with a likelihood-ratio test statistic, which does not follow some standard distribution. This makes the calculation rather involved. The whole procedure is described in the next section.

The above described methods are in no way limited to the space angle as discriminating observable. Any other observable can be used to measure the signal strength. Since the space angle has the largest separation between signal and background it is expected to provide the best measurement though. Additional information can be included too, such that a two-dimensional cut-and-count or fit experiment is performed.

We conclude this introductory discussion by remarking that the blindness principle should be respected, like in the previous chapter, while deciding about the settings of any of the above method. It is not acceptable that the actually observed set of space angles is consulted to optimize the method. Although we already showed the unblinded experimental outcome in Fig. 7.1, this information was not used to develop the following method.

## 7.2 Confidence interval for $\mu$

This section clarifies how we estimate the unknown parameter  $\mu$ , the number of signal events, and its confidence interval from a set of observed space angles  $\{\psi_i\}$ .

Once the signal and background probability density functions are known, we define the likelihood of having  $\mu$  signal events in an observed set of space angles  $\{\psi_i\}$ . Then a likelihood-ratio test statistic is proposed, for which the critical region is found through dedicated Monte Carlo simulations. At the end of this section we describe how the confidence interval in  $\mu$  is found and verify its statistical properties.

### 7.2.1 Space angle pdf

The space angle distribution of signal  $f_S(\psi)$  is found directly from simulated neutralino events, for the various models and both trigger streams. Any source of systematic errors in the simulation potentially influences this distribution, and ultimately the reported confidence interval in  $\mu$ . This will be assessed in the following chapter, in Section 8.1.2.

The background distribution  $f_B(\psi)$  could have been derived from simulation as well, but there is a much better alternative: scrambled, off-source experimental data. The advantage then is that  $f_B(\psi)$  does not depend on simulation and its associated systematic errors. But, when working with the experimental data, we have to respect the blindness rule. A double safety is built in. First of all, we only use *off-source* experimental events, meaning that they are reconstructed at least  $30^\circ$  away from the Sun in azimuth. This avoids that information from possibly present signal events infiltrates into the background model, which is clearly not desired. About one sixth of the events are excluded. Secondly, the space angle of each off-source data event is calculated with respect to a fake Sun position  $(\theta_{\odot}^{\text{fake}}, \phi_{\odot}^{\text{fake}})$ , a process called *scrambling*. Since the detector has a zenith-dependent acceptance we

should keep  $\theta_{\odot}^{\text{fake}} = \theta_{\odot}^{\text{true}}$ , but it is sufficient to scramble the azimuth  $\phi_{\odot}^{\text{fake}}$  to obtain a fake Sun. The background distribution is then built up by repeatedly sampling a new  $\phi_{\odot}^{\text{fake}}$  uniformly between  $0^\circ$  and  $360^\circ$ , each time calculating the space angle between the observed direction and the fake Sun. That is done 10000 times for each off-source data event in the experimental test sample<sup>2</sup>, to smoothen the distribution and to avoid empty intermediate bins.

The resulting, binned distributions  $f_S(\psi)$  and  $f_B(\psi)$  are normalized to one, such that they represent probability density functions (also *pdf*) for signal and background, see Fig. 7.1. The bins were chosen to be two degrees wide, this is motivated in Section 7.3.3. In the following we assume that these pdf's are perfectly known.

## 7.2.2 Signal content likelihood

Once the signal and background space angle pdf's are known it becomes possible to calculate the likelihood of the presence of  $\mu$  signal events in a single experiment that observes exactly  $n_{\text{obs}}$  events with space angles  $\{\psi_i\}$

$$\mathcal{L}(\mu) = \prod_{i=1}^{n_{\text{obs}}} f(\psi_i|\mu), \quad (7.1)$$

where

$$f(\psi|\mu) = \frac{\mu}{n_{\text{obs}}} f_S(\psi) + \left(1 - \frac{\mu}{n_{\text{obs}}}\right) f_B(\psi). \quad (7.2)$$

is the probability to observe  $\psi$  for a single event when  $\mu$  signal events are present among  $n_{\text{obs}}$  total observed events.

In principle we could also include the Poisson probability of observing  $n_{\text{obs}}$  events when  $\mu + \mu_B$  (signal plus background) are expected. The difficulty in that case is to have a reliable estimate of the number of background events  $\mu_B$ . An estimate from simulated background events introduces an additional dependence on systematic errors in the simulation chain. Since these errors could be quite substantial, it seems wise to avoid them as much as possible. Another option is to use an independent experimental data sample, which should then be excluded from use in the confidence interval calculation. To reduce statistical errors a sizable part of the precious data set would have to be sacrificed. And since the benefit of the Poissonian factor does not outweigh the disadvantages, we exclude it from the likelihood function.

The generalisation from a single experiment to multiple, but independent experiments is straightforward after realising that (a) the total number of signal events  $\mu$  is the sum of the signal contributions  $\mu_j$  from the individual experiments  $j$ ; and (b) this contribution is proportional, Eq. 2.7, to the exposure of the experiments, defined as  $\mathcal{E}_j \equiv V_{\text{eff},j} t_{\text{live},j}$  (we have a source flux that is constant in time). The combined likelihood is then simply the product of the individual, independent experiment likelihoods.

We will focus on the case of two (independent) experiments ( $j = 1, 2$ ) with equal live-time  $t_{\text{live}}$ , representing the (independent) standard and string event streams. The elements

<sup>2</sup>Since the Sun was above the horizon while the experimental train sample was collected, it is useless for the construction of the background distribution.

needed from each individual analysis to complete the combination are (a) the effective volume  $V_{\text{eff},j}$ ; (b) the number of observed events  $n_{\text{obs},j}$ ; (c) with space angles  $\{\psi_{j,i}\}$ ; and (d) the signal and background space angle pdf's  $f_{S,j}(\psi)$  and  $f_{B,j}(\psi)$ .

Then, the total number of signal events  $\mu = \mu_1 + \mu_2$ , with  $\mu_j = \frac{\varepsilon_j}{\varepsilon_1 + \varepsilon_2} \mu$ . Since the live-time for our specific case is the same for both experiments, this simplifies to

$$\mu_j = \frac{V_{\text{eff},j}}{V_{\text{eff},1} + V_{\text{eff},2}} \mu.$$

The combined likelihood of  $\mu$  total signal events is the product of the likelihoods of the individual (independent) experiments observing  $\mu_j$  signal events each

$$\begin{aligned} \mathcal{L}(\mu) &= \mathcal{L}_1(\mu_1) \mathcal{L}_2(\mu_2) \\ &= \left( \prod_{i=1}^{n_{\text{obs},1}} f_1(\psi_{1,i} | \mu_1) \right) \left( \prod_{i=1}^{n_{\text{obs},2}} f_2(\psi_{2,i} | \mu_2) \right), \end{aligned} \quad (7.3)$$

with

$$f_j(\psi | \mu_j) = \frac{\mu_j}{n_{\text{obs},j}} f_{S,j}(\psi) + \left( 1 - \frac{\mu_j}{n_{\text{obs},j}} \right) f_{B,j}(\psi), \quad (7.4)$$

the experiment-dependent probability to observe  $\psi$ .

### 7.2.3 Construction of the confidence interval

#### Test statistic

To derive confidence intervals, Feldman and Cousins [171] propose the following likelihood-ratio test statistic

$$R(\mu) = \frac{\mathcal{L}(\mu)}{\mathcal{L}(\hat{\mu})},$$

where  $\hat{\mu}$  is the best fit of  $\mu$  to the observed set of space angles. Therefore  $\mathcal{L}(\mu) \leq \mathcal{L}(\hat{\mu})$  and  $R(\mu) \leq 1$ , for all  $\mu$ . A key element is their suggestion to restrict ourselves to physical values of  $\mu$ , hence  $\mu, \hat{\mu} \in [0, n_{\text{obs}}]$ . Unphysical best fits  $\hat{\mu} < 0$  are not uncommon, e.g. when there is no or little signal and a downward fluctuation of the background near the Sun.

The best fit value  $\hat{\mu}$  maximizes the single likelihood (Eq. 7.1) for a single experiment, and the combined likelihood (Eq. 7.3) for a combined experiment (which may be different than the sum of the best fits to the individual data sets,  $\hat{\mu} \neq \hat{\mu}_1 + \hat{\mu}_2$ ).

#### Frequentist confidence intervals

We follow a fully frequentist method to infer the *confidence interval* (or shorthand *CI*) in the unknown parameter  $\mu$ , the number of neutralino-induced events, from the observed value of the test statistic  $R$ . In this frequentist framework, an interval  $[\mu_{\text{low}}, \mu_{\text{up}}]$  is called confidence interval with confidence level  $\alpha$ , when it is derived such that a fraction  $\alpha$  of  $N$  identical, statistically independent experiments report an interval (not necessarily identical for each experiment) containing the true, but unknown value of  $\mu$ . This concept of coverage

is central in frequentist statistics. The higher the confidence level, the fewer CI outcomes fail to cover the true value. In this work the confidence level is set to  $\alpha = 90\%$ , the final results will be given with  $\alpha = 99\%$  confidence too.

Before deriving the confidence interval, in the unknown parameter  $\mu$ , the frequentist framework tells us to construct the *acceptance interval*, in the observable quantity  $R$ , for all values of  $\mu$ . For a CI with  $\alpha$  confidence, the acceptance interval  $[R_{\text{low}}, R_{\text{up}}]$  for any  $\mu$  must gather a fraction  $\alpha$  of the experimental outcomes  $R$  when the considered  $\mu$  is the true value of the unknown parameter. Such an acceptance interval can be found for any  $\mu$ , provided that we know how  $R$  is distributed when  $\mu$  is the true value. This does not define the acceptance intervals uniquely however. The frequentist experimenter has the freedom to choose what values of  $R$  are accepted, as long as  $\alpha$  probability is collected.

An *ordering principle* dictates which experimental outcomes  $R$  are added to the acceptance interval. Classic ordering principles lead to either one-sided or two-sided intervals. It seems natural to report a central interval when we expect to see a signal, or an upper limit when we do not. In these cases, the question “central interval or upper limit?” has to be answered before the experiment is performed, otherwise the coverage becomes jeopardized.

Feldman and Cousins (FC) suggested an ordering principle, based on their likelihood-ratio test statistic  $R$  [171]. They refer to  $R$  as *rank*, since it ranks the experimental outcomes in order of inclusion in the acceptance interval, starting at high values. It is a *unifying* ordering principle in the sense that the experimental data determine whether the reported CI is one- or two-sided, and not the experimenter, while the coverage is preserved at the same time. This is a very attractive feature in the search for rare signals, and therefore this method is used in this work.

Another attractive feature concerns physical bounds on  $\mu$ . Classic frequentist methods sometimes report CI that overlap with unphysical parts in the parameter space, e.g.  $\mu < 0$ . Therefore, experimenters often resorted to Bayesian methods to avoid these unphysical results. The FC-method provides the long hoped for frequentist answer to these concerns: due to the condition  $\mu, \hat{\mu} \in [0, n_{\text{obs}}]$ , the CI always lies completely in the physical part of the parameter space.

## Constructing the critical region through pseudo-experiments

The acceptance intervals for  $\alpha$  CL generally look like  $[R_{\text{crit}}^{\alpha}(\mu), 1]$  in the FC-approach, since  $R$  are included with decreasing values. Here,  $R_{\text{crit}}^{\alpha}(\mu)$  is an explicit function of  $\mu$ , and referred to as the *critical region*. But how do we obtain that function? According to Wilks' Theorem,  $-2 \ln R$  becomes  $\chi^2$ -distributed in the Gaussian regime ( $n_{\text{obs}} \rightarrow \infty$ ), which has, in our case, one degree of freedom. With  $-2 \ln R$  following identical  $\chi^2$ -statistics for each  $\mu$ , the critical region is constant:  $-2 \ln R_{\text{crit}}^{\alpha}(\mu) = \chi^2(\alpha, 1)$ .

The actual distribution of  $-2 \ln R$  may deviate significantly from  $\chi^2$  however. E.g. when a physical boundary is met ( $\mu \sim 0$  or  $n_{\text{obs}}$ ), the best fit  $\hat{\mu}$  may occur in the unphysical region, while the FC-method restricts itself to the physical region. Therefore, the likelihood (rank) for constrained best fits is lower (higher) than for unconstrained best fits, resulting in a deviation from  $\chi^2$ . Another example is when the free parameter  $\mu$  is extended in a region which has little effect on the space angle distribution ( $\mu \sim 0$ ). The used  $\chi^2$  then has less than one effective degree of freedom.

Figure 7.2 compares the well-known  $\chi^2$  distribution with one degree of freedom to the

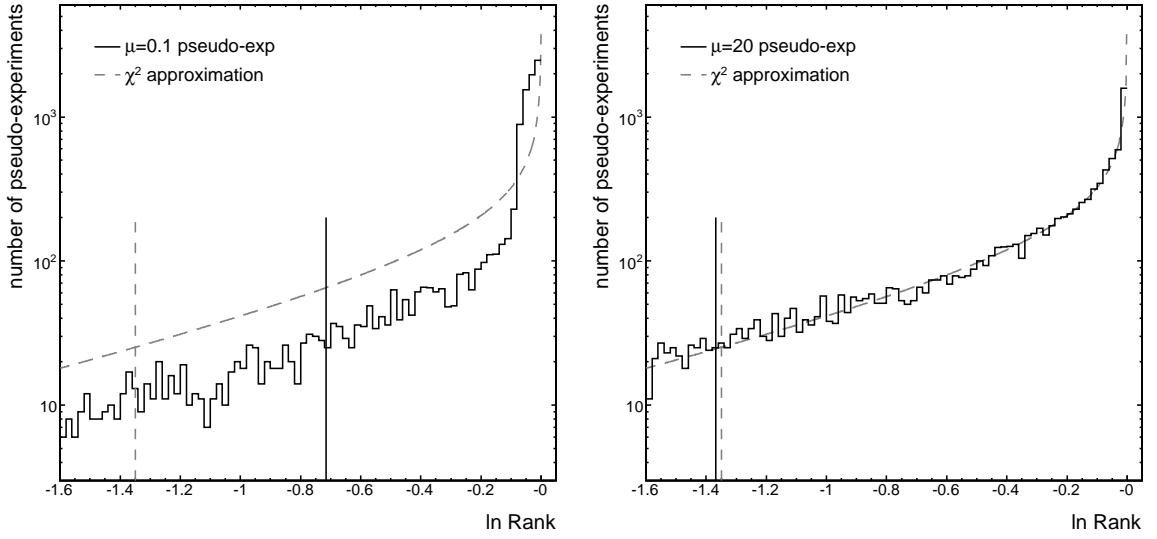


**Figure 7.2** – Distribution of  $\ln R$  for 10000 pseudo-experiments containing  $\mu = 0.1$  (left) and  $\mu = 20$  (right) signal events. The thick grey line shows the  $\chi^2$  distribution with one degree of freedom. Vertical lines (same line style) mark the  $\alpha = 90\%$  quantile of the distributions.

actual distributions of  $\ln R$  obtained from 10000 pseudo-experiments for two values of  $\mu$ . Vertical lines indicate the  $\alpha = 90\%$  critical value from the pseudo-experiments and from the  $\chi^2$  distribution. For  $\mu = 20$  (right panel) the actual and the  $\chi^2$  distribution are almost identical, and the  $\chi^2$  approximation of the critical value is valid. That is not the case for  $\mu = 0.1$  (left panel). With  $\mu$  too close to the physical boundary many experiments have a higher rank than what would be obtained without the restriction to the physical region. The critical value is therefore higher than that of the  $\chi^2$  distribution. As a result, the acceptance interval suggested by  $\chi^2$  collects 96% probability, a substantial overcoverage with respect to the desired 90%.

Since the  $\chi^2$  approximation does not guarantee the correct coverage for all  $\mu$ , dedicated, repeated pseudo-experiments are performed to obtain the distribution of  $\ln R$  and its critical value for each  $\mu$  (like in Fig. 7.2). It is a time consuming procedure, carried out in the following way

1. for each  $\mu \in [0, 50]$ , with step-size  $\Delta\mu = 0.1$ 
  - (a) for each pseudo-experiment  $k = 1 \dots 10000$ 
    - i. sample a set  $\{\psi_i\}_k$  with  $n_{obs}$  space angles from Eq. 7.2, given  $\mu$
    - ii. calculate  $\mathcal{L}_k(\mu)$  with Eq. 7.1
    - iii. find  $\hat{\mu}_k \in [0, n_{obs}]$  with maximum likelihood  $\mathcal{L}_k(\hat{\mu}_k)$
    - iv. calculate  $\ln R_k(\mu)$
  - (b) find the critical value  $\ln R_{crit}^\alpha(\mu)$  such that  $\ln R_k(\mu) \geq \ln R_{crit}^\alpha(\mu)$  for a fraction  $\alpha$  of the 10000 experiments
2. smoothen  $R_{crit}^\alpha(\mu)$  and fit it with a spline

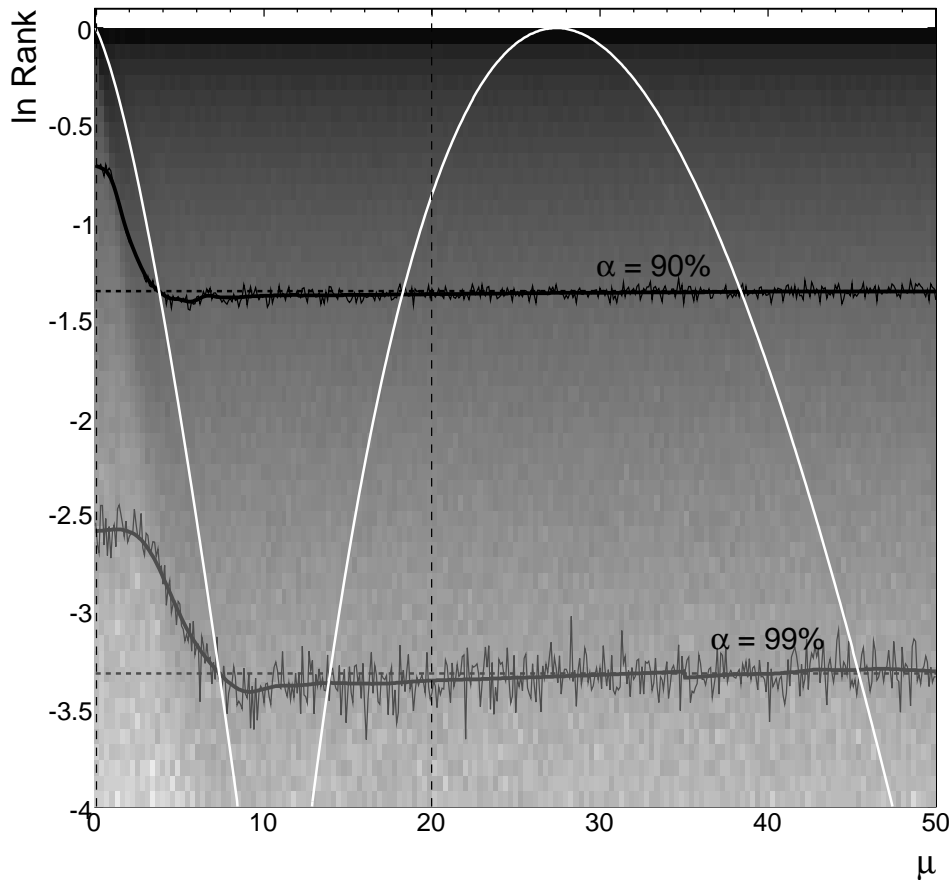


**Figure 7.3** – The rank distribution of 10000 pseudo-experiments is set out in the grey scale (darker means more experiments) along the vertical axis. The critical region  $\ln R_{\text{crit}}^{\alpha}(\mu)$  at 90% (99%) CL is indicated by the thin black (grey) curve, with its smoothed fit superimposed (thick line). The horizontal dashed lines show the critical value from the  $\chi^2$ -approximation. The white parabolas represent  $\ln R(\mu)$  for two pseudo-experiments:  $\mu_{\text{true}} = 0$  (left) and  $\mu_{\text{true}} = 30$  (right).

The critical region for a combined experiment is constructed similarly, the only difference being that the pseudo-experiments  $\{\psi_{j,i}\}_k$  should be sampled from two different parent distributions  $f_j(\psi|\mu_j)$ , Eq. 7.4, and that the best fit value maximizes the combined likelihood, Eq. 7.3.

The outcome of this effort is presented in Fig. 7.3: a two-dimensional distribution of  $\ln R$  versus  $\mu$  (Fig. 7.2 is extracted from two vertical slices, thin dashed lines, in Fig. 7.3). Solid lines mark the critical regions for 90% and 99% CL. In this example the  $\chi^2$  approximation (horizontal dashed line) holds above  $\mu > 10$ , with a constant critical region for  $\alpha = 90\%$  (99%) at  $\ln R_{\text{crit}}^{\alpha} = -\frac{1}{2} \chi_{\text{crit}}^2(\alpha, 1) = -1.35$  ( $-3.32$ ). As we have seen before the validity of the  $\chi^2$  approximation breaks down for too small  $\mu$ , the 90% (99%)  $\chi^2$ -quantiles are too small and lead to overcoverage. Furthermore, the  $\chi^2$  slightly undercovers the region around  $\mu = 5 - 10$  in this example.

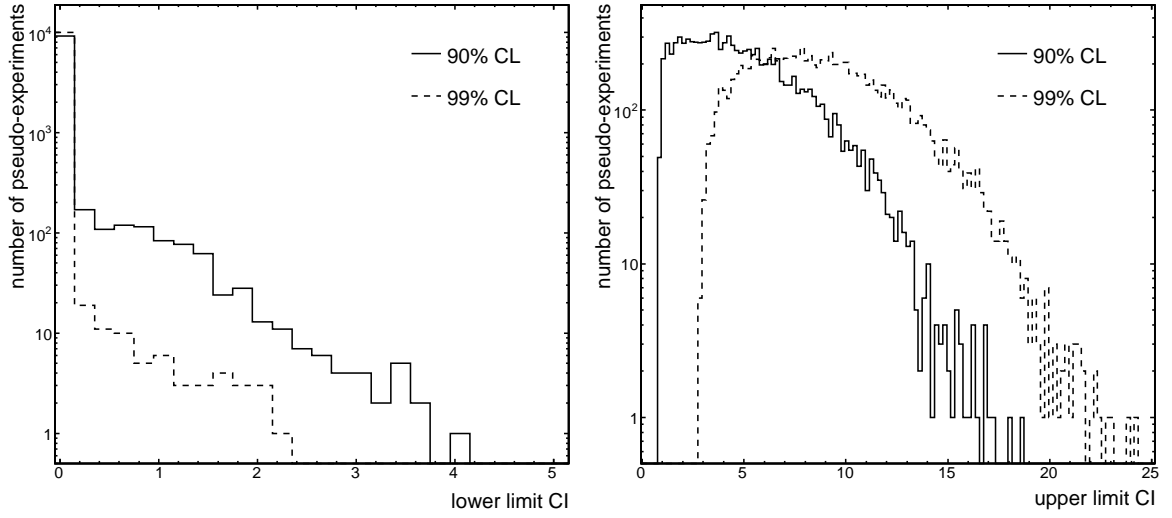


**Figure 7.4** – Distribution of lower limit (left) and upper limit (right) of the confidence intervals at two confidence levels, for 10000 background-only pseudo-experiments.

### The confidence interval

With the critical region defined, the confidence interval  $[\mu_{\text{low}}^{\alpha}, \mu_{\text{up}}^{\alpha}]$  at  $\alpha$  CL for the number of signal events in an observed set of space angles  $\{\psi_i\}$  is given by

$$[\mu_{\text{low}}^{\alpha}, \mu_{\text{up}}^{\alpha}] = \{\mu \mid \ln R(\mu) \geq \ln R_{\text{crit}}^{\alpha}(\mu)\}.$$

If the rank for the inspected  $\mu$  is above the critical value, that  $\mu$  is present in the confidence interval.

Figure 7.3 illustrates  $\ln R(\mu)$  for two pseudo-experiments with  $\mu_{\text{true}} = 0$  and  $\mu_{\text{true}} = 30$  (white curves). The best physical fit to the generated set of space angles is found respectively at  $\hat{\mu} = 0.0$  and  $\hat{\mu} = 27.4$ . The first experiment results in one-sided intervals with upper limits 3.8 and 7.3 for 90% and 99% confidence. For the same CL the second experiment produces two-sided intervals: [18.2, 38.4] and [13.9, 45.4] respectively.

### 7.2.4 Properties of the confidence intervals

In frequentist statistics, the reported confidence interval should contain the true value of the unknown parameter, whatever its value, in a fraction  $\alpha$  of repeated, identical independent experiments. Equivalently, the intervals should not contain the true value in a fraction  $1 - \alpha$  of the experiments. The coverage of the intervals is an essential property, and checked below through pseudo-experiments.

We generate 10000 pseudo-experiments<sup>3</sup>  $\{\psi_i\}_k$  from Eq. 7.2 with e.g.  $\mu_{\text{true}} = 0$ . For each pseudo-experiment  $k$  the confidence interval  $[\mu_{\text{low},k}^{\alpha}, \mu_{\text{up},k}^{\alpha}]$  with  $\alpha$  CL is derived. Then we check whether  $\mu_{\text{true}} = 0$  is inside the interval, and store its lower and upper boundaries. With all experiments performed, the fraction of covering intervals is calculated

<sup>3</sup>The method is completely analogous for combined experiments.

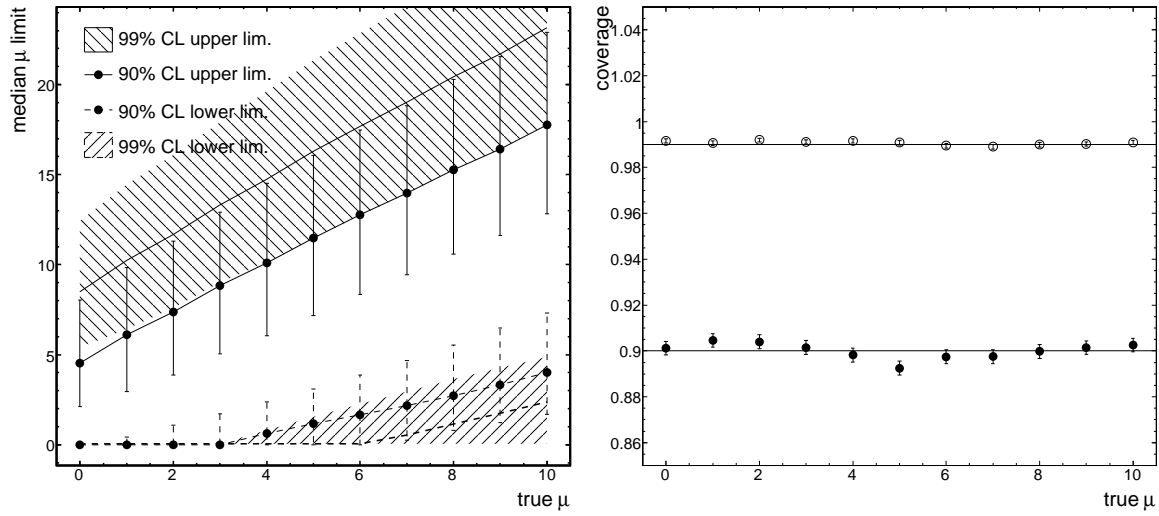


**Figure 7.5** – The median interval (left) and coverage (right) of the intervals as a function of  $\mu_{\text{true}}$ . Lines (shades) are for 90% (99%) confidence level. Vertical bars indicate the  $1\sigma$  spread.

and compared to the quoted  $\alpha$  CL. From the distribution of lower (upper) limits we infer the 50%, 16% and 84% quantiles, representing the median lower (upper) limit  $\bar{\mu}_{\text{low}}^{\alpha}$  ( $\bar{\mu}_{\text{up}}^{\alpha}$ ) and its  $1\sigma$  statistical spread. This procedure is then repeated for various choices of  $\mu_{\text{true}}$ .

Figure 7.4 shows the distribution of lower (left) and upper (right) limits for background-only ( $\mu_{\text{true}} = 0$ ) pseudo-experiments. As expected, a small amount of the experiments report a non-zero lower limit, excluding the true value from the CI. If the coverage is correct, the true value is not contained in a fraction  $1 - \alpha$  of the pseudo-experiments.

In Figure 7.5 (right) the actual coverage of the 90% and 99% CIs is shown for  $\mu \in [0, 10]$ . Since no statistical significant deviation from the expected values 0.9 and 0.99 is found, we conclude that the intervals are indeed confidence intervals.

The left-hand side of the same figure shows the median CI and the  $1\sigma$  spread on its boundaries, for both CL. From repeated background-only experiments, we expect a median interval  $[0, 4.5]$ . For stronger signal fluxes the intervals automatically become double-sided. That is a nice illustration of the unified ordering principle in action. In this example, the presence of four (seven) signal events in the data sample is enough to report a non-zero lower limit or detection with 90% (99%) confidence in more than 50% of the experiments. Usually, when a non-zero lower limit is reported with  $> 3\sigma$  significance (or  $> 99.7\%$  CL) the observation is called an *indication of a source*, while for  $> 5\sigma$  (or  $> 1 - 6 \times 10^{-7}$  CL) it is interpreted as a *discovery of the source*. The signal strength needed to reach these thresholds can be calculated in the same way as before, but requires a lot more than 10000 pseudo-experiments to have a robust construction of the critical region for these high confidence levels.

Last but not least, we remark that, by construction, the method only returns intervals that reside in the physical region.

## 7.3 Results

The above confidence interval calculation method is applied twice, with different purposes. At first, the goal is to find the number of cuts in the L3 filter that lead to the optimal flux sensitivity for each of the trigger streams separately (single likelihood). Once the L3 filter is defined, the second goal is to obtain the final results on the measurement of  $\mu$  combining the likelihoods of both event streams. In the last part of this section, we study the influence of pdf binning.

### 7.3.1 Single stream $\mu$ : definition of the L3 filter

The goal of the event selection procedure, outlined in the previous chapter, is to improve the measurement of the muon flux. This quantity is directly proportional to  $\mu/V_{\text{eff}}$ , see Section 2.3.1. We remind the reader that we postponed the final definition of the L3 filter until the tools to evaluate  $\mu$  were available, see Section 6.5.3. Both  $\mu$  and  $V_{\text{eff}}$  change while iteratively adding cuts to the L3 filter. Obviously, the iteration should stop once  $\mu/V_{\text{eff}}$  does not improve.

The blindness principle must be respected though. We are not allowed to fine-tune the number of L3 cuts on the basis of the value of  $\mu$  obtained from the actually observed set of space angles. Instead, we compute the median 90% CL confidence interval from repeated background-only pseudo-experiments ( $\mu_{\text{true}} = 0$ ), following the prescriptions in Section 7.2.4. In the absence of signal the expected median interval is always one-sided. The ratio  $\bar{\mu}_{90}/V_{\text{eff}}$ , of similar spirit as Eq. 6.6, is decisive for the size of the signal parameter space that is excluded when no signal is present. The lower this ratio, the more sensitive the experiment becomes to exclude neutralino models, therefore it is coined *model rejection potential* (MRP). Instead of maximizing the potential to exclude models, the experimenter could also optimize the potential to discover models<sup>4</sup>. At the moment, since the expected signal flux is rather small we are most interested in the rejection of as much signal models as possible. That is why the MRP,  $\bar{\mu}_{90}/V_{\text{eff}}$ , is our guide to define the L3 filter.

In the previous chapter a high (HE) and low energy (LE) template signal model were used to develop separate sets of L3 selection criteria for the standard and string event stream, see Table 6.8. Two questions need to be answered for each of the fourteen signal models. What is the optimal cut depth (the number of cuts) for each trigger stream? Which template filter is optimal?

For a given neutralino model, template filter and trigger stream we compute  $\bar{\mu}_{90,i}/V_i$  for each L3 cut depth  $i$  that leads to less than 2000 remaining data events<sup>5</sup>. We note that  $\bar{\mu}_{90,i}$  is inferred from the single stream event sets (single likelihood, Eq. 7.1), since the optimal cut depths for the individual streams will also lead to the optimal setting for the combined event stream. In other words, we do not consider the string events while calculating the median upper limit for the standard event stream. For each signal model, we scan over L3 cut depth for both trigger streams and both L3 template filters. The cut depth and template filter yielding the lowest ratio  $\bar{\mu}_{90,i}/V_i$  defines the final L3 filter set-up.

<sup>4</sup>For instance by optimizing for the lowest signal strength needed to report a  $5\sigma$  discovery in 50% of the experiments, the *model discovery potential*.

<sup>5</sup>The construction of the critical region  $R_{\text{crit}}^\alpha(\mu)$  for larger data samples is too time consuming.

single trigger $\bar{\mu}_{90}$	5000	3000	1000	500	250	100	50
hard std	4.2	4.2	4.2	4.3	4.6	4.3	3.9
str	3.0	3.0	3.0	3.0	3.2	6.1	8.2
soft std	4.6	4.6	4.7	4.9	4.2	3.9	6.3
str	3.2	3.2	3.3	3.3	6.0	7.3	9.7

**Table 7.2** – Median 90% CL upper limit on the number of signal events at the optimal cut depth in the L3 filter, assuming background-only scenarios. The event streams are not combined, e.g. the standard events are neglected when calculating the median limit for the string stream.

Table 6.10 in previous chapter already reported the optimal L3 filter settings (second column) for each neutralino model. The HE filter is optimal for nine models: 5000–250 GeV hard and 5000 – 500 GeV soft. The best MRP for all these models is obtained after eight and nine cuts on respectively the standard and string streams. Removing the last L3 cut results in less than 5% loss of muon flux sensitivity. The LE filter is applied to the other five models: 100 – 50 GeV hard and 250 – 50 GeV soft. After ten and twelve cuts on the standard and string triggers the best sensitivity is reached, except for 100 GeV hard and 250 GeV soft for which it is better to drop the final  $L_{dir}$  cut from the standard stream filter. The last cut improves the sensitivity by at most 5% for the string stream and 10% for the standard stream. One could decide to continue the iterative procedure for the standard stream, but at these high cut levels we risk to tune any further selection criterion on the limited statistics in the background train sample.

The median 90% CL upper limits on  $\mu$  for all neutralino models and both trigger streams are summarized in Table 7.2. The expected limit lies between 4 – 6 for the standard trigger, and between 3 – 10 for the string trigger. More stringent limits for the string trigger only reflect the fact that less events are observed after final cuts (see Table 6.11), and not that the string stream is intrinsically more sensitive to the dark matter signal. In fact, once the absolute signal event count  $\bar{\mu}$  is translated to a limit on the signal fraction in the sample  $\bar{\mu}/n_{obs}$ , a different picture emerges. The median signal fraction upper limits smoothly vary from 1 – 3% for the standard trigger and 2 – 4% for the string stream. Lower energy models have a wider signal distribution, see Table 7.1 and Fig. 7.1, resulting in less stringent limits on the fraction of signal events in the data set.

### 7.3.2 Combining all streams: final results

After the event selection was fully defined and carefully checked by the AMANDA collaboration, we were allowed to unblind the position of the Sun. Although the experimental space angle distribution for the various final samples was already shown in Fig. 7.1, this information was not used to derive any of the previous results. At this point the confidence interval in  $\mu$  is calculated for the unblinded experiment. But, contrary to previous section, we exploit the full data sample and combine the likelihood functions of both the standard and the string event stream, Eq. 7.3.

No significant excess of events in the direction of the Sun is observed, see Fig. 7.6. Final sample A and C are best fitted by a pure background distribution ( $\hat{\mu} = 0$ ). For sample B

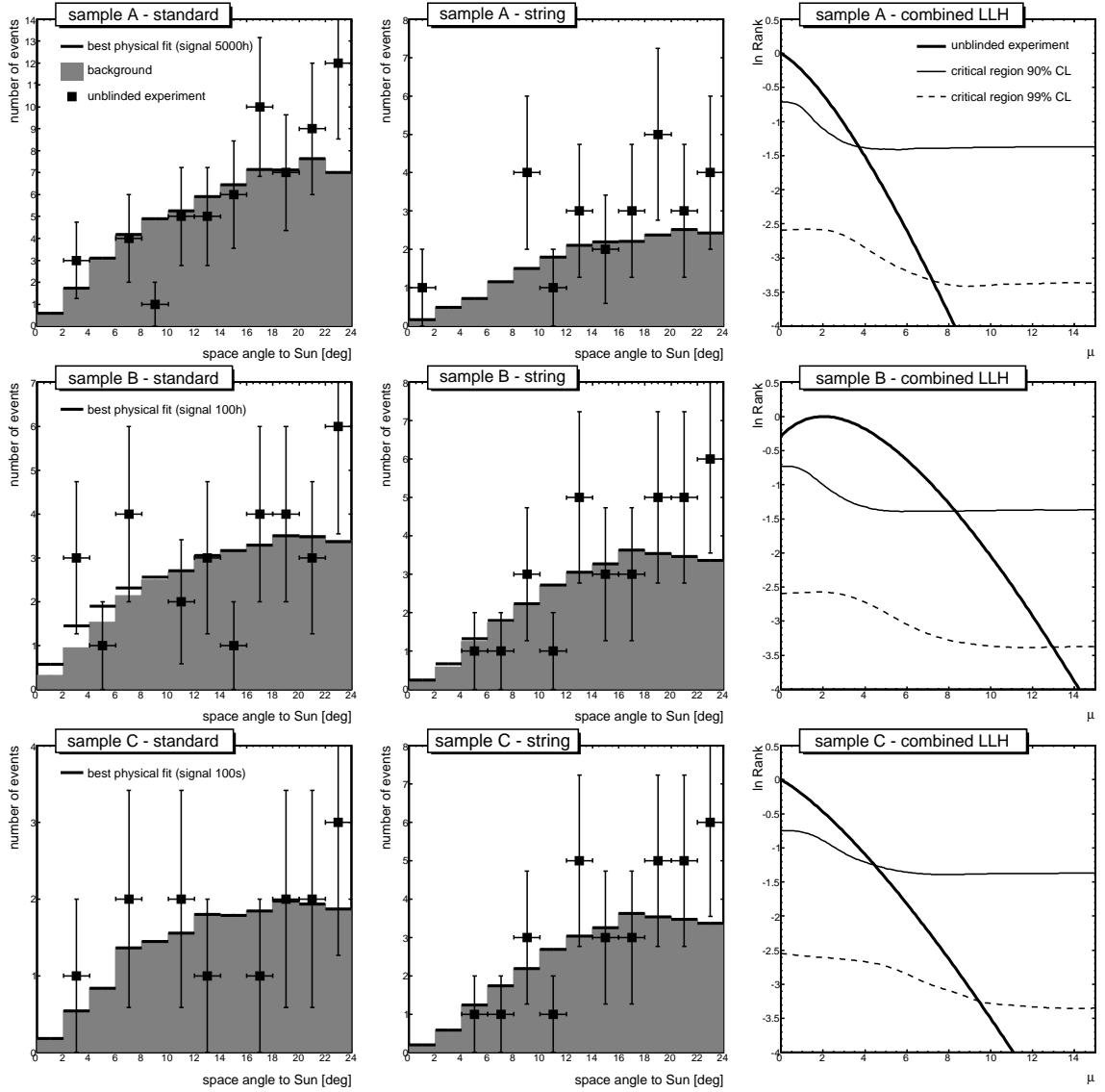


**Figure 7.6** – Space angle distribution close to the Sun for the standard (left column) and string (middle) stream. Shown are the unblinded experiment, the background and the best physical signal+background fit to the experiment (all normalized to the total data set). The right column displays  $\ln R(\mu)$  for the experiment and the 90% and 99% CL critical regions. Illustrated are the 5000 GeV hard (top row), 100 GeV hard (middle) and 100 GeV soft (bottom) neutralino models.

(used by the 100 GeV hard and 250 GeV soft neutralino model) a signal contribution of two events best fits the data (2nd row, right column), which we interpret as due to an upward fluctuation of the background in the  $\psi = 2 - 4^\circ$  and  $\psi = 6 - 8^\circ$  bins for the standard event stream (which dominates the exposure). The lower limit for all neutralino models is zero, so only upper limits are reported. The results are summarized in Table 7.3 (right part) for two confidence levels  $\alpha = 90\%$  ( $\mu_{90}$ ) and  $\alpha = 99\%$  ( $\mu_{99}$ ). Due to the upward fluctuation in the standard stream of sample B, the 250 GeV soft and 100 GeV hard models have a less stringent upper limit than neighbouring models.

We consider these final results in the light of the upper limit expected for the no signal

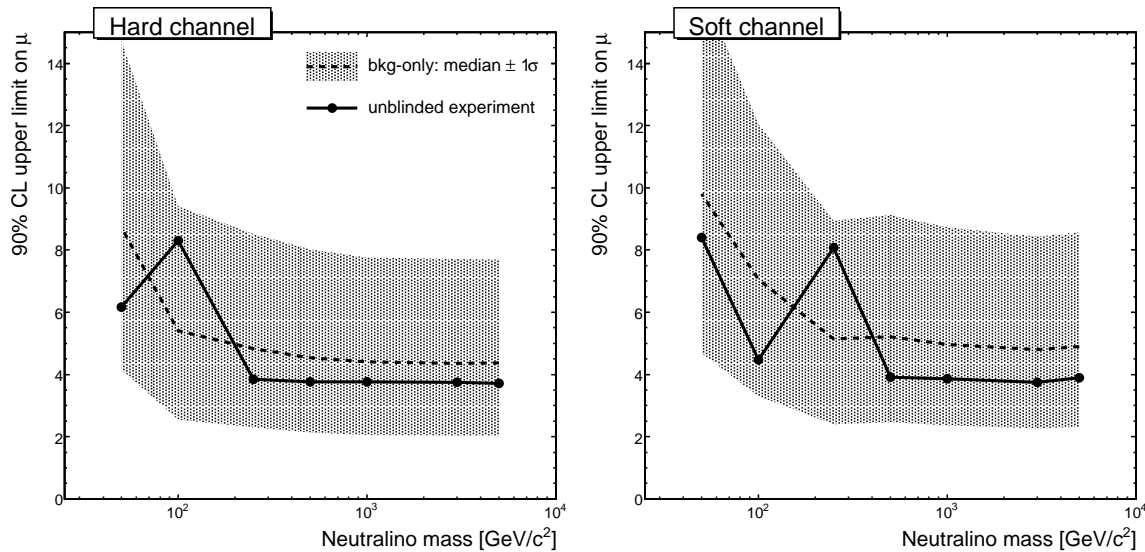


**Figure 7.7** – The unblinded upper limit (markers+solid line) and the  $1\sigma$  band around the median upper limit expected for the no-signal case (dashed line+shaded area) for all neutralino masses and both annihilation channels (left/right). The confidence level is set to 90%.

case. How different are the observed CI compared to the background-only expectation? As in previous section, we perform repeated background-only experiments and calculate the median 90% CL upper limit. To give an idea of the statistical spread in the upper limit distribution, its 16% and 84% quantiles are also reported (left part of Table 7.3). Since this region contains 68% of the background-only experiments, equally distributed around the median, it is equivalent with a Gaussian  $1\sigma$  statistical spread.

Figure 7.7 shows where the actually observed upper limits (markers) are located compared to the expected results from the no signal scenario (shaded area). The probability to obtain at least the observed downward (or upward) fluctuation from the background-only case is shown in the last column of Table 7.3. The observed fluctuations are realized in, depending on signal model and final sample, 20 – 40% of the background-only scenarios. We conclude that all data samples are entirely compatible with background, and, in particular, that no excess is observed in the direction of the Sun. In the following chapter we convert these findings to a.o. upper limits on the muon flux.

### 7.3.3 Effect of pdf binning

The signal and background probability density functions in the likelihoods, Eq. 7.2 and 7.4, are binned. In this section we study the effect of the bin width on the median upper limit, and motivate our choice of 2 degree bins. We compute the combined trigger median 90% CL upper limit for space angle bins of width  $\Delta\psi = 0.5, 1, 2,$  and 5 degrees, and for several signal models. The results are shown in Table 7.4.

We conclude that the sensitivity degrades with increasing bin width, especially when the bins become wider than the signal angular resolution. Well resolved signal models (e.g. 5000 GeV hard) lose 5 – 15% of sensitivity when choosing  $5^\circ$  bins. This is not the case for lower energy models (e.g. 50 GeV soft), since the angular resolution is still worse than

signal model	final sample	expectation $\mu_{\text{true}} = 0$			unblinded experiment			P(obs  $\mu_{\text{true}} = 0$ )
		$\bar{\mu}_{90} - 1\sigma$	$\bar{\mu}_{90}$	$\bar{\mu}_{90} + 1\sigma$	$\hat{\mu}$	$\mu_{90}$	$\mu_{99}$	
5000 hard	A	2.0	4.4	7.7	0.0	3.7	7.2	0.41
3000 hard	A	2.0	4.4	7.7	0.0	3.7	7.3	0.41
1000 hard	A	2.0	4.4	7.8	0.0	3.8	7.3	0.42
500 hard	A	2.1	4.5	8.0	0.0	3.8	7.3	0.40
250 hard	A	2.3	4.8	8.5	0.0	3.9	7.5	0.37
100 hard	B	2.5	5.4	9.4	2.0	8.3	13.0	0.23
50 hard	C	4.2	8.7	14.7	0.0	6.2	12.3	0.32
5000 soft	A	2.3	4.9	8.6	0.0	3.9	7.6	0.36
3000 soft	A	2.3	4.8	8.4	0.0	3.7	7.4	0.35
1000 soft	A	2.4	5.0	8.7	0.0	3.9	7.6	0.36
500 soft	A	2.5	5.2	9.1	0.0	3.9	7.6	0.34
250 soft	B	2.4	5.1	8.9	2.0	8.1	12.6	0.21
100 soft	C	3.3	7.1	12.1	0.0	4.5	9.4	0.28
50 soft	C	4.7	9.8	16.5	0.0	8.4	15.7	0.41

**Table 7.3** – For each neutralino model: its final data sample; the median value and  $1\sigma$  spread of the 90% CL upper limit from repeated background-only experiments; results from the unblinded experiment: best physical fit  $\hat{\mu}$  and upper limit with 90% and 99% confidence; probability to realize at least the observed fluctuation in a background-only scenario. The lower limits are always zero, and the likelihood function combines both trigger streams.

$\frac{\bar{\mu}_{90}(\Delta\psi)}{\bar{\mu}_{90}(\Delta\psi = 2^\circ)}$	HE c8c9		LE c9c12		LE c10c12	
	5000 hard	500 soft	250 soft	100 hard	100 soft	50 soft
$\Delta\psi = 0.5^\circ$	0.97	0.99	0.99	0.99	0.99	0.98
$1.0^\circ$	0.98	0.99	0.99	1.00	1.00	0.99
$2.0^\circ$	1.00	1.00	1.00	1.00	1.00	1.00
$5.0^\circ$	1.14	1.08	1.05	1.05	1.02	1.01
$\psi_{\text{std}}, \psi_{\text{str}} [^\circ]$	(2.7, 3.2)	(3.4, 3.8)	(3.8, 6.7)	(4.0, 7.0)	(4.6, 8.9)	(12.3, 11.9)

**Table 7.4** – Relative change of median 90% CL upper limit for various pdf bin widths, and signal models. A bin width of  $2^\circ$  is chosen as reference. The bottom row reminds the signal angular resolution of both trigger streams (see Table 7.1), where *italic* indicates the one that dominates the total exposure.

the bin width. Below  $2^\circ$  the gain in sensitivity is negligible. For all considered models  $2^\circ$  bins are therefore a good compromise between gain in sensitivity and loss of robustness. Indeed, too small bins lead to increased fluctuations, since each bin contains fewer events. This does not affect the median upper limit too much, which is the outcome of repeated experiments. However, for a single experiment the effect can be substantial.

Therefore, for all signal models, we chose  $\Delta\psi = 2^\circ$  for the binned pdf's  $f_S(\psi)$  and  $f_B(\psi)$  in Section 7.2.1.

# Chapter 8

## Measurement of the neutralino-induced muon flux

In this chapter we conclude the analysis and calculate the neutrino-to-muon conversion rate, the neutralino annihilation rate in the Sun and the neutralino-induced muon flux at the detector. We discuss our final results in the light of those obtained by other experiments and theoretical predictions. But first of all, we study the uncertainties on the elements required for these final calculations.

### 8.1 Uncertainties on $\mu$ , $V_{\text{eff}}$ and $t_{\text{live}}$

The elements  $\mu$ ,  $V_{\text{eff}}$  and  $t_{\text{live}}$  that constitute the conversion rate  $\Gamma_{\nu \rightarrow \mu}$ , outlined in Chapter 2 and repeated in Section 8.2, are subject to both statistical and systematic uncertainties. They are evaluated in this section.

#### 8.1.1 Statistical uncertainties

##### Number of signal events $\mu$

The confidence interval in  $\mu$  is essentially a translation of the statistical fluctuations in the unblinded set of space angles to an uncertainty on  $\mu$ . We made the implicit assumption that the true signal and background probability density functions are known. Both pdf's are extracted from a finite set of events, hence subject to statistical fluctuations, and therefore an approximation of the true distribution. The influence of fluctuations in the signal and background distributions is expected to be small however. While ample simulated neutralino events were used to derive the signal pdf, the off-source data sets were smaller but resulted in a smooth background shape around  $\psi = 0^\circ$ . Although not quantitatively tested with independent samples, we estimate the influence of statistical fluctuations on the CI to be smaller than 1 – 3%. We chose a  $\pm 3\%$  statistical error for the final calculation.

##### Effective volume

In the same way the finite size of the simulated neutralino samples leads to a statistical uncertainty on the effective volume. Tables 8.1 and 8.2 (top row) on p. 145 summarize the

statistical uncertainty on  $V_{\text{eff}}$  at final cut level (standard plus string event stream) for all models. Our calculation takes the Monte Carlo event weights properly into account. The large size of the generated event sample leads to uncertainties at the final cut level smaller than 1% for the higher energy models. For the lowest energy model the event sample after the trigger, reconstruction and event selection is smaller, but the uncertainty remains below 3%.

### Live-time

The live-time of an experimental data file is found by correcting the wall-clock data taking time for the detector dead-time. The former is read from a GPS clock with nanosecond precision, the latter is inferred from an exponential fit to the time gap distribution of consecutive events in the data file. This leads to a statistical error on the per file live-time of  $\Delta t_{\text{live},i}/t_{\text{live},i} < 10^{-3}$ , see Section 4.1.3. The error on the total live-time of the data sample, with  $N \simeq 7 \times 10^4$  files, is much smaller:  $\Delta t_{\text{live}}/t_{\text{live}} = 1/\sqrt{N} \times \Delta t_{\text{live},i}/t_{\text{live},i} < 4 \times 10^{-6}$ . Obviously, this is completely negligible compared to the uncertainties on  $\mu$  and effective volume.

## 8.1.2 Systematic uncertainties

### Introduction

Several sources lead to systematic uncertainties, e.g. the errors on the measurement of or the parameterisation errors on cross sections, the simplifications in the simulation, detector calibrations, ... AMANDA has the bulk of its hardware components irreversibly deployed in a natural medium for many years, under conditions impossible to recreate in a laboratory. Without a strong and very well-known particle source, it is a real challenge to disentangle the effects caused by the detector and those caused by the surrounding medium. The conservative approach is then to look at each source separately and assume no correlations between the various sources of errors.

The majority of the results below concern the systematic effect on the effective volume at the final selection level. Unless otherwise noted, we did not explicitly check the systematic effect on the CI in  $\mu$ . It is expected to be small in all cases anyway.

The dominant contributors to the total systematic uncertainty on the effective volume (neutralino generator, photon propagation and global sensitivity of the optical modules) are evaluated with a dedicated Monte Carlo study for various neutralino models. These samples allow us to check the effect on the CI too. The uncertainties induced by the remaining sources are taken from the AMANDA literature.

When the uncertainty is evaluated from Monte Carlo, we will refer to the simulation set-up used to calculate the effective volume, Table 6.12, as the *baseline* set-up. We remind the reader that it consists of the WIMPSIMP-WF2F2000-GENN++ neutralino generator chain, the MMC muon propagator, the PTD photon propagator and the AMASIM detector simulator. All programs and settings were described earlier, in Section 4.2.

The additional samples are generated for four masses (5000, 500, 250 and 100 GeV) and both extreme annihilation channels, and processed through an identical simulation and analysis chain. Each sample has only one component changed with respect to the baseline

set-up, thereby allowing the study of one effect at a time. The 50 GeV signal models were not done due to time constraints, the values are estimated from the neighbouring models (especially 100 GeV soft) and their trigger dependencies.

## 1. Neutrino oscillation and cross section

The oscillation process of muon-neutrinos to other flavours is not included in the baseline neutralino generator chain, see Section 4.2.2. This recently became possible with WIMPSIM, a newer DARKSUSY-based code. WIMPSIM [97] provides a more complete and realistic picture of the physics processes than WIMPSIMP-WF2F2000-GENN++ [142–144]: all neutrino flavours (compared to only  $\nu_\mu + \bar{\nu}_\mu$ ), three-flavour oscillations (compared to no oscillations), both charged-current and neutral-current interactions (compared to only CC) and cross sections calculated without phase space cuts (compared to internal PYTHIA phase space cuts).

The ignored or incomplete processes affect the triggered event rate and hence the effective volume. The space angle distribution on the other hand remains essentially unaltered, so the effect on the CI in  $\mu$  is negligible. In the following we investigate the effect on the effective volume.

Besides the baseline sample  $S_0$ , we generate two more samples with the WIMPSIM program set up for two oscillation scenarios. The first sample  $S_1$  is for the *standard oscillation scenario* (as defined in [97]), the second  $S_2$  is the *no oscillation scenario*. The rest of the simulation chain is identical for all samples. We already mentioned the eight studied signal models in the introduction.

The PYTHIA version that we used for  $S_0$  is not tuned specifically for neutrino interaction processes and uses some older measurements. This affects e.g. the cross sections (due to phase space cuts) or the inelasticity of the CC interaction (due to older measurements). The WIMPSIM interactions on the other hand are computed with routines specifically written for neutrinos, using updated measurements of the relevant parameters [174]. With oscillations turned on, the  $S_1$  sample therefore represents the state-of-the-art simulation of the neutralino signal. Three systematic effects are considered (we write  $V_i$  for the effective volume of sample  $S_i$ ):

- We first compare the baseline sample with the state-of-the-art sample:  $(\Delta V/V)_a = (V_1 - V_0)/V_0$ . It quantifies the systematic error on the reported baseline effective volume due to a combination of the three-flavour oscillations and the CC interaction modelling.
- A second systematic error is related to the experimental uncertainty in the oscillation parameters. Neutrino oscillations are by now experimentally well established, the measured values of the oscillation parameters clearly deviate from zero, on average by at least  $10\sigma$  [175]. We accommodate for a  $1\sigma$  measurement error in the oscillation parameters by taking  $1/10^{\text{th}}$  of the difference in effective volume for the standard and no oscillation WIMPSIM samples:  $(\Delta V/V)_b = \frac{1}{10}(V_2 - V_1)/V_1$ .
- A third systematic effect, one not evaluated through MC study, comes from remaining errors in the cross section calculation. WIMPSIM is able to reproduce the measured

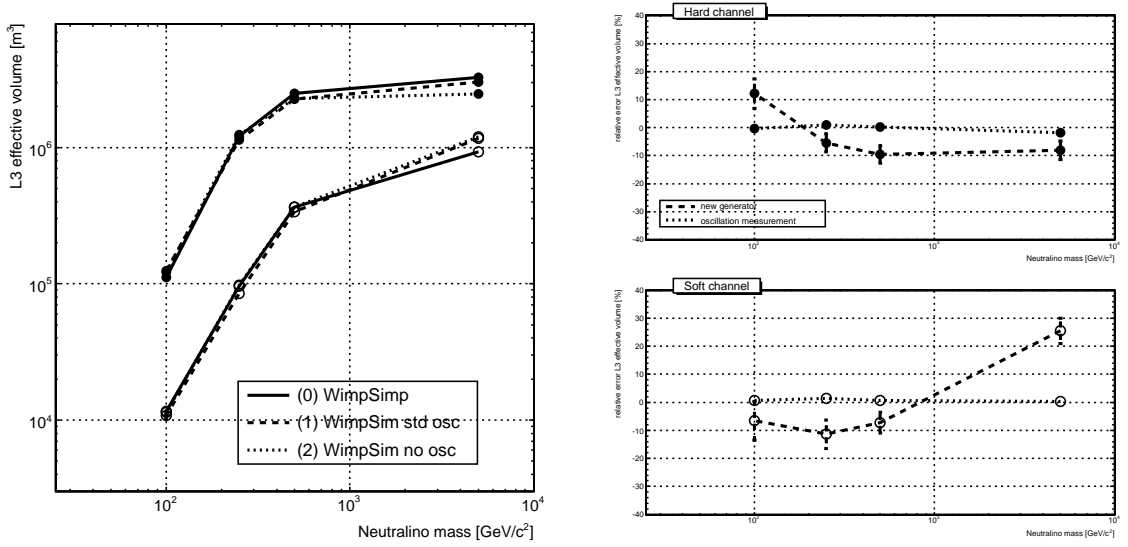


**Figure 8.1** – Left: effective volume at the final selection level, for three samples with different neutralino generator settings. Curves at the top (bottom) represent the hard (soft) annihilation channel. Right: relative uncertainty due to a change in generator settings (see text).

average cross-section up to  $E_\nu < 350$  GeV within a few percent [97]. From this we assign a conservative, constant error of  $(\Delta V/V)_c = 3\%$ .

The results are shown in Fig. 8.1. The difference in effective volume between the three samples (left panel) is translated to uncertainties on two effects (right panel). The  $1\sigma$  error in the oscillation parameters plays a minor role (dotted line), we estimate a  $(\Delta V/V)_b = 2\%$  symmetric error for all models. The difference between the old and new generator is larger and shows a complicated evolution. This is due to several effects (cross sections, oscillations) operating at the same time, more study would be required to fully understand the details. What we can conclude is that the strange trend is not induced by the event selection, a similar behaviour is already seen at trigger level. For the hard channel the effective volume is overestimated by the old generator at high energies,  $(\Delta V/V)_a = -(6 - 10)\%$ . This weakens with decreasing energies for the multiplicity triggered events, resulting in a changed sign for 100 GeV hard (+13%). The sign changes again for 50 GeV hard (−9%) since the string trigger becomes more important and is affected differently than the standard event stream. This model has a similar relative trigger contribution to 100 GeV soft (−8%). Below  $m_\chi = 1000$  GeV the soft channel signal efficiency is overestimated by the old generator. Above 1 TeV it is too conservative.

The three errors are added in quadrature  $\frac{\Delta V}{V} = \sqrt{(\frac{\Delta V}{V})_a^2 + (\frac{\Delta V}{V})_b^2 + (\frac{\Delta V}{V})_c^2}$  and summarized in Tables 8.1 and 8.2 for all signal models. The combined error ranges between  $-(4 - 13)\%$  and  $+(4 - 26)\%$ .

## 2. Tau neutrinos

The neutralino generator WIMPSIMP only produces muon-neutrinos, while annihilations lead to the other neutrino flavours as well. These  $\nu_{e,\tau}$  interactions typically produce compact shower-like events carrying too little angular information to survive the event selection, see Section 2.2.3. Tau leptons from  $\nu_\tau$  interactions decay in 17% of the cases to muons however, and these could survive the event selection. The tau contribution to the effective volume was estimated with WIMPSIMP events to be around 2 – 5%, becoming more important for higher energies [85, 176].

## 3. Density of the interaction medium

The amount of interactions is also directly proportional to the density of the medium, Eq. 2.6. The ice density is known below the 1% level [110], resulting in a negligible uncertainty on the effective volume. The density of the bedrock is much less certain, with an error around 10%. Almost all solar neutralino events, horizontal events below 1 TeV, are the result of a neutrino interacting in ice (the bedrock lies 1000 m below the detector). The uncertainty on the rock density therefore translates to an error on the signal rate smaller than  $\pm 1\%$  [127]. For higher energies, or vertical events, the effect would be larger though.

## 4. Muon propagation

The MMC program, Section 4.2.3, calculates the energy lost by the muon while propagating through the icy detector neighbourhood. The uncertainty on the cross sections and their parameterisation is estimated to be 1% [104]. The effect on the observed event rate was estimated to be around 1% in the context of the search for astrophysical neutrinos [177]. Neutralino-induced muons are located in the sub-TeV energy range, for which ionisation dominates the energy loss processes. Since this process is much better known than the stochastic energy losses occurring at higher energies, the uncertainty on the neutralino effective volume is expected to be smaller than  $\pm 1\%$ .

## 5. Photon propagation

The simulation of the propagation of photons is a very CPUtime consuming process, see Section 4.2.4. For this reason a simplified model of the optical ice properties is implemented, which introduces systematic effects. Another source of systematics is the uncertainty about the optical ice properties themselves. These are inferred from calibration data, collected while light sources were lit deep in the ice, and subject to measurement errors. Both systematic effects are evaluated for various models from dedicated Monte Carlo samples.

Two programs exist that handle the propagation of photons through large volumes of ice: PTD [147] and PHOTONICS [146]. They both model the optical properties as stacked layers, within a single layer constant optical properties are present. PTD has just four template optical layers and the photons only experience the optics of the layer in which they are detected. It is clear that the PTD picture is too simplified for photons that are detected far away from the point of creation. The more recent PHOTONICS package, on the other hand, has many more layers and the detected photons experience the optics of all traversed layers. This is a considerable improvement over the PTD model.

The measurement of the optical properties with dedicated calibration data has been, and still is, a complex long-term effort. Various studies concluded in progressively more accurate descriptions of the optical properties. The parameters of the MAM ice model for PTD are based on optical measurements but tweaked to compensate for PTD-related artifacts, in an attempt to better reproduce the experimental time residual distributions. MAM is used throughout this work because it is the best ice model for PTD. Since PHOTONICS has a completely different approach to vertical layers the tweaked MAM model has no direct PHOTONICS equivalent. Unfortunately, that makes it impossible to disentangle the effects from the implementation and from the underlying ice properties. Two PHOTONICS ice models are considered in this systematics study: MILLENIUM and the more recent AHA model<sup>1</sup>.

Generated neutralino events are run through three different photon propagation set-ups: PTD-MAM (baseline  $S_0$ ), PHOTONICS-AHA ( $S_1$ ) and PHOTONICS-MILLENIUM ( $S_2$ ). Again, the rest of the simulation chain is identical and the eight signal models were mentioned in the introduction. For these three samples, the systematic effects on both effective volume and  $\mu$  are studied. We begin with the latter.

After extraction of the signal space angle pdf, we repeat the construction of the critical region and the calculation of the confidence interval in  $\mu$  for all three samples. Since the signal space angle distributions are almost identical for a given signal model and since the background remains identical, no large influence on the CI is expected. Indeed, the relative change in the upper limit turns out to be smaller than 1% for the highest energy models and at most 3% for the lowest energy models. This is within the statistical uncertainty of the method, see Section 8.1.1, and we conclude that there is a negligible systematic effect of the photon propagation part of the simulation on the reported upper limits.

There is a clear systematic effect on the effective volume however. The simplified PTD-implementation model of the ice layers is the main culprit. Its contribution is estimated by comparing the effective volume of the baseline to that of the best available set-up (PHOTONICS-AHA):  $(\Delta V/V)_a = (V_1 - V_0)/V_0$ . Next, the effect of the ice model itself is evaluated by comparing the results within the same implementation model. We do that for the two ice models available for PHOTONICS:  $(\Delta V/V)_b = (V_2 - V_1)/V_1$ . This is the best we can do at the moment to assess the effect of photon propagation uncertainties. In principle, one should vary the underlying optical properties within their experimental errors and rerun the simulation, but that is simply not feasible within a reasonable amount of time.

To understand the behaviour at the final cut level we start with the trigger level. The top row of Fig. 8.2 shows that PTD leads to less triggers or a smaller effective volume at trigger level. The AHA model produces 15 – 20% more triggered events than MAM (dashed line in the right panel). MILLENIUM yields 5 – 10% fewer triggers than AHA (dotted line in right panel), but still more than MAM. We found that for lower energy models the difference between MAM-AHA and MILLENIUM-AHA becomes stronger for the multiplicity trigger, while this is much less the case for the string trigger. That is understood: the string triggered events have fewer, rather nearby produced hits, and are hence less affected by changes in the photon propagation model.

The event selection changes the relative PTD/PHOTONICS event yields at the final cut

<sup>1</sup>For the AMANDA/IceCube colleagues: version 2 was used.

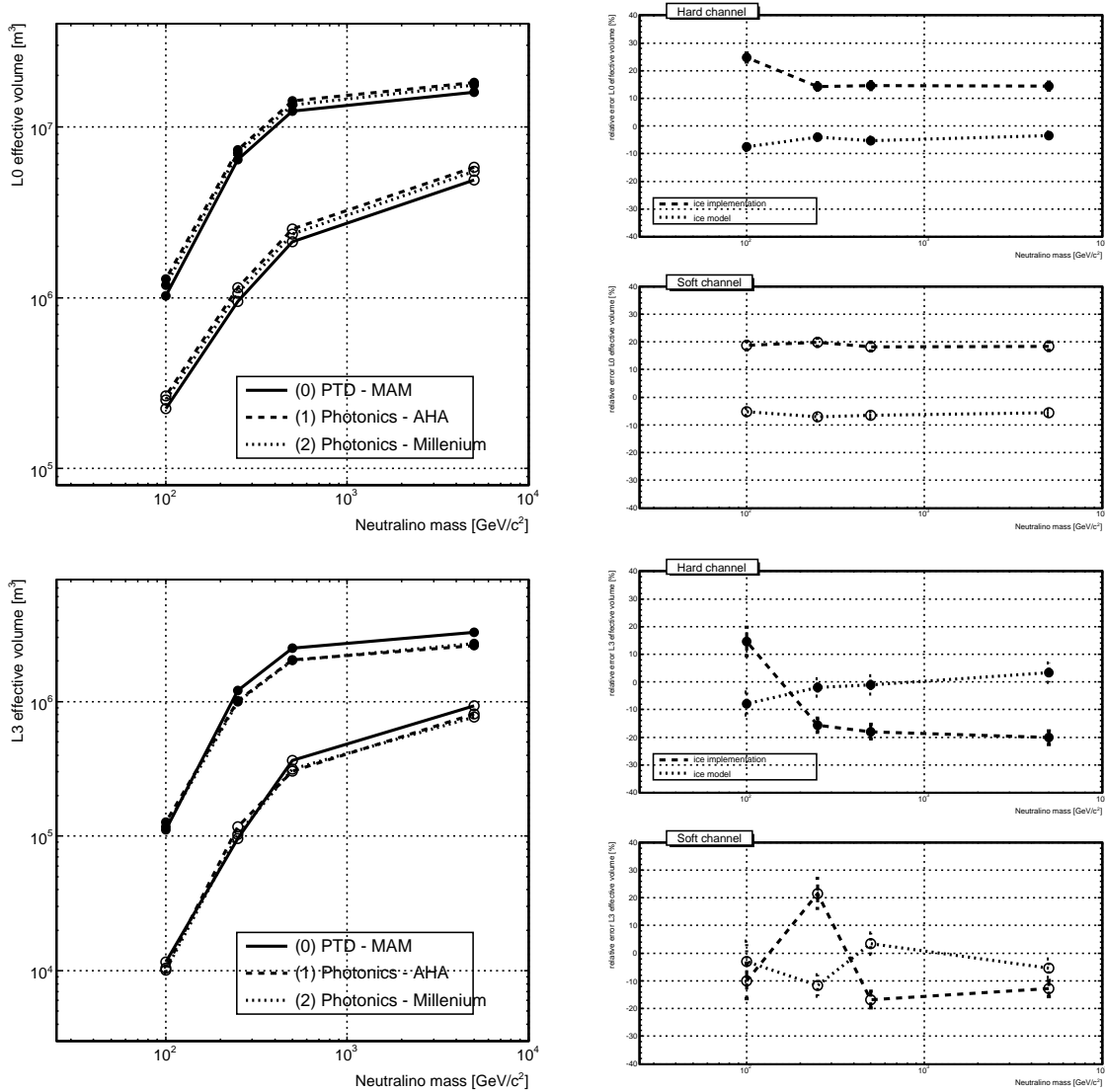


**Figure 8.2** – Left: effective volume for three samples with different photon propagation settings. Curves at the top (bottom) represent the hard (soft) annihilation channel. Right: relative uncertainty due to a change in photon propagation (see text). Top row is at trigger level, bottom row at final selection level.

level with respect to those found at trigger level. Fig. 8.3 illustrates the evolution of the effective volume with cut level (left panels). For the 5000 GeV hard signal model the gain with PHOTONICS at trigger level is completely lost due to a couple of (HE filter) cuts made on observables that appear to have a different distribution when simulated with PTD, see Fig. 8.3 (right panels; e.g. cuts 4, 6 and 8). The PHOTONICS effective volume at the final level turns out to be lower than that of PTD in this case. The 100 GeV hard model uses different, LE filter, observables. Some PTD-PHOTONICS distributions still differ, this time in both directions, so the net effect is small: the PHOTONICS volume remains higher at final cut level. The effective volume at final level for the three set-ups is illustrated in the bottom row of Fig. 8.2.

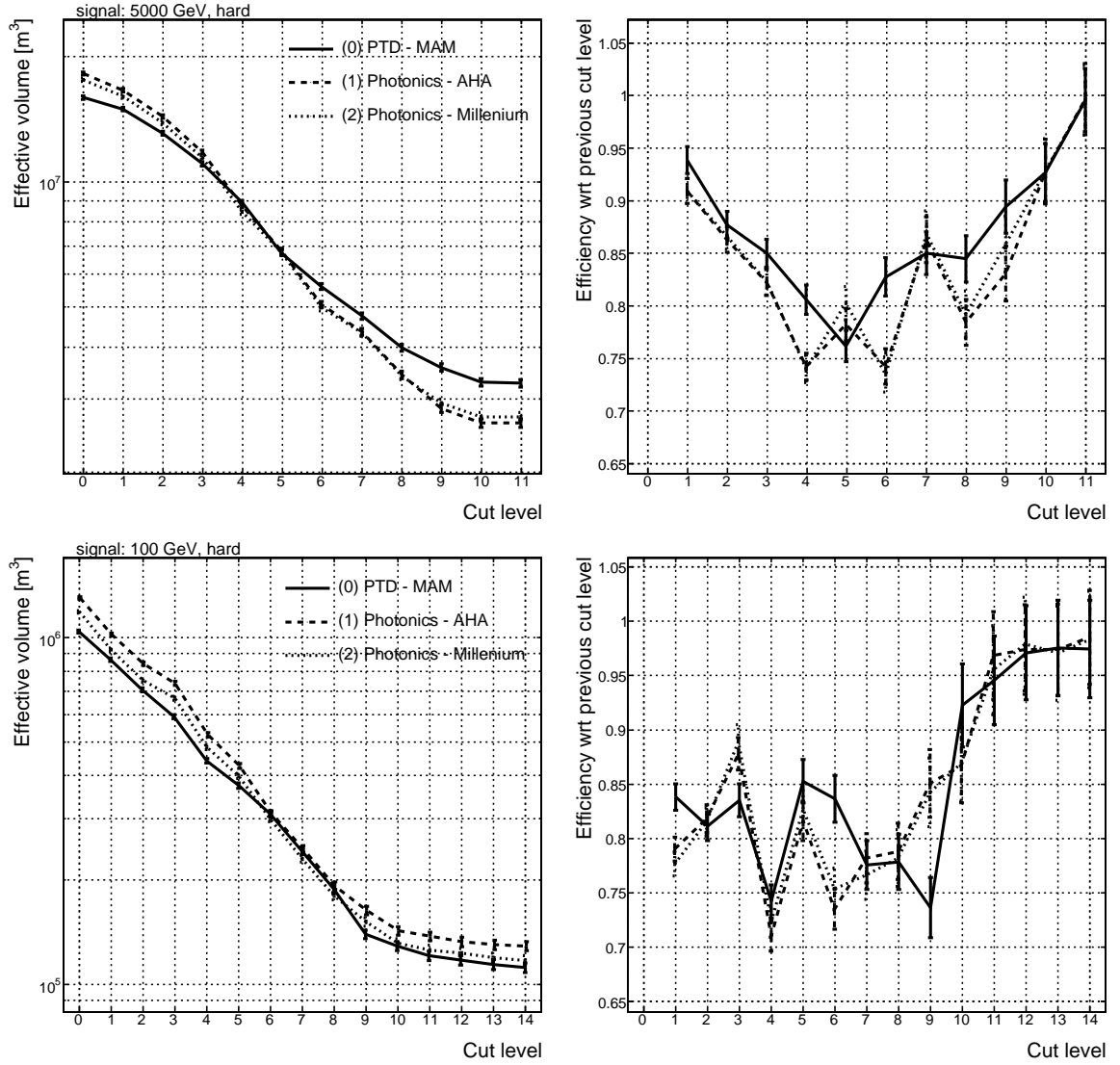


**Figure 8.3** – Left: evolution of effective volume with cut level (0=trigger level, 1=L1, 2=L2,  $\geq 3$ =L3 cuts) for three samples with different photon propagation settings. Right: efficiency of individual cuts. Top row is for the 5000 GeV hard neutralino model, the bottom row is for the 100 GeV hard model.

The first part of the error is the implementation of the ice layers  $(\Delta V/V)_a$ , shown in Fig. 8.2 (bottom row, right panels, dashed line). At first sight the evolution of the uncertainties seems unnatural, but it is perfectly explainable by the energy dependence of the observables and the trigger contribution. The PTD implementation of ice layers overestimates the signal efficiencies for all but two models (100 GeV hard and 250 GeV soft). While the HE filter models suffer a  $(\Delta V/V)_a = -(17 - 21)\%$  error, the situation for the LE filter models is a bit more complicated. We adopt  $-10\%$ ,  $-25\%$  and  $-35\%$  errors for the 100 GeV soft, 50 GeV hard and 50 GeV soft models respectively. The 100 GeV hard and 250 GeV soft models are assigned an error of  $+15\%$  and  $+22\%$ .

The uncertainty  $(\Delta V/V)_b$  due to the underlying optical properties of the ice is also

shown in Fig 8.2 (dotted line). We assume here that the same exercise for P<sub>TD</sub> ice models would produce similar results. The optical property errors are smaller than those induced by the ice layer implementation. We conservatively assume that the errors are symmetric and assign a 4% error to all models except 100 GeV hard (8%) and 250 GeV soft (10%).

The uncertainties from both photon propagation related sources are quadratically summed  $\frac{\Delta V}{V} = \sqrt{\left(\frac{\Delta V}{V}\right)_a^2 + \left(\frac{\Delta V}{V}\right)_b^2}$  and summarized in Tables 8.1 and 8.2. The errors range between  $-(8 - 35)\%$  and  $+(4 - 24)\%$ .

## 6. OM sensitivity

In the simulation we have set the relative light collection efficiency of the optical modules on strings 1 – 4 to 75% of that of the modules on the other strings. In reality each OM has its own individual sensitivity due to shading by the power cable, residual air bubbles from the hole refreeze process, transmittivity of the glass sphere, aging of the optical gel, the efficiency of the PMT. It is very difficult to learn something about the OM efficiencies, when we lack a very accurate model of the surrounding medium. Again, we assume no correlation with the other systematic effects, and consider two effects on the efficiency: a global shift for all OMs and individual shifts.

The experimental trigger rate fluctuates over the seasons, with a spread of about 7 Hz, see Figure 4.2. Atmospheric muon simulations were performed by [125] with various settings of the global OM sensitivity. It makes sense to assume that the change in the simulated trigger rate is maximal when the sensitivity of all OMs is simultaneously scaled up or down, a global shift. Also, this change should remain within the 7 Hz seasonal variation, which turns out to occur for a shift of  $\pm 7\%$  on the global OM efficiency [125].

We produce two additional simulation samples with OMs that are globally 7% less efficient ( $S_1$ ) and 7% more efficient ( $S_2$ ). Again, the rest of the chain is identical and the eight considered signal models are already introduced. For these three samples ( $S_1$ ,  $S_2$  and the baseline  $S_0$ ), the systematic effect on both the effective volume and the CI in  $\mu$  is studied.

Like before, the space angle distributions of the various samples are too similar to induce a clear systematic effect on the confidence interval. The results are entirely compatible with statistical fluctuations, and no systematic error is assigned.

Then we compare the effective volumes of both globally scaled samples  $i = 1, 2$  to that of the baseline:  $(\Delta V/V) = (V_i - V_0)/V_0$ . The effect is important for horizontal events, and increasingly so for lower energies. The low energy models reside close to the trigger thresholds, which is effectively higher in the horizontal than in the vertical direction. In these cases a few more (less) hits can make the difference between being triggered (or not), and between being well reconstructed (or not).

The result of this procedure is shown in Figure 8.4. No significant asymmetry was found, so the reported errors are symmetric. The smaller the mass, the stronger the effect on the effective volume. That is exactly what we expected. The influence of a global shift in OM efficiency on the effective volume is around 15 – 20% for the high energy models. For the low masses, the string trigger tempers the large errors induced by the multiplicity trigger (the latter reach 35% for the 100 GeV soft model). Therefore we believe that an uncertainty of 28% on the 50 GeV models is conservative.

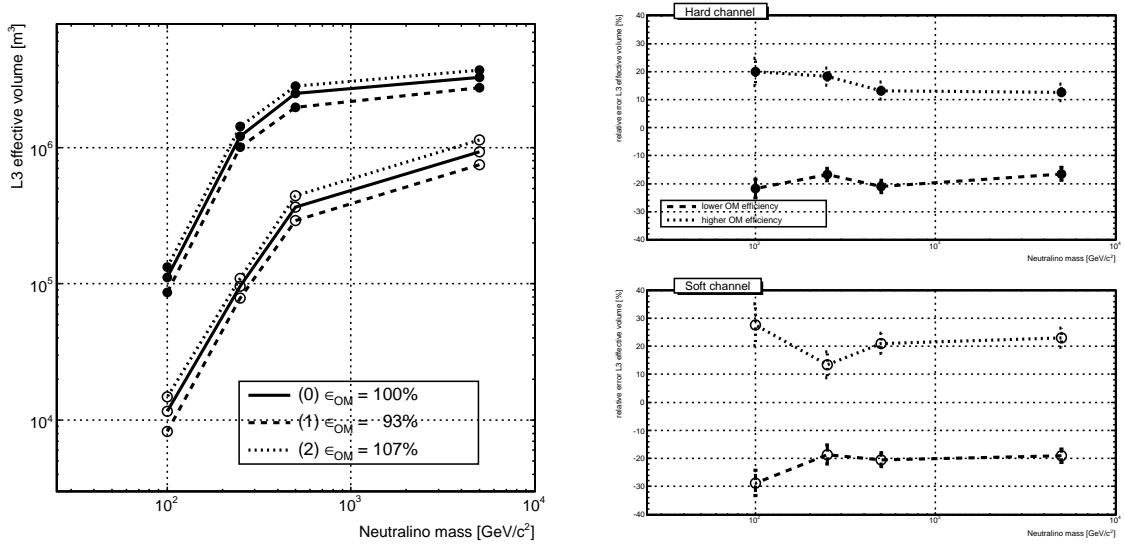


**Figure 8.4** – Left: effective volume at the final selection level, for three samples with different settings of the global scale of the OM efficiency. Curves at the top (bottom) represent the hard (soft) annihilation channel. Right: relative uncertainty due to a change in global OM efficiency (see text).

A MC study was performed in [85, 176] to investigate the effect of a 20% spread in efficiency for the individual modules. They found that the effective volume does not deviate by more than 5% from its baseline value. That is kind of expected, since individual gains/losses in OM efficiency are averaged out over the whole detector.

Since the curves in Fig. 8.4 suffer slightly from statistical fluctuations, we smoothed the evolution before calculating the quadratic sum of the uncertainties from the global shift and the individual spread. The outcome can be found in Tables 8.1 and 8.2.

## 7. Time and geometry calibration

A Monte Carlo study was performed in [176] to assess the influence of timing and geometry calibration uncertainties on the effective volume. These turned out to decrease the effective volume by less than 5%. This result is in agreement with an earlier conclusion that the reconstruction error does not depend very strongly on uncertainties in the timing calibration constants [122]. To be conservative we assume a 5% symmetric error.

### 8.1.3 Total uncertainty

We assume that all sources of uncertainties, whether statistical or systematic, are independent. In that case the total uncertainty on the effective volume is the sum of the squared uncertainties of each individual source

$$\frac{\Delta V}{V} = \sqrt{\sum_i \left(\frac{\Delta V}{V}\right)_i^2}$$

Neutralino mass - hard channel	5000	3000	1000	500	250	100	50
<i>Statistical uncertainty</i>	1	1	1	1	1	1	2
<i>Systematic uncertainty</i>							
1. Neutrino oscillation and cross section	+4 -9	+4 -9	+4 -10	+4 -11	+4 -7	+14 -4	+4 -10
2. Tau neutrinos	5	4	3	2	2	2	2
3. Density of the medium	1	1	1	1	1	1	1
4. Muon propagation	1	1	1	1	1	1	1
5. Photon propagation	+4 -21	+4 -20	+4 -19	+4 -18	+4 -17	+17 -8	+4 -25
6. OM sensitivity	16	17	18	19	21	24	28
7. Time and geometry calibration	5	5	5	5	5	5	5
<i>Total uncertainty on <math>V_{\text{eff}}</math></i>	+18 -29	+19 -29	+20 -29	+20 -29	+22 -28	+33 -26	+30 -40

**Table 8.1** – Summary of the relative uncertainties (in %) on the final level effective volume for the hard annihilation channel models.

Neutralino mass - soft channel	5000	3000	1000	500	250	100	50
<i>Statistical uncertainty</i>	1	1	1	1	1	2	3
<i>Systematic uncertainty</i>							
1. Neutrino oscillation and cross section	+26 -4	+18 -4	+5 -5	+4 -9	+4 -13	+4 -9	+4 -11
2. Tau neutrinos	4	3	2	2	2	2	2
3. Density of the medium	1	1	1	1	1	1	1
4. Muon propagation	1	1	1	1	1	1	1
5. Photon propagation	+4 -18	+4 -18	+4 -18	+4 -18	+24 -10	+4 -11	+4 -35
6. OM sensitivity	22	22	22	22	24	28	28
7. Time and geometry calibration	5	5	5	5	5	5	5
<i>Total uncertainty on <math>V_{\text{eff}}</math></i>	+35 -29	+29 -29	+23 -29	+23 -30	+34 -29	+30 -32	+30 -47

**Table 8.2** – Summary of the relative uncertainties (in %) on the final level effective volume for the soft annihilation channel models.

Tables 8.1 and 8.2 summarize the results for the hard and soft channel respectively. The errors are asymmetric due to the generator and the photon propagation. For all other sources we assumed, conservatively, symmetric errors. The total uncertainty is in the range  $+(18 - 35)\%$  and  $-(26 - 47)\%$ . The dominant contributions come from the photon propagation and the OM sensitivity, for some models the signal generator has a large effect too.

The uncertainty on the confidence interval  $\frac{\Delta\mu}{\mu}$  is only induced by statistical fluctuations in the space angle pdf's, since no significant systematic effects have been found. This error,  $\pm 3\%$ , is small with respect to that on the effective volume. The error on the live-time is even completely negligible.

In Section 8.2.5 we will see how these errors propagate to an error on the conversion rate.

## 8.2 Calculation of physical quantities

### 8.2.1 Conversion rate

The analysis in Chapter 6 selected a final sample of experimental events that was checked for the presence of signal events in Chapter 7. Unfortunately, we did not observe an excess of events in the direction of the Sun and upper limits on the number of signal events  $\mu \leq \mu_{\text{CL}}$  were derived, see Table 7.3.

A more fundamental quantity than the number of observed signal events is the rate  $\Gamma_{\nu \rightarrow \mu}$  of signal events observed in a volume of effective size  $V_{\text{eff}}$  during a time  $t_{\text{live}} = 383.6$  d. This quantity is coined the *neutrino-to-muon conversion rate*, and, in the absence of signal, we set an upper limit to it

$$\Gamma_{\nu \rightarrow \mu} \leq \Gamma_{\nu \rightarrow \mu}^{\text{CL}} = \frac{\mu_{\text{CL}}}{V_{\text{eff}} t_{\text{live}}}, \quad (8.1)$$

where  $\mu_{\text{CL}}$  and  $V_{\text{eff}}$  are affected by the experiment (and simulation) threshold on the muon energy, and hence  $\Gamma_{\nu \rightarrow \mu}$  as well.

The effective volume  $V_{\text{eff}}$  represents the size of the volume with 100% detection efficiency for the complete experiment (trigger, reconstruction and event selection), see Section 6.1. This quantity is energy and direction dependent: low energy or horizontal events will be more difficult to observe than high energy or vertical events. We reported  $V_{\text{eff}}$  for each signal model in Table 6.12. It was evaluated from simulation, which contains an intrinsic threshold on the muon energy of  $E_{\mu} \geq E_{\mu}^{\text{thr}} = 10$  GeV (Section 4.2.2).

### 8.2.2 Annihilation rate

The neutrino-to-muon conversion rate is directly proportional to the annihilation rate  $\Gamma_{\text{A}}$  of neutralinos in the centre of the Sun through

$$\Gamma_{\nu \rightarrow \mu} = \frac{\Gamma_{\text{A}}}{4\pi D^2} \int_0^{m_{\chi}} dE_{\nu} \left( \frac{dN_{\nu}}{dE_{\nu}} \right)_{\text{det}} \sigma_{\nu+N \rightarrow \mu+\dots}(E_{\nu} | E_{\mu} \geq E_{\mu}^{\text{thr}}) \rho_{\text{N}}. \quad (8.2)$$

The annihilations produce an isotropic flux of neutrinos with an energy spectrum  $\left( \frac{dN_{\nu}}{dE_{\nu}} \right)_{\text{det}}$  at the detector, which is located at a distance  $D$  from the Sun. The interaction part

is taken care of by  $\sigma_{\nu N}(E_\nu|E_\mu \geq E_\mu^{\text{thr}})$ , the charged-current neutrino-nucleon cross-section (including muon energy threshold), and the number density of nucleons in ice,  $\rho_N = \rho_{\text{ice}} N_A$ .

The only unknown in this expression is the neutrino energy spectrum, which receives contributions from each annihilation channel  $X$ , weighted by its branching ratio

$$\left(\frac{dN_\nu}{dE_\nu}\right)_{\text{det}} = \sum_X BR(\chi\chi \rightarrow X) \left(\frac{dN_\nu}{dE_\nu}\right)_{X,\text{det}}.$$

This total energy spectrum depends on the supersymmetric parameters: branching ratios and energy spectra are determined respectively by the composition and the mass of the neutralino, see Section 2.1.1. Unfortunately these SUSY parameters are unknown, so we are forced to arbitrarily choose the mass and the branching ratios to translate the measured conversion rate to an annihilation rate. Still, we want to report results that are as model independent as possible and meaningful for a large range of models.

The most natural way forward is to do the calculation for several well-chosen models. Since the sensitivity of our experiment (detector and offline analysis) to  $\Gamma_{\nu \rightarrow \mu}$  is energy dependent we sample neutralino models for different energy ranges. First of all, we chose seven masses between 50 – 5000 GeV. Afterwards, we perform the calculation for the most (hard) and least (soft) energetic spectrum for each of these masses. The hardest energy spectrum typically occurs for 100% annihilation to  $W^+W^-$  (or  $\tau^+\tau^-$  when  $m_\chi < m_W$ ), the softest spectrum when all annihilations go to  $b\bar{b}$ . Since any other choice of branching ratios leads to an intermediate energy spectrum, the experimental outcome lies between that of the hard and soft channel. Hence this procedure outlines the range of upper limits for plausible models, without being too model-dependent.

Note that the annihilation rate can easily be compared to theoretical predictions (depending on SUSY model assumptions and the galactic halo profile) or results from other experiments.

### 8.2.3 Muon flux

Historically, it became common practice to compare experiments through the muon flux rather than the annihilation rate. The muon flux above some muon energy threshold is inferred from the annihilation rate

$$\Phi_\mu(E_\mu \geq E_{\text{thr}}) = \frac{\Gamma_A}{4\pi D^2} \int_{E_{\text{thr}}}^{m_\chi} dE_\mu \frac{dN_\mu}{dE_\mu}, \quad (8.3)$$

where  $\frac{dN_\mu}{dE_\mu}$  includes the combined effect of neutrino production (SUSY model dependent), propagation, the interaction kinematics and subsequent muon energy losses. A more detailed expression can be found in [178]. At least the energy threshold enters in a non-trivial way, making the muon flux less suitable than  $\Gamma_A$  for comparison between experiments with different thresholds.

### 8.2.4 Neutralino-proton cross section

Equation 2.2, in Section 2.1.1, has shown us that the annihilation rate is proportional to the total neutralino-nucleon scattering cross section,  $\sigma_{\text{tot}} = \sigma_{\chi H}^{SD} + \sigma_{\chi H}^{SI} + 0.07\sigma_{\chi He}^{SI}$ , when

the capture and annihilation processes are in equilibrium in the Sun. According to [178], that is the case for the models within the reach of the current neutrino detectors.

Assuming that capture is dominated either by spin-dependent ( $\sigma_{tot} \simeq \sigma_{\chi H}^{SD}$ ) or spin-independent ( $\sigma_{tot} \simeq \sigma_{\chi H}^{SI} + 0.07\sigma_{\chi He}^{SI}$ ) scattering processes, one can infer respectively the SD and the SI neutralino-proton cross section from the annihilation rate. A detailed derivation of the proportionality factors between  $\Gamma_A$  and  $\sigma_{\chi p}^{SD}$  or  $\sigma_{\chi p}^{SI}$  was performed by [178], and included other elements than  $H$  and  $He$  in the Sun as well.

Several astrophysical and nuclear physics uncertainties enter the calculation, but their effect remains rather small. When the gravitational effects from planets on the capture rate is not considered, the uncertainty on the conversion to the spin-dependent cross section is not more than 3%. Otherwise, one must take a factor of two uncertainty. The translation to the SI cross section is uncertain within 25% due to the nuclear form factor  $F(E)$  (see Section 1.3.2) and the abundance of heavy elements in the Sun.

These neutralino-proton cross section measurements can be directly compared to the results from direct searches which were presented in Section 1.3.2.

## 8.2.5 Incorporation of uncertainties

The uncertainties (statistics and systematics) on  $V_{\text{eff}}$ ,  $\mu$  and  $t_{\text{live}}$  were presented in the first section of this chapter. How do these errors propagate to an error on the conversion rate  $\Gamma_{\nu \rightarrow \mu}$ ?

Ideally, the uncertainties (in statistical slang also *nuisance parameters*) should be included in the construction of the confidence interval in  $\mu$  to ensure proper coverage of the interval in  $\Gamma_{\nu \rightarrow \mu}$ . However, personal opinions diverge and no well-established method exists. E.g. for Poissonian statistics a semi-Bayesian procedure was suggested by [179, 180], which is the standard method within the collaboration for cut-and-count type of analyses. Other methods have been proposed as well [181, 182]. Since our test statistic  $R$  is not Poissonian, all methods are rather involved and not entirely objective. For these reasons we adopt a simpler method. It is easy to compute and keeps the confidence interval, with its well defined statistical properties, away from subjective methods that deal with nuisance parameters.

Basically, we simply vary  $V_{\text{eff}}$  and  $\mu$  (the error on  $t_{\text{live}}$  is negligible) within their  $1\sigma$  error band and calculate the new  $\Gamma'_{\nu \rightarrow \mu}$ . The toy Monte Carlo that we used assumes Gaussian errors ( $V'_{\text{eff}} \sim \mathcal{N}(V_{\text{eff}}, \Delta V_{\text{eff}})$  and  $\mu' \sim \mathcal{N}(\mu, \Delta\mu)$ ). The distribution  $\Gamma'_{\nu \rightarrow \mu}/\Gamma_{\nu \rightarrow \mu}$  for two choices of  $(\Delta\mu/\mu, \Delta V/V)$  is presented in Fig. 8.5 (left and central panel). The 16% and 84% quantiles of these asymmetric distributions represent the  $1\sigma$  uncertainty on  $\Gamma_{\nu \rightarrow \mu}$ .

After repeating this procedure for numerous settings  $(\Delta\mu/\mu, \Delta V/V)$  we found that

$$\pm \frac{\Delta\Gamma}{\Gamma} = \sqrt{\left(\frac{\Delta\mu}{\mu}\right)^2 + \left(\frac{\Delta V}{V}\right)^2 \left(\frac{1}{1 \mp \frac{\Delta V}{V}}\right)^2} \quad (8.4)$$

is a very good general approximation of the uncertainty on the conversion rate. The error is asymmetric due to the non-linear  $V_{\text{eff}}$ -dependence of the conversion rate. A small downward (large upward) fluctuation of  $V_{\text{eff}}$  leads to a large upward (small downward) fluctuation of  $\Gamma_{\nu \rightarrow \mu}$ . The rightmost panel in Fig 8.5 illustrates Eq. 8.4 (solid lines) for a 3% and 25%

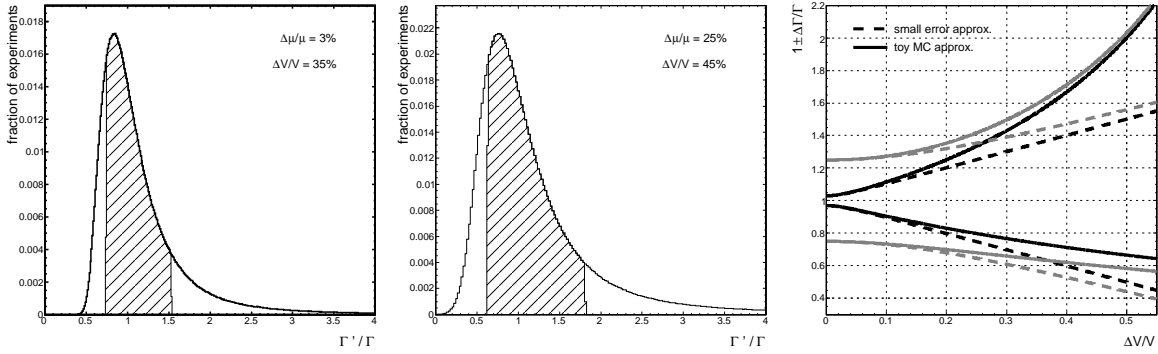


**Figure 8.5** – Left, central: Distribution of  $\Gamma$  due to a spread in effective volume and  $\mu$ . Right: evolution of the  $1\sigma$  error band with  $\Delta V/V$  for two choices of  $\Delta\mu/\mu$  (black = 3%, grey = 25%). While the solid line illustrates Eq. 8.4, the dashed line shows the small error approximation.

error on  $\mu$ . Also shown in the same figure is the result obtained by the usual theory on small error propagation (dashed lines). As expected, this approximation, which differs from Eq. 8.4 only by the factor  $(1 \mp \frac{\Delta V}{V})^{-2}$ , breaks down for large ( $>10\%$ ) errors in  $V_{\text{eff}}$ .

Remember that we have found  $\mathcal{O}(30\%)$  errors on the effective volume, so the small error approximation is not valid. Since the error on  $\mu$  is smaller than 3% the effective volume completely dominates the total error on the conversion rate. Along the same line, we assume that the uncertainty on the factors in Eq. 8.2 and Eq. 8.3 are negligible compared to that on  $\Gamma_{\nu \rightarrow \mu}$ . Hence, the inclusion of systematic uncertainties on the annihilation rate and muon flux simply involves a scaling of the limits with  $1 \pm \frac{\Delta\Gamma_{\nu \rightarrow \mu}}{\Gamma_{\nu \rightarrow \mu}}$ . The systematics scale factors are found in the last column of Tables 8.3 and 8.4. The relative uncertainties on  $\Gamma_{\nu \rightarrow \mu}$  range between  $-(15 - 25)\%$  and  $+(35 - 90)\%$ .

The uncertainties on the cross section calculation are not negligible however, but still smaller than those on the conversion rate. We add the errors from the translation and the conversion rate in quadrature.

### 8.3 Final results

We repeat that no excess of events in the direction of the Sun has been observed, which led to upper limits on the number of signal events  $\mu$ , Table 7.3 and Figure 7.7. Our results for  $V_{\text{eff}}$  and  $t_{\text{live}}$  were presented in Tables 6.12 and 4.2. Through Eq. 8.1 we obtain the 90% CL upper limit on the neutrino to muon conversion rate  $\Gamma_{\nu \rightarrow \mu}^{90\%}$ . The translation, Eq. 8.2 and 8.3, to upper limits on the annihilation rate  $\Gamma_{\text{A}}^{90\%}$  and muon flux  $\Phi_{\mu}^{90\%}$  is done with the formalism of [143, 183]. The neutrino to muon conversion rate has a 10 GeV threshold on the muon energy, due to our neutralino simulation set-up. To compare our results to other experiments with lower thresholds, we calculate the muon flux limits for a 1 GeV muon energy threshold. Our final results with 90% CL are summarized in Tables 8.3 and 8.4. In the same tables we also provide the muon flux upper limit with 99% CL ( $\Phi_{\mu}^{99\%}$ ), and the 90% CL sensitivity to the muon flux ( $\overline{\Phi}_{\mu}^{90\%}$ ). The latter quantity is the median upper limit

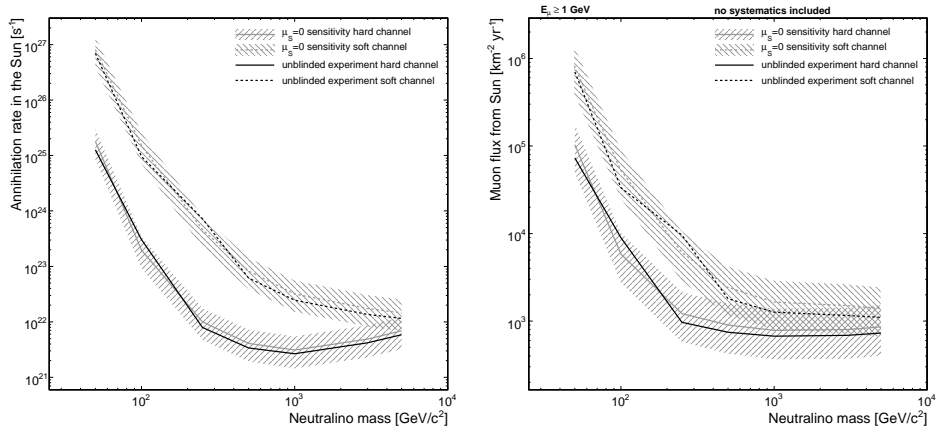


**Figure 8.6** – For all neutralino models and the combined trigger stream: the upper limit for the unblinded experiment (black) and the median value and  $1\sigma$  spread of the upper limit distribution for background-only experiments (grey). The left panel shows the annihilation rate in the Sun, the right panel the muon flux from the Sun above 1 GeV. Systematic uncertainties are not included, the confidence level is set at 90%.

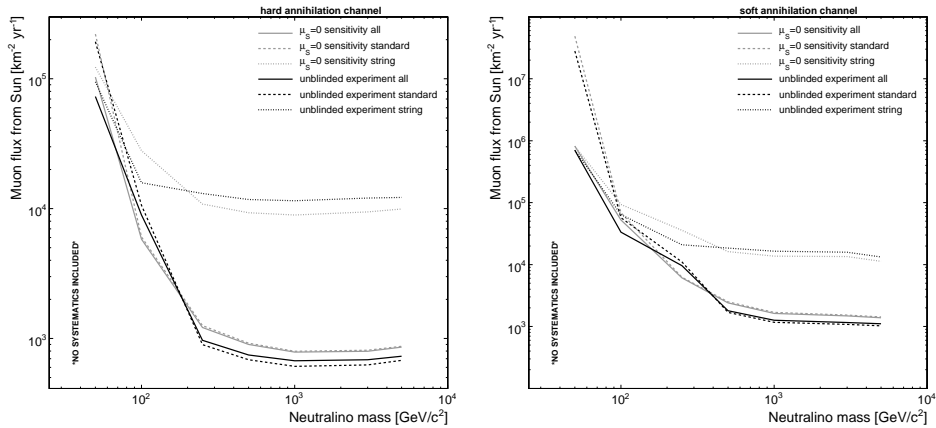


**Figure 8.7** – Upper limit with 90% CL on the flux of muons above 1 GeV from the Sun, for repeated background-only experiments (grey) and the unblinded experiment (black). We differentiate between the various trigger classes and annihilation channels (left: hard channel, right: soft channel). No systematic uncertainties are included. Mind the different scales in both panels.

for repeated background-only experiments, a concept discussed in the previous chapter.

Figure 8.6 is a graphic representation of the obtained 90% CL upper limits on the annihilation rate and the muon flux. These limits (black) are compared to what is expected in the no-signal case (grey area), the information is equivalent to that in Fig. 7.7. Above  $m_\chi \geq 1000$  GeV the muon flux limits of both annihilation channels are within a factor of two. The difference becomes more pronounced for low masses, with a factor ten difference for  $m_\chi = 50$  GeV.

Take note that these upper limits do not include systematic uncertainties. We already mentioned that various prescriptions co-exist. Also for practical reasons we decided to keep the systematics away from the CI construction. Instead scale factors (last column) are

hard channel		$\Gamma_{\nu \rightarrow \mu}^{90\%}$ [ $\text{km}^{-3} \text{yr}^{-1}$ ]	$\Gamma_A^{90\%}$ [ $\text{s}^{-1}$ ]	$\Phi_{\mu}^{90\%}$ [ $\text{km}^{-2} \text{yr}^{-1}$ ]	$\overline{\Phi}_{\mu}^{90\%}$ [ $\text{km}^{-2} \text{yr}^{-1}$ ]	$\Phi_{\mu}^{99\%}$ [ $\text{km}^{-2} \text{yr}^{-1}$ ]	syst. unc. $1 - / + \frac{\Delta\Gamma}{\Gamma}$
5000	<b>all</b>	<b><math>1.16 \times 10^3</math></b>	<b><math>5.89 \times 10^{21}</math></b>	<b><math>7.31 \times 10^2</math></b>	<b><math>8.60 \times 10^2</math></b>	<b><math>1.42 \times 10^3</math></b>	<b>0.84 / 1.41</b>
	std	$1.08 \times 10^3$	$5.47 \times 10^{21}$	$6.79 \times 10^2$	$8.71 \times 10^2$		
	str	$1.94 \times 10^4$	$9.83 \times 10^{22}$	$1.22 \times 10^4$	$9.96 \times 10^3$		
3000	<b>all</b>	<b><math>1.04 \times 10^3</math></b>	<b><math>4.21 \times 10^{21}</math></b>	<b><math>6.87 \times 10^2</math></b>	<b><math>7.99 \times 10^2</math></b>	<b><math>1.33 \times 10^3</math></b>	<b>0.84 / 1.40</b>
	std	$9.52 \times 10^2$	$3.85 \times 10^{21}$	$6.27 \times 10^2$	$8.11 \times 10^2$		
	str	$1.84 \times 10^4$	$7.42 \times 10^{22}$	$1.21 \times 10^4$	$9.45 \times 10^3$		
1000	<b>all</b>	<b><math>1.07 \times 10^3</math></b>	<b><math>2.67 \times 10^{21}</math></b>	<b><math>6.73 \times 10^2</math></b>	<b><math>7.85 \times 10^2</math></b>	<b><math>1.30 \times 10^3</math></b>	<b>0.83 / 1.40</b>
	std	$9.67 \times 10^2$	$2.42 \times 10^{21}$	$6.11 \times 10^2$	$7.97 \times 10^2$		
	str	$1.82 \times 10^4$	$4.57 \times 10^{22}$	$1.15 \times 10^4$	$8.95 \times 10^3$		
500	<b>all</b>	<b><math>1.54 \times 10^3</math></b>	<b><math>3.39 \times 10^{21}</math></b>	<b><math>7.47 \times 10^2</math></b>	<b><math>9.00 \times 10^2</math></b>	<b><math>1.45 \times 10^3</math></b>	<b>0.83 / 1.41</b>
	std	$1.42 \times 10^3$	$3.11 \times 10^{21}$	$6.86 \times 10^2$	$9.19 \times 10^2$		
	str	$2.43 \times 10^4$	$5.34 \times 10^{22}$	$1.18 \times 10^4$	$9.31 \times 10^3$		
250	<b>all</b>	<b><math>3.15 \times 10^3</math></b>	<b><math>7.95 \times 10^{21}</math></b>	<b><math>9.68 \times 10^2</math></b>	<b><math>1.22 \times 10^3</math></b>	<b><math>1.89 \times 10^3</math></b>	<b>0.82 / 1.39</b>
	std	$2.91 \times 10^3$	$7.36 \times 10^{21}$	$8.96 \times 10^2$	$1.26 \times 10^3$		
	str	$4.26 \times 10^4$	$1.08 \times 10^{23}$	$1.31 \times 10^4$	$1.08 \times 10^4$		
100	<b>all</b>	<b><math>6.78 \times 10^4</math></b>	<b><math>3.03 \times 10^{23}</math></b>	<b><math>8.94 \times 10^3</math></b>	<b><math>5.81 \times 10^3</math></b>	<b><math>1.40 \times 10^4</math></b>	<b>0.75 / 1.35</b>
	std	$8.05 \times 10^4$	$3.60 \times 10^{23}$	$1.06 \times 10^4$	$6.05 \times 10^3$		
	str	$1.20 \times 10^5$	$5.37 \times 10^{23}$	$1.58 \times 10^4$	$2.79 \times 10^4$		
50	<b>all</b>	<b><math>8.21 \times 10^5</math></b>	<b><math>1.27 \times 10^{25}</math></b>	<b><math>7.30 \times 10^4</math></b>	<b><math>1.03 \times 10^5</math></b>	<b><math>1.45 \times 10^5</math></b>	<b>0.77 / 1.66</b>
	std	$2.17 \times 10^6$	$3.35 \times 10^{25}$	$1.93 \times 10^5$	$2.21 \times 10^5$		
	str	$1.07 \times 10^6$	$1.64 \times 10^{25}$	$9.49 \times 10^4$	$1.23 \times 10^5$		

**Table 8.3** – Final results for the hard annihilation channel: unblinded conversion rate ( $E_{\mu} \geq 10 \text{ GeV}$ ), annihilation rate and muon flux ( $E_{\mu} \geq 1 \text{ GeV}$ ) upper limits at 90% CL. Also shown are the median 90% CL upper limit in the no-signal scenario and the unblinded 99% CL upper limit. The last column contain the scale factors needed to include systematic uncertainties on these upper limits. Results are also broken up according to their trigger stream.

provided in the table, which can be used to incorporate systematic errors in a qualitative way. Then the statistical coverage of the unscaled limits is guaranteed, but the reader is free to interpret our results in the context of systematics. The same scale factors should be used for  $\Gamma_{\nu \rightarrow \mu}$ ,  $\Gamma_A$  and  $\phi_{\mu}$ . The systematic uncertainty on the muon flux is shown in Fig. 8.8 as a shaded band around the result without systematics. Our preference is to consider the most conservative bound as the final outcome of this analysis.

For each model we evaluated the upper limit on  $\mu$  for the individual trigger streams (standard and string) as well, using the single experiment likelihood (Eq. 7.1). These limits are translated to limits on conversion rate, annihilation rate and muon flux in the same way as for the combined event stream. The results are presented in the same table as before and in Figure 8.7. We observe that the combined (grey solid) muon flux sensitivity is always better than for a single trigger experiment (grey dashed, dotted), as expected. For the unblinded limits that turns out differently, due to statistical fluctuations. The *standard trigger* limit (black dashed) is slightly better than the *all trigger* limit (black solid) for all signal models that use final data sample A (5000 – 250 GeV hard, 5000 – 500 GeV soft).

soft channel	$\Gamma_{\nu \rightarrow \mu}^{90\%}$ [ $\text{km}^{-3} \text{yr}^{-1}$ ]	$\Gamma_A^{90\%}$ [ $\text{s}^{-1}$ ]	$\Phi_{\mu}^{90\%}$ [ $\text{km}^{-2} \text{yr}^{-1}$ ]	$\overline{\Phi}_{\mu}^{90\%}$ [ $\text{km}^{-2} \text{yr}^{-1}$ ]	$\Phi_{\mu}^{99\%}$ [ $\text{km}^{-2} \text{yr}^{-1}$ ]	syst. unc. $1 - / + \frac{\Delta\Gamma}{\Gamma}$
5000 <b>all</b>	<b><math>4.19 \times 10^3</math></b>	<b><math>1.15 \times 10^{22}</math></b>	<b><math>1.10 \times 10^3</math></b>	<b><math>1.38 \times 10^3</math></b>	<b><math>2.14 \times 10^3</math></b>	<b>0.74 / 1.41</b>
std	$3.88 \times 10^3$	$1.07 \times 10^{22}$	$1.02 \times 10^3$	$1.43 \times 10^3$		
str	$5.04 \times 10^4$	$1.38 \times 10^{23}$	$1.32 \times 10^4$	$1.13 \times 10^4$		
3000 <b>all</b>	<b><math>4.53 \times 10^3</math></b>	<b><math>1.36 \times 10^{22}</math></b>	<b><math>1.16 \times 10^3</math></b>	<b><math>1.48 \times 10^3</math></b>	<b><math>2.28 \times 10^3</math></b>	<b>0.77 / 1.40</b>
std	$4.22 \times 10^3$	$1.27 \times 10^{22}$	$1.08 \times 10^3$	$1.53 \times 10^3$		
str	$6.19 \times 10^4$	$1.86 \times 10^{23}$	$1.58 \times 10^4$	$1.34 \times 10^4$		
1000 <b>all</b>	<b><math>6.00 \times 10^3</math></b>	<b><math>2.46 \times 10^{22}</math></b>	<b><math>1.26 \times 10^3</math></b>	<b><math>1.63 \times 10^3</math></b>	<b><math>2.48 \times 10^3</math></b>	<b>0.81 / 1.40</b>
std	$5.53 \times 10^3$	$2.27 \times 10^{22}$	$1.17 \times 10^3$	$1.68 \times 10^3$		
str	$7.80 \times 10^4$	$3.20 \times 10^{23}$	$1.64 \times 10^4$	$1.36 \times 10^4$		
500 <b>all</b>	<b><math>1.06 \times 10^4</math></b>	<b><math>6.17 \times 10^{22}</math></b>	<b><math>1.80 \times 10^3</math></b>	<b><math>2.40 \times 10^3</math></b>	<b><math>3.52 \times 10^3</math></b>	<b>0.81 / 1.42</b>
std	$9.96 \times 10^3$	$5.79 \times 10^{22}$	$1.69 \times 10^3$	$2.50 \times 10^3$		
str	$1.09 \times 10^5$	$6.36 \times 10^{23}$	$1.85 \times 10^4$	$1.61 \times 10^4$		
250 <b>all</b>	<b><math>7.60 \times 10^4</math></b>	<b><math>7.24 \times 10^{23}</math></b>	<b><math>9.62 \times 10^3</math></b>	<b><math>6.12 \times 10^3</math></b>	<b><math>1.50 \times 10^4</math></b>	<b>0.74 / 1.41</b>
std	$8.71 \times 10^4$	$8.30 \times 10^{23}$	$1.10 \times 10^4$	$6.26 \times 10^3$		
str	$1.65 \times 10^5$	$1.57 \times 10^{24}$	$2.09 \times 10^4$	$3.58 \times 10^4$		
100 <b>all</b>	<b><math>3.32 \times 10^5</math></b>	<b><math>9.58 \times 10^{24}</math></b>	<b><math>3.34 \times 10^4</math></b>	<b><math>5.27 \times 10^4</math></b>	<b><math>7.04 \times 10^4</math></b>	<b>0.77 / 1.48</b>
std	$5.70 \times 10^5$	$1.65 \times 10^{25}$	$5.73 \times 10^4$	$6.86 \times 10^4$		
str	$6.38 \times 10^5$	$1.84 \times 10^{25}$	$6.42 \times 10^4$	$9.38 \times 10^4$		
50 <b>all</b>	<b><math>4.83 \times 10^6</math></b>	<b><math>6.96 \times 10^{26}</math></b>	<b><math>7.00 \times 10^5</math></b>	<b><math>8.16 \times 10^5</math></b>	<b><math>1.30 \times 10^6</math></b>	<b>0.77 / 1.89</b>
std	$1.95 \times 10^8$	$2.80 \times 10^{28}$	$2.82 \times 10^7$	$4.89 \times 10^7$		
str	$4.88 \times 10^6$	$7.02 \times 10^{26}$	$7.06 \times 10^5$	$8.17 \times 10^5$		

**Table 8.4** – Final results for the soft annihilation channel: unblinded conversion rate ( $E_{\mu} \geq 10 \text{ GeV}$ ), annihilation rate and muon flux ( $E_{\mu} \geq 1 \text{ GeV}$ ) upper limits at 90% CL. Also shown are the median 90% CL upper limit in the no-signal scenario and the unblinded 99% CL upper limit. The last column contain the scale factors needed to include systematic uncertainties on these upper limits. Results are also broken up according to their trigger stream.

These numbers are only meant to illustrate the outcome of a single trigger experiment. We do not want to confuse the reader and clearly state that our final result remains the combined trigger limit (bold values in the table).

Based on the muon flux sensitivities we also conclude that the string trigger is vital for the lowest energy models. Without the string trigger, the sensitivity for the 50 GeV soft model would suffer a loss of a factor 60! For the 50 GeV hard and 100 GeV soft models the combined trigger sensitivity improves by a factor 2 and 1.3. For the other models the gain is at most 5%. The string trigger is therefore really essential in this low energy region, even for horizontal fluxes.

The cross section was translated from the annihilation rate, using the formalism of [178]. Table 8.5 presents the 90% CL upper limits on the spin-independent and the spin-dependent neutralino-proton scattering cross section, without and with systematic uncertainties (only the conservative case for the systematic uncertainties is considered). We obtain spin-dependent results in the range ( $10^{-4} - 1$ ) pb, the spin-independent limits are typically three orders of magnitude better.

	$\sigma_{\chi P}^{SI} [\text{cm}^2]$		$\sigma_{\chi P}^{SD} [\text{cm}^2]$	
	w/o syst.	with syst.	w/o syst.	with syst.
5000 hard	$7.12 \times 10^{-41}$	$1.05 \times 10^{-40}$	$1.06 \times 10^{-37}$	$1.50 \times 10^{-37}$
3000 hard	$1.88 \times 10^{-41}$	$2.76 \times 10^{-41}$	$2.74 \times 10^{-38}$	$3.84 \times 10^{-38}$
1000 hard	$1.50 \times 10^{-42}$	$2.21 \times 10^{-42}$	$1.95 \times 10^{-39}$	$2.73 \times 10^{-39}$
500 hard	$5.75 \times 10^{-43}$	$8.51 \times 10^{-43}$	$6.23 \times 10^{-40}$	$8.79 \times 10^{-40}$
250 hard	$4.67 \times 10^{-43}$	$6.83 \times 10^{-43}$	$3.74 \times 10^{-40}$	$5.20 \times 10^{-40}$
100 hard	$5.48 \times 10^{-42}$	$7.84 \times 10^{-42}$	$2.45 \times 10^{-39}$	$3.31 \times 10^{-39}$
50 hard	$1.11 \times 10^{-40}$	$1.89 \times 10^{-40}$	$2.89 \times 10^{-38}$	$4.81 \times 10^{-38}$
5000 soft	$1.39 \times 10^{-40}$	$2.06 \times 10^{-40}$	$2.08 \times 10^{-37}$	$2.93 \times 10^{-37}$
3000 soft	$6.06 \times 10^{-41}$	$8.91 \times 10^{-41}$	$8.84 \times 10^{-38}$	$1.24 \times 10^{-37}$
1000 soft	$1.39 \times 10^{-41}$	$2.04 \times 10^{-41}$	$1.79 \times 10^{-38}$	$2.51 \times 10^{-38}$
500 soft	$1.05 \times 10^{-41}$	$1.56 \times 10^{-41}$	$1.13 \times 10^{-38}$	$1.61 \times 10^{-38}$
250 soft	$4.25 \times 10^{-41}$	$6.29 \times 10^{-41}$	$3.40 \times 10^{-38}$	$4.80 \times 10^{-38}$
100 soft	$1.73 \times 10^{-40}$	$2.67 \times 10^{-40}$	$7.73 \times 10^{-38}$	$1.15 \times 10^{-37}$
50 soft	$6.09 \times 10^{-39}$	$1.17 \times 10^{-38}$	$1.59 \times 10^{-36}$	$3.01 \times 10^{-36}$

**Table 8.5** – Upper limit at 90% CL on the spin-independent and spin-dependent neutralino-proton cross section. We quote values without and with systematic uncertainties.

## 8.4 Comparison with other experimental results

This section puts our final results into the perspective of other experimental results and theoretical predictions. So far, no experiment has seen significant evidence from neutralino annihilations in the Sun.

### 8.4.1 Muon flux

Figure 8.8 (top) compares the 90% CL upper limits (including systematics) on the muon flux set by various solar neutralino searches in AMANDA data. Two lines are present for each analysis, corresponding to both annihilation channels (bottom line is always the hard channel). The band around our limit shows the size of the systematic error, we interpret the upper edge as our final result. The reported limits of the 2001 search [129, 152] were affected by a bug in the calculation of the effective volume, and is therefore too conservative [150]. The upper limits for the 2003 data analysis are the result of a similar analysis as this work, except for the selection part that opted for a multi-dimensional approach [130]. The dashed curves were obtained as a side result of a maximum-likelihood search for point sources in the complete AMANDA data set of 953 days of live-time [184]. Even though we have less than half of the live-time of the latter analysis, our results are the most sensitive of all AMANDA analyses for neutralinos lighter than roughly 200 GeV.

The markers represent theoretical model predictions. They were computed by scanning over a reduced MSSM phase space with seven free parameters, referred to as MSSM-7 [143, 185]. At each point in this multi-dimensional space several quantities are calculated: the neutralino mass, its admixture, the relic density, the annihilation rate in the Sun, the muon flux from the Sun, the spin-independent and spin-dependent neutralino-nucleon cross

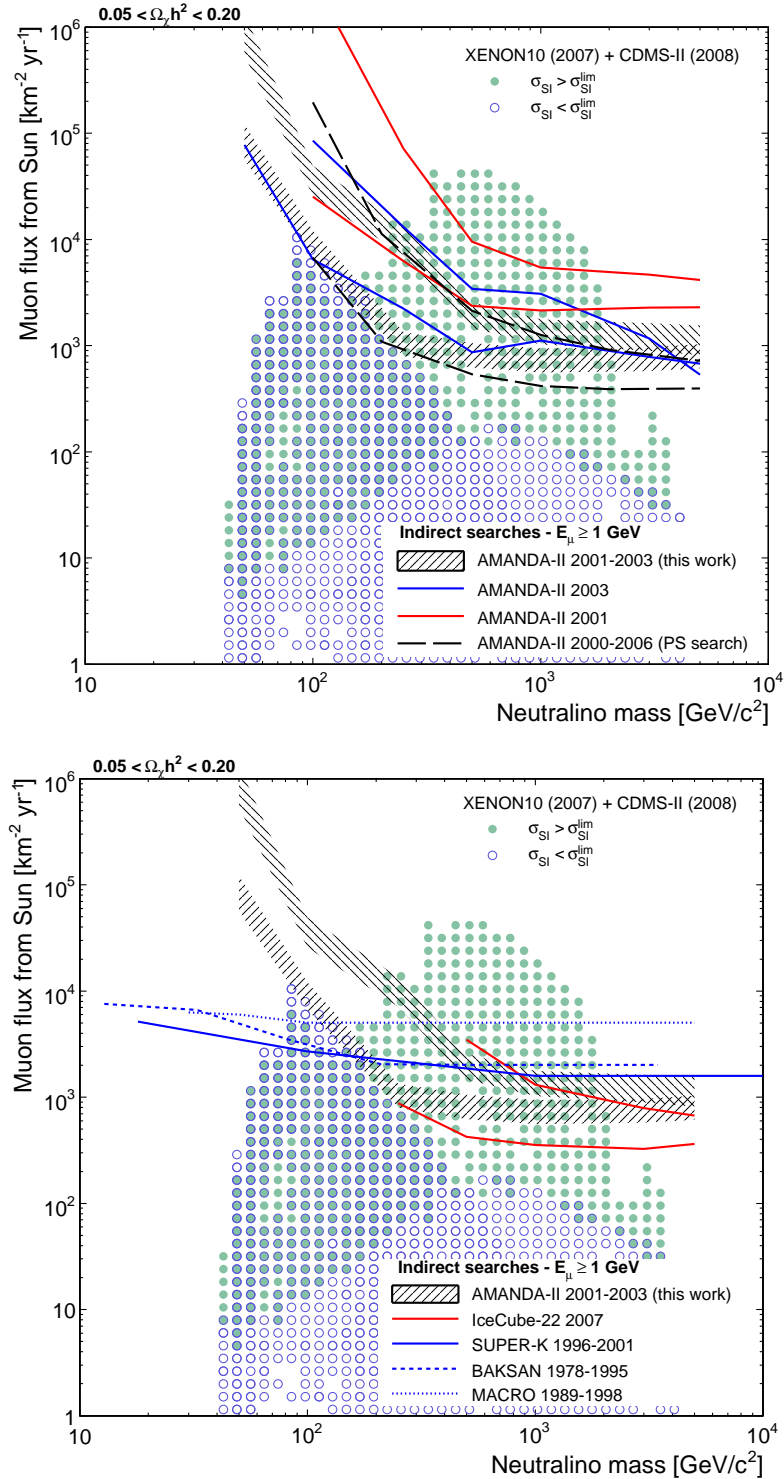


**Figure 8.8** – Upper limit on the muon flux from the Sun at 90% CL, including systematics. Top: comparison between various AMANDA searches. Bottom: comparison of various indirect experiments. The AMANDA and IceCube limits are shown for the soft (top line) and hard (bottom line) annihilation channels. In both figures the MSSM-7 phase space is indicated by markers, which are either allowed (blue hollow) or disfavoured (green solid) by the spin-independent cross section limits set by direct searches. See text for more details.

section, ... The information of the spin-independent cross section is compared to the upper limits set by the direct search experiments CDMS [55] and XENON10 [56], see Section 1.3.2. The colour code in the figure shows whether the calculated cross section is above (green solid) or below (blue hollow) the experimental limit. The XENON10 experiment provides the strongest limit below  $m_\chi = 40$  GeV, for higher masses CDMS is more sensitive. Our upper limits enter the region not completely tested by direct detection experiments for masses below 200 GeV.

Figure 8.8 (bottom) presents the same theoretical models, but the muon flux upper limits of different indirect experiments: an early configuration of IceCube with 22 strings [85], Super-K [82], BAKSAN [80] and MACRO [79]. Below 200 GeV Super-K, with its low threshold, sets the strongest limits, while above 200 GeV the AMANDA and IceCube neutrino telescopes benefit from their much larger volume. IceCube is more sensitive for higher masses with respect to AMANDA, due to the larger instrumented volume. For lower masses however, the higher IceCube trigger threshold starts to play a role and no search was conducted.

### 8.4.2 Cross sections

In Fig. 8.9 we compare the spin-dependent neutralino-proton elastic cross section limits from various experiments. It is clear that the enormous mass of hydrogen in the Sun allows a much stronger constraint on the spin-dependent cross section than those set by Earthbound direct detection experiments like CDMS [55], COUPP [58] and KIMS [59]. The shaded area shows the MSSM-7 phase space, that is compatible with the direct search results on the spin-independent coupling. These models are only just out of reach for AMANDA and IceCube.

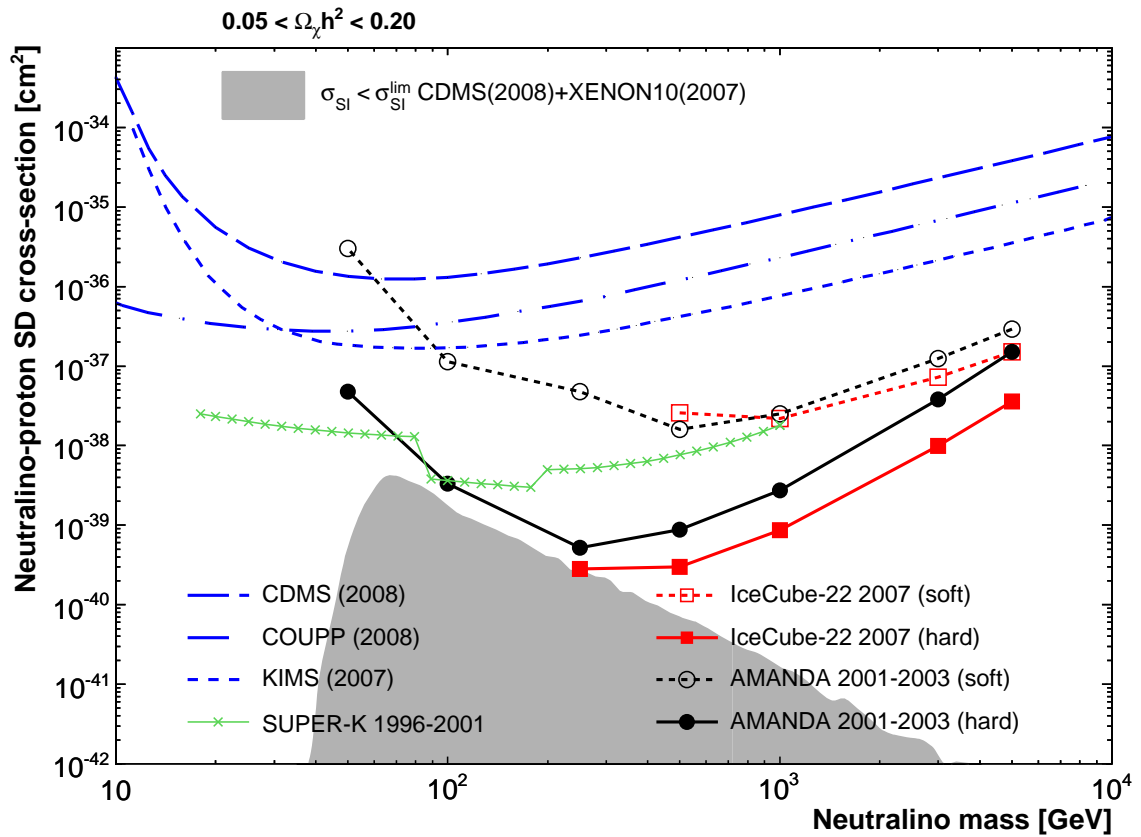


**Figure 8.9** – Upper limit at 90% CL on the spin-dependent scattering cross section on protons. The AMANDA and IceCube results are calculated separately for the hard and soft annihilation channel, including systematics. The other bounds were obtained by direct searches (CDMS, COUPP, KIMS) and by an indirect search for neutrinos in the Sun (Super-Kamiokande). The shaded area represents the MSSM-7 parameter space not excluded by the spin-independent cross section results from CDMS and XENON10.

# Chapter 9

## Conclusions and outlook

The aim of this work was to search for GeV–TeV neutrinos from the Sun in a data set of  $3.5 \times 10^9$  events collected by the AMANDA neutrino detector during 384 effective days of operation in 2001–2003. Such a neutrino flux is predicted when GeV–TeV mass particles self-annihilate near the solar centre. These heavy particles may well constitute the, so far unidentified, dark matter which permeates our universe according to the current standard model of cosmology. The indirect detection via neutrinos of dark matter annihilations would give an eagerly awaited clue about the dark matter identity. We focused on the supersymmetric neutralino, but performed the analysis in a model-independent way. Our results are therefore relevant for any GeV–TeV dark matter particle annihilating to Standard Model particles.

After the preparatory work in Chapters 4 and 5, the first objective in our data analysis was to reduce the atmospheric background in the data sample by selecting well-reconstructed, horizontal tracks. The considered neutralino mass phase space spans two decades, with the lower end residing close to the AMANDA trigger threshold. To obtain good overall sensitivity we defined two event classes (due to differences in event topologies of standard and string triggers) and two neutralino signal templates (due to the energy-dependent response of the detector) for which separate event selection criteria were optimized. This work was described in Chapter 6. We achieved a background reduction around  $10^{-7}$ , while preserving 1%–19% of the triggered neutralino events (depending on neutralino mass and the dominant annihilation channel). The final data samples contained around 400–700 events.

Our second objective in the data analysis was to search for an excess of events from the direction of the Sun over the expected atmospheric background. In Chapter 7 we presented a novel likelihood-ratio method to infer a physically relevant confidence interval in the number of signal events from the distribution of the space angle between the direction of the observed events and the Sun. To maximize the benefit from the specific characteristics of both triggers we extended the method by allowing the combination of the likelihood-functions from both trigger event streams.

The principal result of our work is that in the direction of the Sun no statistically significant deviation (excess or deficit) from the atmospheric background was observed in the final data sample. The resultant 90% confidence level upper limits on the number of signal events were calculated for several neutralino models with masses between 50–

5000 GeV, each time for the hard and soft annihilation channel. These upper limits were then translated to upper limits on the neutrino-to-muon conversion rate in the detector, the neutralino annihilation rate in the Sun, the neutralino-induced muon flux at the detector and the neutralino-proton elastic scattering cross sections. E.g. the 90% CL upper limits on the muon flux range between  $6.7 \times 10^2 - 7.3 \times 10^4 \text{ km}^{-2} \text{ yr}^{-1}$  for the hard annihilation channel and  $1.1 \times 10^3 - 7.0 \times 10^5 \text{ km}^{-2} \text{ yr}^{-1}$  for the soft channel.

In a final study we examined the effect of systematic uncertainties on these limits, concluding that they are affected by 35–90% mainly due to the poorly known absolute sensitivity of the optical modules and due to the approximative description of the optical properties of the ice. Including these uncertainties in an ad hoc fashion and assuming the most conservative systematic error, our 90% CL upper limits on the muon flux range between  $9.4 \times 10^2 - 1.2 \times 10^5 \text{ km}^{-2} \text{ yr}^{-1}$  for the hard channel and  $1.5 \times 10^3 - 1.3 \times 10^6 \text{ km}^{-2} \text{ yr}^{-1}$  for the soft channel. Under the same assumptions, the bounds on the spin-dependent cross section reside in the range 0.0001 – 1 pb, which is much more constraining than the upper limits reported by direct detection experiments.

We also found that the string trigger improves AMANDA's trigger efficiency for signal events by 25% to a factor 140 (depending on the neutralino model), even though it concerns horizontal events and though the string trigger was tailored for vertical events. Some of this gain is preserved after the complete analysis, which was designed to keep the event streams from both triggers in parallel. The improvement of the combined trigger sensitivity over the standard trigger sensitivity ranges between 30% and a factor 60, while for masses above 250 GeV the gain is not more than 5%. We therefore concluded that the string trigger is vital for neutralinos lighter than 100 GeV.

An important point of improvement for the analysis would be the reduction of the systematic uncertainties related to the optical model of the ice and to the optical module sensitivity, especially at the lowest energies where a  $> 50\%$  error is reached. Unfortunately, this is a very complex exercise due to correlations, which is under intense study in the collaboration at the moment. The PHOTONICS implementation model is now the standard tool in AMANDA and IceCube, providing a more accurate description of the propagation of photons through the detector. The second uncertainty, on the optical module sensitivity, is reduced by performing an absolute calibration of modules prior to deployment. It is too late to do that for AMANDA, but efforts for its successor IceCube are well under way.

We also note that the reported confidence intervals (i.e. upper limits) were derived without incorporating systematic uncertainties in the space angle likelihood descriptions. Instead, the reader can include the systematic effects in an ad hoc fashion by applying a scale factor, like we did in one of the previous concluding paragraphs. This is the simplest approach, but it does not guarantee a frequentist coverage of the scaled limits. In the literature various methods are proposed to incorporate systematics in the construction of the confidence intervals, but they tend to be complicated to implement. Nevertheless, we encourage future pursuits along these lines.

A possible point of improvement is the optimization criterion. The muon flux sensitivity of the analysis is proportional to the ratio  $\bar{\mu}/V_{\text{eff}}$ . Optimal event selection criteria are typically found by maximizing the Model Rejection Potential  $V_{\text{eff}}/\bar{\mu}(n_{\text{bkg}})$ , which is based on the Poisson expectation of the upper limit in a background-only scenario, and well suited

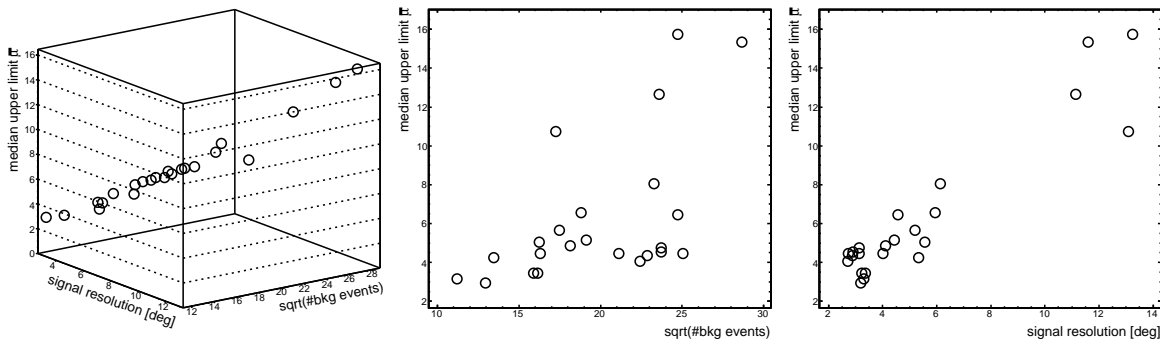


**Figure 9.1** – Two and one-dimensional dependencies of the median signal event upper limit  $\bar{\mu}$  on the (square root of) the number of background events  $n_{\text{bkg}}$  and the signal resolution  $\psi_{\text{sig}}$ . The markers represent the outcome of the likelihood-ratio test procedure for several signal models and various cut levels.

to reduce the background. This criterion does not necessarily improve the signal resolution, even though it is a sensitive element in the calculation of the median upper limit  $\bar{\mu}$  through the likelihood-ratio test. Unfortunately, it is impracticable to evaluate  $\bar{\mu}$  at each step in the optimization of the event filter, due to the CPUtime requirements. However, we ran into a possible way forward. In a preliminary study we found that it is possible to describe the median upper limit as a one-to-one function of the number of background events *and* the signal resolution, see Fig. 9.1. Such a functional form  $\bar{\mu}(n_{\text{bkg}}, \psi_{\text{sig}})$ , once proven to be valid for general situations as well, could then replace the average Poisson upper limit  $\bar{\mu}(n_{\text{bkg}})$  in the Model Rejection Potential. Further study can put this on solid ground.

An analysis of a larger AMANDA data sample, collected between 2001–2006, is under way. It exploits a multi-dimensional classifier to reduce the background and is therefore expected to improve over our results at low masses by a larger factor than what is expected from additional statistics alone. For high masses this intrinsic improvement should be small when compared to low masses.

Finally, the most obvious improvement for this search is to enlarge the detection volume. When completed in 2011, AMANDA's successor, the IceCube, will have 80 strings and a  $1 \text{ km}^3$  instrumented volume. This is 60 times larger than the volume encompassed by AMANDA. IceCube is still under construction and currently 75% complete. The first results from early detector configurations are being published. In Fig. 8.8 we showed the recent IceCube 22-string upper limits on the muon flux from neutralino annihilations in the Sun, which are very restrictive for high masses. The loss in sensitivity at low energies will be compensated for by an additional array of six densely instrumented strings located in the deep, clean ice at the centre of IceCube, the so-called *DeepCore*. The denser DeepCore allows to explore the low energy region down to 50 GeV, see Fig. 9.2, while the increased veto possibility may open the window for detection of neutrinos from above the horizon until energies of 10 TeV. The sensitivity of the IceCube+DeepCore array was recently reanalyzed, using the most up to date simulation and reconstruction tools and applying a more advanced event selection. This study suggests an even more optimistic situation than Figure 9.2, with an improvement in sensitivity of at least a factor three. However, at the moment, these

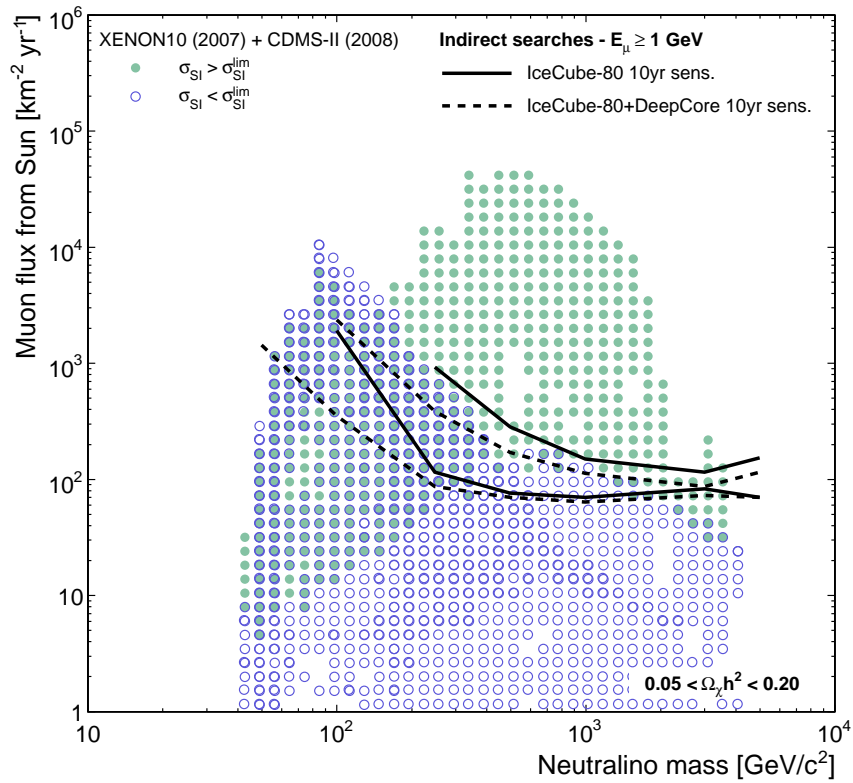


**Figure 9.2** – Muon flux sensitivity for ten years of operation of the IceCube detector in its 80-string configuration (solid line) and with the addition of the DeepCore array (dashed line). Markers as in Fig. 8.8.

results are considered preliminary.

Nevertheless, it is clear that the IceCube detector has bright prospects to discover a dark matter signal from the Sun, or in the worst case, rule out a large part of the theoretical parameter space.

# Bibliography

- [1] The Particle Data Group Collaboration, C. Amsler *et al.*, *Review of particle physics*, Phys. Lett. **B667** (2008) 1.
- [2] N. Copernicus, *De revolutionibus orbium coelestium*, 1543.
- [3] E. Hubble, *A relation between distance and radial velocity among extra-galactic nebulae*, Proc. Nat. Acad. Sci. **15** (1929) 168–173.
- [4] A. A. Penzias and R. W. Wilson, *A Measurement of excess antenna temperature at 4080-Mc/s*, Astrophys. J. **142** (1965) 419–421.
- [5] R. H. Dicke, P. J. E. Peebles, P. G. Roll and D. T. Wilkinson, *Cosmic Black-Body Radiation*, Astrophys. J. **142** (1965) 414–419.
- [6] The Supernova Search Team Collaboration, A. G. Riess *et al.*, *Observational Evidence from Supernovae for an Accelerating Universe and a Cosmological Constant*, Astron. J. **116** (1998) 1009–1038.
- [7] The Supernova Cosmology Project Collaboration, S. Perlmutter *et al.*, *Measurements of Omega and Lambda from 42 High-Redshift Supernovae*, Astrophys. J. **517** (1999) 565–586.
- [8] The WMAP Collaboration, E. Komatsu *et al.*, *Five-Year Wilkinson Microwave Anisotropy Probe (WMAP) Observations: Cosmological Interpretation*, Astrophys. J. Suppl. **180** (2009) 330–376.
- [9] G. F. Smoot *et al.*, *Structure in the COBE differential microwave radiometer first year maps*, Astrophys. J. **396** (1992) L1–L5.
- [10] W. Hu and S. Dodelson, *Cosmic Microwave Background Anisotropies*, Ann. Rev. Astron. Astrophys. **40** (2002) 171–216.
- [11] The WMAP Collaboration, M. R. Nolta *et al.*, *Five-Year Wilkinson Microwave Anisotropy Probe (WMAP) Observations: Angular Power Spectra*, Astrophys. J. Suppl. **180** (2009) 296–305.
- [12] F. Zwicky, *Die Rotverschiebung von extragalaktischen Nebeln*, Helvetica Physica Acta **6** (1933) 110–127.

- [13] V. C. Rubin and J. Ford, W. Kent, *Rotation of the Andromeda Nebula from a Spectroscopic Survey of Emission Regions*, *Astrophysical Journal* **159** (February 1970) 379.
- [14] K. G. Begeman, A. H. Broeils and R. H. Sanders, *Extended rotation curves of spiral galaxies: Dark haloes and modified dynamics*, *Mon. Not. Roy. Astron. Soc.* **249** (1991) 523.
- [15] D. Clowe *et al.*, *A direct empirical proof of the existence of dark matter*, *Astrophys. J.* **648** (2006) L109–L113.
- [16] M. Kamionkowski and S. M. Koushiappas, *Galactic Substructure and Direct Detection of Dark Matter*, *Phys. Rev.* **D77** (2008) 103509.
- [17] G. Bertone, D. Hooper and J. Silk, *Particle dark matter: Evidence, candidates and constraints*, *Phys. Rept.* **405** (2005) 279–390.
- [18] J. M. Frere, F.-S. Ling and G. Vertongen, *Bound on the Dark Matter Density in the Solar System from Planetary Motions*, *Phys. Rev.* **D77** (2008) 083005.
- [19] J. F. Navarro, C. S. Frenk and S. D. M. White, *The Structure of Cold Dark Matter Halos*, *Astrophys. J.* **462** (1996) 563–575.
- [20] B. Moore, F. Governato, T. R. Quinn, J. Stadel and G. Lake, *Resolving the Structure of Cold Dark Matter Halos*, *Astrophys. J.* **499** (1998) L5.
- [21] W. J. G. de Blok, S. S. McGaugh, A. Bosma and V. C. Rubin, *Mass Density Profiles of LSB Galaxies*, *Astrophys. J.* **552** (2001) L23–L26.
- [22] W. J. G. de Blok and A. Bosma, *H alpha rotation curves of Low Surface Brightness galaxies*, *Astron. Astrophys.* **385** (2002) 816.
- [23] A. A. Klypin, A. V. Kravtsov, O. Valenzuela and F. Prada, *Where are the missing galactic satellites?*, *Astrophys. J.* **522** (1999) 82–92.
- [24] B. Moore *et al.*, *Dark matter substructure within galactic halos*, *Astrophys. J.* **524** (1999) L19–L22.
- [25] A. V. Maccio' *et al.*, *On the origin and properties of Ultrafaint Milky Way Satellites in a LCDM Universe*, [0903.4681](https://arxiv.org/abs/0903.4681).
- [26] J. F. Navarro, C. S. Frenk and S. D. M. White, *The Assembly of Galaxies in a Hierarchically Clustering Universe*, *Mon. Not. Roy. Astron. Soc.* **275** (1994) 56–66.
- [27] J. R. Primack, *Cosmology: small scale issues*, [arXiv:0902.2506](https://arxiv.org/abs/0902.2506) [[astro-ph.CO](https://arxiv.org/abs/0902.2506)].
- [28] M. Milgrom, *A Modification of the Newtonian dynamics as a possible alternative to the hidden mass hypothesis*, *Astrophys. J.* **270** (1983) 365–370.
- [29] R. H. Sanders and S. S. McGaugh, *Modified Newtonian Dynamics as an Alternative to Dark Matter*, *Ann. Rev. Astron. Astrophys.* **40** (2002) 263–317.

- [30] J. D. Bekenstein, *Relativistic gravitation theory for the MOND paradigm*, Phys. Rev. **D70** (2004) 083509.
- [31] G. W. Angus, H. Shan, H. Zhao and B. Famaey, *On the law of gravity, the mass of neutrinos and the proof of dark matter*, Astrophys. J. **654** (2007) L13–L16.
- [32] J.-P. Bruneton, S. Liberati, L. Sindoni and B. Famaey, *Reconciling MOND and dark matter?*, [0811.3143](#).
- [33] M. Taoso, G. Bertone and A. Masiero, *Dark Matter Candidates: A Ten-Point Test*, [arXiv:0711.4996](#) [astro-ph].
- [34] G. Jungman, M. Kamionkowski and K. Griest, *Supersymmetric dark matter*, Phys. Rept. **267** (1996) 195–373.
- [35] G. L. Fogli *et al.*, *Observables sensitive to absolute neutrino masses: A reappraisal after WMAP-3y and first MINOS results*, Phys. Rev. **D75** (2007) 053001.
- [36] J. R. Primack, *Whatever happened to hot dark matter?*, SLAC Beam Line **31N3** (2001) 50–57.
- [37] L. Chuzhoy and E. W. Kolb, *Reopening the window on charged dark matter*, [arXiv:0809.0436](#) [astro-ph].
- [38] G. G. Raffelt, *Particle Physics from Stars*, Ann. Rev. Nucl. Part. Sci. **49** (1999) 163–216.
- [39] S. W. Randall, M. Markevitch, D. Clowe, A. H. Gonzalez and M. Bradac, *Constraints on the Self-Interaction Cross-Section of Dark Matter from Numerical Simulations of the Merging Galaxy Cluster 1E 0657-5*, [0704.0261](#).
- [40] M. E. Peskin and D. V. Schroeder, *An Introduction to quantum field theory*. Reading, USA: Addison-Wesley, 1995.
- [41] F. Halzen and A. D. Martin, *Quarks and Leptons: An introductory course in modern particle physics*. New York, Usa: Wiley, 1984. New York, Usa: Wiley ( 1984) 396p.
- [42] J. Wess and B. Zumino, *Supergauge Transformations in Four-Dimensions*, Nucl. Phys. **B70** (1974) 39–50.
- [43] S. P. Martin, *A Supersymmetry Primer*. 1997. [hep-ph/9709356](#).
- [44] J. Edsjö, *Aspects of neutrino detection of neutralino dark matter*. PhD thesis, Uppsala University, April 1997. [hep-ph/9704384](#).
- [45] M. P. Hertzberg, M. Tegmark and F. Wilczek, *Axion Cosmology and the Energy Scale of Inflation*, Phys. Rev. **D78** (2008) 083507.
- [46] I. Antoniadis, *A Possible new dimension at a few TeV*, Phys. Lett. **B246** (1990) 377–384.

- [47] H.-C. Cheng, J. L. Feng and K. T. Matchev, *Kaluza-Klein dark matter*, Phys. Rev. Lett. **89** (2002) 211301.
- [48] D. Hooper and S. Profumo, *Dark matter and collider phenomenology of universal extra dimensions*, Phys. Rept. **453** (2007) 29–115.
- [49] J. Ellis, *Prospects for Discovering Supersymmetry at the LHC*, [arXiv:0810.1178 \[hep-ph\]](#).
- [50] J. L. Feng, J.-F. Grivaz and J. Nachtman, *Searches for Supersymmetry at High-Energy Colliders*, [0903.0046](#).
- [51] J. Engel and P. Vogel, *Neutralino inelastic scattering with subsequent detection of nuclear gamma rays*, Phys. Rev. **D61** (2000) 063503.
- [52] J. D. Lewin and P. F. Smith, *Review of mathematics, numerical factors, and corrections for dark matter experiments based on elastic nuclear recoil*, Astropart. Phys. **6** (1996) 87–112.
- [53] J. Ellis, K. A. Olive and C. Savage, *Hadronic Uncertainties in the Elastic Scattering of Supersymmetric Dark Matter*, [arXiv:0801.3656 \[hep-ph\]](#).
- [54] C. Savage, G. Gelmini, P. Gondolo and K. Freese, *Compatibility of DAMA/LIBRA dark matter detection with other searches*, [arXiv:0808.3607 \[astro-ph\]](#).
- [55] The CDMS Collaboration, Z. Ahmed *et al.*, *Search for Weakly Interacting Massive Particles with the First Five-Tower Data from the Cryogenic Dark Matter Search at the Soudan Underground Laboratory*, Phys. Rev. Lett. **102** (2009) 011301.
- [56] The XENON Collaboration, J. Angle *et al.*, *First Results from the XENON10 Dark Matter Experiment at the Gran Sasso National Laboratory*, Phys. Rev. Lett. **100** (2008) 021303.
- [57] The XENON10 Collaboration, J. Angle *et al.*, *Limits on spin-dependent WIMP-nucleon cross-sections from the XENON10 experiment*, Phys. Rev. Lett. **101** (2008) 091301.
- [58] The COUPP Collaboration, E. Behnke *et al.*, *Improved Spin-Dependent WIMP Limits from a Bubble Chamber*, Science **319** (2008) 933–936.
- [59] The KIMS Collaboration, H. S. Lee *et al.*, *Limits on WIMP-nucleon cross section with CsI(Tl) crystal detectors*, Phys. Rev. Lett. **99** (2007) 091301.
- [60] The DAMA Collaboration, R. Bernabei *et al.*, *First results from DAMA/LIBRA and the combined results with DAMA/NaI*, Eur. Phys. J. **C56** (2008) 333–355.
- [61] C.-L. Shan, *Determining the Mass of Dark Matter Particles with Direct Detection Experiments*, [0903.4320](#).
- [62] The DM-TPC Collaboration, J. Monroe, *Neutrino backgrounds to dark matter searches and directionality*, J. Phys. Conf. Ser. **136** (2008) 022037.

- [63] P. Gondolo *et al.*, *DarkSUSY: Computing supersymmetric dark matter properties numerically*, JCAP **0407** (2004) 008.
- [64] The H.E.S.S. Collaboration, F. Aharonian *et al.*, *HESS observations of the galactic center region and their possible dark matter interpretation*, Phys. Rev. Lett. **97** (2006) 221102.
- [65] E. A. Baltz *et al.*, *Pre-launch estimates for GLAST sensitivity to Dark Matter annihilation signals*, JCAP **0807** (2008) 013.
- [66] W. de Boer, C. Sander, V. Zhukov, A. V. Gladyshev and D. I. Kazakov, *EGRET excess of diffuse galactic gamma rays as tracer of dark matter*, Astron. Astrophys. **444** (2005) 51.
- [67] G. Johannesson, *A first look at the GeV Excess with Fermi LAT*, in *Proc. XLIV Rencontre De Moriond*. 2009.
- [68] G. Weidenspointner *et al.*, *An asymmetric distribution of positrons in the Galactic disk revealed by  $\gamma$ -rays*, Nature **451** (2008) 159–162.
- [69] I. Cholis, G. Dobler, D. P. Finkbeiner, L. Goodenough and N. Weiner, *The Case for a 700+ GeV WIMP: Cosmic Ray Spectra from ATIC and PAMELA*, [0811.3641](#).
- [70] The HEAT Collaboration, S. W. Barwick *et al.*, *Measurements of the cosmic-ray positron fraction from 1-GeV to 50-GeV*, Astrophys. J. **482** (1997) L191–L194.
- [71] The AMS Collaboration, M. Aguilar *et al.*, *The Alpha Magnetic Spectrometer (AMS) on the International Space Station. I: Results from the test flight on the space shuttle*, Phys. Rept. **366** (2002) 331–405.
- [72] The Pamela Collaboration, O. Adriani *et al.*, *Observation of an anomalous positron abundance in the cosmic radiation*, Submitted to Nature (2008).
- [73] The Pamela Collaboration, O. Adriani *et al.*, *A new measurement of the antiproton-to-proton flux ratio up to 100 GeV in the cosmic radiation*, Submitted to Phys. Rev. Lett. (2008).
- [74] The ATIC Collaboration, J. Chang *et al.*, *An excess of cosmic ray electrons at energies of 300-800 GeV*, Nature **456** (2008) 362–365.
- [75] The PPB-BETS Collaboration, S. Torii *et al.*, *High-energy electron observations by PPB-BETS flight in Antarctica*, [0809.0760](#).
- [76] The H.E.S.S. Collaboration, F. Aharonian *et al.*, *The energy spectrum of cosmic-ray electrons at TeV energies*, [arXiv:0811.3894 \[astro-ph\]](#).
- [77] D. Malyshev, I. Cholis and J. Gelfand, *Pulsars versus Dark Matter Interpretation of ATIC/PAMELA*, [0903.1310](#).
- [78] G. Bertone, E. Nezri, J. Orloff and J. Silk, *Neutrinos from dark matter annihilations at the galactic centre*, Phys. Rev. **D70** (2004) 063503.

- [79] The MACRO Collaboration, M. Ambrosio *et al.*, *Limits on dark matter WIMPs using upward-going muons in the MACRO detector*, Phys. Rev. **D60** (1999) 082002.
- [80] The BAKSAN Collaboration, M. M. Boliev *et al.*, *BAKSAN neutralino search*, in *Dark Matter In Astro- And Particle Physics*, H. V. Klapdor-Kleingrothaus and Y. Ramachers, eds., p. 711. Singapore: World Sci., 1997.
- [81] The The Baikal Collaboration Collaboration, V. Aynutdinov *et al.*, *Nearly Vertical Muons From the Lower Hemisphere in the BAIKAL Neutrino Experiment*, in *First Workshop on Exotic Physics with Neutrino Telescopes (EPNT06)*, C. de los Heros, ed. Uppsala University, 2006.
- [82] The Super-Kamiokande Collaboration, S. Desai *et al.*, *Search for dark matter WIMPs using upward through-going muons in Super-Kamiokande*, Phys. Rev. **D70** (2004) 083523.
- [83] The Super-Kamiokande Collaboration, S. Desai *et al.*, *Study of TeV Neutrinos with Upward Showering Muons in Super-Kamiokande*, Astropart. Phys. **29** (2008) 42–54.
- [84] The IceCube Collaboration, J. Ahrens *et al.*, *Sensitivity of the IceCube detector to astrophysical sources of high energy muon neutrinos*, Astropart. Phys. **20** (2004) 507–532.
- [85] The IceCube Collaboration, R. Abbasi *et al.*, *Limits on a muon  $\tilde{\chi}$  from neutralino annihilations in the Sun with the IceCube 22-string detector*, submitted to PRL (2009).
- [86] The ANTARES Collaboration, E. Aslanides *et al.*, *A deep sea telescope for high energy neutrinos*, [astro-ph/9907432](#).
- [87] The ANTARES Collaboration, . M. Ageron, *Performance of the First ANTARES Detector Line*, [0812.2095](#).
- [88] U. F. Katz, *KM3NeT: Towards a km<sup>3</sup> Mediterranean neutrino telescope*, Nucl. Instrum. Meth. **A567** (2006) 457–461.
- [89] The KM3NeT Collaboration, J. Carr *et al.*, *Sensitivity studies for the cubic-kilometre deep-sea neutrino telescope KM3NeT*, [0711.2145](#).
- [90] A. Gould, *Cosmological density of WIMPs from solar and terrestrial annihilations*, Astrophys. J. **388** (1992) 338–344. IASSNS-AST-91-34.
- [91] F. Halzen and D. Hooper, *Prospects for detecting dark matter with neutrino telescopes in light of recent results from direct detection experiments*, Phys. Rev. **D73** (2006) 123507.
- [92] T. Bruch, J. Read, L. Baudis and G. Lake, *Detecting the Milky Way's Dark Disk*, [arXiv:0804.2896 \[astro-ph\]](#).
- [93] R. C. Gilmore, *Mass Limits on Neutralino Dark Matter*, Phys. Rev. **D76** (2007) 043520.

- [94] V. Barger, W.-Y. Keung, G. Shaughnessy and A. Tregre, *High energy neutrinos from neutralino annihilations in the Sun*, Phys. Rev. **D76** (2007) 095008.
- [95] M. Cirelli *et al.*, *Spectra of neutrinos from dark matter annihilations*, Nucl. Phys. **B727** (2005) 99–138.
- [96] P. Crotty, *High-energy neutrino fluxes from supermassive dark matter*, Phys. Rev. **D66** (2002) 063504.
- [97] M. Blennow, J. Edsjö and T. Ohlsson, *Neutrinos from WIMP Annihilations Using a Full Three-Flavor Monte Carlo*, JCAP **0801** (2008) 021.
- [98] L. Wolfenstein, *Neutrino oscillations in matter*, Phys. Rev. **D17** (1978) 2369–2374.
- [99] S. P. Mikheev and A. Y. Smirnov, *Resonance enhancement of oscillations in matter and solar neutrino spectroscopy*, Sov. J. Nucl. Phys. **42** (1985) 913–917.
- [100] R. Gandhi, C. Quigg, M. H. Reno and I. Sarcevic, *Neutrino interactions at ultrahigh energies*, Phys. Rev. **D58** (1998) 093009.
- [101] J. Pumplin *et al.*, *New generation of parton distributions with uncertainties from global QCD analysis*, JHEP **07** (2002) 012.
- [102] R. Gandhi, C. Quigg, M. H. Reno and I. Sarcevic, *Ultrahigh-energy neutrino interactions*, Astropart. Phys. **5** (1996) 81–110.
- [103] C. Wiebusch, *The Detection of Faint Light in Deep Underwater Neutrino Telescopes*. PhD thesis, RWTH Aachen, December 1995.
- [104] D. Chirkin and W. Rhode, *Muon Monte Carlo: A high-precision tool for muon propagation through matter*, [hep-ph/0407075](https://arxiv.org/abs/hep-ph/0407075).
- [105] G. L. Fogli, E. Lisi, A. Mirizzi, D. Montanino and P. D. Serpico, *Oscillations of solar atmosphere neutrinos*, Phys. Rev. **D74** (2006) 093004.
- [106] G. Jungman and M. Kamionkowski, *Neutrinos from particle decay in the sun and earth*, Phys. Rev. **D51** (1995) 328–340.
- [107] P. B. Price, *Kinetics of Conversion of Air Bubbles to Air-Hydrate Crystals in Antarctic Ice*, Science **267** (1995) 1802–1804.
- [108] P. B. Price and L. Bergström, *Optical Properties of Deep Ice at the South Pole: Scattering*, Applied Optics **36** (1997) 4181–4194.
- [109] N. E. Bramall, R. C. Bay, K. Woschnagg, R. A. Rohde and P. B. Price, *A deep high-resolution optical log of dust, ash, and stratigraphy in South Pole glacial ice*, Geophysical Research Letters **32** (November 2005).
- [110] P. B. Price, O. V. Nagornov, R. Bay, D. Chirkin, Y. He, P. Miocinovic, A. Richards, K. Woschnagg, B. Koci and V. Zagorodnov, *Temperature profile for glacial ice at the South Pole: Implications for life in a nearby subglacial lake*, Proc. Natl. Acad. Sci. USA **99** (June 2002) 7844–7847.

- [111] The AMANDA Collaboration, M. Ackermann *et al.*, *Optical Properties of Deep Glacial Ice at the South Pole*, *Journal of Geophysical Research* **111** (July 2006).
- [112] F. Ameli, M. Bonori and F. Massa, *Optical background measurement in a potential site for the NEMO KM undersea neutrino telescope*, *European Physical Journal C* **25** (2002) 67–75.
- [113] I. Priedea, A. Jamiesona, A. Hegera, J. Craiga and A. Zuur, *The potential influence of bioluminescence from marine animals on a deep-sea underwater neutrino telescope array in the Mediterranean Sea*, *Deep Sea Research* **55** (2008) 1474–1483.
- [114] The AMANDA Collaboration, P. Askebjør *et al.*, *Optical properties of the South Pole ice at depths between 0.8-km and 1-km*, *Science* **267** (1995) 1147–1150.
- [115] The AMANDA Collaboration, P. Askebjør *et al.*, *Optical Properties of Deep Ice at the South Pole: Absorption*, *Applied Optics* **36** (1997) 4168–4180.
- [116] E. G. Anassontzis, P. Ioannou, C. Kourkoumelis, L. K. Resvanis and H. Bradner, *Light transmissivity in the NESTOR site*, *Nucl. Instrum. Meth.* **A349** (1994) 242–246.
- [117] The ANTARES Collaboration, J. A. Aguilar *et al.*, *Transmission of light in deep sea water at the site of the Antares neutrino telescope*, *Astropart. Phys.* **23** (2005) 131–155.
- [118] W. Wagner, *Design and Realisation of a new AMANDA Data Acquisition System with Transient Waveform Recorders*. PhD thesis, Universität Dortmund, October 2004.
- [119] J. Lundberg, *On the Search for High-Energy Neutrinos: Analysis of data from AMANDA-II*. PhD thesis, Uppsala University, June 2008.
- [120] T. Messarius, *Entwurf und Realisierung des AMANDA-Softwaretriggers für das TWR-Datenauslese-System*. PhD thesis, Universität Dortmund, July 2006.
- [121] The AMANDA Collaboration, E. Andres *et al.*, *The AMANDA neutrino telescope: Principle of operation and first results*, *Astropart. Phys.* **13** (2000) 1–20.
- [122] A. Biron, *Reconstruction uncertainties due to time calibration errors*, AMANDA Internal Report 20001101, DESY-Zeuthen, November 2000.
- [123] The IceCube Collaboration, M. Ackermann and E. Bernardini for the IceCube Collaboration, *An Investigation of Seasonal Variations in the Atmospheric Neutrino Rate with the AMANDA-II Neutrino Telescope*, in *Proceedings of the 29th International Cosmic Ray Conference, Pune, India, 3-10 August 2005*, vol. 9 of HE2.2, pp. 107–110. 2005.
- [124] H. Wissing, *Climatology from muon rates*, Presented at IceCube meeting DESY-Zeuthen, October 2006.

- [125] A. Davour, *Search for low mass WIMPs with the AMANDA neutrino telescope*. PhD thesis, Uppsala University, 2007.
- [126] T. Becka, *Detection of atmospheric muon neutrinos and search for extraterrestrial neutrino sources in the AMANDA data 2002*. PhD thesis, Johannes-Gutenberg-Universität Mainz, January 2005.
- [127] M. Ackermann, *Searches for signals from cosmic point-like sources of high energy neutrinos in 5 years of AMANDA-II data*. PhD thesis, Humboldt-Universität Berlin, 2006.
- [128] C. Walck, *A Study of Life and Death of the AMANDA Detector*, tech. rep., Stockholm University, 2003.
- [129] Y. Minaeva, *Search for Neutralino Dark Matter with the AMANDA-II Neutrino Telescope*. PhD thesis, Stockholm University, 2004.
- [130] T. Burgess, *A Search for Solar Neutralino Dark Matter with the AMANDA-II Neutrino Telescope*. PhD thesis, Stockholm University, March 2008.
- [131] R. Ehrlich, *The Search for Neutralino Dark Matter with the AMANDA Neutrino Telescope*. PhD thesis, University of Maryland, 2008.
- [132] D. Heck, J. Knapp, J. N. Capdevielle, G. Schatz and T. Thouw, *CORSIKA: A Monte Carlo code to simulate extensive air showers*, Tech. Rep. FZKA-6019, Forschungszentrum Karlsruhe, 1998.
- [133] The KASCADE Collaboration, T. Antoni *et al.*, *The cosmic ray experiment KASCADE*, Nucl. Instrum. Meth. **A513** (2003) 490–510.
- [134] D. Chirkin, *Cosmic ray energy spectrum measurement with the Antarctic Muon and Neutrino Detector Array (AMANDA)*. PhD thesis, UC Berkeley, 2003. UMI-31-21434.
- [135] D. Chirkin, *dCORSIKA Update Report*, 2003.
- [136] B. Wiebel-Sooth, P. L. Biermann and H. Meyer, *Cosmic Rays VII. Individual element spectra: prediction and data*, Astron. Astrophys. **330** (1998) 389–398.
- [137] N. N. Kalmykov and S. S. Ostapchenko, *The Nucleus-nucleus interaction, nuclear fragmentation, and fluctuations of extensive air showers*, Phys. Atom. Nucl. **56** (1993) 346–353.
- [138] N. N. Kalmykov, S. S. Ostapchenko and A. I. Pavlov, *EAS and a quark - gluon string model with jets*, Bull. Russ. Acad. Sci. Phys. **58** (1994) 1966–1969.
- [139] N. N. Kalmykov, S. S. Ostapchenko and A. I. Pavlov, *Quark-gluon string model and EAS simulation problems at ultra-high energies*, Nucl. Phys. Proc. Suppl. **52B** (1997) 17–28.

- [140] A. Gazizov and M. Kowalski, *ANIS: High energy neutrino generator for neutrino telescopes*, Comput. Phys. Commun. **172** (2005) 203–213.
- [141] P. Lipari, *Lepton spectra in the earth's atmosphere*, Astropart. Phys. **1** (1993) 195–227.
- [142] A. Rizzo, *GenN++: Generator of neutrino-nucleon interactions*. Vrije Universiteit Brussel, March 2006.
- [143] L. Bergström, J. Edsjö and P. Gondolo, *Indirect detection of dark matter in km-size neutrino telescopes*, Phys. Rev. **D58** (1998) 103519.
- [144] J. Edsjö, *wf2f2000*, 2003.
- [145] T. Sjöstrand, P. Eden, C. Friberg, L. Lonnblad, G. Miu, S. Mrenna and E. Norrbin, *High-energy-physics event generation with PYTHIA 6.1*, Comput. Phys. Commun. **135** (2001) 238–259.
- [146] J. Lundberg *et al.*, *Light tracking for glaciers and oceans: Scattering and absorption in heterogeneous media with photonics*, Nucl. Instrum. Meth. **A581** (November 2007) 619–631.
- [147] A. Karle, *Monte Carlo simulation of photon transport and detection in deep ice: muons and cascades*, in *Simulation and analysis methods for large neutrino telescopes*, C. Spiering, ed. 1999.
- [148] G. Hill *et al.*, *Evidence for insufficient absorption in the AMANDA Monte Carlo*, <http://icecube.wisc.edu/~ghill/absorption/absorption.html>, 2001.
- [149] S. Hundertmark, *AMASIM neutrino detector simulation program*, in *Simulation and analysis methods for large neutrino telescopes*, C. Spiering, ed. 1999.
- [150] D. Hubert, *Aspects of neutralino weights and effective volumes*, IceCube Internal Report icecube/200711001, Vrije Universiteit Brussel, November 2007.
- [151] C. de los Heros, *Genniup*. Uppsala University, February 2004.
- [152] The AMANDA Collaboration, M. Ackermann *et al.*, *Limits to the muon flux from neutralino annihilations in the Sun with the AMANDA detector*, Astropart. Phys. **24** (2006) 459–466.
- [153] J. Edsjö, *WIMPSIM: WIMPANN and WIMPEVENT*, September 2006.
- [154] T. Burgess, *WimpEventF2k*. Stockholm University, April 2007.
- [155] A. R. Smith and R. J. McDonald, *Radioactivities in AMANDA Optical Module #13-457*, AMANDA Internal Report 19990201, LBNL, February 1999.
- [156] M. Ribordy, *AMANDA-II/2000 data statistics, OM selection and retriggering procedure*, AMANDA Internal Report 20020601, DESY Zeuthen, June 2002.

- [157] A. C. Pohl, *A statistical tool for finding non-particle events from the AMANDA neutrino telescope*, Master's thesis, Uppsala University, September 2004.
- [158] The AMANDA Collaboration, J. Ahrens *et al.*, *Muon track reconstruction and data selection techniques in AMANDA*, Nucl. Instrum. Meth. **A524** (2004) 169–194.
- [159] The AMANDA Collaboration, J. Ahrens *et al.*, *Search for neutrino-induced cascades with the AMANDA detector*, Phys. Rev. **D67** (2003) 012003.
- [160] D. Pandel, *Bestimmung von Wasser- und Detektorparametern und Rekonstruktion von Myonen bis 100 TeV mit dem Baikal-Neutrinoteleskop NT-72*, Master's thesis, Humboldt-Universität Berlin, February 1996.
- [161] G. Japaridze and M. Ribordy, *Photon arrival time distribution convoluted to a gaussian time measurement uncertainty*, AMANDA Internal Report 20031201, December 2003.
- [162] P. Steffen, *Direct-Walk II (Improved Version of Direct Walk)*, AMANDA Internal Report 20020201, DESY Zeuthen, February 2002.
- [163] A. Davour and C. de los Heros, *Optimizing Direct Walk for short tracks*, AMANDA Internal Report 20031102, Uppsala University, November 2003.
- [164] P. Steffen, *AMANDA Pattern Recognition*, June 2002.
- [165] T. Neunhoffer, *Estimating the angular resolution of tracks in neutrino telescopes based on a likelihood analysis*, Astropart. Phys. **25** (2006) 220–225.
- [166] M. Gaug, P. Niessen and C. Wiebusch, *Investigations on Smoothness observables*, AMANDA Internal Report 20000201, DESY Zeuthen, February 2000.
- [167] M. Ackermann *et al.*, *Zeuthen processing 2000-2003*, <http://www-zeuthen.desy.de/nuastro/protected/point/combined00-03/Processing.html>, 2005.
- [168] A. Davour, *WIMP filter*, <http://www3.tsl.uu.se/~akesson/wimpfilter.html>, 2006.
- [169] J. R. Klein and A. Roodman, *Blind analysis in nuclear and particle physics*, Ann. Rev. Nucl. Part. Sci. **55** (2005) 141–163.
- [170] G. C. Hill and K. Rawlins, *Unbiased cut selection for optimal upper limits in neutrino detectors: The model rejection potential technique*, Astropart. Phys. **19** (2003) 393–402.
- [171] G. J. Feldman and R. D. Cousins, *A Unified approach to the classical statistical analysis of small signals*, Phys. Rev. **D57** (1998) 3873–3889.
- [172] G. Punzi, *Sensitivity of searches for new signals and its optimization*, in *PHYSTAT2003: Statistical Problems in Particle Physics, Astrophysics, and Cosmology*. 2003. [physics/0308063](https://arxiv.org/abs/physics/0308063). Menlo Park, California, United States, 8-11 Sep 2003.

- [173] G. C. Hill, J. Hodges, B. Hughey, A. Karle and M. Stamatikos, *Examining the balance between optimising an analysis for best limit setting and best discovery potential*, in *PHYSTAT05: Statistical Problems in Particle Physics, Astrophysics and Cosmology*. 2005. Oxford, England, United Kingdom, 12-15 Sep 2005.
- [174] J. Edsjö, *Calculation of neutrino cross sections and the nuNevent neutrino-nucleon scattering Monte Carlo*, September 2007.
- [175] M. Maltoni, T. Schwetz, M. A. Tortola and J. W. F. Valle, *Status of global fits to neutrino oscillations*, *New J. Phys.* **6** (2004) 122.
- [176] G. Wikström, *A search for solar dark matter with the IceCube neutrino telescope*. PhD thesis, Stockholm University, 2009.
- [177] The IceCube Collaboration, A. Achterberg *et al.*, *Five years of searches for point sources of astrophysical neutrinos with the AMANDA-II neutrino telescope*, *Phys. Rev.* **D75** (2007) 102001.
- [178] G. Wikström and J. Edsjö, *Limits on the WIMP-nucleon scattering cross-section from neutrino telescopes*, [0903.2986](#).
- [179] J. Conrad, O. Botner, A. Hallgren and C. Perez de los Heros, *Including systematic uncertainties in confidence interval construction for Poisson statistics*, *Phys. Rev.* **D67** (2003) 012002.
- [180] G. C. Hill, *Comment on 'Including systematic uncertainties in confidence interval construction for Poisson statistics'*, *Phys. Rev.* **D67** (2003) 118101.
- [181] R. Cousins, *Treatment of nuisance parameters in high energy physics, and possible justifications and improvements in the statistics literature*, in *Proceedings of PhyStat2005, Oxford, England*. 2005.
- [182] K. Cranmer, *Statistical Challenges for Searches for New Physics at the LHC*, in *Proceedings of PhyStat2005, Oxford, England*. 2005.
- [183] J. Edsjö, *Conversion scripts*, <http://copsosx03.physto.se/cgi-bin/edsjo/amanda/convfact.cgi>, 1998.
- [184] J. R. Braun, *A Maximum-Likelihood Search for Neutrino Point Sources with the AMANDA-II Detector*. PhD thesis, UW Madison, April 2009.
- [185] L. Bergström, T. Bringmann and J. Edsjö, *New Positron Spectral Features from Supersymmetric Dark Matter - a Way to Explain the PAMELA Data?*, [arXiv:0808.3725](#) [astro-ph].

# Glossary

<b>AMANDA</b>	Antarctic Muon And Neutrino Detector Array
<b>AMASIM</b>	Simulation program of the AMANDA detector hardware
<b>ANIS</b>	MC event generator for neutrinos
<b>CC</b>	Charged-current interaction
<b>CDMS</b>	Direct dark matter detection experiment
<b>CL</b>	Confidence level
<b>CMB</b>	Cosmic Microwave Background radiation
<b>COBE</b>	Satellite that measured the temperature anisotropies in the CMB
<b>CORSIKA</b>	MC event generator for air showers
<b>COUPP</b>	Direct dark matter detection experiment
<b>DAQ</b>	Data AcQuisition
<b>DM</b>	Dark matter
<b>f.o.m.</b>	Figure of merit, used during the optimization of the event selection
<b>GenN++</b>	MC event generator for neutralino-induced neutrinos, C++ derivative of Genniup
<b>Genniup</b>	MC event generator for neutralino-induced neutrinos
<b>IceCube</b>	1 km <sup>3</sup> neutrino telescope, AMANDA's successor
<b>KIMS</b>	Direct dark matter detection experiment
<b>LKP</b>	Lightest Kaluza-Klein particle
<b>LLH</b>	Likelihood
<b>LSP</b>	Lightest supersymmetric particle
<b>MAM</b>	Optical model of South Pole ice for PTD
<b>MC</b>	Monte Carlo simulation program or technique
<b>MMC</b>	MC program to propagate muons
<b>MOND</b>	Modified Newtonian Dynamics
<b>MSSM</b>	Minimal supersymmetric extension of the Standard Model
<b>NC</b>	Neutral-current interaction
<b>OM</b>	Optical Module
<b><math>\Lambda</math>CDM</b>	Current standard model of cosmology
<b>pADC</b>	peak-sensing Analog to Digital Converter
<b>Photonics</b>	MC program to propagate photons through ice
<b>PMT</b>	Photo-multiplier tube
<b>PTD</b>	MC program to propagate photons through ice

---

<b>QGSJET</b>	Hadron interaction model
<b>SD</b>	Spin-dependent
<b>SI</b>	Spin-independent
<b>SLART</b>	Format of analysis files (SiegLinde Analysis Root Tree)
<b>SM</b>	Standard Model of particle physics
<b>Standard stream</b>	Events that satisfy the multiplicity trigger condition
<b>String stream</b>	Events that satisfy exclusively the string trigger condition
<b>Super-K</b>	Super-Kamiokande, a neutrino detector
<b>SUSY</b>	Supersymmetry, a proposed extension of the Standard Model
<b>TDC</b>	Time to Digital Converter
<b>XENON10</b>	Direct dark matter detection experiment
<b>WIMP</b>	Weakly interacting massive particle
<b>WMAP</b>	Satellite that measured the temperature anisotropies in the CMB

# Samenvatting

Het al dan niet bestaan van onzichtbare materie in het heelal is sinds het eerste vermoeden daarvan door Fred Zwicky in 1933 en vooral sinds de meting van de rotatiesnelheden van sterrenstelsels in de jaren 1970 een van de centrale thema's in de kosmologie. In de afgelopen decennia werd de gravitationele invloed van deze zogenaamde donkere materie waargenomen op alle trappen van de kosmologische afstandsladder. Hiermee werd de donkere materie gaandeweg een algemeen aanvaard element in de beschrijving van de samenstelling van het heelal. Sterker nog, de meeste kosmologen gaan er nu zelfs van uit dat het overgrote deel van de materie in het universum donker is. Ondanks sterke aanwijzingen dat het om niet-baryonische en niet-relativistische materiedeeltjes gaat, geven de huidige observaties verder geen duidelijke informatie over de fysische aard van de donkere materie. Ook het Standaard Model van de elementaire deeltjes fysica biedt geen oplossing in de vorm van een reeds gekend elementaire deeltje met de vereiste eigenschappen. Daarom heeft het mysterie rond de aard van de donkere materie misschien ook verregaande gevolgen voor ons begrip van de subatomaire wereld.

Anticiperend op nieuwe natuurkundige wetmatigheden die eventueel te ontdekken vallen bij de binnenkort bereikbare energieschalen in botsingsexperimenten, werden uitbreidingen voorgesteld voor het Standaard Model die o.a. nieuwe, hypothetische elementaire deeltjes bevatten. Mogelijk is het donkere materie deeltje het *neutralino*, dat voorkomt in supersymmetrische uitbreidingen en dat een massa heeft in het  $\text{GeV}/c^2$ – $\text{TeV}/c^2$  domein. Indien deze hypothese correct is, dan is de zon in staat om neutralino's te vangen uit de halo van donkere materie die ons sterrenstelsel omgeeft. In het binnenste van de zon zou daarom op dit ogenblik een groot aantal neutralino's aanwezig zijn, die bovendien paarsgewijs annihilieren. Deze annihilaties leiden tot een continue stroom van neutrino's met  $\text{GeV}$ – $\text{TeV}$  energie die de aarde bereiken. Het doel van dit onderzoekswerk is om deze neutrino's te detecteren met behulp van de AMANDA neutrino detector en zo een licht te werpen op de identiteit van de donkere materie.

We speuren in de data set verzameld door de Antarctic Muon And Neutrino Detector Array (AMANDA) in 2001–2003 naar signalen van neutralino-annihilaties in de zon. De data set bevat 3.5 miljard gebeurtenissen, hoofdzakelijk neergaande muonen die gecreëerd werden in botsingen van kosmische stralen in de atmosfeer boven de detector. In de thesis wordt een analyse voorgesteld die deze achtergrond gebeurtenissen verwijdert op basis van de gereconstrueerde richting en de kwaliteit van de reconstructie. Om de gevoeligheid voor zowel laag als hoog energetische neutrino's te vrijwaren, definiëren we twee klassen gebeurtenissen (wegens de trigger-afhankelijke topologie van de gebeurtenissen) en twee neutralino signaal templates (wegens de energie-afhankelijke respons van de detector) waarvoor afzonderlijke

selectiecriteria geoptimaliseerd worden.

Na het uitvoeren van deze selectie gaan we na hoeveel gebeurtenissen overblijven die afkomstig zijn van de zon. Hiervoor wordt een vernieuwende likelihood-ratio analyse gebruikt op basis van de waargenomen verdeling van de ruimtehoek tussen de richting van de zon en die van de gereconstrueerde gebeurtenis. Deze methode wordt opgesteld volgens de frequentistisch statistische voorschriften en geeft steeds aanleiding tot fysisch relevante betrouwbaarheidsintervallen, wat een belangrijk aspect is in de zoektocht naar zwakke signalen. Daarnaast combineert de methode de likelihood-functies van beide trigger topologieën, waardoor de ruimtehoek-verdelingen van beide klassen gebeurtenissen maximaal benut worden.

De hierboven vermelde analyses worden volledig blind geoptimaliseerd, wat wil zeggen dat de positie van de zon onbekend blijft tot de keuze van de selectie criteria en de instelling van de gebruikte algoritmes vastliggen. Hierna bekijken we de echte locatie van de zon, en vinden we dat de richting van de waargenomen gebeurtenissen statistisch volledig compatibel is met de verwachting voor achtergrondprocessen. We besluiten dus dat er geen statistisch significante aanwijzing is voor neutrino's van de zon in de beschouwde data set. Deze resultaten vertalen we in bovenlimieten met 90% betrouwbaarheid op de annihilatie-rate van neutralino's in de zon, de neutralino-geïnduceerde muonflux aan de detector en de elastische werkzame doorsnede van neutralino's op protonen. Dit wordt gedaan voor zeven neutralinomassa's (tussen  $50 \text{ GeV}/c^2$  en  $5000 \text{ GeV}/c^2$ ) en telkens twee extreme annihilatiekanalen (hard en zacht neutrino-energie spectrum).

In een afsluitende Monte Carlo studie vinden we dat de benaderingen in de implementatie van de lichtpropagatie doorheen ijs en de absolute gevoeligheid van de optische detector-modules de dominante bronnen van systematische onzekerheden zijn. Uitgaande van een conservatieve aanpak bekomen we een totale (statistische en systematische) onzekerheid van 35–90% op het eindresultaat, afhankelijk van het neutralinamodel onder studie. Wanneer deze onzekerheid in rekening wordt gebracht, liggen de bovenlimieten op de muon flux tussen  $9.4 \times 10^2 - 1.2 \times 10^5 \text{ km}^{-2} \text{ yr}^{-1}$  voor het hard kanaal en  $1.5 \times 10^3 - 1.3 \times 10^6 \text{ km}^{-2} \text{ yr}^{-1}$  voor het zacht annihilatiekanaal. We concluderen daarnaast dat de string trigger essentieel is voor de gevoeligheid van de analyse voor neutralino's lichter dan  $100 \text{ GeV}/c^2$ , met een winst van een factor 60 in gevoeligheid voor het laagst energetische model. De limieten op de spin-afhankelijke werkzame doorsnede vallen tussen  $0.0001 - 1 \text{ pb}$ , wat een heel competitief resultaat is in vergelijking met deze gerapporteerd door zoektochten naar neutralino's met een directe detectiemethode.

*Het denken mag zich nooit onderwerpen,  
noch aan een dogma,  
noch aan een partij,  
noch aan een hartstocht,  
noch aan een belang,  
noch aan een vooroordeel,  
noch aan om het even wat,  
maar uitsluitend aan de feiten zelf,  
want zich onderwerpen betekent het einde van alle denken.*

Henri Poincaré

21 november 1909

Uit een redevoering ter gelegenheid van de 75ste  
verjaardag van de Université Libre de Bruxelles.

